

School of Electrical Engineering, Computing and
Mathematical Sciences

Curtin Institute of Radio Astronomy

Characterising the Local Interstellar Medium using
Low-Frequency Pulsar Polarimetry

Mengyao Xue

This thesis is presented for the Degree of

Doctor of Philosophy

of

Curtin University

November 2019

To the best of my knowledge and belief this thesis contains no material previously published by any other person except where due acknowledgement has been made. This thesis contains no material which has been accepted for the award of any other degree or diploma in any university.

.....

Mengyao Xue

November 18, 2019

Acknowledgements

This work would not have been possible without the continuous support of my supervisors, family, and friends. First and foremost, I would like to express my deepest thanks to my supervisors: Dr. Ramesh Bhat, Dr. Charlotte Sobey, Dr. Stephen Ord, and Dr. Steven Tremblay. Your patience and thorough guidance helped me build up my understanding of pulsar and radio astronomy. Your support and mentoring meant so much to me throughout the entire process of this work.

The staff and students of CIRA have provided numerous useful discussions and help in every aspect relating to this work, instrumentation, software, science, English writing, etc. As an international student from a completely different cultural background, I really appreciate the inclusive environment of CIRA.

To my parents, your words and deeds benefit me for my entire life. Your support and encouragement motivated me to start this journey on science research.

To Shiyong, thanks for your love and support. Your optimistic and positive attitude toward life and work always cheers me up when I am depressed.

Abstract

The combination of new-generation low-frequency aperture arrays and advances in signal processing techniques is reinvigorating the field of low frequency pulsar astronomy — an area that has played an important role in early pulsar discoveries and science, however was reduced in prominence in the later decades. One of the reasons for this is the substantial temporal smearing of pulsar signals at the low frequencies due to interstellar medium (ISM) propagation effects. However, from another perspective, the sensitivity of ISM propagation effects to the observing frequency makes low-frequency pulsar observations powerful tools to study ISM properties, such as the electron density distribution and the Galactic magnetic fields. In this thesis, I studied the small-scale structure of the local ISM using new, low-frequency, polarimetric observations of pulsars obtained using the Murchison Widefield Array (MWA), which is Australia’s low-frequency (80–300 MHz) precursor to the Square Kilometre Array (SKA) project. The MWA is a relatively new instrument, and its high-time and high-frequency resolution mode (voltage capture system) for pulsar observations was commenced in 2014. As a result, gearing up for the research work for this thesis involved further development and testing of the MWA’s pulsar capabilities, especially the verification of its polarimetric calibration and performance.

I undertook an initial census of known pulsars in the 170 – 200 MHz band of the MWA, where the large field-of-view of the array was exploited at the expense of the achievable sensitivity. This involved the processing of over a Petabyte of data that covered $\sim 17,000$ deg² of the sky. This census resulted in a collection of 50 pulsars, including six millisecond pulsars. Combining these detections with published observational data from other telescopes, multi-frequency pulse profiles were constructed for a number of pulsars. These results were then used to improve

pulsar population models in our Galaxy, and providing further insights into pulsar detection prospects with Phase 1 of the low-frequency component of the SKA (SKA1-Low). A conservative forecast from this analysis is that SKA1-Low can potentially detect ~ 9400 pulsars, which is more than triple the number of pulsars known to date.

The development of the tied-array mode was realised later on (commissioned in 2016) and was demonstrated to achieve the full-array sensitivity. It was designed for generating calibrated full polarimetric data products. However, verifying the polarimetric performance of this new capability was an important prerequisite before putting it into science applications. Using observations of two bright southern pulsars, PSRs J0742–2822 and J1752–2806, I undertook an empirical characterisation of the MWA’s polarimetric performance. The results demonstrated that the MWA can be reliably calibrated for zenith angles less than 45° and frequencies less than 270 MHz. My analysis also led to first low-frequency polarimetric studies of these two pulsars, as well as high-precision determinations of their Faraday rotation measurements. Additionally, the degree of linear polarisation of PSR J0742–2822 showed a steady (and rapid) decline at the lower frequencies of the MWA, which stands in contrast with the generally expected trend for pulsar emission, and can be attributed to depolarisation caused by stochastic Faraday rotation from turbulent ISM in the Gum Nebula.

In order to further investigate this curious observational result, and to probe the turbulent, magneto-ionic ISM in the direction of the Gum Nebula, I then undertook detailed polarimetric studies of six pulsars located in the general direction of the Gum Nebula. Depolarisation at low-frequencies were seen for four of these pulsars, whose degree of linear polarisation were measurable at multiple different frequency bands. This reinforced my earlier hypothesis that the turbulent plasma within the Gum Nebula is the likely cause of the observed stochastic Faraday rotation. Specifically, the Vela pulsar was studied in great detail, since its propagation effects vary significantly as a function of the observing epoch. The results are discussed in a more general (and wider) context of the three-dimensional model of the Gum Nebula, which is an important component of the electron density model of the Galaxy.

Statement of Contribution by Others

The content of Chapter 3 is my own work, excepting the following. Nine hours of MWA archival data from the MWA FRB searching project were processed by Dr. Steven Tremblay. Nicholas Swainston developed the software to generate a list of known pulsars covered in the primary beam of a given observation, and this was integrated into the pulsar processing pipeline. Dr. Simon Johnston provided high-frequency pulse profiles for 16 pulsars observed by the Parkes and GMRT telescopes for multi-frequency comparison studies. A/Prof. David Kaplan provided useful guidance on estimating the system sensitivity ($A_{\text{eff}}/T_{\text{sys}}$) for the MWA primary beam when the array is pointed toward a given direction. Dr. Ramesh Bhat, Dr. Steven Tremblay, Dr. Stephen Ord and Dr. Charlotte Sobey provided guidance in terms of the structure and contextual discussion as well as improving the English and the clarity of presentation. Bradley Meyers and Samuel McSweeney also helped with improving the language and stylistic aspects of the presentation.

The content of Chapter 4 is my own work, excepting the following. The MWA observation of PSR J1752–2806 at 118 MHz was processed by Nicholas Swainston. Dr. Charlotte Sobey helped with the calculation of the ionospheric Faraday rotation measures. Dr. Ramesh Bhat, Dr. Steven Tremblay, Dr. Stephen Ord and Dr. Charlotte Sobey provided guidance in terms of the structure and contextual discussion as well as improving the English and the clarity of presentation. Bradley Meyers and Samuel McSweeney also helped with improving the language and stylistic aspects of the presentation.

The content of Chapter 5 is my own work, excepting the following. The two MWA observations of PSR J0835–4510 obtained in May 2019 were processed by Dr. Ramesh Bhat. Dr. Charlotte Sobey provided the fitting script for the depolarisation factor. Dr. Ramesh Bhat, Dr. Steven Tremblay, Dr. Stephen Ord and Dr. Charlotte Sobey provided guidance in terms of the structure and contextual discussion as well as improving the English and the clarity of presentation. Bradley Meyers and Samuel McSweeney also helped with improving the language and stylistic aspects of the presentation.

(Signature of Candidate)

(Signature of Supervisor)

Contents

Acknowledgements	v
Abstract	vii
List of Tables	xvii
List of Figures	xix
1 Introduction	1
1.1 Motivation and overview	1
1.2 Pulsars	5
1.2.1 Populations and astrophysical applications	6
1.3 Observable properties of pulsars	10
1.3.1 Pulse profiles and the emission beam structure	10
1.3.2 Pulse profile evolution with frequency	13
1.3.3 Flux density spectra	14
1.3.4 Polarisation properties	17
1.4 Effects of the interstellar medium (ISM)	20
1.4.1 Dispersion	20
1.4.2 Faraday rotation	24
1.4.3 Scattering	25

1.4.4	Scintillation	26
1.4.5	Pulsar measurements and ISM inhomogeneities	29
1.5	Pulsar studies at low radio frequencies	30
1.6	Thesis structure	33
2	Instrumentation and Methodologies	35
2.1	Overview of the Murchison Widefield Array	35
2.2	The Voltage Capture System	38
2.3	The MWA primary beam model	39
2.4	Processing MWA VCS data	43
2.4.1	Incoherent summation	44
2.4.2	Tied-array beam processing	45
2.4.2.1	Phase rotations for delay compensation	46
2.4.2.2	Jones Matrix	46
2.4.2.3	Calibration	47
2.4.2.4	Beamforming	49
2.5	RM synthesis and deconvolution	52
3	A Census of Southern Pulsars at 185 MHz	59
3.1	Summary	59
3.2	Introduction	60
3.3	Observations and analysis	64
3.3.1	The MWA and the Voltage Capture System	64
3.3.2	Observations	65
3.3.3	Pre-processing	66
3.3.4	Processing pipeline	67
3.3.4.1	Sample Selection	67

3.3.4.2	Pulsar Folding	68
3.3.4.3	Calculation of Flux Densities	69
3.4	Results	71
3.5	Discussion	74
3.5.1	Multi-frequency Pulse Profiles	74
3.5.2	Detection limits	76
3.5.3	Future detection prospects	81
3.6	Conclusion	83
4	Polarimetric Verification and Analysis of two Bright Southern Pulsars	91
4.1	Summary	91
4.2	Introduction	92
4.3	Observation and data processing	96
4.3.1	Target pulsars	96
4.3.2	Observing strategy	97
4.3.3	Calibration	102
4.3.4	Beamforming	102
4.3.5	Data reduction and analysis	104
4.3.6	Archival VCS data	105
4.4	Verification of the polarimetric response	106
4.4.1	Determining the optimal calibration strategy	107
4.4.2	Reproducibility of pulse profiles	108
4.5	Faraday rotation measures	110
4.6	Polarimetric profiles	113
4.6.1	PSR J0742–2822	113

4.6.2	PSR J1752–2806	113
4.6.3	Comparison with the literature	120
4.7	Discussion	122
4.7.1	Frequency-dependent degree of linear polarisation	122
4.7.2	Limitations of data reduction and future work	125
5	Probing the ISM towards the Gum Nebula using Pulsar Measurements	129
5.1	The Gum Nebula and its neighbourhood	129
5.2	Observations and data processing	135
5.3	RM determination for target pulsars	138
5.4	Multi-frequency polarimetric profiles and scattering timescales	144
5.5	Depolarisation at low frequencies	146
5.5.1	PSR J0742–2822	154
5.5.2	PSR J0835–4510	155
5.5.3	PSR J0630–2834	155
5.5.4	PSR J0837–4135	158
5.5.5	Phase-related depolarisation analysis	161
5.6	Long-term variations in the propagation properties of the ISM	166
5.6.1	DM and RM variations towards the Vela pulsar	168
5.6.2	Scatter broadening measurements for the Vela pulsar	172
5.7	Discussion	178
5.8	Conclusion	180
6	Summary and future prospects	183
	Appendices	189

A Statement of Originality	191
A.1 Statement of contribution for Chapter 3	191
A.2 Statement of contribution for Chapter 4	196
B Copyright permission	201
Bibliography	203

List of Tables

3.1	Parameters for 50 MWA pulsar detections	86
4.1	Observing parameters for PSR J0742–2822, PSR J1752–2806, and calibrator sources.	100
4.2	Summary of the centre observing frequencies	103
4.3	RM results for PSRs J0742–2822 and J1752–2806.	112
5.1	Observation parameters	137
5.2	Measured DMs, RMs and inferred $\langle B_{\parallel} \rangle$ for the target pulsars. . .	143
5.3	DM and RM measurements for target pulsars	167

List of Figures

1.1	The $P - \dot{P}$ diagram for known pulsars	7
1.2	Schematic diagram of a rotating neutron star	11
1.3	Multi-frequency profiles for PSR J1136+1551	15
1.4	P.A. curves with different impact angle	19
1.5	Dispersed and dedispersed pulse for PSR J1136+1551	23
2.1	MWA tiles and analog beamformer	37
2.2	The signal path of the MWA	40
2.3	The MWA tile beam as a function of frequency	41
2.4	The MWA tile beam at different elevation	42
2.5	The MWA-VCS processing	44
2.6	Auto-correlated noise	52
2.7	RM synthesis and deconvolution	56
3.1	Catalogued pulsars in Galactic coordinates	62
3.2	The sky coverage of the MWA-VCS observations	66
3.3	The MWA tile beam model at 185 MHz	68
3.4	The data processing workflow	70
3.5	Profile gallery for 50 MWA pulsar detection	73
3.6	Multi-frequency pulse profiles for a subset of MWA detection	77
3.7	S/N for detection and non-detection	80
3.8	Simulated pulsar population with the MWA result	84

4.1	Locations and MWA pointing directions for target pulsars and calibrators	99
4.2	SNR Check-board plots of the total intensity among different combination of pulsar and calibrator pointings	108
4.3	Check-board plots for the instrumental polarisation leakage among different combination of pulsar and calibrator pointings	109
4.4	RM CLEAN-ed Faraday spectra for PSR J1752–2806	114
4.5	RM CLEAN-ed Faraday spectrum for PSR J0742–2822	115
4.6	Polarimetric profiles for PSR J0742–2822 at multiple MWA frequency bands	116
4.7	Polarimetric profile and PA curve for PSR J0742–2822	117
4.8	Polarimetric profiles for PSR J1752–2806 at multiple MWA frequency bands	118
4.9	Polarimetric pulse profiles and PA curves for PSR J1752–2806	119
4.10	Multi-frequency polarimetric profiles for the two pulsars	121
4.11	Degree of linear polarisation as function of frequency for PSRs J0742–2822 and J1752–2806	123
4.12	The deviation in normalised Stokes Q gain value between the analytical and FEE beam models	126
5.1	An $H\alpha$ image of the Gum Nebula	130
5.2	The 2D model of the Gum nebula area	134
5.3	Faraday spectra for J0630	139
5.4	Faraday spectra for J0742	139
5.5	Faraday spectra for J0737	140
5.6	Faraday spectra for J0835	141
5.7	Faraday spectra for J0837	142
5.8	Faraday spectra for J0959	142
5.9	The multi-freq polarimetric profiles for J0630	147

5.10	The multi-frequencies polarimetric profiles for J0742	148
5.11	The multi-frequencies polarimetric profiles for J0835	149
5.12	The multi-frequencies polarimetric profiles for J0835	150
5.13	The polarimetric profiles and P.A. curves for J0630, J0742, and J0737	151
5.14	The polarimetric profiles and P.A. curves for J0835, J0837, and J0959	152
5.15	Degree of linear polarisation as function of frequency for J0742 . .	156
5.16	Degree of linear polarisation as function of frequency for J0835 . .	157
5.17	Degree of linear polarisation as function of frequency for J0630 . .	159
5.18	Degree of linear polarisation as function of frequency for J0837 . .	160
5.19	Phase-related polarisation degree for J0742	163
5.20	Phase-related polarisation degree for J0835	164
5.21	Phase-related polarisation degree for J0630	165
5.22	The long-term variation of the RM, DM for the Vela pulsar	170
5.23	Schematic plots explaining the observed DM and RM variation for the Vela pulsar based on Hamilton85 model	173
5.24	Schematic plots describing my explanation of the observed DM and RM variation for the Vela pulsar	174
5.25	Schematic plots describing my explanation of the observed DM and RM variation for the Vela pulsar	175
5.26	Scattering profiles for J0835 at different epoch	177

Chapter 1

Introduction

1.1 Motivation and overview

The interstellar medium (ISM) accounts for around 10% of the total baryonic mass in our Galaxy, and plays an important role in its evolution ([Draine, 2011](#)). Matter is exchanged between stars and the ISM through star formation processes, including stellar winds, nova and supernova explosions. Having a good understanding of the physics of the ISM is therefore important for developing an improved understanding of our own Galaxy, as well as for its comparison to other similar galaxies.

The ISM is complex, and astronomers spend a great deal of effort trying to understand its physical properties using multiple different methods and tracers. The physics and properties of the ISM is quite complex. Pulsars, as one of such tracers, are particularly useful probes of the ISM because they are distributed throughout the Galaxy. Since a large number of pulsars have distance measurements (obtained using methods that may or may not depend on the Galactic electron density models), they can potentially provide information about the three-dimensional structure of the ISM. Distance measurements that are independent of the Galactic electron density model (e.g. [Taylor & Cordes, 1993](#); [Cordes & Lazio, 2002](#); [Yao et al., 2017](#)) include annual parallax via Very Long Baseline

Interferometry (VLBI; e.g. [Chatterjee et al., 2009](#); [Deller et al., 2009, 2019](#)), optical astrometry (e.g. [Caraveo et al., 2001](#); [Jennings et al., 2018](#)), and pulsar timing (e.g. [Hotan et al., 2006](#); [Matthews et al., 2016](#)). Model-dependent approaches include HI kinematic distances (e.g. [Weisberg et al., 1979](#); [Koribalski et al., 1995](#); [Weisberg et al., 2008](#)), associations with globular clusters, associations with Nebulae (supernova remnants, HII regions, etc).

There is a long history of radio astronomers using pulsars to probe the ISM properties in our Galaxy. Many attempts have been made to use the dispersion measure (DM) of a large sample of pulsars to map out the Galactic electron density distribution, e.g. [Manchester & Taylor \(1981\)](#), [Lyne et al. \(1985\)](#), [Taylor & Cordes \(1993\)](#), [Cordes & Lazio \(2002\)](#), and [Yao et al. \(2017\)](#). Having a well-modeled Galactic electron density distribution can provide estimates of the distances to pulsars for which independent distance determinations are difficult to achieve. In addition to the DM, the Faraday rotation measure (RM) obtained from pulsar observations is often used to model both large scale (e.g. [Han et al., 2006](#); [Sobey et al., 2019](#)), and local (e.g. [Rand & Kulkarni, 1989](#)) Galactic magnetic fields. Apart from studying our own Galaxy, this foreground provides an estimate of the Galactic contribution to the observational properties of Fast Radio Bursts (FRBs; [Lorimer et al., 2007](#)), which are thought to originate at cosmic distances (e.g. [Thornton et al., 2013](#); [Chatterjee et al., 2017](#)). It is also important to have a good understanding of the Galactic foreground for measuring the Cosmic Microwave Background (CMB; e.g. [Planck Collaboration et al., 2011](#)) and the Epoch of Reionisation (EoR; e.g. [Barry et al., 2019](#)).

The ISM affects pulsar signals passing through it in many different ways. In addition to dispersion and Faraday rotation, which are integrated effects caused by the ionised ISM column along the line-of-sight, inhomogeneous turbulent structures in the ISM also give rise to interstellar scintillation and broadening of the pulsar profiles, as a result of multi-path scattering. All these propagation effects are strongly dependent on the observing frequency. Dispersion and Faraday ro-

tation are proportional to the inverse square of the observing frequency, ν , while the scattering time scale has a much steeper dependence, proportional to ν^{-4} (for a thin screen model) — that is, these effects are all significantly stronger at low radio frequencies. Pulsars detected at low radio frequencies are therefore more likely to be relatively nearby pulsars with low to moderate DMs (Pilia et al., 2016). On the other hand, high-DM pulsars towards the Galactic plane (especially those close to the Galactic centre) are less likely to be detected at low frequencies because of substantial DM smearing, and/or the pulse broadening caused by scattering, aside from the bright sky background prevalent at low frequencies. All of these lead to lower signal-to-noise ratios in the observed pulse profiles. Despite these difficulties, low-frequency observations of pulsars are extremely important because they allow astronomers to characterise the ISM more precisely than that may be possible through observations at higher frequencies, where the propagation effects tend to be more subtle. A further advantage for observing pulsars towards lower frequencies is that they are generally intrinsically brighter, due to their steep, power law spectral indices (see Section 1.3.3).

The local ISM, which is within a few hundred parsecs (pc) around our solar system, includes multiple prominent structures such as the Local Bubble (e.g. Cox & Reynolds, 1987), Loop I (North Polar Spur; Berkhuijsen et al., 1971), and the Gum Nebula — the largest H α emission nebula (Gum, 1952). It presents a unique laboratory to study the properties of the small-scale structure in the ISM, including the distribution of the ionised gas, physical processes driving its turbulence, and the structure of the magnetic field at spatial scales of $\sim 10 - 100$ AU. Pulsar measurements can meaningfully, and uniquely, contribute to our understanding of these structures. For example, based on 15 years of observational data on the Vela pulsar (PSR J0835–4510), Hamilton et al. (1985) found that its DM has steadily decreased while the RM steadily increased. This intriguing observational result was interpreted in terms of the relative motion of magnetised filaments in the region of the supernova remnant.

The primary aim of this thesis is to study the small-scale structure of the local ISM using new, low-frequency (< 300 MHz), polarimetric observations of pulsars obtained using the Murchison Widefield Array (MWA; [Tingay et al., 2013](#)). The MWA is a relatively new radio telescope, and its high-time and high-frequency resolution mode for pulsar observations commenced in 2014 ([Bhat et al., 2014](#)). The MWA and its pulsar mode are described in detail in Chapter 2. Further development of the MWA pulsar mode capabilities, particularly testing and science verification of the polarimetry, thus formed a vital component of this thesis. Progress on this front was realised in two stages: (1) an initial census of Southern sky pulsars using the MWA's incoherent mode ([Xue et al., 2017](#), Chapter 3), and (2) the verification of the MWA's polarimetric, tied-array mode using two known pulsars, PSRs J0742–2822 and J1752–2806 ([Xue et al., 2019](#), Chapter 4).

This initial pulsar census provided a collection of bright pulsars at low frequencies in the Southern sky. It is important to have such a reference sample of pulsars from observations at low-frequency, because inferring pulsars' behaviour at low frequencies by extrapolating from their properties at higher frequencies have limitations due to the uncertain flux density spectral index, pulse profile evolution with frequency, and propagation effects such as pulse broadening caused by interstellar scattering. This census provided a short list of pulsars that can be used for further detailed analysis (e.g. for polarimetric studies, single pulse studies, etc.). They were also used to obtain useful further insights into the pulsar detection prospects with the upcoming SKA1-Low (i.e. Phase I of the low-frequency component of the Square Kilometre Array).

The polarimetric verification of the MWA's tied-array mode (commissioned in 2016; [Bhat et al., 2016](#)), was an important prerequisite in order to gear up this new capability for science applications. Using two bright southern pulsars, PSRs J0742–2822 and J1752–2806, I undertook an empirical verification, with the goal of characterising the polarimetric performance of the MWA in its tied-array

mode. This forms the subject of Chapter 4.

Following the successful demonstration of the MWA's polarimetric capability, the focus of my work shifted to probing the magneto-ionic turbulent ISM toward the Gum Nebula, using full polarimetric MWA observations of selected pulsars located in the general direction of the Gum Nebula, including new measurements for one of the brightest, and most well-studied, Vela pulsar. This forms the subject matter of Chapter 5.

1.2 Pulsars

Pulsars are rapidly rotating and highly magnetised (the strength of the magnetic field, $B \sim 10^{12}$ G) neutron stars with a typical radius of ~ 10 km and a typical mass of $\sim 1.4 M_{\odot}$. The concept of a neutron star was first proposed by [Baade & Zwicky \(1934\)](#) when they attempted to explain the mechanism of supernova explosions. This new form of star was proposed to be the end point of the evolution of a massive star whose initial mass is ~ 10 to $30 M_{\odot}$. According to the theory of stellar structure and evolution, massive stars undergo a rapid collapse and violent explosion after they run out of light atomic nuclei fuel for nuclear fusion, which produce the radiation pressure to resist gravity and thus maintain equilibrium. The material ejected from supernova explosions interact with the interstellar medium, forming the supernova remnant. The remaining core of the progenitor star will form a neutron star (or a black hole, if the initial stellar mass is even larger).

These prophetic remarks seemed at that time to be beyond any possibility of actual observation, since a neutron star would be small, cold and inert, and would emit very little electromagnetic radiation. However, more than 30 years later, the discovery of pulsars provided a totally unexpected confirmation of the original hypothesis.

In 1967, a periodic radio signal of astronomical origin was discovered by Jocelyn Bell and Antony Hewish ([Hewish et al., 1968](#)) at a fairly low radio fre-

quency of 81.5 MHz. This astronomical object (now known as PSR B1919+21, or PSR J1921+2153) was eventually identified as a rapidly rotating neutron star. Since then, more than 2700 radio pulsars have been discovered¹ [Manchester et al. \(2005a\)](#). They are named according to their right ascensions and declinations in B1950 or J2000 coordinates with a PSR prefix followed by a ‘B’ or a ‘J’, respectively.

Pulsar emission takes place at the expense of the rotational kinetic energy of the neutron star (e.g. [Ostriker & Gunn, 1971](#)). Therefore, the rotational spin periods P of isolated pulsars gradually increase with time. The time derivative of the pulse period, $\dot{P} = dP/dt$, is also an important observable parameter and indicates the spin-down rate. P and \dot{P} can be obtained to very high precisions from pulsar timing measurements. These measurements provide unique insights into the spin evolution of neutron stars and are summarised in the ‘ $P-\dot{P}$ ’ diagram (Figure 1.1)

1.2.1 Populations and astrophysical applications

Aside from 29 pulsars in the large and small Magellanic clouds, the remainder of the ~ 2700 known radio pulsars are located in our Galaxy. Moreover, 149 of these pulsars reside in 28 Galactic globular clusters², and there is a concentrated distribution of pulsars towards the Galactic plane. Since they are the result of violent supernova explosions, pulsars are thought to receive impulsive natal ‘kicks’, and are therefore distributed over a much larger range in galactic latitude than their massive progenitors (O and B type stars). Observational studies of proper motion measurements suggest that pulsars often have large space velocities ($\sim 100 \text{ km s}^{-1}$, or more; e.g. [Chatterjee et al., 2009](#); [Deller et al., 2019](#)), which corroborates the natal kick hypothesis. The origin of these kicks may be to do with the asymmetries in the supernova explosions (e.g. [Lyne & Lorimer, 1994](#)).

¹ATNF Pulsar Database v1.60; www.atnf.csiro.au/research/pulsar/psrcat

²www.naic.edu/~pfreire/GCpsr.html

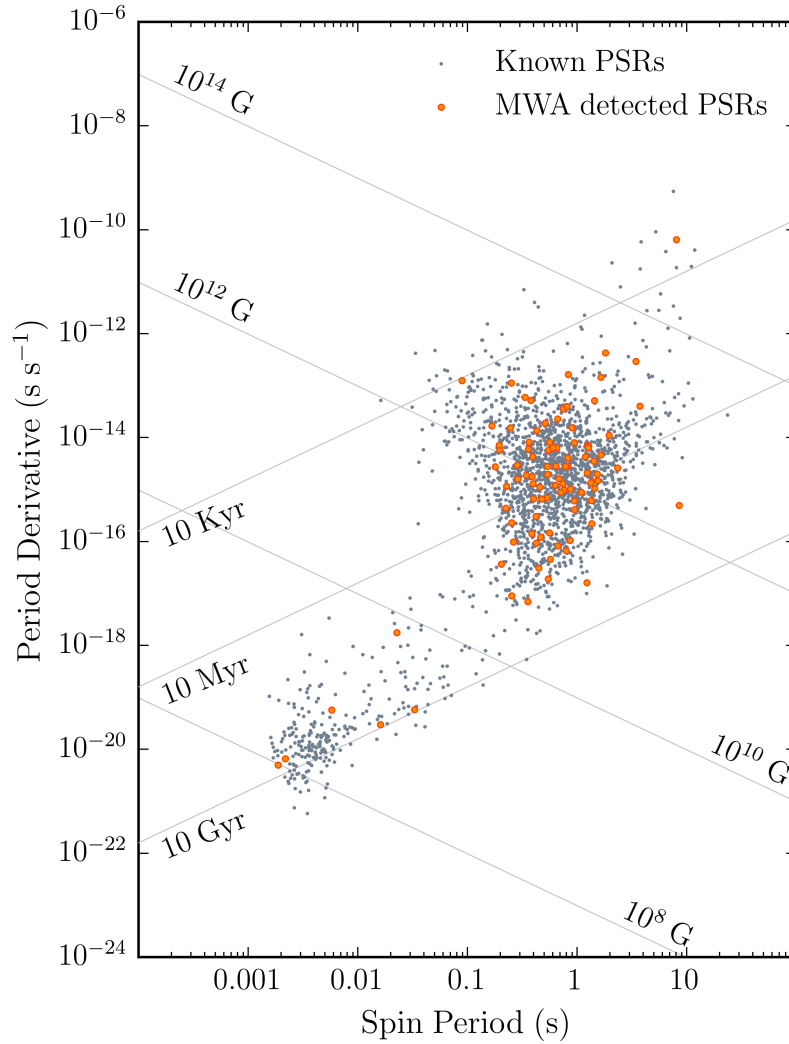


Figure 1.1: The $P - \dot{P}$ diagram for known radio pulsars (gray dots) and 102 MWA detected pulsars (orange dots; [Xue et al., 2017](#), Smith et al. in prep.) with available period (P) and period derivative (\dot{P}) measurements. The central clump represents non-recycled pulsars and the bottom-left clump represents millisecond pulsars. Lines of constant magnetic field strength (10^8 to 10^{14} G) and characteristic age (10^4 to 10^{10} yr) are drawn and suitably labelled.

Pulsars can nominally be classified into ‘normal pulsars’ (also called ‘non-recycled pulsars’) and ‘millisecond pulsars’ (MSPs, also called ‘recycled pulsars’). There is a clear distinction between normal pulsars and MSPs in the ‘ $P - \dot{P}$ ’ diagram (Figure 1.1).

MSPs typically have rotational periods in the range of about ~ 1 -10 milliseconds and occupy the lower left part of the $P - \dot{P}$ diagram. They are old, rapidly rotating neutron stars that have been ‘spun up’ or ‘recycled’ through the accretion of matter from a companion star in a close binary system (e.g. Lorimer, 2008). The first MSP discovered was PSR B1937+21 (PSR J1939+2134) (Backer et al., 1982). This neutron star has a remarkably short rotation period, 1.558 ms, close to the fastest MSP currently known (PSR J1748–2446ad, $P = 1.39$ ms; Hessels et al., 2006). MSPs tend to have some different properties than normal pulsars (e.g. the evolution of pulse profile width with observing frequencies; Kramer et al., 1999). Bright millisecond pulsars with short periods and narrow pulse widths are ideal tools for high-precision timing measurements. They can be used to develop pulsar-based time standard with precision that rival those achievable with the best terrestrial clocks (Matsakis et al., 1997; Hobbs et al., 2019a). A large sample of millisecond pulsars can be employed to form a so-called pulsar timing array (PTA). It offers us the best chance to detect the stochastic gravitational wave background, which is thought to be produced by the mergers of massive black holes as galaxies formed and evolved. Pulsar timing arrays are amongst some of the highest-profile programs around the world, with projects underway in Australia³, Europe⁴, North America⁵, as well as internationally combined efforts⁶ (Hobbs et al., 2010; van Haasteren et al., 2011; Hobbs, 2013; Manchester & IPTA, 2013; McLaughlin, 2013).

The first binary pulsar, PSR B1913+16 (PSR J1915+1606), was discovered

³The Parkes Pulsar Timing Array (PPTA; www.atnf.csiro.au/research/pulsar/ppta)

⁴The European Pulsar Timing Array (EPTA; www.epta.eu.org)

⁵North American Nanohertz Observatory for Gravitational Waves (NANOGrav; nanograv.org)

⁶The International Pulsar Timing Array (IPTA; ipta4gw.org)

by [Hulse & Taylor \(1975\)](#) using the Arecibo radio telescope. This binary system consists of two neutron stars with nearly equal masses, and has an orbital period of about 7.75 hours. One of the neutron stars is a pulsar with a period of 59 milliseconds, whilst no periodic radio pulsation signals have yet been detected from the other neutron star — probably because of the unfavorable viewing angle. The orbital size of this system has shrunk since its discovery, and is in perfect agreement with the expected value from gravitational radiation at the expense of orbital energy ([Taylor & Weisberg, 1982](#); [Taylor et al., 1992](#)). The measurement of orbital shrinkage due to this effect was the first experimental demonstration of the existence of gravitational waves as predicted by Einstein’s general theory of relativity, and its discoverers won the Physics Nobel prize in 1993. Another fascinating system is a double neutron star binary, in which both objects have been observed as radio pulsars. This is the first ‘double pulsar’ system ([Burgay et al., 2003](#); [Lyne et al., 2004](#)), which consists of a 22.7 ms pulsar (PSR J0737–3039A) in a 2.4-hour orbit with a much younger 2.77 s pulsar (PSR J0737–3039B). The system has already proven to be a powerful laboratory for fundamental gravitational physics ([Kramer et al., 2006](#)).

The interior structure of neutron stars, or the equation of state that accurately describes it, remains uncertain, notwithstanding the fact that significant constraints have been obtained using precision timing observations of higher-mass pulsars (e.g. [Demorest et al., 2010](#); [Antoniadis et al., 2013](#); [Cromartie et al., 2019](#)). Some of the models predict a maximum neutron star mass of about $2 M_{\odot}$ ([Lattimer & Prakash, 2001](#)), although this upper limit may be relaxed (or can be larger) when the magnetic field is extremely strong ([Cardall et al., 2001](#)).

The currently known Galactic population of pulsars represents the ‘tip of the iceberg’ of the predicted total detectable Galactic population, which is estimated to be $\sim 120,000$ ([Faucher-Giguère & Kaspi, 2006](#)). [Lorimer et al. \(2006\)](#) used results from the most successful pulsar surveys to date, notably the Parkes Multi-beam Pulsar Survey ([Manchester et al., 2001](#)) and the high-latitude pulsar survey

(Burgay et al., 2006, which used the same observing system), to form a data set comprising 1008 pulsars. Based on these, they formed models for the pulsar period, luminosity and spatial distributions in the Galaxy. They also developed a pulsar population simulation software package called PSRPOP⁷, which has been widely used to predict the expected yields of future pulsar surveys, or to study different features of the pulsar population. The original Fortran version has been rewritten using the PYTHON programming language; this new PSRPOPpy⁸ package provides increased modularity and accessibility for new contributors (Bates et al., 2014). PSRPOPpy has been used in this work to generate pulsar population models using pulsar detections made with the MWA’s incoherently summed data as inputs. These models were then used to forecast the detection prospects with the SKA1-Low, as discussed in Chapter 3.

1.3 Observable properties of pulsars

The observed radio emission from pulsars is generally thought to be produced by the acceleration of charged particles along highly magnetised field lines surrounding neutron stars. The overall magnetic field structure of pulsars is thought to be dipolar to the first order, and the magnetic axis is inclined to the rotation axis. A pulse signal is observed whenever the emission beam sweeps past the line-of-sight of the observer, producing a ‘lighthouse-like’ effect (see Fig.1.2). If the magnetic axis and the rotation axis are almost orthogonal, the beam from both magnetic poles can sweep past our line-of-sight, producing pulses separated by about 180° in pulse longitude (the less intense pulse is called an ‘interpulse’).

1.3.1 Pulse profiles and the emission beam structure

With the exception of a small fraction of relatively nearby bright pulsars, it is generally difficult to detect individual pulses from the vast majority of the

⁷psrpop.sourceforge.net

⁸github.com/samb8s/PsrPopPy

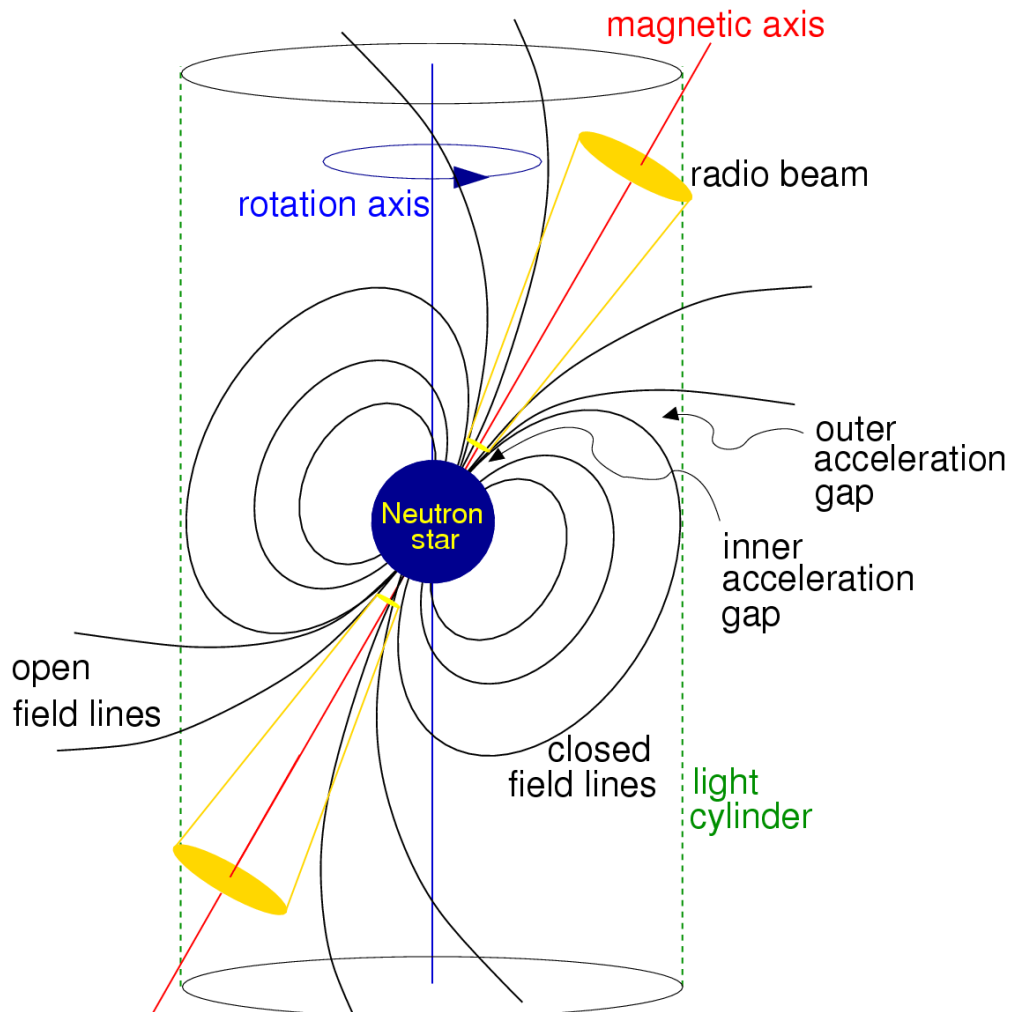


Figure 1.2: A schematic diagram of the magnetic dipole model for a radio pulsar. The emission beam is centred on the magnetic axis, which is inclined to the rotation axis, thereby producing the ‘lighthouse’ effect. The light cylinder is the boundary of the magnetosphere of the neutron star, where the surrounding magnetospheric plasma co-rotates at the speed of light. Field lines that close within the light cylinder are classified as *closed field lines*, while others are classified as *open field lines*. Acceleration regions in the magnetosphere where plasma is depleted are marked as ‘gaps’. Image courtesy of [Lorimer & Kramer \(2005\)](#).

pulsar population, because their radio emission is typically of the order of a few mJy. Even with highly sensitive radio telescopes, individual pulses can only be observed for a small subset of the total pulsar population. For most pulsars, in order to increase the signal-to-noise ratio of the pulse profile, we need to synchronously average (fold) the observation along the time axis according to the rotation period of the pulsar, and create an integrated pulse profile from hundreds, or even thousands, of individual pulses.

Although the individual pulses often show significant difference in their intensities and shapes from one rotation period to another, the integrated pulse profile for a given pulsar is usually quite stable (except for some pulsars whose emission switches between two or more modes, often referred to as ‘mode changing’ pulsars; e.g. [Lyne, 1971](#); [Lyne et al., 2010](#)). The integrated pulse profile reflects the overall statistical properties of pulsar emission (for a large sample of pulses), while the individual pulses reflect the instantaneous state of the emission region (e.g. [Lange et al., 1998](#)).

The integrated pulse profile for each pulsar has a characteristic shape, which represents a cross-sectional cut through the pulsar’s emission beam. Some pulsars have relatively simple profiles (i.e. consisting of a single component), while others contain multiple components with more complex structure in the pulse profile. The observed pulse shape depends critically on the size and structure of the emission beam, as well as the angle between our line-of-sight and the beam centre.

In order to explain these different kinds of observed pulse profiles, several models of the pulsar beam structure have been introduced. The basic hollow cone model, which was developed shortly after the discovery of pulsars ([Radhakrishnan & Cooke, 1969](#); [Komesaroff, 1970](#)), was later extended by introducing an additional axial beam ([Backer et al., 1976](#)), which produces a ‘core’ component that has been observed in some pulse profiles. Based on this, a nested cone structure, which consists of one or more emission cones (core, inner cone, and outer cone) that are concentric about the magnetic pole, was developed by multi-

ple investigators (e.g. Rankin, 1993a,b; Sieber, 1997). Lyne & Manchester (1988) suggested a somewhat different model: a patchy beam structure that can explain many components (up to more than 10 in some pulsars, e.g. PSR J0437–4715) as the cutting of emission beams more or less randomly footed on the polar cap. Occasionally, these subbeams can form regular patterns such as those seen in drifting subpulses (Backer, 1973; Basu & Mitra, 2018).

1.3.2 Pulse profile evolution with frequency

For most pulsars, the observed pulse profiles change as a function of frequency. In some cases, the profile evolution with frequency is mild, while in some other cases, it can be dramatic. The pulse width for non-recycled pulsars usually tends to decrease with increasing observing frequency. For example, Johnston et al. (2008) showed that for non-recycled pulsars with single component profiles, the pulse width generally narrowed by $\sim 30\%$ from 240 to 3100 MHz. For non-recycled pulsars with double or more complex pulse profiles, the separation between components tend to decrease with increasing radio frequency (e.g. Komesaroff et al., 1970). An example can be seen in Figure 1.3, which presents the multi-frequency profiles for PSR J1136+1551 (B1133+16), a bright, well-studied pulsar whose pulse profile consists of two distinct components.

One of the theoretical explanations for this is the radius-to-frequency mapping (RFM) model. Its concept was introduced by Ruderman & Sutherland (1975), as part of their pulsar emission theory. They suggested the radio emission of a pulsar is generated by the ultra-relativistic plasma motion along magnetic field lines. Thus, the emission frequency is related to local plasma conditions. Different altitudes have different local plasma conditions, and as a result, observations at different frequencies sample different open field line regions. Consequently, radio emission at lower frequencies arises from higher altitudes in the magnetosphere than those at higher frequencies. At higher altitudes from the pulsar surface, the magnetic field lines are sparser, and therefore low-frequency emitting regions

extend larger than those at high frequencies (as is the case for PSR J1136+1551 in Figure 1.3). Based on this model, Cordes (1978) calculated the emission height with the separation angle of profile components.

However, a radically different approach suggests that the curvature radiation by the motion of particles along the magnetic field lines should be broad-band and all emission is created at a single emission height. The observations can be explained by the propagation of natural polarisation modes in the pulsar magnetosphere (Barnard & Arons, 1986; McKinnon, 1997). This model assumes that one of the polarisation modes can escape the magnetosphere directly, while the emission of the other mode is ducted along the field lines before it can escape to reach the observer.

There is still no clear conclusion for the cause of the profile width change as a function of the observing frequency, since the emission mechanism and emission height of pulsars are not yet fully understood. Furthermore, except for those studied with Pushchino (e.g. Kuzmin et al., 1998) or LOFAR (e.g. Bilous et al., 2015; Pilia et al., 2016), for the majority of the known pulsars to date⁹ (~ 2700), there is still a lack of knowledge of their pulse profiles at frequencies below 300 MHz. In order to better understand the emission mechanism of pulsars, it is therefore important to obtain pulse profiles at low radio frequencies for a large sample of pulsars, which may also help develop a more complete picture of their profile evolution with frequency.

1.3.3 Flux density spectra

The mean flux densities of pulsars often have a strong inverse dependence on the observing frequency (e.g. Sieber, 1973; Maron et al., 2000; Bates et al., 2013; Jankowski et al., 2018). This is one of the basic observables of pulsar emission and can provide constraints on the energetics of the pulsar emission mechanism (e.g. Bhat et al., 2014; Bilous et al., 2016). Flux density measurements are also crucial

⁹ATNF Pulsar Database v1.60; www.atnf.csiro.au/research/pulsar/psrcat

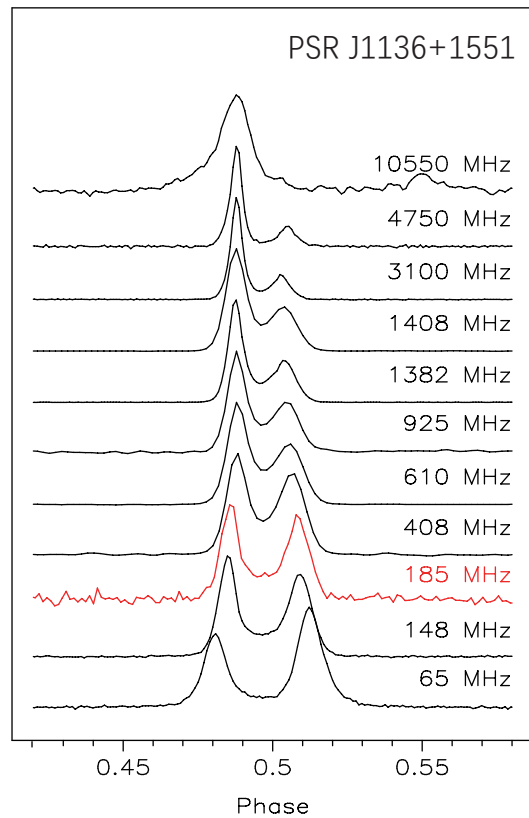


Figure 1.3: The integrated pulse profiles for PSR J1136+1551 at multiple observing frequencies. The red line indicates the pulse profile obtained using the MWA while the black lines indicate pulse profiles obtained using other radio telescopes (including LOFAR, the Lovell telescope, Parkes, and Effelsberg) from the literature (Bilous et al., 2016; Gould & Lyne, 1998; Johnston & Kerr, 2018; Johnston et al., 2005, 2006; Seiradakis et al., 1995).

for deriving the pulsar luminosity function, which is used to study the birth rates and initial spin period distribution of the Galactic population of radio pulsars (Bates et al., 2013; Lorimer et al., 2006), and for planning the optimal frequency coverage of future pulsar surveys. Across the usual radio frequency range of pulsar observations (0.1 – 10 GHz), pulsar spectra tend to approximately follow a simple power law ($S \propto \nu^{-\alpha}$), where S is the flux density observed at frequency ν and α is the spectral index (Sieber, 1973). Generally, pulsar spectra tend to follow a simple power law, however, some sub-sets of pulsars, e.g. magnetars (neutron stars with extremely strong magnetic field, $\sim 10^{13} - 10^{15}$ G, see Mereghetti et al. 2015), tend to have a more complex spectral behaviour. Moreover, low-frequency observations show that some pulsars tend to have a low-frequency turnover at $\lesssim 100$ MHz (e.g. Malofeev, 1996), or a break in power law (e.g. Maron et al., 2000; Bilous et al., 2016). There are also observational evidences for a curvature nature of spectra (flatter at lower frequencies) of pulsars (Malofeev et al., 2000).

A number of works have been done to estimate the average pulsar spectral index. Lorimer et al. (1995) presented an average spectral index $\alpha = -1.6 \pm 0.3$ from the observation of 280 pulsars between 0.4 and 1.6 GHz, while Maron et al. (2000) derived a mean of -1.8 ± 0.2 with a similar data set but extended frequency range. Malofeev et al. (2000) obtained the mean index of -1.47 ± 0.76 at observing frequencies of $\sim 100 - 400$ MHz. They explained the difference between their results and previous works in terms of a steepening of the spectral index at higher radio frequencies. More recently, Bates et al. (2013) provided an estimation based on their pulsar population synthesis. Their results suggest pulsar spectral indices could be described by a Gaussian distribution with a mean value of -1.41 and a standard deviation of 0.96 . The mean spectral indices of millisecond pulsars are observed to be consistent with that of the normal pulsar population (Kramer et al., 1998; Toscano et al., 1998).

1.3.4 Polarisation properties

The radio emission of pulsars is often highly polarised. Most pulsars show a significant amount of linear polarisation and many of them show some level of circular polarisation. The degree of linear polarisation of pulsar radio emission is about 20 percent, on average, and can reach 100 per cent in some cases (e.g. [Weltevrede & Johnston, 2008](#); [Han et al., 2009](#)). For circular polarisation, the polarisation degree is about 10 per cent, on average (e.g. [Gould & Lyne, 1998](#); [Weisberg et al., 1999](#); [Johnston & Kerr, 2018](#)).

In order to conveniently describe the polarisation state of partially polarised electromagnetic wave, George Gabriel Stokes defined a set of four parameters in 1852. Eq. (1.1) shows the definition and expression of these four Stokes parameters, I , Q , U , and V

$$\mathbf{s} = \begin{bmatrix} I \\ Q \\ U \\ V \end{bmatrix} \equiv \begin{bmatrix} |E_x|^2 + |E_y|^2 \\ |E_x|^2 - |E_y|^2 \\ 2 \operatorname{Re}(E_x E_y^*) \\ -2 \operatorname{Im}(E_x E_y^*) \end{bmatrix} = \begin{bmatrix} E_x^2 + E_y^2 \\ E_x^2 - E_y^2 \\ 2E_x E_y \cos \delta \\ 2E_x E_y \sin \delta \end{bmatrix} \quad (1.1)$$

where E_x and E_y represent the electric field that can be obtained by orthogonal linear feeds in a radio antenna; δ is the phase difference between the two orthogonal components, x and y , which are perpendicular to the wave propagation direction z .

Stokes I gives the total intensity and Stokes V gives the circular polarisation of the observed source. The complex linear polarisation vector, \mathbf{P} , is obtained from the observed Q and U Stokes parameters, and is given by

$$\mathbf{P} = Q + iU \quad (1.2)$$

And the intensity of linear polarisation is

$$L = \sqrt{Q^2 + U^2} \quad (1.3)$$

The observed linear polarisation position angle (P.A.), χ , is also derived from these parameters, and is defined as

$$\chi = \frac{1}{2} \arctan \left(\frac{U}{Q} \right). \quad (1.4)$$

The radio emission from pulsars is broadly thought to originate within the open field lines of the magnetosphere, with the emission beam centred on the magnetic axis (e.g. [Komesaroff, 1970](#)). Consequently, the P.A. will be determined by the direction of the magnetic field line as it sweeps across our line-of-sight. The P.A. measured as a function of the rotational phase, referred to as the P.A. curve, is generally expected to delineate an S-shape, i.e., the P.A. will vary more slowly at the outer wings of the pulse profile compared to the centre. This is popularly referred to as the rotating vector model (RVM; [Radhakrishnan & Cooke, 1969](#)). Conventionally, the rotation phase of the pulsar, ϕ , is defined to be zero at the *fiducial plane*, which is defined by the rotation axis and the vector pointing from the pulsar to the observer. According to the RVM model, the P.A., χ , can be expressed as a function of rotation phase:

$$\tan \chi = \frac{\sin \alpha \sin \phi}{\sin(\alpha + \beta) \cos \alpha - \cos(\alpha + \beta) \sin \alpha \cos \phi}, \quad (1.5)$$

where α is the inclination angle of the magnetic axis with respect to the rotation axis; β is the *impact angle*, which represents the closest approach of the observing line-of-sight to the magnetic axis. Fitting the RVM model to the observed P.A. curve provides an estimation of the geometry of the emission beam (e.g. [Narayan & Vivekanand, 1982](#); [Everett & Weisberg, 2001](#)). Figure 1.4 illustrates how the P.A. curve looks like when different impact angle is adopted.

The degree of linear polarisation generally tends to decrease with increasing observing frequency (e.g. [Morris et al., 1981](#); [von Hoensbroech et al., 1998a](#)). The physical explanation for this is not straightforward, though may be due to higher frequencies traversing more of the magnetosphere ([Johnston et al., 2008](#)), or the birefringence of plasma in the open field-line region of pulsar magnetospheres (e.g. [McKinnon, 1997](#)).

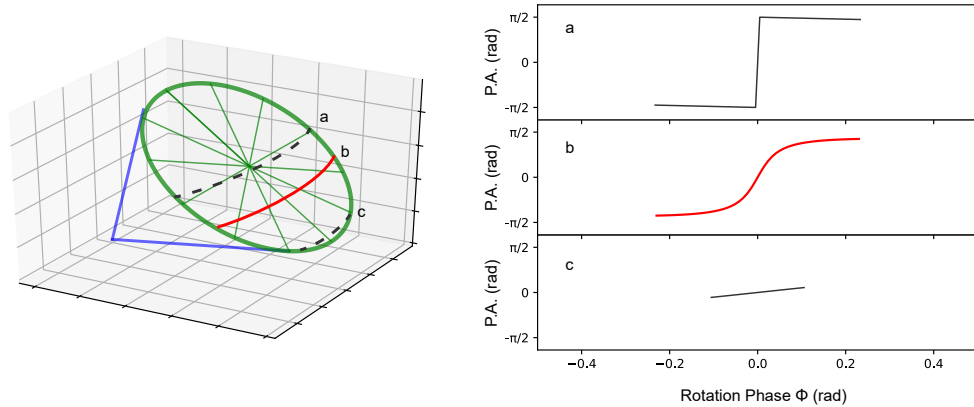


Figure 1.4: Modeled P.A. curves with three different values for the impact angle β . The inclination angle between the magnetic axis and the rotation axis, α , is fixed to 45° while the radius of the emission beam is fixed to 30° . The left panel is a schematic plot of the emission beam (not to scale). In the right panel, case (a), (b), and (c) illustrate the P.A. curve whose $\beta = 0^\circ, 2^\circ, 24^\circ$, respectively. Case (b) presents a nice ‘S-shape’ curve (plotted in red).

For some pulsars, especially those with moderate or low levels of linear polarisation, their P.A. curves show interruptions of approximately 90° , referred to as orthogonal jumps (e.g. [McKinnon & Stinebring, 1998](#)). For example, [Karastergiou et al. \(2011\)](#) present the polarimetric profiles for PSR J0738–4042 at different epochs, and find that the presence of orthogonal jumps in the P.A. curves are associated with reduced degrees of linear polarisation. Such observational evidence affirms the concept that pulsar emission is possibly comprised of two superposed orthogonal polarisation modes (OPMs): the ‘ordinary’ (O) mode, and the ‘extraordinary’ (X) mode. [Novick et al. \(1977\)](#) suggested that there could be birefringent plasma in pulsar magnetospheres. When propagating through these birefringent plasma, the X-mode emission stays on its original path and continues to propagate close to the magnetic axis after exiting the birefringent medium, while the O-mode emission is refracted along the magnetic-field lines by the birefringent medium. The refractive index is however frequency-dependent

(von Hoensbroech et al., 1998b), and therefore the O-mode emission is refracted further away from the magnetic axis at low radio frequencies. As a result, the opening angle between these two modes increases towards low-frequencies. The observed polarisation intensity $L = |L_X - L_O|$ is in the same orientation with the dominant component (either O or X). If both modes are beamed roughly in the same direction, as is the case for high radio frequencies, then the two modes will have similar intensities and depolarise each other, leading to weak or no observed polarisation. Therefore, as the two propagation modes separate more at lower frequencies, the observed radio emission of pulsars is expected to have a higher degree of linear polarisation. There have been a number of associated studies from both observational (e.g. Edwards & Stappers, 2004; Noutsos et al., 2015; Xue et al., 2019) and theoretical (e.g. Gangadhara, 1997; Melrose et al., 2006; van Straten & Tiburzi, 2017) points of view. Yet, the nature of the OPMS continues to be one of the least understood aspects of pulsar emission.

1.4 Effects of the interstellar medium (ISM)

The radio signals that pulsars emit interact with the interstellar medium (ISM) and undergo multiple propagation effects before they are received by the telescope. The ISM accounts for around 10% of the total baryonic mass in the Milky Way Galaxy. Except for $\sim 1\%$ that exists in the form of interstellar dust, the remainder $\sim 99\%$ exists in the form of interstellar gas. Around 20% of the interstellar gas is ionised, which has more interaction with the electromagnetic radiation.

1.4.1 Dispersion

When the radio signals from pulsars traverse the ISM, they experience a frequency-dependent refractive index due to the ionised component of the ISM. This is given

by,

$$\mu = \sqrt{1 - \frac{\omega_p^2}{\omega^2}}, \quad (1.6)$$

where ω is the angular frequency of the observing band ($\omega = 2\pi\nu$), and ω_p is the plasma frequency:

$$\omega_p = \sqrt{\frac{4\pi n_e e^2}{m_e}}. \quad (1.7)$$

where e is the elementary charge, m_e is the electron mass, and n_e is the electron density.

The group velocity of the propagating wave v_g is

$$v_g = c\mu. \quad (1.8)$$

According to the Taylor series expansion,

$$\frac{1}{v_g} \simeq \frac{1}{c} \left(1 + \frac{1}{2} \left(\frac{\nu_p}{\nu} \right)^2 \right). \quad (1.9)$$

Therefore, the time for the electromagnetic signal at frequency ν to traverse the ISM from the pulsar to the Earth over a distance d can be expressed as

$$t = \left(\int_0^d \frac{dl}{v_g} \right) = \frac{1}{c} \int_0^d \left(1 + \frac{1}{2} \left(\frac{\nu_p}{\nu} \right)^2 \right) dl = \frac{d}{c} + \frac{e^2}{2\pi m_e c} \frac{1}{\nu^2} \int_0^d n_e dl. \quad (1.10)$$

The integrated column density of free electrons along the line-of-sight is defined as the dispersion measure (DM; [Davidson & Terzian, 1969](#)), and is given by

$$\text{DM} \equiv \int_0^d n_e dl, \quad (1.11)$$

which is usually expressed in the units of pc cm^{-3} .

According to Eq. (1.10), signals at lower observing frequencies arrive at the telescope later than those at higher frequencies. The time delay between two frequencies, ν_1 and ν_2 (where $\nu_1 < \nu_2$) can be expressed as:

$$\Delta t = \frac{e^2}{2\pi m_e c} \left(\frac{1}{\nu_1^2} - \frac{1}{\nu_2^2} \right) \times \text{DM}. \quad (1.12)$$

Substituting the values of e , m_e , c , and applying the units typically used in practice, the equation can be re-written as

$$\frac{\Delta t}{\text{ms}} \simeq 4.15 \times 10^6 \left[\left(\frac{\nu_1}{\text{MHz}} \right)^{-2} - \left(\frac{\nu_2}{\text{MHz}} \right)^{-2} \right] \times \frac{\text{DM}}{\text{pc cm}^{-3}}. \quad (1.13)$$

It is important to note that approximating the numerical factor to 4.15 is primarily for convenience and can be used for first order estimation. In practice, using the full precision of the coefficient, 4.148808, is necessary in order to apply dispersion correction in observations.

By measuring the time delay for the pulsar signal at multiple different frequency bands, we can directly obtain its DM. It is crucial to correct the time delay caused by the dispersion effect at different observing frequency channels before adding them together in order to increase the detected signal-to-noise ratio of the target pulsar. Figure 1.5 shows an example of the dispersion effect on the pulse signal at a range of observing frequencies.

For some pulsars, their distances can be measured independently (e.g. using parallax, kinematic distances from HI absorption, or other methods). Combining their independent distance measurements with DMs provides useful information to model the Galactic electron density distribution. Some notable Galactic electron density models are TC93 (Taylor & Cordes, 1993), NE2001 (Cordes & Lazio, 2002), and YMW16 (Yao et al., 2017). These n_e distribution models make it possible to directly estimate the unknown distance d to a pulsar using its DM.

Moreover, a precise DM correction is important for pulsar timing, which is also being used for the search of gravitational waves via pulsar timing arrays (e.g. You et al., 2007). Measuring DMs at low radio frequencies can reach much higher precision because the time delay caused by dispersion $\Delta t \propto \nu^{-2}$, which means this propagation effect is much more pronounced at lower observing frequencies (e.g. Bhat et al., 2018; Kaur et al., 2019).

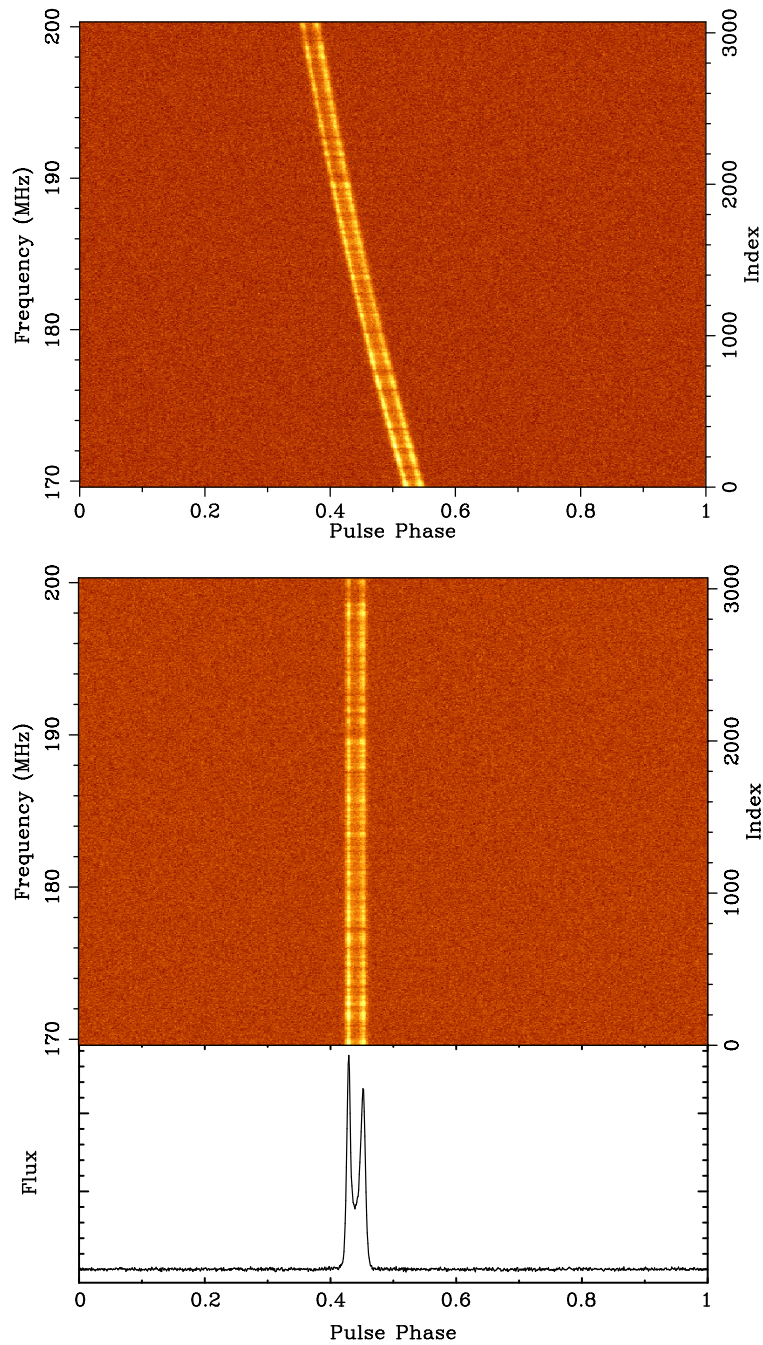


Figure 1.5: The total intensity plotted against the pulse phase and the observing frequency for PSR J1136+1551 (pulse period $P=1.188$ s; $DM=4.841$ pc cm $^{-3}$). This 25-minute observation was obtained using the MWA’s high time ($100 \mu\text{s}$) and frequency (10 kHz) resolution mode, centred at 184.96 MHz with 30.72 MHz bandwidth. The upper panel shows the dispersion from the ionised ISM, which causes the pulsar signals at the lowest band arriving ~ 198 ms later than those at the highest band. The bottom panel shows the dedispersed pulse.

1.4.2 Faraday rotation

As polarised pulsar signals travel through the magneto-ionised ISM, they undergo the Faraday rotation effect (e.g. [Smith, 1968](#)). This effect causes the P.A. of the pulsar emission to rotate by an amount that is proportional to the wavelength squared:

$$\chi(\lambda^2) = \chi_0 + \text{RM} \lambda^2, \quad (1.14)$$

where λ is the observing wavelength, and χ_0 indicates the intrinsic P.A. of the pulsar emission. The coefficient is known as rotation measure (RM, with units of rad m^{-2}), which can be expressed as a function of the integrated column density of electrons and the strength of the Galactic magnetic field along the line-of-sight (B_{\parallel}):

$$\text{RM} = \frac{e^3}{2\pi m_e^2 c^4} \int_0^d n_e B_{\parallel} dl. \quad (1.15)$$

Traditionally, the RMs of pulsars were obtained through measuring the gradient of the observed P.A. as a function of the wavelength squared (e.g. [Rand & Lyne, 1994](#)), or through a brute force search in the RM space to find the value that provides the maximum linear polarisation (e.g. [Han et al., 1999](#)). In recent polarimetric studies of pulsars with LOFAR ([Noutsos et al., 2015](#); [Sobey et al., 2019](#)), an advanced technique, known as RM Synthesis ([Burn, 1966](#); [Brentjens & de Bruyn, 2005](#)), is used to measure RMs. This method is also applied to MWA data to measure RMs in my work, and is described in detail in [Section 2.5](#).

With the information of both RM and DM, the Galactic magnetic field parallel to the line-of-sight, B_{\parallel} , can be estimated ([Manchester, 1972](#); [Lyne & Smith, 1989](#)):

$$\langle B_{\parallel} \rangle = 1.23 \mu\text{G} \left(\frac{\text{RM}}{\text{rad m}^{-2}} \right) \left(\frac{\text{DM}}{\text{pc cm}^{-3}} \right)^{-1}. \quad (1.16)$$

Therefore, polarisation observations of pulsars can be used as efficient 3-D probes of the Galactic magnetic field structure. There have been multiple works trying to model the structure of the Galactic magnetic field using RM measurements of

pulsars, e.g., [Han et al. \(1999, 2006\)](#), [Noutsos et al. \(2008\)](#), [Van Eck et al. \(2011\)](#), and [Sobey et al. \(2019\)](#).

1.4.3 Scattering

The electron density distribution in our Galaxy is far from homogeneous, and is concentrated into clumps on a wide range of length scales (e.g. [Armstrong et al., 1981](#)). This inhomogeneity leads to multipath propagation effects including scattering and scintillation (see Section [1.4.4](#)).

The variation in electron densities distort and scatter the pulse profile shape. This effect can be approximated as a thin scattering screen of dense plasma located between the pulsar and Earth that refracts the pulsar signal. Electromagnetic waves with larger angles of refraction arrive at later times, which is observed as a broadening of the pulse shape.

Consider the distance between the pulsar and the observer to be d , and the distance between the scattering screen and the observer to be d_s . The radio signal received by the observer at an angle θ will have a time delay,

$$\Delta t(\theta) = \frac{\theta^2 d_s}{c}. \quad (1.17)$$

The observed intensity, I , can be modelled (and is often observed) as the intrinsic pulse shape convolved with an exponential decay as a function of time,

$$I(t) \propto e^{-\Delta t/\tau_s}, \quad (1.18)$$

where the scattering timescale τ_s represents the time to decay in intensity by $1/e$ ([Taylor & Cordes, 1993](#)) and can be used to characterise the temporal broadening.

The corresponding scattering disk size θ_s and the scattering timescale τ_s follows the relation:

$$\tau_s = \frac{\theta_s^2 d_s}{c}. \quad (1.19)$$

The scattering timescale shows a power law relationship with the observing frequency:

$$\tau_s \propto \nu^{-\alpha}. \quad (1.20)$$

For the thin screen model as described above, the scaling index $\alpha = 4$ (Scheuer, 1968). In reality the variations in electron density in the ISM show a distribution of scales rather than a single thin screen. Assuming $\delta n_e \propto n_e$, and adopting a power-law wavenumber spectrum for δn_e , the power spectrum of electron density irregularities, $P_{\delta n_e}(q)$, can be expressed as:

$$P_{\delta n_e}(q) = C_n^2 q^{-\beta}, \kappa_o \leq q \leq \kappa_i \quad (1.21)$$

where $q = (q_x^2 + q_y^2 + q_z^2)^{1/2}$ is the magnitude of the three-dimensional wavenumber; κ_i and κ_o are the ‘inner’ and ‘outer’ scales of the fluctuations in δn_e , respectively; C_n^2 is the spectral coefficient for a truncated power-law spectrum of spatial fluctuations in the interstellar free-electron density, which represents the ‘level of turbulence’ (Cordes et al., 1985). The scattering index α and the exponent of the wavenumber spectrum β have the following relation, $\alpha = 2\beta/(\beta - 2)$ (Lee & Jokipii, 1976). For a Kolmogorov spectrum that follows the turbulent cascade model, the wavenumber spectrum $\beta = 11/3$, and therefore with such model, $\alpha = 22/5 = 4.4$ (e.g. Lee & Jokipii, 1976; Armstrong et al., 1995). There are observational evidences in favour of and against a purely Kolmogorov spectrum. In general, for small scales (up to $\sim 10^{11}$ m), the Kolmogorov spectrum seems to be quite successful in explaining the observations, while for large scales (\gtrsim refractive scales) some observations tend to favor a wavenumber spectrum with larger β than Kolmogorov spectrum which means a smaller α , i.e., a flatter scaling index for the observed scattering (Geyer et al., 2017; Kirsten et al., 2019).

1.4.4 Scintillation

The inhomogeneous ISM that causes pulse broadening (scattering) can also cause the observed intensity of the pulsar signal to vary in both time and frequency,

which is referred to as interstellar scintillation (ISS). The interstellar scintillation of pulsar signals was first identified shortly after the discovery of pulsars (Lyne & Rickett, 1968), and was explained in terms of diffraction from small-scale irregularities in the ionised ISM (Rickett, 1969). Since pulsars are point sources, their angular size is small enough to show diffractive interstellar scintillation (DISS).

The scintillation pattern can be measured from the two-dimensional image of pulse intensity as a function of observation time and frequency, referred to as the dynamic spectrum. The enhanced regions of flux density in this frequency-time plane are called scintles. Their size in frequency, i.e., scintillation bandwidth, also referred to as the decorrelation bandwidth, $\Delta\nu_{\text{DISS}}$, is usually defined as the half-width at half-maximum of the autocorrelation function of the dynamic spectrum. Similarly, the scintle size in time, or the scintillation timescale Δt_{DISS} , can be measured as the $1/e$ width along the time axis.

The signals received over the time τ_s have a phase variation of $\delta\Phi \sim 2\pi\nu\tau_s$. As in optics, diffraction can only occur when the phases of the electromagnetic waves do not differ by more than ~ 1 rad. Consider a circular region on the scattering screen centred around the source at which the phase differences are $\lesssim 1$ rad, the size of this region is known as the field coherence scale, given by

$$s_0 = 1/(k\theta_s), \quad (1.22)$$

where the wavenumber $k = 2\pi/\lambda$, and θ_s is the scattering disk size.

The scattering time scale, τ_s , and the decorrelation bandwidth, $\Delta\nu_{\text{DISS}}$, have the following relation,

$$2\pi\tau_s\Delta\nu_{\text{DISS}} = C_1. \quad (1.23)$$

The ‘constant’ C_1 is close to unity (Rickett, 1977); however, its value changes somewhat for different geometries and models of the turbulence wavenumber spectrum. For a Kolmogorov spectrum, $C_1 = 1.16$ (e.g. Lambert & Rickett, 1999).

As discussed in the previous subsection, $\tau_s \propto \nu^{-\alpha}$; therefore, the decorrelation bandwidth $\Delta\nu_{\text{DISS}} \propto \nu^\alpha$. Since τ_s increases with distance to the scattering screen d_s , we expect $\Delta\nu_{\text{DISS}}$ to decrease accordingly. For a Kolmogorov spectrum, $\Delta\nu_{\text{DISS}} \propto \nu^{4.4} d^{-2.2}$, and $\Delta t_{\text{DISS}} \propto \nu^{1.2} d^{-0.6}$.

Therefore, for nearby pulsars whose $\Delta\nu_{\text{DISS}}$ is too large to observe at high radio frequencies, we can probe their DISS properties using low-frequency observations. For example, using 185 MHz data from the MWA, [Bhat et al. \(2016\)](#) measured the diffractive scintillation properties for a close-by millisecond pulsar, PSR J0437–4715 with $\text{DM} = 2.645 \text{ pc cm}^{-3}$ and distance $\sim 157 \pm 3 \text{ pc}$ ([Deller et al., 2008](#)). The measured $\Delta\nu_{\text{DISS}} = 1.7 \text{ MHz}$, and $\Delta t_{\text{DISS}} = 260 \text{ s}$ at 185 MHz. While for the Rotating Radio Transient (RRAT) J2325–0530, with $\text{DM} = 14.966 \text{ pc cm}^{-3}$ and distance $\sim 0.7 - 1.5 \text{ kpc}$, [Meyers et al. \(2019\)](#) measured $\Delta\nu_{\text{DISS}} = 102 \pm 72 \text{ MHz}$, and $\Delta t_{\text{DISS}} = 3478 \pm 2550 \text{ s}$ at 1.4 GHz, but could only obtain an upper limit, $\Delta\nu_{\text{DISS}} \lesssim 0.01 \text{ MHz}$, at 154 MHz.

The relationship between the scintillation timescales and the relative motion of the pulsar allows us to determinate the pulsars' speed transverse to the line-of-sight, V_{ISS} . The scintillation timescale, Δt_{DISS} , and field coherence scale, s_0 , are related to V_{ISS} by

$$V_{\text{ISS}} = \frac{s_0}{\Delta t_{\text{DISS}}}. \quad (1.24)$$

Using the definition of s_0 Eq. (1.22), together with Eq. (1.24), Eq. (1.19) and Eq. (1.23)

$$V_{\text{ISS}} = A \left(\frac{d_s}{\text{kpc}} \right)^{1/2} \left(\frac{\Delta\nu_{\text{DISS}}}{\text{MHz}} \right)^{1/2} \left(\frac{\nu}{\text{GHz}} \right)^{-1} \left(\frac{\Delta t_{\text{DISS}}}{\text{s}} \right)^{-1}, \quad (1.25)$$

where the constant A depends on multiple different factors including the form of the turbulence spectrum, the relative geometry and location between the pulsar and the scattering screen, etc. Its numerical value varies across different authors: e.g. $A = 3.85 \times 10^4 \text{ km s}^{-1}$ ([Gupta, 1995](#)), and $A = 2.53 \times 10^4 \text{ km s}^{-1}$ ([Cordes & Rickett, 1998](#)).

Another branch of strong ISS is refractive interstellar scintillation (RISS). Unlike DISS, which was recognised soon after the discovery of pulsars, RISS was not noticed until 1982. [Sieber \(1982\)](#) first recognised a strong correlation between the characteristic time scales of long-term intensity variations and the dispersion measure, indicating that slow (longer-term) intensity modulations could be attributed to the ISM instead of intrinsic variations in the pulsar emission, as was previously thought ([Helfand et al., 1977](#)). [Rickett et al. \(1984\)](#) proposed that the long term propagation effect can be explained in terms of the focusing and defocusing of the electron-magnetic radiation, caused by larger-scale inhomogeneities in the ISM. In contrast to Δt_{DISS} , the characteristic time scale, $\Delta t_{\text{RISS}} \propto \nu^{-2.2} d^{1.6}$, which is shorter at higher observing frequencies and increases with distance. For nearby pulsars observed at metre wavelengths, their Δt_{RISS} can range from weeks to months. For example, for PSR J0332+5434 ($\text{DM} = 26.764 \text{ pc cm}^{-3}$, distance $\sim 1 \text{ kpc}$), [Stinebring et al. \(1996\)](#) found that its $\Delta t_{\text{RISS}} \sim 22$ days, based on over 5 years observations.

1.4.5 Pulsar measurements and ISM inhomogeneities

The inhomogeneities in the ISM, e.g., due to its turbulent structure, causes fluctuations in density, velocity, as well as the magnetic field strength and direction, over a large range of spatial scales, which stimulates the formation of stars and the evolution of the Galaxy.

The spectral energy density scale of interstellar turbulence is thought to follow a power-law (Eq. 1.21), over at least 12 decades in spatial scales, all the way from 10^6 m to 10^{18} m (e.g. [Lee & Lee, 2019](#)). Multiple different pulsar measurements have been used to constrain this density power spectrum. A Kolmogorov-like power law in small scale structure ($10^6 - 10^{12} \text{ m}$) was inferred from studies of pulsar scintillation (e.g. [Lee & Jokipii, 1975, 1976](#); [Armstrong et al., 1981, 1995](#)) and angular broadening (of both pulsars and extragalactic sources) using VLBI observations (e.g. [Vandenberg, 1974](#); [Gwinn et al., 1993](#); [Popov et al., 2019](#)).

Fluctuations on spatial scales ranging from $\sim 3 \times 10^{11}$ to 5×10^{12} m can be studied by measuring pulsars' DM variations (e.g. Phillips & Wolszczan, 1991). Recently, Petroff et al. (2013) analysed the DM variations of 168 pulsars and constructed their DM structure functions; only three pulsars showed significant DM variations that exceeded the predictions based on a Kolmogorov power spectrum. They concluded that this excess is likely due to the pulsars' local environment – the supernova remnants near PSRs J0835–4510 and J1833–0827, and the pulsar wind nebula around PSR J0908–4913. Moreover, the structure function of RM variations (mostly obtained from extragalactic radio sources) can provide constraints on large scales, $\sim 3 \times 10^{15} - 2 \times 10^{18}$ m, i.e. between ~ 0.1 to 70 pc (e.g. Simonetti et al., 1984; Simonetti & Cordes, 1988; Lazio et al., 1990).

1.5 Pulsar studies at low radio frequencies

Although low-frequency observations (< 300 MHz) played a considerably important role in early pulsar discoveries and science (e.g. Taylor & Manchester, 1977; Taylor & Stinebring, 1986), the vast majority of currently known pulsars¹⁰ (~ 2700) were discovered and studied at relatively high radio frequencies, between 300 MHz and a few GHz. This is due to a compromise between three frequency-dependent effects: (1) the greater broadening of pulsed signals towards lower frequencies due to the ISM propagation effects, particularly multipath scattering, which scales with the observing frequency ($\propto \nu^{-4}$, e.g. Bhat et al. 2004), (2) the increase in telescope system temperature towards lower frequencies due to the diffuse Galactic continuum emission ($\propto \nu^{-2.6}$; Lawson et al. 1987), and (3) the decrease in flux densities towards higher frequencies due to pulsars' steep intrinsic spectral indices ($\propto \nu^{-1.4}$, on average; Bates et al. 2013).

Pulsars are once again being routinely observed and studied at low frequencies, thanks to advances in instrumentation and computing; in particular, there

¹⁰ATNF Pulsar Database v1.60; www.atnf.csiro.au/research/pulsar/psrcat

have been multiple recently upgraded or constructed telescopes operating below 300 MHz and their associated computing facilities: e.g., the Giant Metrewave Radio Telescope (GMRT; [Swarup et al., 1991](#); [Roy et al., 2010](#)), the Long Wavelength Array (LWA; [Taylor et al., 2012](#); [Stovall et al., 2015](#)), the Low-Frequency Array (LOFAR; [van Haarlem et al., 2013](#); [Stappers et al., 2011](#)), and the MWA ([Tingay et al., 2013](#); [Tremblay et al., 2015](#)). Besides the MWA, all other facilities are located in the Northern Hemisphere. In fact, 22% of the known pulsar population can only be observed at low frequencies using the MWA ($-90^\circ \leq \delta \lesssim -50^\circ$). Moreover, the sensitivity of aperture array telescopes decreases rapidly for lower elevation pointings ($\lesssim 30^\circ$; [Noutsos et al., 2015](#); [Stovall et al., 2015](#)), which means reduced sensitivity at declinations below approximately -10° for LOFAR and -30° for the LWA and above approximately $+30^\circ$ for the MWA. These telescopes are situated over a range of longitudes, and there is a significant overlap in the observable sky. This is particularly useful for monitoring observations and verifying results (e.g. [Hermsen et al., 2013](#); [Dolch et al., 2014](#); [Mereghetti et al., 2016](#)).

Low-frequency observations of pulsars provide useful insights into the physics of the radio emission mechanism and the ISM properties (e.g. [Stappers et al., 2011](#)), especially in a multi-frequency context. For example, using the RFM to explain profile evolution with frequency (e.g. [Ruderman & Sutherland, 1975](#)). Furthermore, pulse profiles are often observed to show an increasingly rapid evolution towards lower frequencies (e.g. [Bhat et al., 2014](#); [Pilia et al., 2016](#)). This is possibly due to the frequency-dependence of the emission beam opening angle ([Thorsett, 1991](#); [Xilouris et al., 1996](#)), which also depends on the pulsar spin period and spin-down rate ([Kijak & Gil, 1998, 2003](#)). Therefore, comparing low-frequency observations to those at higher frequencies for a representative sample of pulsars can enable us to better understand the beam geometry and provide further insights into the enigmatic radio emission mechanism from pulsar magnetospheres.

Low-frequency pulsar observations also provide precise measurements of properties of the ionised ISM, including electron densities (e.g. [Hassall et al., 2012](#); [Bilous et al., 2016](#)) and magnetic fields (e.g. [Noutsos et al., 2015](#); [Howard et al., 2016](#)). This is due to the steep frequency dependence of the propagation effects, as described in Section 1.4. For example, [Stovall et al. \(2015\)](#) compared the DMs obtained from LWA 10 – 88 MHz data with the catalogue DM for 44 known pulsars, and found that the largest DM difference occurred for PSR J0034–0721, indicating a DM variation rate of $0.016 \text{ pc cm}^{-3} \text{ yr}^{-1}$. Their DM measurements reached errors on the order of $10^{-5} \text{ pc cm}^{-3}$. [Meyers et al. \(2018\)](#) updated the DM for the intermittent pulsar J1107–5907 from 40.2 pc cm^{-3} ([Lorimer et al., 2006](#)) to 40.75 pc cm^{-3} using MWA 140 – 170 MHz observations. Using MWA 80 – 220 MHz data, [Kaur et al. \(2019\)](#) precisely measured the DM for PSR J2241–5236, a promising MSP for PTAs, with an uncertainty on the order of $10^{-6} \text{ pc cm}^{-3}$. Using observations from the German LOng-Wavelength (GLOW) consortium (part of LOFAR), [Donner et al. \(2019\)](#) reported strong and rapid DM variations toward PSR J2219+4754, as well as observational evidence for a frequency dependence of its DM, possibly caused by small-scale density variations in the interstellar electron content. Recently, using LOFAR observations at 110 – 190 MHz, [Sobey et al. \(2019\)](#) determined RMs towards 137 pulsars in the northern sky, producing a low-frequency RM catalogue of pulsars, and achieving over 20 times better precision (on average) than most literature measurements. Scattering studies with low-frequency instruments ([Geyer et al., 2017](#); [Kirsten et al., 2019](#); [Bansal et al., 2019](#)) suggest a relatively small scattering spectral index α , compared to the theoretical prediction of the single, isotropic thin screen model. An anisotropic scattering mechanism ([Stinebring et al., 2001](#)) is one of the possible explanations for these deviations in scattering spectral index. Furthermore, [Michilli et al. \(2018a\)](#) observed an additional component that is trailing the main peak in the integrated pulse profile of PSR J2219+4754 using their analysis of six years of LOFAR data at 150 MHz. This was not seen in contemporaneous

Lovell observations at 1.5 GHz. They suggested the most likely cause of this component to be an echo from the ionised ISM, which could be studied using future high-resolution images at 150 MHz that may help resolve the spatial structure of the ionised ISM.

A major motivation for the Square Kilometre Array (SKA) is the science facilitated using pulsar observations (e.g. [Keane et al., 2015](#); [Janssen et al., 2015](#); [Karastergiou et al., 2015](#)). The MWA is the low-frequency precursor telescope to the SKA. Therefore, pulsar observations using the same observing environment and frequencies are necessary to prepare for pulsar science with the SKA-Low. The SKA-Low is expected to detect ~ 9400 pulsars ([Xue et al., 2017](#)) and vastly improve our knowledge of the Galactic neutron star population as well as generate a three-dimensional tomography of the magneto-ionic properties of the Galaxy.

1.6 Thesis structure

A brief overview of radio pulsars and the ISM propagation effects on pulsar radio emission have been introduced in this Chapter. Chapter 2 presents the related instrumentation and observation methodology, including a detailed description of the MWA, its data processing procedures, the RM synthesis technique and its applications relevant in this work. Chapter 3 presents the initial census of Southern pulsars with the MWA, as published in [Xue et al. \(2017\)](#). Chapter 4 presents the polarimetric verification of the MWA tied-array beamforming process using the analysis of two bright Southern pulsars, as published in [Xue et al. \(2019\)](#). Chapter 5 presents polarimetric studies for six pulsars in the general direction of the Gum Nebula using the MWA to probe the ISM properties in the Gum Nebula. A summary and future prospects are in Chapter 6.

Chapter 2

Instrumentation and Methodologies

2.1 Overview of the Murchison Widefield Array

The Murchison Widefield Array (MWA), operating in the frequency range 80–300 MHz, is located at the Murchison Radio-astronomy Observatory (MRO) in Western Australia. It is the low-frequency precursor telescope of the Low Frequency Aperture Array component of the Square Kilometre Array (SKA-Low), planned to be built at the same site. The MRO is located in a radio quiet zone protected by the Australian Government, and therefore has a relatively low level of radio frequency interference (RFI), mostly caused by aircrafts and satellites.

The Phase I MWA ([Tingay et al., 2013](#)) consisted of 128 ‘tiles’, where each tile is a dipole array composed of 16 dual-polarisation dipole antennas that are regularly arranged in a 4×4 grid with ~ 1.1 m separation and mounted on a 5×5 m steel wire mesh ground screen, as shown in [Figure 2.1](#). These tiles are distributed across a ~ 3 km diameter region; 25% of them are closely placed within a dense ~ 100 -m diameter core.

As an aperture array radio telescope, the MWA has no moving parts. All telescope functions, including pointing, are performed by electronic manipulation

of dipole signals (Lonsdale et al., 2009). Signals from the 16 dipoles of a tile are combined by an analog beamformer, where a set of switchable delays (between 0 and 13.5 ns) are employed to steer the ‘tile beam’ (or ‘primary beam’) toward one of the 197 predetermined (and coarsely spread) sky positions (known as ‘sweet spots’). The analog signal from each tile is then amplified, digitised, and channelised in the receiver box (Prabu et al., 2015). There are, in total, 16 receiver boxes deployed at the site. In each receiver box, 16 streams of dual-polarisation analog signals from a group of eight tiles are filtered to a bandpass of 80–300 MHz and then channelised to 24×1.28 MHz coarse frequency channels by an Polyphase Filter Bank (PFB) based on Field Programmable Gate Array (FPGA). This first stage channelisation produces a signal stream with a total bandwidth of 30.72 MHz, which can be either contiguous (the most common observing mode) or non-contiguous (the so-called ‘picket-fence’ observing mode) (Prabu et al., 2015). The signal then undergoes a second stage channelisation, producing 128×10 kHz fine channels, resulting in a time resolution of $100 \mu\text{s}$. This task is performed by dedicated hardware that is designed to perform the second (fine) PFB operation. (Ord et al., 2015).

Between late 2016 and mid-2017, the MWA underwent a major upgrade. This involved the addition of 128 new tiles to the Phase I configuration to create a larger array (i.e. the Phase II MWA) consisting of 256 deployed tiles extending out to a maximum baseline of ~ 6 km (Wayth et al., 2018). In this upgrade, the existing signal path and electronics (receivers and correlator) has remained the same. As a result, 128 tiles are available at any given time because of the limitation set by the maximum signal throughput of the MWA hardware. In order to satisfy the requirements of the MWA’s various science goals, the array switches between two types of configuration, namely, *compact* and *extended*, and the switching is done approximately once a year. The compact configuration makes use of the 56 tiles in the MWA’s core, along with 72 new tiles that are arranged in two regular hexagonal configurations (Wayth et al., 2018) located

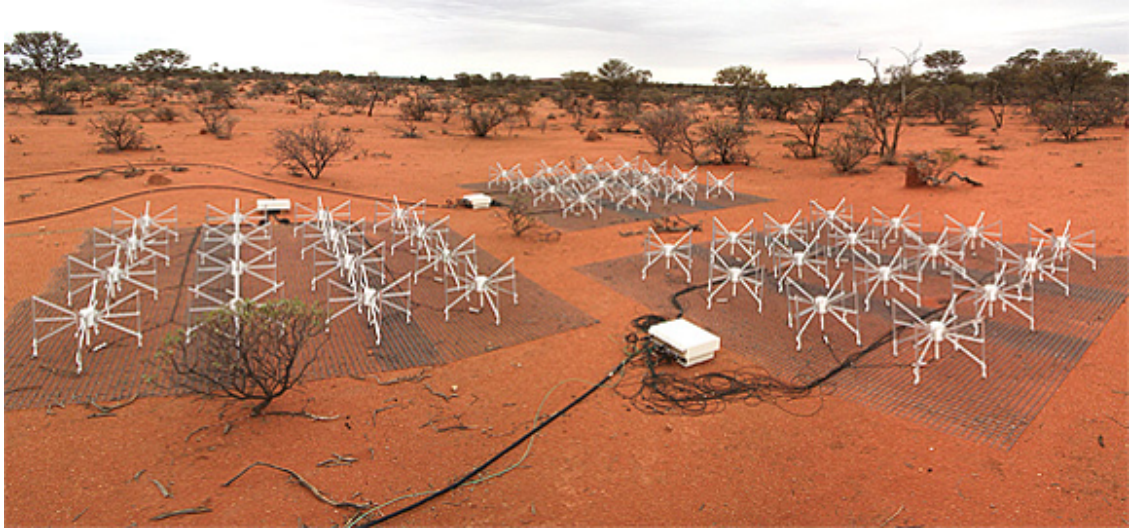


Figure 2.1: A photograph of three MWA tiles with the corresponding analog beamformer units (the ‘white box’) at the MRO site. Within each tile, the centres of 16 dual-polarisation dipoles are equally spaced by ~ 1.1 m over a 5×5 m steel wire mesh ground screen. Thus, the observing element has effectively a physical size of approximately 4.4×4.4 m.

nearby. This regular antenna arrangement is especially useful for the study of the Epoch of Reionisation (EoR) power spectrum (one of the MWA’s key science goals), because the large number of identical (and therefore, redundant) baselines help both boost the sensitivity (e.g. [Parsons et al., 2012](#)) and enable the recovery of antenna gains during calibration without requiring a sky model (e.g. [Li et al., 2018](#)). The compact configuration is also advantageous for doing pulsar surveys as it provides a larger tied-array beam (because of the shorter baselines, see section [2.4.2](#)), thereby increasing the survey efficiency significantly. The extended configuration replaces the 56 closely-spaced core tiles of the Phase I MWA with 56 sparsely-spaced tiles placed within a ~ 5.3 km diameter region. This allows for higher spatial resolution imaging ($\sim 1.30'$ at 154 MHz), and reducing the expected classical confusion by a factor of ~ 8 , comparing with the Phase I MWA ([Wayth et al., 2018](#)). For the work presented in this thesis, we used Phase I MWA observations (Chapters 3 and 4), and a combination of Phase I and Phase II

compact- and extended-configuration observations (Chapter 5).

2.2 The Voltage Capture System

The MWA was initially designed as an imaging interferometer, with the primary science goals of detecting the signatures of EoR, and conducting surveys of Galactic and extragalactic radio sources in the Southern Hemisphere, explore the southern radio sky for ‘slow’ radio transients, and solar and space weather studies (Bowman et al., 2013). In the standard signal path of the MWA, the output signal streams from the fine PFBs are injected into the MWA correlator to generate cross-power spectra with an integration time, or time resolution, of 0.25 s or 0.5 s (Ord et al., 2015). Although the original standard MWA observing mode does not provide the high time resolution data products required for pulsar studies, the signal path is flexible enough that such an application could be added.

The Voltage Capture System (VCS, Tremblay et al., 2015) extended the capabilities of the MWA to record the high time ($100 \mu\text{s}$) and frequency (10 kHz) resolution 4-bit+4-bit complex voltage stream output from the fine PFB stage. The VCS enabled further expanding the capabilities of the MWA to time domain astrophysics, particularly high-time resolution science applications such as pulsar astronomy, FRB searches, and solar science. The VCS generates 32×242 MB files for each second of observation, where each file contains one eighth of the fine channels from one quarter of the tiles, making the total data rate equal to 7.744 GB per second (28 TB per hour). The maximum recording time for one MWA-VCS observation is ~ 1.5 hours because of the limitation on data storage (50 TB) of the VCS server on site (highlighted by the gray dashed box in Figure 2.2). Therefore, new VCS observations cannot be recorded before the previous one has been transferred to a data archive server hosted at the Pawsey Supercomputing Centre in Perth. This server reorders the data into 24×313 MB files per second of observations, one for each coarse channel, in a process termed *recombine*. Each observation is identified and named by an ‘Obs id’, which is the

GPS time when the observation commenced. Note that the VCS records fine-channelised signals instead of the ‘original’ digitised voltages. However, because the data are critically sampled in the two PFB stages, the original voltages can be reconstructed (under certain conditions). In practice, only the second (fine) PFB ‘inversion’ is implemented so far, yielding a higher time-resolution (albeit coarser frequency resolution) data product that is suitable for performing coherent dedispersion (see section 2.4.2.4).

2.3 The MWA primary beam model

The MWA tiles have a fairly complex beam response: it varies as a function of the pointing position, as well as with the observing frequency (Sutinjo et al., 2015a). The beam size is significantly larger at lower observing frequencies, as shown in Figure 2.3. When pointing toward directions that are far away from the zenith, a grating lobe, whose gain is stronger than a ‘normal’ side lobe (sometimes mimicing the main beam in shape and sensitivity) may occur, as can be seen in Figure 2.4. Pulsars have been detected in the grating lobe for several MWA-VCS observations (Xue et al., 2017).

The MWA tile beam model is used to remove the direction-dependent effects from the observation of a calibrator source, to determine the direction-independent gain for each tile (see section 2.4.2.3), and also to generate the Jones matrix (see Section 2.4.2.2) for the observation of the target source. Any differences between our model and the actual behaviour of the tile beam will affect the polarimetry, primarily in the form of instrumental leakage between Stokes parameters (Sutinjo et al., 2015a; Lenc et al., 2017).

There are three specific beam models currently available, with varying levels of sophistication:

- (1) The analytical beam model: the simple summation of 16 ideal dual-polarisation Hertzian dipoles above an infinite ground screen. This is the simplest beam

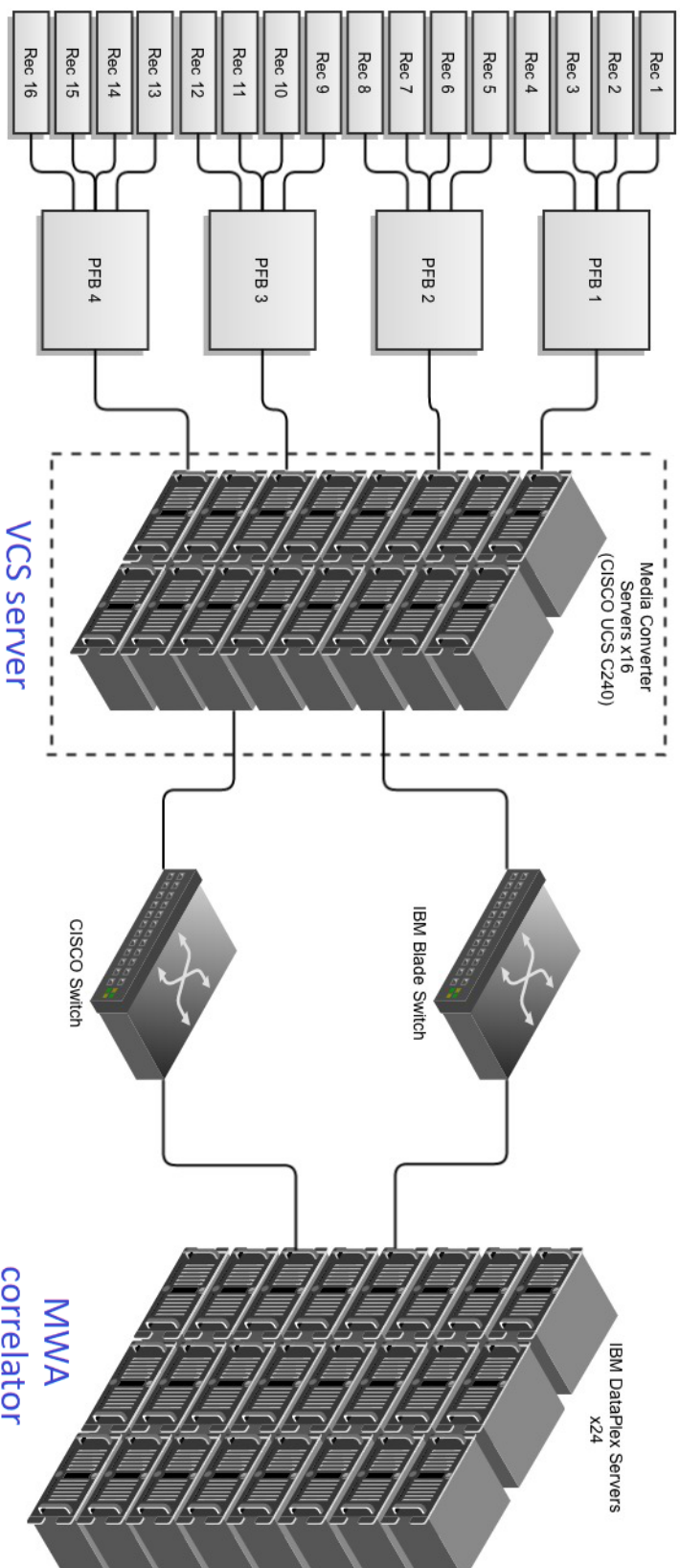


Figure 2.2: A schematic of the MWA signal path (adapted from Figure 1 in Tremblay et al., 2015). The coarse-channelised output of the 16 MWA receivers undergoes the second stage of channelisation through one of the four polypphase filter banks (PFBs), forming a signal stream with a frequency resolution of 10 kHz and a time resolution of 100 μ s, which is then transferred to one of the 16 Media Converter Servers. In the standard MWA imaging mode, the Media Converter Servers format the output from the PFBs and pass it to the correlator server. In the VCS observation mode, they record the voltage output of the PFBs to corresponding redundant arrays of independent disks (RAID).

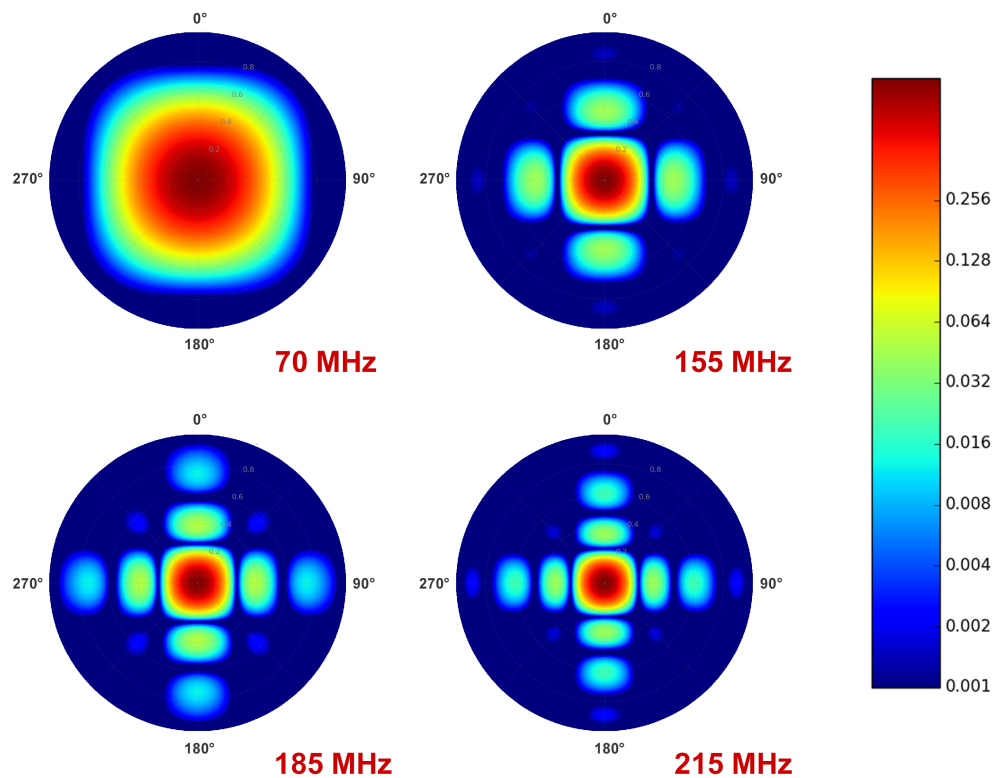


Figure 2.3: The power pattern of the MWA tile beam when pointed towards the zenith at four different observing frequencies. The maximum value of the power pattern has been normalised to unity. The colour scale, shown by the colour bar, is logarithmic.

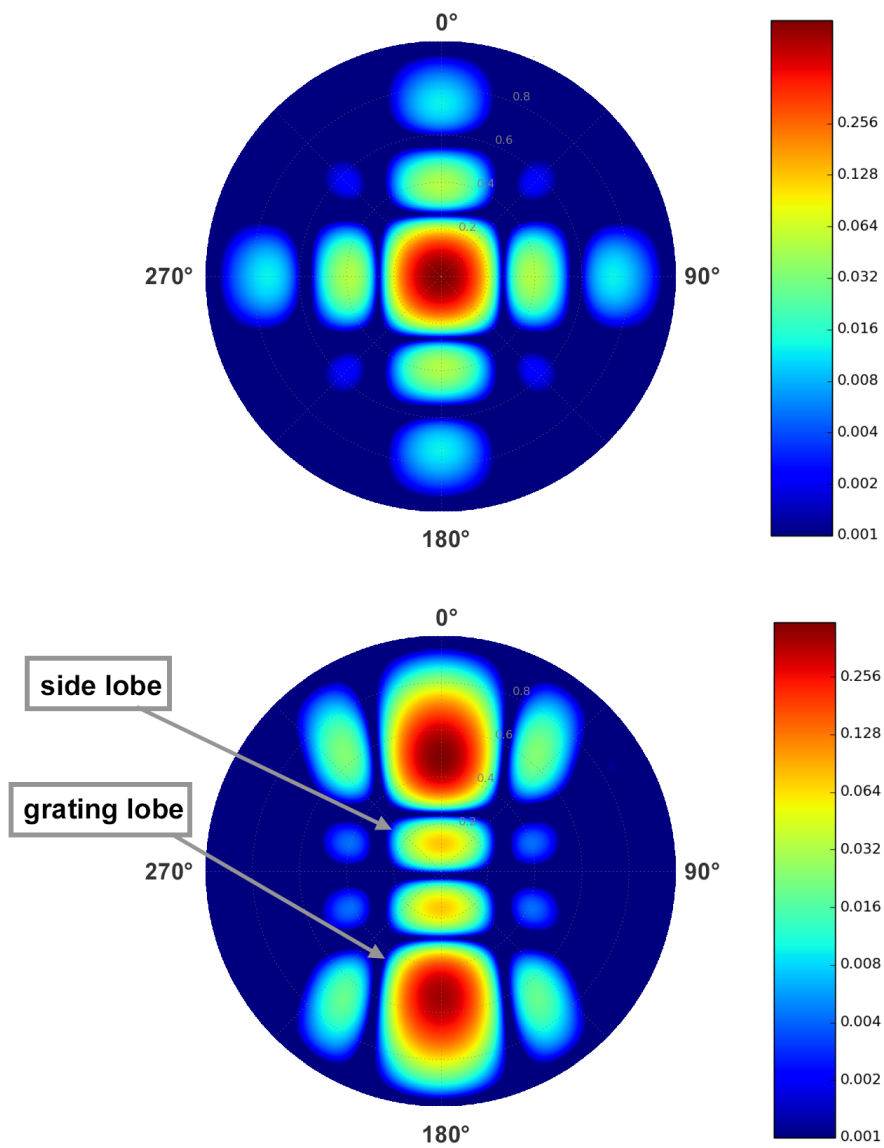


Figure 2.4: The MWA tile beam pattern for different pointing directions (observed at 185 MHz). The top panel shows the MWA tile beam when pointed toward the zenith; the bottom panel shows a pointing toward $(Az, ZA) = (0, 45^\circ)$, when a strong grating lobe that is nearly identical to (but mirroring) the main beam can be seen. The maximum value of the power pattern has been normalised to unity and the colour scale is logarithmic.

model available.

- (2) The Average Embedded Element (AEE) beam model (Sutinjo et al., 2015a): makes use of an average of 16 embedded dipole element patterns from simulations made with the computational electromagnetics software FEKO¹. It has improved accuracy compared to the analytical beam model.
- (3) The Full Embedded Element (FEE) beam model: requires FEKO simulations for all 16 embedded element patterns (dual polarization for each) at each frequency (Sokolowski et al., 2017). This is the most accurate model available to date.

For the AEE and FEE beam models, the improvement in accuracy comes at the cost of greater computational complexity and therefore requires significantly more computational resources. In the current MWA tied-array processing, only the simplest analytical beam model is used. Verification that this model provides sufficiently reliable results for zenith angles $\lesssim 45^\circ$ and frequencies $\lesssim 270$ MHz is shown in Chapter 4. Indeed, incorporating the FEE beam model in the tied-array processing will help further improve the quality of the output data products; the related implementation and verification are planned for future works.

2.4 Processing MWA VCS data

Once the voltage data from the 128 tiles are channelised and recorded on the VCS server on-site, they are transferred to the Pawsey Supercomputing Centre through a dedicated optical fiber, recombined, and then archived on tape storage. These data can be reduced in different ways, providing users with maximum flexibility. As Figure 2.5 shows, in principle, data can be processed in three different ways: (1) incoherent summation; (2) coherent beam-forming (i.e. tied-array processing); and (3) off-line correlation. These processing methods are described in the following subsections.

¹altairhyperworks.com/product/FEKO

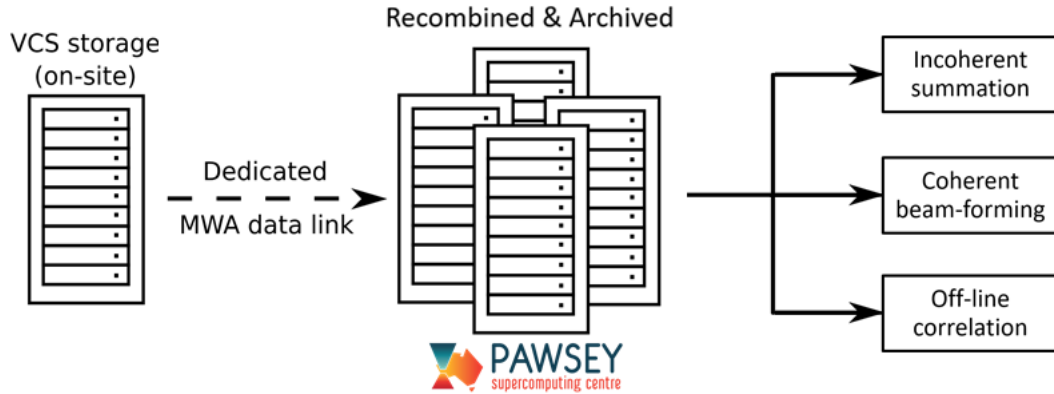


Figure 2.5: The workflow diagram for MWA-VCS data processing. The voltage data recorded on the VCS server on-site are transferred to the Pawsey Supercomputing Centre (located in Perth) through a dedicated optical fiber, and then recombined and archived there. Further processing and analysis of the MWA-VCS data (incoherent and coherent beamforming, and/or offline correlation) are performed on the Galaxy supercomputer in the Pawsey Centre.

2.4.1 Incoherent summation

The least compute-intensive way to process MWA-VCS data is to simply sum the detected power from all 128 tiles incoherently. In short, voltages from each tile, v_i , are multiplied by their complex conjugates, v_i^* , to form the power, and then summed together, as shown in the following expression:

$$P_{\text{incoh}}(t, \nu) = \sum_i^N (v_i v_i^*) \quad (2.1)$$

where N is the number of tiles that are used in the incoherent summation and v_i is the voltage sample from the i th tile at the given time t and frequency channel ν .

Each MWA tile produces two voltage streams with two orthogonal polarisations, denoted as x and y . The observed voltages can be expressed as a vector

$$\mathbf{v} = \begin{bmatrix} v_x \\ v_y \end{bmatrix}. \quad (2.2)$$

The incoherent summation of the total power is then

$$P_{\text{incoh}} = \sum_i^N (\mathbf{v}_i \mathbf{v}_i^H) = \sum_i^N (v_{i,x} v_{i,x}^* + v_{i,y} v_{i,y}^*) \quad (2.3)$$

where H denotes the Hermitian transpose.

The output is then written to a PSRFITS format file (Hotan et al., 2004) for further scientific analysis. The resulting data rate is 105 GB per hour. This incoherent summation preserves the full single tile field-of-view (FoV; i.e. $\sim 450^\circ$ at 185 MHz) and increases the theoretical sensitivity by a factor of \sqrt{N} over a single tile.

Generating the incoherent sum is relatively computationally inexpensive and straightforward. It was used for interesting case studies during the early MWA-VCS commissioning phase of the telescope’s operation, e.g. low frequency studies of the bright millisecond pulsar J0437–4715 (Bhat et al., 2014), and studies of giant pulses from the Crab pulsar (Oronsaye et al., 2015). The large FoV facilitates an efficient pulsar census over a large sky area. Such a census using incoherently summed MWA-VCS archival data is described in detail in Chapter 3 and published in Xue et al. (2017).

2.4.2 Tied-array beam processing

The signals from each tile can also be coherently summed to achieve the full theoretical sensitivity of the MWA and preserve the beam polarimetry. This process is equivalent to combining the array elements to form a tied-array (phased array) beam. The procedure involves calibrating the array to determine the direction-independent complex gains for each tile and then applying phase rotations to correct for geometric delays according to the desired look-direction of the target

position. The theory and processing procedure are summarised in the subsequent sections; for further details, see [Ord et al. \(2019\)](#).

2.4.2.1 Phase rotations for delay compensation

In order to calculate the phase rotation required for the signals from each tile, one needs the information about the locations of the tiles, the cable lengths, and the telescope pointing position. This information can be accessed from a metadata FITS file that is generated for each MWA observation.

The location of each tile is measured relative to the ‘array centre’, an arbitrarily chosen reference position approximately in the centre of the physical array ([Tingay et al., 2013](#); [Wayth et al., 2018](#)). For a given tile, i , the geometric delay-distance can be calculated using its position in local geocentric coordinates (X_i, Y_i, Z_i) , the hour angle H and the declination δ of the pointing position:

$$w_i = \cos(\delta) \cos(H)X_i - \cos(\delta) \sin(H)Y_i + \sin(\delta)Z_i. \quad (2.4)$$

The overall time delay Δt_i associated with each tile contains contributions from both the geometric distance w_i and the electrical cable length L_i :

$$\Delta t_i = (w_i + L_i) / c. \quad (2.5)$$

Therefore, the phase correction for tile i at frequency channel ν can be expressed as:

$$\phi_{i,\nu} = 2\pi\Delta t_i\nu. \quad (2.6)$$

2.4.2.2 Jones Matrix

Each MWA tile has its own instrumental response, which can be represented by a 2×2 complex matrix known as the Jones matrix, \mathbf{J} . The measured voltages are the result of this response acting on the received signal, \mathbf{e} :

$$\mathbf{v}_i = \mathbf{J}_i\mathbf{e}. \quad (2.7)$$

The Jones matrix for a given tile i can be decomposed into two parts, the direction-independent gain \mathbf{G}_i and the alignment matrix \mathbf{A} , which is the direction-dependent primary beam pattern toward the pointing position:

$$\mathbf{J}_i = \mathbf{G}_i \mathbf{A}. \quad (2.8)$$

The visibility matrix for a given observation is the outer product of the voltages from a pair of tiles, i and j :

$$V_{ij} = \langle \mathbf{v}_i \mathbf{v}_j^H \rangle = \mathbf{J}_i \langle \mathbf{e} \mathbf{e}^H \rangle \mathbf{J}_j^H, \quad (2.9)$$

where $\langle \rangle$ denotes the average over a time and frequency range in which the variation of the Jones matrix is negligible. The outer product $\langle \mathbf{e} \mathbf{e}^H \rangle$ is known as the coherency matrix \mathbf{P} , and has the following relationship with the Stokes parameters (I , Q , U and V):

$$\mathbf{P} = \langle \mathbf{e} \mathbf{e}^H \rangle = \begin{pmatrix} \langle e_x e_x^* \rangle & \langle e_x e_y^* \rangle \\ \langle e_y e_x^* \rangle & \langle e_y e_y^* \rangle \end{pmatrix} = \frac{1}{2} \begin{pmatrix} I + Q & U + iV \\ U - iV & I - Q \end{pmatrix}. \quad (2.10)$$

Therefore, as Eqs. (2.9) and (2.10) show, the measured visibilities can be related to the polarisation states of sources in the telescope's FoV. This fact makes it possible to determine the Jones matrix of each tile by means of a calibration procedure.

2.4.2.3 Calibration

The Jones matrix for each tile is estimated using a calibration process. For the MWA tied-array processing pipeline, the calibration can be performed by the *Real Time System* (RTS, [Mitchell et al., 2008](#)), which is specifically designed for low-frequency radio interferometers like the MWA, with a large number of antennas that are subject to significantly varying ionospheric effects.

The RTS determines the unknown Jones matrices from the measured visibilities using a set of N_c calibrator sources in the primary beam. For each calibrator

source c , the coherency matrix $\mathbf{P}_{ij,c}$ is determined. The modeled visibilities can be expressed as:

$$V_{ij,\nu}^{\text{model}} = \sum_{c=1}^{N_c} \mathbf{J}_{i,c} \mathbf{P}_{ij,c} \mathbf{J}_{j,c}^{\text{H}} e^{-i\phi_{ij,c,\nu}}. \quad (2.11)$$

where $\phi_{ij,\nu}$ is the relative phase shift at the frequency ν .

The modeled visibilities are then subtracted from the actual visibility set to obtain residual visibilities:

$$V_{ij,\nu}^{\text{residual}} = V_{ij,\nu} - V_{ij,\nu}^{\text{model}}. \quad (2.12)$$

The calibrator c is then added back into the data with its current best-fit position to form a visibility set dominated by itself:

$$V_{ij,c,\nu} = V_{ij,\nu}^{\text{residual}} + \mathbf{J}_{i,c} \mathbf{P}_{ij,c} \mathbf{J}_{j,c}^{\text{H}} e^{-i\phi_{ij,c,\nu}}. \quad (2.13)$$

The phase rotation toward the calibrator position is then applied, resulting in a measured $V'_{ij,c,\nu}$:

$$V'_{ij,\nu} = V_{ij,\nu}^{\text{residual}} e^{i\phi_{ij,\nu}} + \mathbf{J}_i \mathbf{P}_{ij,c} \mathbf{J}_j^{\text{H}}. \quad (2.14)$$

The calibration procedure aims to find a solution for the Jones matrices for which $V_{ij,\nu}^{\text{residual}} e^{i\phi_{ij,c,\nu}} = 0$ and therefore

$$\mathbf{J}_{i,c} \mathbf{P}_{ij,c} \mathbf{J}_{j,c}^{\text{H}} = V'_{ij,c,\nu}. \quad (2.15)$$

This calibration strategy is known as *peeling*, and has been incorporated into the calibration process of multiple radio interferometer instruments including LOFAR (Noordam, 2004) and GMRT (Bhatnagar & Nityananda, 2001). The modeled calibrator sources are processed one by one, starting with the brightest, and adding subsequent sources in brightness order. To calibrate MWA observations with the RTS, a dedicated software tool is used to generate the calibrator source list at MWA frequencies for a given calibration observation.

2.4.2.4 Beamforming

The Jones matrices obtained from the calibration process contain an alignment component of the tile beam pointing towards the calibrator direction. Therefore, in order to apply the Jones matrices to form the tied-array beam, the calibration Jones matrix, $J_{i,c}$, is multiplied by the inverse of the alignment component of the calibration observation, A_c , and then multiplied by the alignment component of the target observation, A_s . That is, the Jones matrix can be applied to the target observation as:

$$\mathbf{J}_{i,s} = \mathbf{G}_i \mathbf{A}_s = \mathbf{J}_{i,c} \mathbf{A}_c^{-1} \mathbf{A}_s. \quad (2.16)$$

The next step involves applying the phase rotations associated with the geometric delay of each tile, i , to the measured voltage:

$$\mathbf{v}'_i = \begin{pmatrix} v_x e^{-i\phi_{i,\nu,x}} \\ v_y e^{-i\phi_{i,\nu,y}} \end{pmatrix}. \quad (2.17)$$

The obtained voltage \mathbf{v}'_i is the incident signal, modified by the instrument Jones matrix plus noise:

$$\mathbf{v}'_i = \mathbf{J}_i \mathbf{e} + \mathbf{n}_i. \quad (2.18)$$

Using the Jones matrix $\mathbf{J}_{i,s}$ obtained in the previous step, the inverse operation is performed as below:

$$\mathbf{J}_i^{-1} \mathbf{v}'_i = \mathbf{e} + \mathbf{J}_i^{-1} \mathbf{n}_i. \quad (2.19)$$

This product is then summed across all N antennas:

$$\sum_i^N \mathbf{J}_i^{-1} \mathbf{v}'_i = \sum_i^N (\mathbf{e} + \mathbf{J}_i^{-1} \mathbf{n}_i). \quad (2.20)$$

Assuming a perfect calibration solution, this sum forms an estimate, \mathbf{e}' , of the true incident electric field \mathbf{e} , corrupted by noise $\boldsymbol{\sigma}$:

$$\mathbf{e}' = \mathbf{e} + \boldsymbol{\sigma}, \quad (2.21)$$

where

$$\boldsymbol{\sigma} = \frac{1}{N} \sum_i^N \mathbf{J}_i^{-1} \mathbf{n}_i. \quad (2.22)$$

For the current MWA-VCS processing pipeline, there are two types of standard output data products generated by the beamformer. First, the two polarisations of the estimated incident electric field,

$$\mathbf{e}' = \begin{bmatrix} e_x \\ e_y \end{bmatrix}, \quad (2.23)$$

can be output to a VDIF² format file. Before writing this data product out to a file, it is first upsampled by means of an algorithm that (approximately) inverts the channelisation carried out by the fine polyphase filter bank. That is, this process resynthesises the 1.28-MHz coarse channel data and recovers the full Nyquist time resolution before the fine channelisation (see [Kaur et al. 2019](#) for further details, and [Crochiere & Rabiner 1983](#) for a fuller description of the original algorithm). It was developed specifically to enable coherent de-dispersion ([van Straten & Bailes, 2011](#)), which is particularly important for the studies of millisecond pulsars at the MWA's low frequencies (e.g. [Kaur et al., 2019](#)).

Another option for the beamformer output is to write the Stokes parameters to PSRFITS format files ([Hotan et al., 2004](#)).

As shown in Eq. (2.10), the four Stokes parameters I , Q , U , V can be estimated from the coherency matrix $\mathbf{P} = \langle \mathbf{e}\mathbf{e}^H \rangle$. If the noise $\boldsymbol{\sigma}$ is not negligible, the instantaneous coherency matrix is:

$$\mathbf{e}'\mathbf{e}'^H = (\mathbf{e} + \boldsymbol{\sigma})(\mathbf{e} + \boldsymbol{\sigma})^H \quad (2.24)$$

$$\mathbf{e}'\mathbf{e}'^H = \mathbf{e}\mathbf{e}^H + \boldsymbol{\sigma}\boldsymbol{\sigma}^H + \mathbf{O}(\boldsymbol{\sigma}). \quad (2.25)$$

²Specifications of this data format can be found at: <http://www.vlbi.org/vdif/>

The obtained coherency matrix is time averaged, and the linear terms of the (thermal) noise, which is expected to follow a Gaussian distribution, have an overall average of zero. Therefore, the result is dominated by the signal ($\mathbf{e}\mathbf{e}^H$) and the noise squared term ($\boldsymbol{\sigma}\boldsymbol{\sigma}^H$). The noise squared term $\boldsymbol{\sigma}\boldsymbol{\sigma}^H$ can be expressed as:

$$\begin{aligned}\boldsymbol{\sigma}\boldsymbol{\sigma}^H &= \frac{1}{N^2} \left(\sum_i^N \mathbf{J}_i^{-1} \mathbf{n}_i \right) \left(\sum_i^N \mathbf{J}_i^{-1} \mathbf{n}_i \right)^H \\ &= \frac{1}{N^2} \left[\sum_i^N (\mathbf{J}_i^{-1} \mathbf{n}_i) (\mathbf{J}_i^{-1} \mathbf{n}_i)^H + \sum_i^N \sum_{j, i \neq j}^N (\mathbf{J}_i^{-1} \mathbf{n}_i) (\mathbf{J}_j^{-1} \mathbf{n}_j)^H \right].\end{aligned}\quad (2.26)$$

The first term $\sum_i^N (\mathbf{J}_i^{-1} \mathbf{n}_i) (\mathbf{J}_i^{-1} \mathbf{n}_i)^H$ is the sum of the autocorrelation of the noise contribution from each tile. The second term $\sum_i^N \sum_{j, i \neq j}^N (\mathbf{J}_i^{-1} \mathbf{n}_i) (\mathbf{J}_j^{-1} \mathbf{n}_j)^H$ is the sum of the cross correlation noise from all the tile pair combinations. It is reasonable to assume the noise at each tile is uncorrelated, and therefore the time average of the second term is negligible. Subtracting the auto-correlations from each tile is therefore increasing the signal-to-noise ratio of the final data product. This strategy is implemented in the MWA tied-array processing pipeline.

Therefore, the final output Stokes parameters can be expressed as:

$$I = \left[e'_x e'^*_x - \frac{1}{N^2} \sum_i^N e'_{i,x} e'^*_{i,x} \right] + \left[e'_y e'^*_y - \frac{1}{N^2} \sum_i^N e'_{i,y} e'^*_{i,y} \right], \quad (2.27)$$

$$Q = \left[e'_x e'^*_x - \frac{1}{N^2} \sum_i^N e'_{i,x} e'^*_{i,x} \right] - \left[e'_y e'^*_y - \frac{1}{N^2} \sum_i^N e'_{i,y} e'^*_{i,y} \right], \quad (2.28)$$

$$U = 2 \times \text{Re} \left[e'_x e'^*_y - \frac{1}{N^2} \sum_i^N e'_{i,x} e'^*_{i,y} \right], \quad (2.29)$$

$$V = -2 \times \text{Im} \left[e'_x e'^*_y - \frac{1}{N^2} \sum_i^N e'_{i,x} e'^*_{i,y} \right]. \quad (2.30)$$

The noise level varies between observations. Therefore, for some observations, subtracting the auto-correlated noise provides a significant improvement

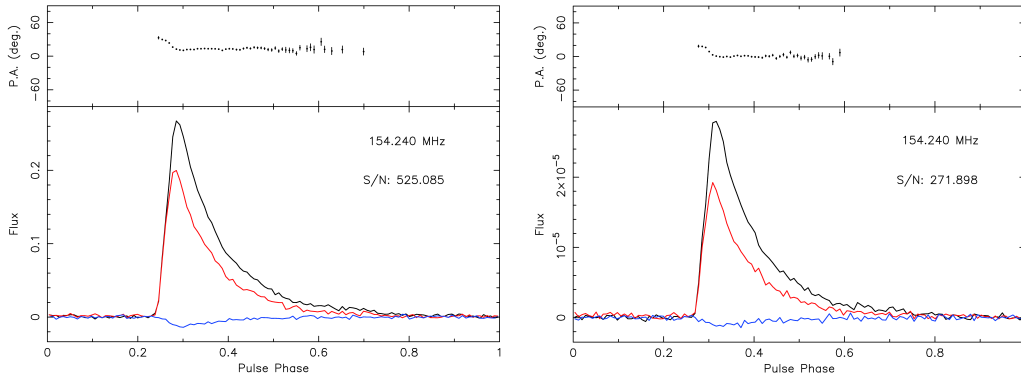


Figure 2.6: The integrated pulse profile of PSR J0742-2822 from a 50-min MWA-VCS observation. The left panel shows the beamformed output with the auto-correlated noise subtracted, while the right panel show the same with the auto-correlated noise included.

in the signal-to-noise ratio, while for some other observations, the difference can be marginal. Figure 2.6 shows an example observation of a bright pulsar, PSR J0742-2822, in which subtracting the auto-correlated noise improves the signal-to-noise ratio of the pulse profile almost by a factor of two. This auto-correlated noise subtraction is applied in all of the coherently-summed tied-array observations presented in this thesis.

2.5 RM synthesis and deconvolution

As described in Section 1.4.2, the RM synthesis technique is used to determine the Faraday rotation measures for polarimetric studies of pulsars presented in this work. The concept of RM synthesis was first advanced by Burn (1966) and was further developed by Brentjens & de Bruyn (2005). Compared to the traditional RM determination method (i.e., gradient fitting between P.A. and λ^2), RM synthesis significantly reduces the $n\pi$ ambiguity problem (Brentjens & de Bruyn, 2005), which is a well-documented problem in RM determination. When Stokes Q and U are obtained at a single frequency, the polarisation position angle,

$\chi = \frac{1}{2} \arctan\left(\frac{U}{Q}\right)$, has multiple solutions separated by $n\pi$. Moreover, by using RM synthesis, emission at different ‘Faraday depths’ along the same line-of-sight can, in principle, be distinguished. This is useful for polarimetric studies of radio galaxies and active galactic nuclei (AGN) (e.g. [Sokoloff et al., 1998](#)), because both polarised emission and Faraday rotation can occur in the extended and diffuse media. When all of the polarised emission is observed at a single Faraday depth, ϕ is equivalent to the RM.

According to [Burn \(1966\)](#), Faraday depth, ϕ , is defined as:

$$\phi = C \int_{\text{source}}^{\text{telescope}} n_e \mathbf{B} \cdot d\mathbf{l}, \quad (2.31)$$

where n_e is the electron density, \mathbf{B} is the magnetic field vector, and \mathbf{l} is the displacement vector between the source and the observer. The coefficient of proportionality $C = \frac{e^3}{2\pi m_e^2 c^4}$. Considering n_e in cm^{-3} , \mathbf{B} in μG , and \mathbf{l} in pc, the coefficient $C = 0.81$, and the Faraday depth ϕ has units of rad m^{-2} . The dot product implies that only the magnetic field component that is parallel to the line-of-sight (B_{\parallel}) contributes to the Faraday depth. The Faraday depth ϕ is defined to be positive (or negative) depending on whether the magnetic field is pointing toward (or away from) us.

When all of the polarised emission is observed at a single Faraday depth, ϕ is equivalent to the RM, which is defined as the gradient of the P.A. as a function of wavelength squared, λ^2 (see Eq. 1.14). This is the case for pulsar observations for which we fold and dedisperse the data according to the target pulsar’s period and DM, respectively. Therefore, we use ϕ to represent RM hereafter in this section.

As mentioned in section 1.3.4, the polarisation vector P consists of Stokes Q and Stokes U ($P = Q + iU$, see Eq. 1.2). P can be expressed in an exponential form:

$$P = L e^{2i\chi}, \quad (2.32)$$

where L is the intensity of linear polarisation ($L = \sqrt{Q^2 + U^2}$, see Eq. 1.3). The observed P.A., χ , can be expressed as $\chi(\lambda^2) = \chi_0 + \phi \lambda^2$. Therefore, by integrating

over all Faraday depths, the observed polarisation vector, $P(\lambda^2)$, can be expressed as:

$$P(\lambda^2) = \int_{-\infty}^{+\infty} F(\phi) e^{2i\phi\lambda^2} d\phi, \quad (2.33)$$

where $F(\phi)$, as defined in [Burn \(1966\)](#), is the ‘Faraday dispersion function’ (FDF; also known as ‘Faraday spectrum’), which describes the intrinsic polarisation vector at each Faraday depth.

Since χ_0 is a constant for all ϕ , Eq. (2.33) has a similar format to the Fourier transform. Therefore, transforming from λ^2 space to Faraday space using the Fourier inversion theorem, $F(\phi)$ can be expressed as the Fourier transform of Eq. (2.33):

$$F(\phi) = \int_{-\infty}^{+\infty} P(\lambda^2) e^{-2i\phi\lambda^2} d\lambda^2. \quad (2.34)$$

In reality, observations are made at a set of finite, discrete, and positive λ^2 , which depends on the observing frequency and bandwidth recorded from the telescope. Therefore, in practice, $F(\phi)$ is expressed as the following discrete sum ([Heald et al., 2009](#)):

$$F(\phi) \approx K \sum_{i=1}^N W_i P(\lambda_i^2) e^{-2i\phi(\lambda_i^2 - \lambda_0^2)}, \quad (2.35)$$

where W_i are weights given to each observing wavelength λ_i (according to the transform window shape we want to use, e.g. uniform, or tapered), and the normalisation factor K is the inverse of the discrete sum of the weights. We centre the function around λ_0^2 , which is usually the weighted mean of the N individual observed λ_i^2 .

The FDF can be considered as the observed polarisation vector P convolved with a response function, the so-called rotation measure spread function (RMSF):

$$R(\phi) \approx K \sum_{i=1}^N W_i e^{-2i\phi(\lambda_i^2 - \lambda_0^2)}. \quad (2.36)$$

This function was originally referred to as the rotation measure transfer function (RM-TF) by [Brentjens & de Bruyn \(2005\)](#). It was renamed by [Heald et al. \(2009\)](#), as it is more analogous to the point spread function in optical telescope images.

The FDF recovered from the observed P using Eq. (2.35) is called the ‘dirty FDF’ because it is an imperfect reconstruction of $F(\phi)$ due to the incomplete sampling in the λ^2 domain. These effects can be reduced using a deconvolution procedure, analogous to the CLEAN algorithm, which is a well-known synthesis imaging technique ([Högbom, 1974](#)).

This deconvolution, referred to as RM-CLEAN, is performed in practice, using a python pipeline³ developed by [Heald et al. \(2009\)](#); see also [Michilli et al. \(2018b\)](#). $P(\phi)$ is first cross-correlated with the RMSF in a user-defined ϕ step and range; ϕ_m denotes where the cross-correlation results in the maximum value. If $P(\phi_m)$ is greater than the user-defined noise cutoff, a term of $gP(\phi_m)R(\phi - \phi_m)$ is subtracted from the reconstructed FDF, where g is a gain scale factor. We record $gP(\phi_m)$ as a ‘clean component’. This process is repeated until $P(\phi_m)$ is less than the user-defined noise cutoff, or a maximum number of iterations have been performed. By convolving the clean components with a restoring Gaussian beam whose FWHM = $3.8/\Delta\lambda^2$ ([Schnitzeler et al., 2009](#)), and adding each to the residual $F(\phi)$, we obtain the deconvolved $F(\phi)$ spectrum, which is also known as the RM-CLEAN-ed FDF.

RM synthesis is now fully achievable using modern telescopes (and computing). For telescopes such as LOFAR and the MWA, their low observation frequencies and large fractional bandwidths provide an RMSF with a narrow FWHM ($< 1 \text{ rad m}^{-2}$), which can be used to precisely determine RMs.

As previously mentioned, because we fold the pulsar observations according to target pulsar’s period and dedisperse at its catalogued DM, we expect the observed polarised emission to be composed of a single RM. However, in many cases, a secondary peak in FDF at ϕ between $\pm 7 \text{ rad m}^{-2}$ (centred around 0 rad m^{-2}),

³<https://github.com/gheald/RMtoolkit>

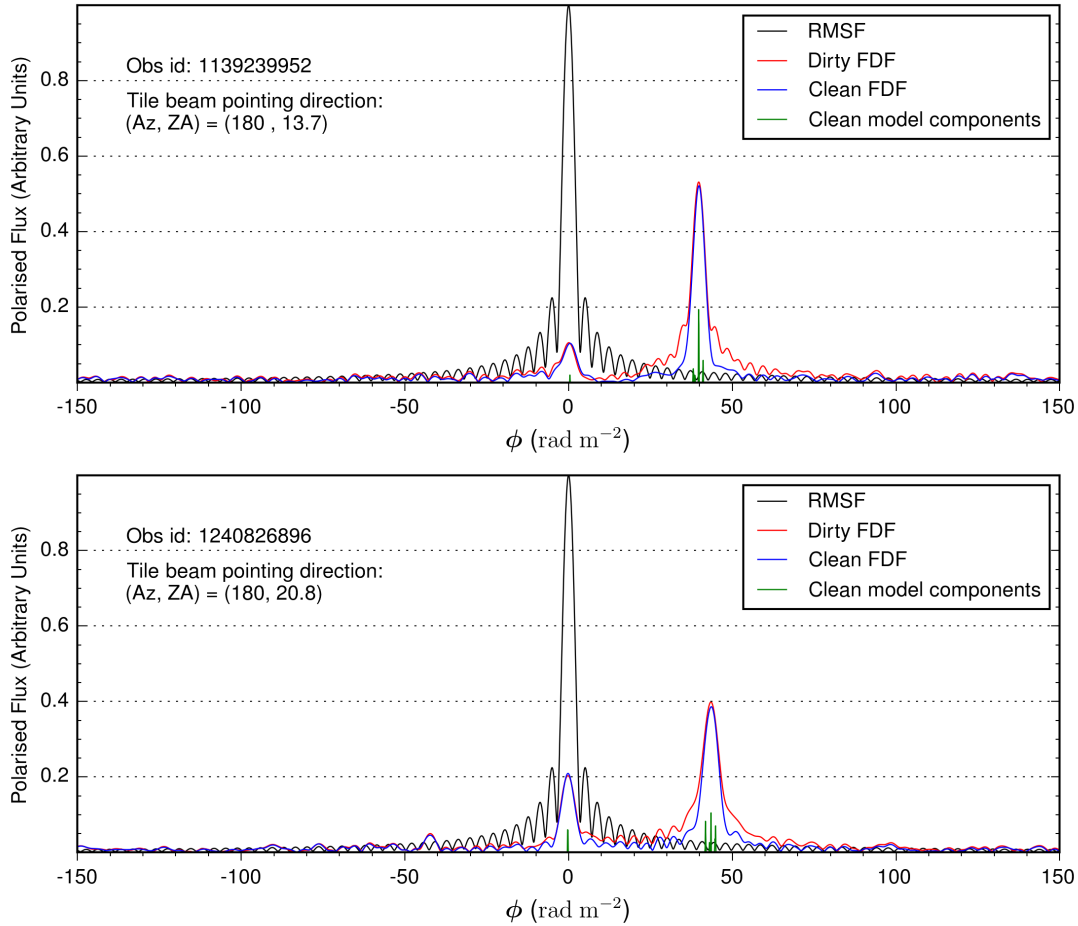


Figure 2.7: Faraday spectra for two MWA observations toward the Vela pulsar using contiguous observing frequency channels across 170–200 MHz. The black lines indicate the rotation measure spread function of the instrument (RMSF), which is the same for these two observations since the frequency channels are identical. The red, blue, and green lines represent the dirty $F(\phi)$ spectra, the cleaned $F(\phi)$ spectra after deconvolving the RMSF, and clean model components, respectively. Pointing directions for the two observations are different (and are labeled on each panel). The distance between the Vela pulsar and the beam centre is larger for the first pointing (-4.8°) than the second one (-2.3°). However, the second observation shows a stronger ‘instrumental peak’ in the FDF near 0 rad m^{-2} , which suggests a larger degree of instrumental leakage.

can also be seen (Figure 2.7). This ‘zero peak’ is generated by the instrumental polarisation leakage. We can use the relative heights of the instrumental peak and source peak in the $F(\phi)$ spectra as a rough estimation of the percentage of instrumental polarisation leakage. As shown in Figure 2.7, the two panels show the RMSF (centred around 0 rad m^{-2}), the dirty $F(\phi)$ spectra, the cleaned $F(\phi)$ spectra (centred around 40 rad m^{-2}), and resulting clean components for two MWA observations of the Vela pulsar with the same frequency coverage (170–200 MHz, with 10 kHz resolution), and hence, have the same native resolution in Faraday space, on for RMSF. However, their pointing directions are different, and thus have different tile beam responses. Both observations were pointed along the meridian, however, the first observation (Obs id: 1139239952) had a smaller zenith angle (13.7°) than the second observation (Obs id: 1240826896; 20.8°). The corresponding pointing declinations are -40.4° and -47.5° respectively (and the Vela pulsar’s declination is -45.2°). The distance between the Vela pulsar and the beam centre (-4.8°) is larger for the first pointing than the second one (-2.3°). However, we can see that the second observation shows a stronger peak in both the dirty and cleaned $F(\phi)$ spectra at $\phi \approx 0$, which indicates a stronger instrumental leakage. A possible explanation is to do with our use of the simple analytical beam model (see Section 2.3), which approximates the actual polarimetric response of the beam, and tend to worsen for pointings that are away from the zenith, thereby leading to greater instrumental leakage. The comparison shown in Figure 2.7, which also indicates that the tile beam pointing direction is a more dominant factor for the strength of the instrumental leakage than the distance between the tied-array beam centre and the tile beam pointing centre. Using the height of the ‘instrumental peak’ in the FDF, the degree of leakage can be estimated, and this is further discussed in Chapter 4, where an empirical verification of the polarimetric behaviour of the MWA tied-array processing is carried out (Xue et al., 2019).

Chapter 3

A Census of Southern Pulsars at 185 MHz

This work was published by:

Xue, M., Bhat, N. D. R., Tremblay, S. E., Ord, S. M., Sobey, C., Swainston, N. A., Kaplan, D. L., Johnston, Simon, Meyers, B. W., McSweeney, S. J., “A Census of Southern Pulsars at 185 MHz”, 2017, Publications of the Astronomical Society of Australia, Volume 34, id.e070 14 pp.

3.1 Summary

In this published work, we present the results from an initial time-resolved census of known pulsars using the MWA. This involved the processing of 37 hours of MWA-VCS archival data (~ 1 PB) from observations made over a 30.72 MHz band centred at 185 MHz, which were obtained from a total 46 individual observing sessions. It covers $\sim 17,000$ deg² of sky (albeit with varying sensitivity), which corresponds to $\sim 55\%$ of the sky observable by the MWA, i.e. at declination $\delta \lesssim 30^\circ$. For each observation, the detected powers from each of the 128 MWA tiles were incoherently summed, which yields $\sim 10\%$ of the sensitivity achievable with the MWA in the coherent combination of signals. The incoher-

ent summation, however, preserves the large field-of-view provided by the MWA — 450 deg² at 185 MHz, allowing multiple pulsars to be observed *simultaneously* and thus facilitates an expedited initial census of the Southern sky pulsar at low frequencies.

The processing resulted in the successful detection of 50 pulsars, with peak signal-to-noise $(S/N)_{\text{peak}} \gtrsim 4$. This includes six millisecond pulsars and two in binary systems. For ten pulsars, we present the lowest-frequency detections ever published. For a subset of the detected pulsars, we also present their multi-frequency pulse profiles, by combining our data with those from other telescopes, thereby demonstrating a number of pulse-profile evolution behaviours across a large range in frequency (up to ~ 10 GHz).

Since the MWA is the low-frequency precursor to the SKA, our census results also provide useful insights into pulsar detection prospects with Phase 1 of SKA-Low (SKA1-Low). Using our census results and the PsrPopPy¹ (Bates et al., 2014) package, we have simulated pulsar populations and mock SKA1-Low surveys, using the specifications as outlined in the SKA Baseline Design document v2². We predict that SKA1-Low could potentially detect ~ 9400 pulsars, which is more than three times the currently known pulsar population. This demonstrates just one of many ways the SKA will revolutionise radio astronomy.

3.2 Introduction

Pulsars were discovered through observing their pulsed emission at a very low radio frequency of 81.5 MHz (Hewish et al., 1968). Although low-frequency observations (<300 MHz) played a considerable role in early pulsar science (e.g. Taylor & Manchester, 1977; Taylor & Stinebring, 1986), the vast majority of the 2536 pulsars now catalogued³(Manchester et al., 2005b) were discovered and

¹github.com/samb8s/PsrPopPy

²www.skatelescope.org/key-documents

³Version 1.54 of the pulsar catalogue retrieved from www.atnf.csiro.au/people/pulsar/psrcat

studied at higher frequencies, between 300 MHz and a few GHz. This is due to a compromise between three frequency-dependent effects (1) the greater broadening of pulsed signals towards lower frequencies due to interstellar medium (ISM) propagation effects, particularly multipath scattering, which is a strong function of the observing frequency ($\propto \nu^{-4}$, e.g. [Bhat et al. 2004](#)), (2) the increase in telescope system temperature towards lower frequencies due to the diffuse Galactic continuum emission ($\propto \nu^{-2.6}$; [Lawson et al. 1987](#)), and (3) the decrease in flux densities towards higher frequencies due to pulsars' steep intrinsic spectral indices ($\propto \nu^{-1.4}$, on average; [Bates et al. 2013](#)).

Pulsars are once again being routinely observed and studied at low frequencies due to advances in instrumentation and computing. This includes recently upgraded or constructed telescopes operating below 300 MHz and their associated computing facilities: the Giant Metrewave Radio Telescope (GMRT; [Swarup et al., 1991](#); [Roy et al., 2010](#)), the Long Wavelength Array (LWA; [Taylor et al., 2012](#); [Stovall et al., 2015](#)), the Low-Frequency Array (LOFAR; [van Haarlem et al., 2013](#); [Stappers et al., 2011](#)), and the Murchison Widefield Array (MWA; [Tingay et al., 2013](#); [Tremblay et al., 2015](#)). Besides the MWA, all of these facilities are located in the Northern Hemisphere. Consequently, 22% of the known pulsar population can only be observed at low frequencies using the MWA ($-90^\circ \leq \delta \lesssim -50^\circ$). Moreover, the sensitivity of aperture array telescopes decreases rapidly for lower elevation pointings ($\lesssim 30^\circ$; [Noutsos et al., 2015](#); [Stovall et al., 2015](#)), corresponding to declinations below approximately -10° for LOFAR and -30° for the LWA and above approximately $+30^\circ$ for the MWA. However, these telescopes are also situated over a range of longitudes, and there is a significant overlap in the area of observable sky, as shown in [Figure 3.1](#). This is particularly useful for monitoring observations and verifying results (e.g. [Hermsen et al., 2013](#); [Dolch et al., 2014](#); [Mereghetti et al., 2016](#)).

Low-frequency observations of pulsars provide insights into the physics of the radio emission mechanism and the ISM (e.g. [Stappers et al., 2011](#)), especially

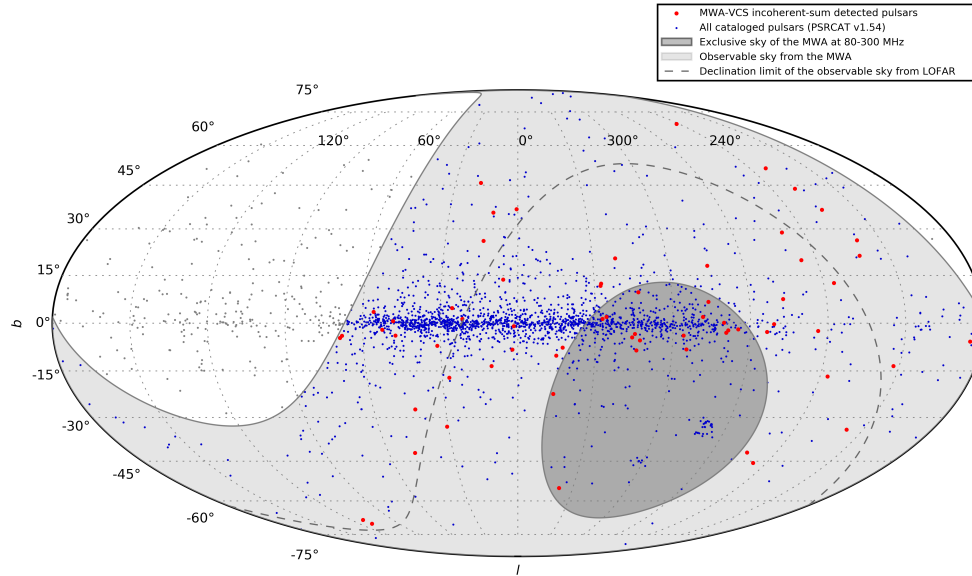


Figure 3.1: The locations of catalogued pulsars in Galactic coordinates (blue points; using version 1.54 of the pulsar catalogue). The observable sky from the MWA telescope ($\delta \lesssim +30^\circ$) and the area where the MWA can exclusively observe pulsars below 300 MHz ($\delta \lesssim -50^\circ$) are indicated by the light and dark shaded regions, respectively. The grey dashed line indicates the declination limit of the observable sky from LOFAR ($\delta \gtrsim -10^\circ$). We note that for aperture arrays like the MWA and LOFAR, observations can be made at any zenith angle, the sensitivity falls off with the zenith angle, and is significantly reduced when pointed to elevations $\lesssim 30^\circ$ (Noutsos et al., 2015). In this figure, we use hard limits purely for illustration. The positions of the pulsars detected at 185 MHz in this work, using the MWA in incoherent-sum mode, are also shown (red circles).

in a multi-frequency context. For example, the widths of integrated pulse profiles generally widen with decreasing observing frequencies (e.g. [Johnston et al., 2008](#)). This behaviour is often explained by the radius-to-frequency mapping (RFM) model, whereby lower-frequency emission arises from higher altitudes in the pulsar magnetosphere (e.g. [Cordes, 1978](#); [Mitra & Rankin, 2002](#)). Therefore, we assume that pulse profiles observed at a range of frequencies allow us to trace the open dipolar field line region of the pulsar magnetosphere, which increases in size towards higher altitudes. The simplest pulse profiles often show the clearest examples of RFM, while multi-component profiles often show more complex behaviour ([Johnston et al., 2008](#)). Furthermore, pulse profiles are often observed to show an increasingly rapid evolution towards lower frequencies (e.g. [Bhat et al., 2014](#); [Pilia et al., 2016](#)). This is possibly due to the frequency-dependence of the emission beam opening angle ([Thorsett, 1991](#); [Xilouris et al., 1996](#)), which also depends on the pulsar spin period and spin-down ([Kijak & Gil, 1998, 2003](#)). Therefore, comparing low-frequency observations to those at higher frequencies for a representative sample of pulsars can enable us to understand the beam geometry better and provide further insights into the enigmatic radio emission mechanism from pulsar magnetospheres.

Low-frequency pulsar observations also provide precise measurements of properties of the ionised ISM, including electron densities (e.g. [Hassall et al., 2012](#); [Bilous et al., 2016](#)) and magnetic fields (e.g. [Noutsos et al., 2015](#); [Howard et al., 2016](#)), due to the steep power-law dependence on frequency of the propagation effects. For example, [Stovall et al. \(2015\)](#) were able to study the ISM propagation effects using 44 pulsars detected at frequencies less than 100 MHz with the LWA.

A major motivation for the Square Kilometre Array (SKA) is the science facilitated using pulsar observations. The MWA is the low-frequency precursor telescope to the SKA. Therefore, pulsar observations using the same observing environment and frequencies are necessary to prepare for pulsar science with the SKA-Low.

In this work, we present an initial low-frequency census of known (catalogued) pulsars in the Southern Hemisphere. The descriptions of our MWA observations and data processing methods are outlined in Section 3.2. In Section 3.3 we provide a summary of the 50 pulsars detected to date. We discuss our results in Section 3.4, including the investigation of the population of pulsars observable using SKA-Low, and summarise our work in Section 3.5.

3.3 Observations and analysis

3.3.1 The MWA and the Voltage Capture System

The MWA is located at the Murchison Radio-Astronomy Observatory (MRO) in Western Australia. The remote, radio-quiet environment minimises radio frequency interference (RFI). The MWA consists of an array of 128 tiles, distributed with baselines up to ~ 3 km, where each tile comprises 16 dual-polarisation dipole antennas arranged in a regular 4×4 grid. Since the array has no moving parts, tile beams are formed by electronic manipulation of the dipole signals in an analogue beamformer (Tingay et al., 2013). A bandwidth of 30.72 MHz can be flexibly recorded over a frequency range of 80–300 MHz.

Although the MWA was originally designed as an imaging interferometer, the Voltage Capture System (VCS; Tremblay et al., 2015) has extended the capabilities of this telescope, allowing it to record high-time and frequency resolution voltage data. VCS observations are channelised to a frequency resolution of 10 kHz and a time resolution of $100 \mu\text{s}$, allowing the MWA to provide phase-resolved observations of pulsars (e.g. Bhat et al., 2014). Commissioning of the MWA-VCS was completed in 2014.

VCS data recorded from each MWA tile can be reduced in different ways, providing its user with maximum flexibility. The least compute-intensive method is to perform an incoherent sum: voltages from each tile are multiplied by their complex conjugate to form the power, and then summed together. This incoherent

sum preserves the full single tile field-of-view (FoV; $\sim 450 \text{ deg}^2$ at 185 MHz) and increases the sensitivity by a factor of \sqrt{N} over a single tile theoretically, where N is the number of tiles summed. The VCS raw data can also be processed to generate a coherent sum of the tile signals by applying a phase rotation to each voltage stream and then summing to increase the sensitivity over a single tile by a factor of N theoretically, and reducing the FoV to ~ 2 arcmin in diameter. Forming a single coherent tied-array beam requires 2-3 times more compute time, in addition to manually-generated calibration solutions (e.g. [Bhat et al. 2016](#)). We therefore conducted an initial pulsar census using the incoherently summed data. Pulsars detected using the coherently beamformed data will be reported in a future publication.

3.3.2 Observations

Approximately 84 hours of observations were made at a frequency of 185 MHz during the first two years of MWA-VCS operations⁴. These data are from 104 observing sessions, ranging from 5 minutes to 1.5 hours in duration, and were collected for a variety of scientific projects, e.g. pulsar emission studies, millisecond pulsar monitoring, and searches for Fast Radio Bursts (e.g. [Thornton et al. 2013](#)). These observations are drift scans, i.e. the elevation and azimuth were fixed throughout the pointing instead of tracking a particular source. Each observation is identified by the GPS start time ('OBS ID' hereafter). The VCS system records data at a rate of 28 TB/hr, and the total size of the entire data set is approximately 2.6 PB⁵. These raw data are archived at the Pawsey Supercomputing Centre.

We processed 37 hours of VCS data from 46 individual observing sessions that cover the sky efficiently, i.e. we have excluded duplicate sky pointings. These observations amount to $\sim 17,000 \text{ deg}^2$ of the sky (albeit with varying sensitivity),

⁴This frequency was chosen because the beam is comparatively well-understood and the band is nearly free from RFI

⁵1 petabyte (PB) = 1024 terabytes (TB)

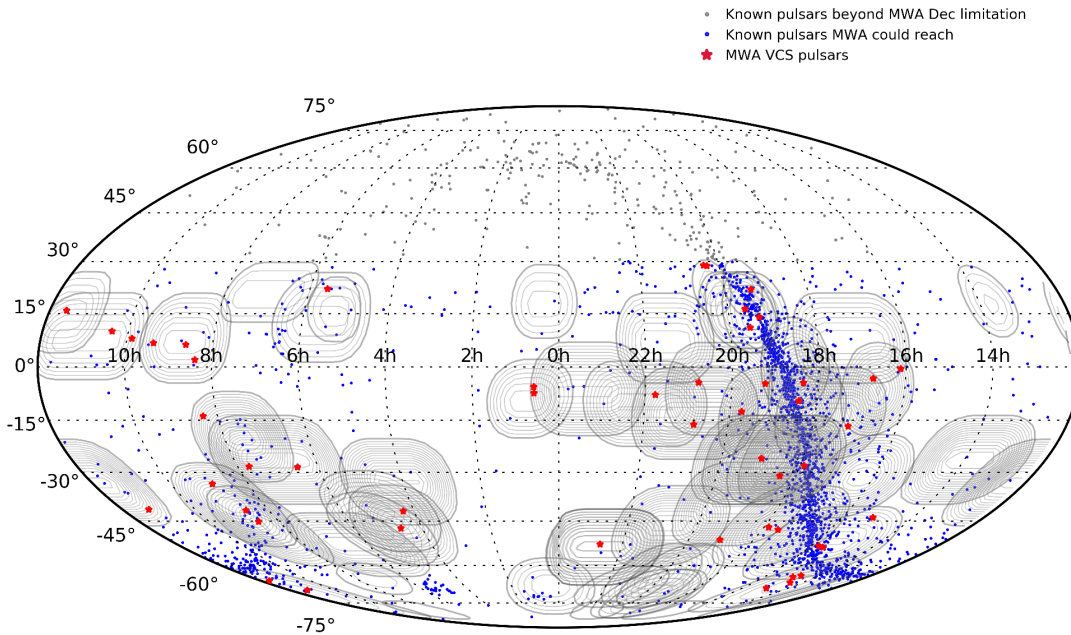


Figure 3.2: The sky coverage of the MWA-VCS observations processed in this work. Grey contour lines represent the beam pattern (for beam powers greater than 25% of that at zenith); blue points indicate all known pulsars (catalogue v1.54); red stars show the pulsars detected in this work.

which corresponds to $\sim 55\%$ of the whole $\delta \lesssim 30^\circ$ sky (see Figure 3.2).

3.3.3 Pre-processing

As described in Tremblay et al. (2015), the channelised raw voltage data are recorded in 32 files, each being a fine polyphase filter bank (PFB) output per tile per polarisation per second. We generate an incoherent beam (as described in Section 3.3.1) for each second of the observation, and write out every 200-seconds of data to a file in the PSRFITS format (Hotan et al., 2004), retaining a frequency resolution of 10 kHz and a time resolution of $100 \mu\text{s}$. Therefore, each observation typically consists of multiple PSRFITS files. These PSRFITS files are then processed by the Wide-field Pulsar Pipeline (WIPP), described in Section

3.3.4.

3.3.4 Processing pipeline

The incoherently-summed MWA data preserves the large FoV and, therefore, multiple pulsars may be located within the tile beam in each observation. We developed a Wide-field Pulsar Pipeline (WIPP) that automatically identifies and folds all known pulsars positioned within the beam out to an established threshold.

3.3.4.1 Sample Selection

For each observation, the WIPP automatically generates a list of pulsars to fold using the pulsar catalogue (v1.54) and information about the telescope pointing direction (taking into account that during drift scans pulsars may enter and leave the beam), the beam model, and the dispersion measures (DMs) of the pulsars. Since each MWA tile is a regularly distributed aperture array, the resulting beam pattern is complex, changing as a function of azimuth, elevation, and frequency (Sutinjo et al., 2015b). An example is shown in Figure 3.3. We used the MWA beam model to identify known pulsars located within the beam out to 25% of the beam power towards zenith, at any time during the observations, and include even those located within a grating lobe in some cases.

According to the NE2001 Galactic electron density model (Cordes & Lazio, 2002), the scattering time associated with lines-of-sight towards the Galactic plane with a DM greater than $300 \text{ cm}^{-3} \text{ pc}$ is typically more than 3 seconds. Since we are unlikely to detect pulsars with such long scattering times at 185 MHz, we limited our selection of pulsars to those with a DM of less than $300 \text{ cm}^{-3} \text{ pc}$. This excluded a substantial fraction ($\sim 40\%$) of the pulsars located near the Galactic plane. Moreover, we did not make any assumptions regarding the pulsars' expected flux densities and included all pulsars, whether or not they have a catalogued flux density measurement. Typically, a source list of $\sim 10\text{--}200$ pulsars was

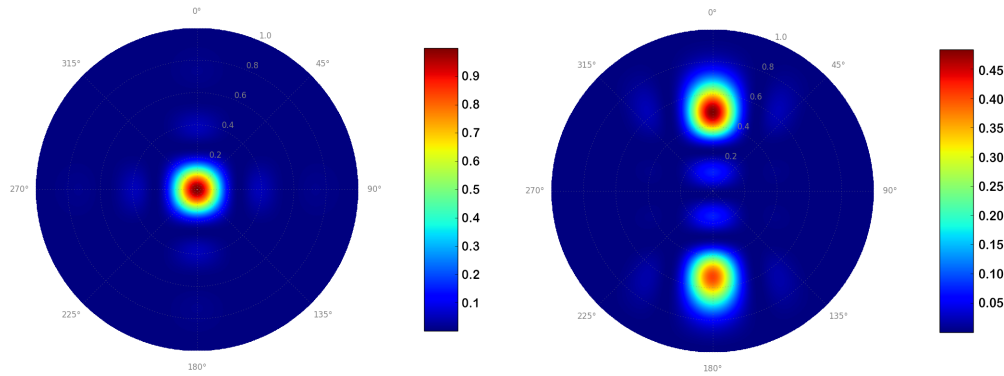


Figure 3.3: The MWA tile beam model at 185 MHz, indicating the power relative to pointing at zenith, see colour bars for scale. Left: an example of a pointing towards the zenith (observation ID 1088850560). Right: an example of the main beam and a grating lobe (upper and lower part of the figure, respectively; observation ID 1140972392; 0° azimuth, 45° elevation).

generated per observation, with larger numbers for pointings near the Galactic plane.

3.3.4.2 Pulsar Folding

The WIPP attempts to detect every pulsar in the source list generated for each observation. The pipeline uses the `prepfold` function of the PRESTO⁶ software package (Ransom, 2001) to dedisperse and fold the data using ephemerides from the pulsar catalogue.

We folded the data twice: with and without searching in DM, period, and period-derivative space. This identified changes in the ephemeris values and prevented the algorithm from locking on to the radio-frequency interference (RFI). We also applied an RFI mask output obtained from `rfifind` in PRESTO, but this did not significantly alter the results which is likely due to the pristine RFI environment (Offringa et al., 2015; Sokolowski et al., 2017). For pulsars with

⁶www.cv.nrao.edu/~sransom/presto

rotational periods < 6.4 ms, we retained the $100 \mu\text{s}$ time resolution of the data. Otherwise, 64 or 100 pulse phase bins were used for the initial detections. A flow chart of the processing procedure is shown in Figure 3.4. After automatically folding the known pulsars in the source lists, each PRESTO output was inspected by eye to identify those successfully detected.

3.3.4.3 Calculation of Flux Densities

For each pulsar detected, we determined the peak signal-to-noise ratio, $(\text{S/N})_{\text{peak}}$, and calculated the flux density using the MWA system performance parameters, including the system temperature, T_{sys} , and the telescope gain, G . The mean flux density, S_{mean} , was calculated using the radiometer equation, as applied to pulsar observations (e.g. Lorimer & Kramer, 2005):

$$S_{\text{mean}} = \frac{(\text{S/N})_{\text{peak}} T_{\text{sys}}}{G \sqrt{n_p t_{\text{int}} \Delta f}} \sqrt{\frac{W}{P - W}}, \quad (3.1)$$

where t_{int} is the integration time, $\Delta f = 30.72$ MHz is the observation bandwidth, and $n_p = 2$ is the number of polarisations summed. The quantity P indicates the pulse period and W represents the equivalent pulse width.

Assuming 100% antenna efficiency, the system temperature includes the contributions from the antenna temperature and the receiver temperature: $T_{\text{sys}} = T_{\text{ant}} + T_{\text{rec}}$. Measurements of T_{rec} for the MWA are available at different frequencies in 1.28 MHz steps (e.g. 23 K at 184.96 MHz and 50 K at 87.68 MHz; Prabu et al., 2015). The antenna temperature, T_{ant} , for a given pointing direction in azimuth, θ , and elevation, ϕ , was determined by integrating the sky temperature $T_{\text{sky}}(\theta, \phi)$ over the modelled MWA beam. An all-sky survey at 408 MHz (Haslam et al., 1981, 1982), scaled to our observing frequency, was used to estimate T_{sky} . For our observations, the T_{sys} ranges roughly from 150 K to 1000 K, with a median value of 284 K.

The incoherent gain $G(\theta, \phi)$ of the MWA for a given pointing direction can be calculated using the beam power pattern $P(\theta, \phi)$ and the offset of the target source

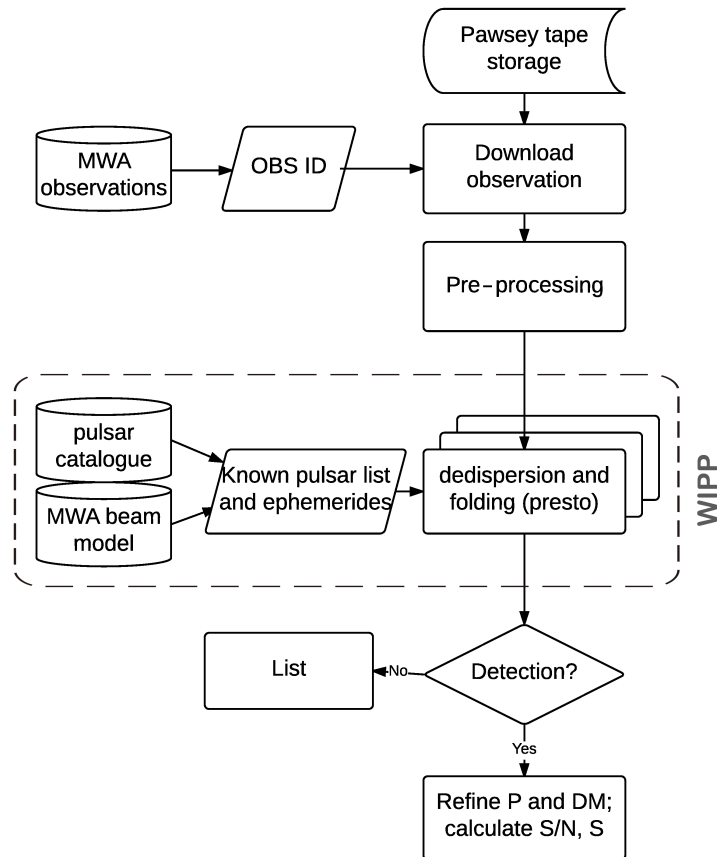


Figure 3.4: The data processing flow: from downloading MWA-VCS archival data (from the Pawsey Supercomputing Centre) to detecting catalogued pulsars. Automatic processing procedures included in the WIPP are shown within the grey dashed line. The WIPP processes multiple pulsars in each observation. This is different from the type of processing generally employed for most traditional pulsar-capable telescopes, where there is typically only one pulsar per pointing.

from the zenith. Following [Oronsaye et al. \(2015\)](#), we rewrite the expression of the incoherent gain as:

$$G(\theta, \phi) = G_{\text{zenith}} \times \frac{P(\theta, \phi)}{P_{\text{zenith}}} = \frac{\lambda^2 (16\sqrt{N})}{2\pi 2k_{\text{B}}} \times \frac{P(\theta, \phi)}{P_{\text{zenith}}}, \quad (3.2)$$

where λ is the observing wavelength, N is the number of MWA tiles, and k_{B} is the Boltzmann constant. The gain value for our detections ranges from 0.003 to 0.024 K/Jy, with a median value of 0.013 K/Jy.

With a typical $T_{\text{sys}} \sim 300$ K, a typical Gain ~ 0.013 K/Jy, assuming 1 hour integration time and a duty-cycle of 5%, the detection limit would be ~ 56 mJy for a 5σ detection at 185 MHz, which is equivalent to ~ 19 mJy at 400 MHz assuming a spectral index of -1.4 .

3.4 Results

In total we processed 37 hours of VCS data, and folded 1227 catalogued pulsars using our pipeline. We successfully detected 50 pulsars with $(\text{S/N})_{\text{peak}} \gtrsim 4$, after manually inspecting the PRESTO outputs. The detection and telescope parameters at 185 MHz are summarised in [Table 3.1](#). The quoted errors on the flux densities (S_{185}) are essentially the uncertainties from our estimation of S/N and hence largely reflect the quality of our detections. However, these errors do not account for large flux density variations arising from other substantial sources of error such as the calibration technique we adopted (see [section 3.3.4.3](#)), or those due to scintillation effects. In particular, long-term (refractive) scintillation effects can lead to flux variability of a factor of ~ 2 – 3 at the MWA’s frequencies (e.g. [Gupta et al., 1993](#); [Bhat et al., 1999](#)). The average pulse profiles of the 50 pulsars are shown in [Figure 3.5](#). For ten pulsars, with declination $\delta < -50^\circ$, these are the lowest frequency detections published.

The detected pulsars have a wide range of periods (1.74 ms–1.96 s), DMs (2.64–180 cm^{-3} pc), and estimated flux densities at 185 MHz (~ 30 –2400 mJy). We detected six millisecond pulsars (MSPs): PSRs J0034–0534, J0437–4715,

J1022+1001, J1902–5105, J2145–0750, and J2241–5236. Four of these are regularly monitored as part of the pulsar timing array project at Parkes (Manchester et al., 2013). MSPs J1902–5105 and J2241–5236 were discovered by observing unidentified *Fermi* Large Area Telescope (LAT) sources using the Parkes radio telescope (Keith et al., 2011; Kerr et al., 2012), and have flux density measurements at 1.4 GHz. The low-frequency flux density of PSR J2241–5236 has also been measured using continuum imaging studied with the MWA (60 mJy at 200 MHz; Murphy et al., 2017). For J1902–5105, there are no low-frequency flux density measurements in the literature. Using MWA-VCS observations, we estimate a flux density of 362 ± 55 mJy at 185 MHz. Using the pulsar’s flux density measured with Parkes at 1.4 GHz (1.2 mJy), we calculated the spectral index α (assuming a single power law $S_\nu \propto \nu^\alpha$) to be approximately -2.8 .

We also detected two non-recycled pulsars which are in binary systems, PSRs J0823+0159 and J1141–6545. The latter is in an eccentric, relativistic 4.74 hour orbit that shows no evidence of being recycled (Kaspi et al., 2000) and is an excellent laboratory for testing theories of gravity (Bhat et al., 2008). PSR J0823+0159, on the other hand, is in a wide-orbit (1232-day period) binary system, with a relatively low mass companion (Hobbs et al., 2004).

We were unable to obtain meaningful estimates of the mean flux density for PSRs J0534+2200 and J0835–4510 (i.e. the Crab and Vela pulsars) because their pulse profiles are severely scattered (the scattering tail extends over the entire pulsar period), and consequently the off-pulse RMS noise could not be determined reliably. PSRs J0742–2822, J1534–5334, and J1820–0427 also show some degree of scattering; however, their pulses are not broadened as significantly, and we were able to estimate their flux densities. More detailed analyses of scattering is reported in Kirsten et al. (2019).

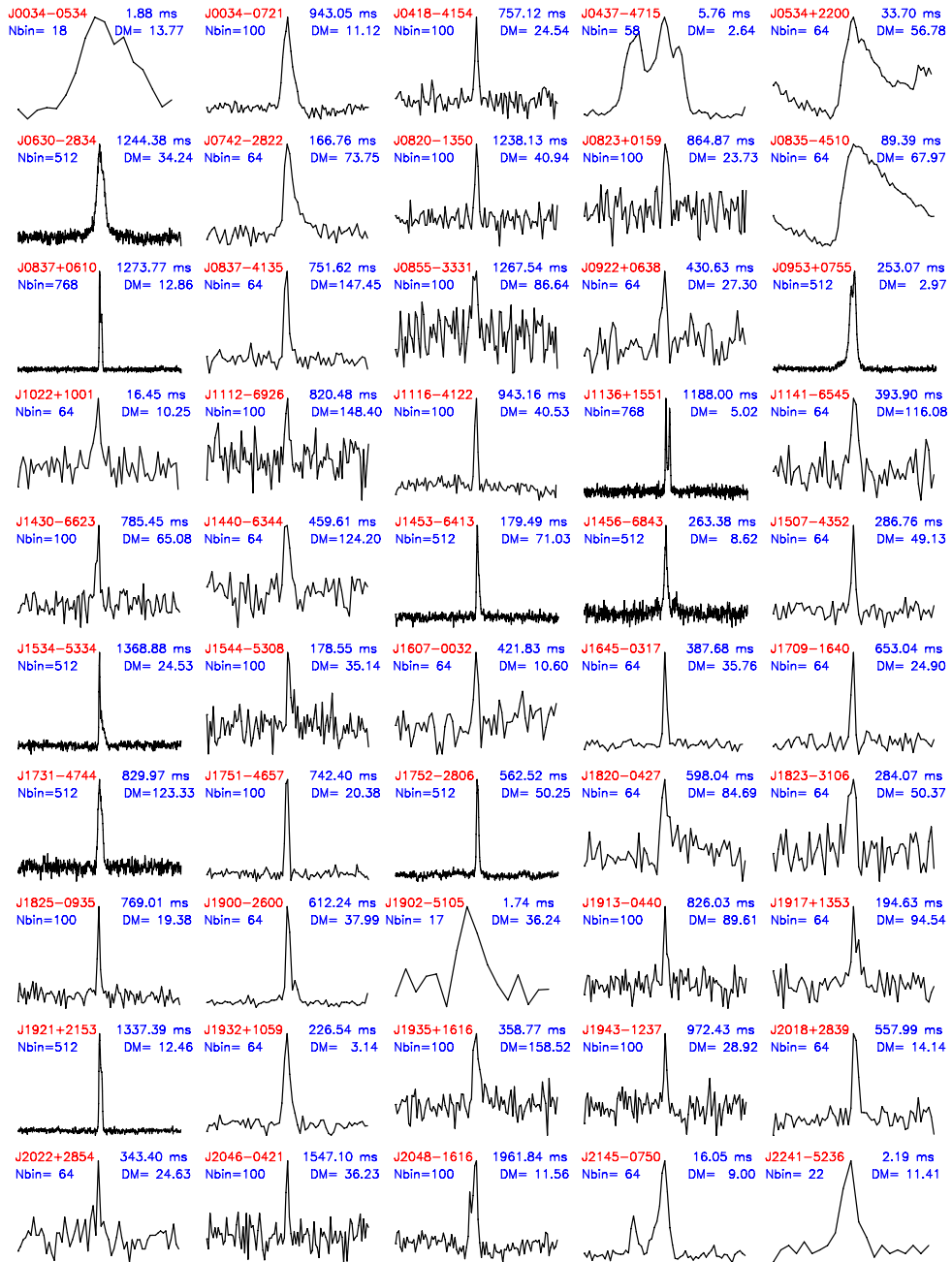


Figure 3.5: Average pulse profiles for the 50 catalogued pulsars successfully detected using MWA-VCS incoherently-summed data at 185 MHz, including 6 MSPs. The period, DM and number of phase bins for each pulsar are also shown. For high-S/N pulsars that we selected to present multi-frequency profiles (Figure 6), we have adopted pulse profiles of higher time resolution than as described in Section 2.4.2.

3.5 Discussion

Our discussion is focused on three main points. Firstly, for a subset of our pulsars, we compare our MWA profiles to those from observations made at multiple frequencies. Secondly, we estimate detection limits of this census. Finally, we review the prospects for detecting pulsars with the full sensitivities of MWA and SKA1-Low.

3.5.1 Multi-frequency Pulse Profiles

We have selected 16 pulsars with relatively high signal-to-noise ($S/N > 15$) for comparison with pulse profiles across different frequencies. The higher frequency profiles are obtained from observations using Parkes and GMRT (Johnston et al., 2008; Johnston & Kerr, 2018), Effelsberg 100-m (von Hoensbroech et al., 1998b; Kijak et al., 1998), and Lovell telescopes (Gould & Lyne, 1998). Lower frequency profiles are from recent LOFAR work (Pilia et al., 2016) and the Pushchino telescope (Kuz'min & Losovskii, 1999) retrieved from the EPN database⁷.

Figure 3.6 shows the evolution of the profiles with observing frequency. For pulsars located north of $\delta = -28^\circ$, our MWA profiles bridge the gap between observations using LOFAR and Pushchino and those at higher frequencies. For nine pulsars located south of $\delta = -28^\circ$, the MWA provides the lowest-frequency detections, extending the frequency range available for those pulsars by a factor of 1.3–7.4.

Examples of pulsars with profiles that support the RFM model include PSRs J1136+1551, J1752–2806, and J2048–1616. For example, the two-component profile of PSR J1136+1551 shows a systematic increase in pulse width and the separation of profile components towards lower frequencies. Our MWA observations are well in accordance with this trend. PSR J2048–1616 has a profile with three significant components at low frequencies and the pulse width becomes

⁷<http://www.epta.eu.org/epndb/>

narrower at higher frequencies; our MWA detection follows this trend. PSR J1752–2806’s pulse profile has a single component that becomes narrower with increasing frequency, although this trend does not hold at the highest observing frequency, 8.4 GHz, due to the appearance of a post-cursor component.

There are also examples of pulsars which do not follow expectations based on the RFM model. PSR J0630–2834 has a single, broad component profile across all frequencies that does not show a significant change in pulse width. Another pulsar with a two-component pulse profile, PSR J0837+0610, shows the components narrowing towards lower frequencies.

The multi-frequency pulse profiles for PSR J1456–6843 show a more complex profile evolution. The MWA profile is narrower than those at higher frequencies, possibly due to the pre- and postcursor components moving away from the main pulse and becoming less significant. The MWA has the ability to carry out multi-band observations (80–300 MHz) by taking advantage of its flexible design, and this capability has been used for detailed profile and spectral studies (Meyers et al., 2017). Future MWA observations at frequencies below and above 185 MHz can therefore provide further information towards investigating the profile evolution in such pulsars.

PSR J0953+0755 also shows a rapid profile evolution towards lower frequencies. A single component is apparent at high frequency, while a precursor evolves away from, and increases in brightness relative to, the main pulse, becoming a two-component profile below 200 MHz. There are few published pulse profiles for PSR J1534–5334. Interestingly, scattering tails are apparent at the Parkes 1.4 and 3.1 GHz frequencies, as well as at 185 MHz.

MSPs J0437–4715 and J2145–0750 are detected with high S/N using the MWA. PSR J0437–4715 is known to show a complex profile evolution across frequencies, where the outer components have significantly different spectra from the central components and become almost as strong as the central component at 200 MHz (Bhat et al., 2014). PSR J2145–0750 has also been detected with

LOFAR (Kondratiev et al., 2016a). Further detailed study of these two MSPs will be published in an upcoming paper (Bhat et al. *in prep.*). The other four MSPs detected using the incoherently-summed MWA data have limited time resolution or S/N; therefore, we do not comment further on their profiles.

3.5.2 Detection limits

To further investigate MWA’s pulsar detection prospects, we summarise all our detections, as well as non detections, in Figure 3.7. We used the mean flux density at 400 MHz (S_{400}) as an indicator of each pulsar’s brightness because these measurements are the closest in frequency most widely available from the pulsar catalogue.

As described in Tingay et al. (2013), the effective collecting area over system temperature ($A_{\text{eff}}/T_{\text{sys}}$) for a single MWA tile is around $0.1 \text{ m}^2/\text{K}$ at 185 MHz. The noise level, σ , of MWA-VCS incoherently summed data can be expressed as:

$$\sigma = \frac{2k_{\text{B}}}{\sqrt{n_{\text{p}}t_{\text{int}}\Delta f N}} \frac{T_{\text{sys}}}{A_{\text{eff}}}, \quad (3.3)$$

where t_{int} is the integration time (typically 1 hour), and N is the number of MWA tiles incoherently summed (usually 128). Thus, the $1\text{-}\sigma$ noise level is 5 mJy. Recently, Murphy et al. (2017) carried out a pulsar spectral study using the MWA imaging data. Their $1\text{-}\sigma$ RMS is 15 mJy beam^{-1} . The lower noise level of our data is partly due to the lack of confusion as we are using the time-variability to negate the confusion noise that limits MWA continuum imaging observations (Condon, 1974; Franzen et al., 2016). Of the 50 detections in this work, PSR J0855–3331 has the lowest S_{400} , which is 7.7 mJy. Therefore, we estimate a detection limit of $\approx 7 \text{ mJy}$ for incoherently summed MWA data.

The predicted mean S/N in Figure 3.7(b) is calculated using the following equation:

$$(\text{S/N})_{\text{predicted}} = S_{400} \left(\frac{185}{400} \right)^{-1.4} \frac{G\sqrt{n_{\text{p}}t_{\text{int}}\Delta f}}{T_{\text{sys}}}. \quad (3.4)$$

To obtain the predicted S/N at 185 MHz using the catalogue value for S_{400} , we

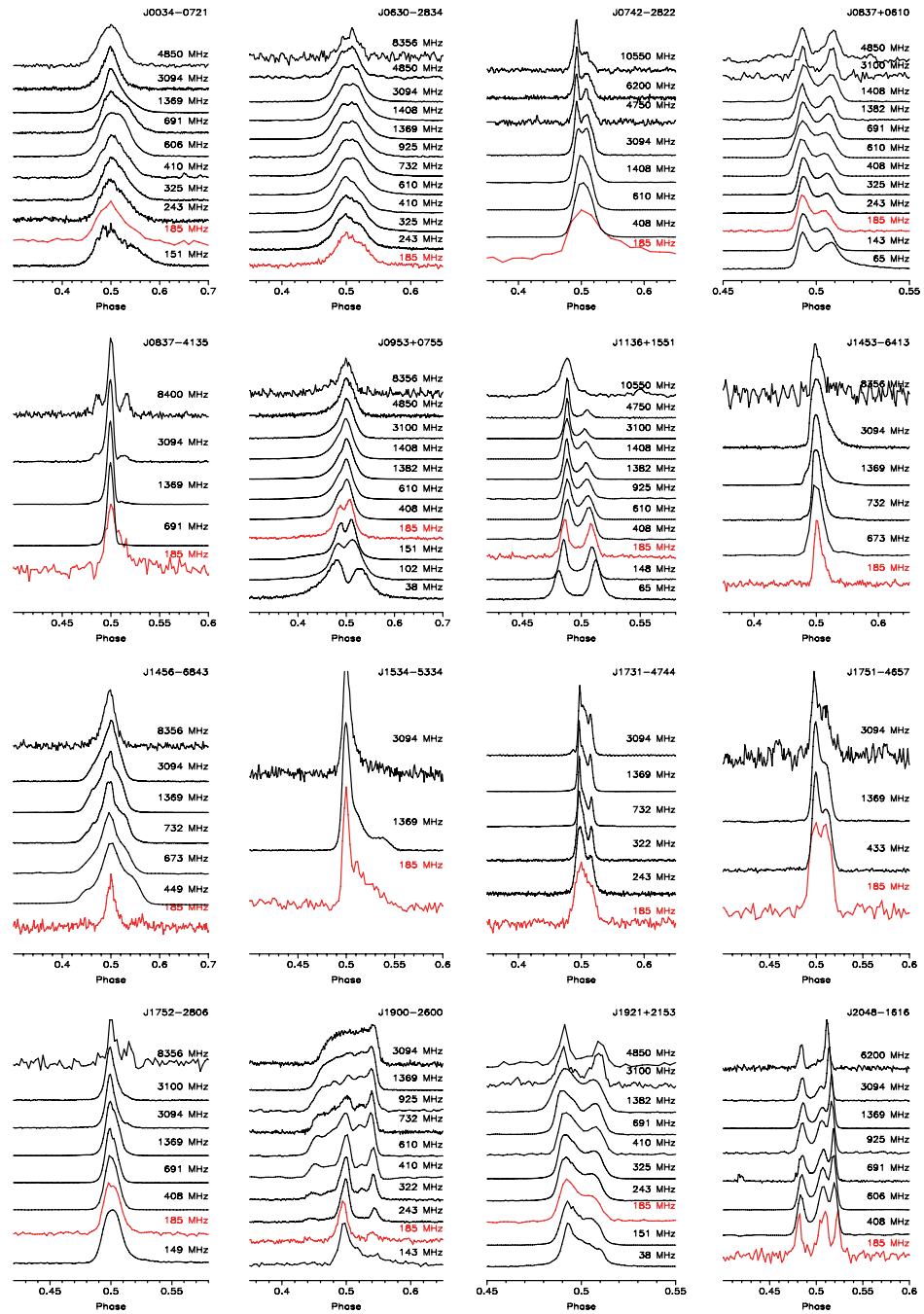


Figure 3.6: Multi-frequency pulse profiles for 16 pulsars. MWA detections (at 185 MHz) are shown in red. The range in pulse phase (x-axis) is chosen to suit the pulse structure and width. The profiles are normalized to the maximum value and nominally aligned based on their measured peak strengths or a suitable fiducial point. The references for the other pulse profiles in black are described in the text.

assumed a spectral index of -1.4 (the mean value calculated in [Bates et al. 2013](#)). This value was found to have a rather large standard deviation (0.96), and introduces additional uncertainty for pulsars whose spectral indices depart from this value. To compare the measured S/N with the $(S/N)_{\text{predicted}}$, calculated using Eq. (3.4), we scaled our measured $(S/N)_{\text{peak}}$ to the equivalent mean S/N:

$$(S/N)_{\text{actual}} = (S/N)_{\text{peak}} \sqrt{\frac{W}{P - W}}. \quad (3.5)$$

Figure 3.7(c) shows the comparison of $(S/N)_{\text{predicted}}$ and $(S/N)_{\text{actual}}$ for pulsars we detected. There is a noticeable scattering of data points from the grey dashed line that represents $\frac{(S/N)_{\text{predicted}}}{(S/N)_{\text{actual}}} = 1$. Possible reasons for this may include: (1) the spectral index deviation from -1.4 , (2) the error of equivalent pulse width and the pulse width difference between 185 MHz and 400 MHz, (3) the flux density fluctuation caused by long-term (refractive) scintillation, and (4) uncertainty in the calibration technique we adopted. For instance, PSR J1921+2153 which has a $(S/N)_{\text{predicted}}$ of 1.6 and a $(S/N)_{\text{actual}}$ of 20 has a very steep spectral index (~ -3) while the PSR J0437-4715 which has a $(S/N)_{\text{predicted}}$ of 27 and a $(S/N)_{\text{actual}}$ of 85 has a significantly large pulse width at 185 MHz.

Of the 1227 pulsars we attempted to detect, there are 254 pulsars above the MWA incoherent sensitivity limit (i.e. $S_{400} > 7$ mJy). The large number of non-detected pulsars may be due to several reasons. For very short period pulsars, like PSR J1939+2134 ($P = 1.56$ ms, $DM = 71$ cm $^{-3}$ pc), the DM smearing within each 10 kHz channel is 1.20 ms (at our lowest frequency channel), which is a substantial fraction (77%) of the pulse period. Furthermore, the pulse profile is expected to be highly scattered at our observing frequency (see [Kondratiev et al. 2016b](#)). Similarly, for PSR J1810+1744 ($P = 1.66$ ms, $DM = 40$ cm $^{-3}$ pc), the DM smearing within one fine channel is 0.68 ms (41% of the pulse period). This makes detection of these pulsars difficult since we have not coherently de-dispersed our data. PSR J1902-5105 has the lowest P/DM value of all the pulsars we detected ($P/DM = 0.048$ ms cm 3 pc $^{-1}$) which corresponds to a DM

smearing of 35% of the pulse period. However, the DM smear within a 10 kHz fine channel can only explain a small fraction of our non-detections.

We assumed a spectral index of -1.4 , even though it has a significant standard deviation (0.96) (Bates et al., 2013). Furthermore, some pulsars tend to have a flatter spectral index, or show a turn over at low frequencies, or even a broken power law spectra (e.g. Maron et al., 2000; Murphy et al., 2017). All of these can potentially lead to non-detection. Low-frequency pulsar observations are therefore very useful in constraining the spectral behaviour of such pulsars.

Other factors influencing non-detection include the effects of scattering and scintillation. For high DM pulsars, pulse profiles become broader at lower observing frequencies, making their detection more difficult. Scintillation effects may also lead to non-detectability at low frequencies, particularly for low to moderate DM pulsars ($\text{DM} < 50 \text{ cm}^{-3} \text{ pc}$), whose apparent fluxes can vary by factor of $\sim 2-3$, and can thus sometimes appear to be fainter than their true fluxes.

Of the 60 pulsars detected by Murphy et al. (2017) using MWA imaging data, 26 were also detected in our observations and a further 11 were not observed in VCS mode (see Table 3.1). Six of the 23 pulsars not detected in this work have $\text{DM} > 200 \text{ cm}^{-3} \text{ pc}$ and consequently their profiles may be significantly scattered at 185 MHz. The Murphy et al. (2017) detections also include the MSP J1810+1744 with $P = 1.66 \text{ ms}$ and $\text{DM} = 40 \text{ cm}^{-3} \text{ pc}$, for which DM smearing over the 10 kHz channel may degrade its S/N. For the remaining 16, it is possible that long-term (refractive) scintillation effects may be a plausible reason, as such effects can give rise to flux variations of a factor of $\sim 2-3$ at low frequencies (Gupta et al., 1993; Bhat et al., 1999). For most pulsars in both our sample and Murphy et al. (2017) (with the exceptions of PSRs J0835–4510 and J0034–0534), the measured flux densities tend to agree within a factor of three (the flux variation that can be caused by scintillation). In the case of MSP J0034–0534, the measured flux density differs by a factor of six, and in the case of PSR J0835–4510, its long scattering tail prevented us from obtaining a meaningful estimate of its

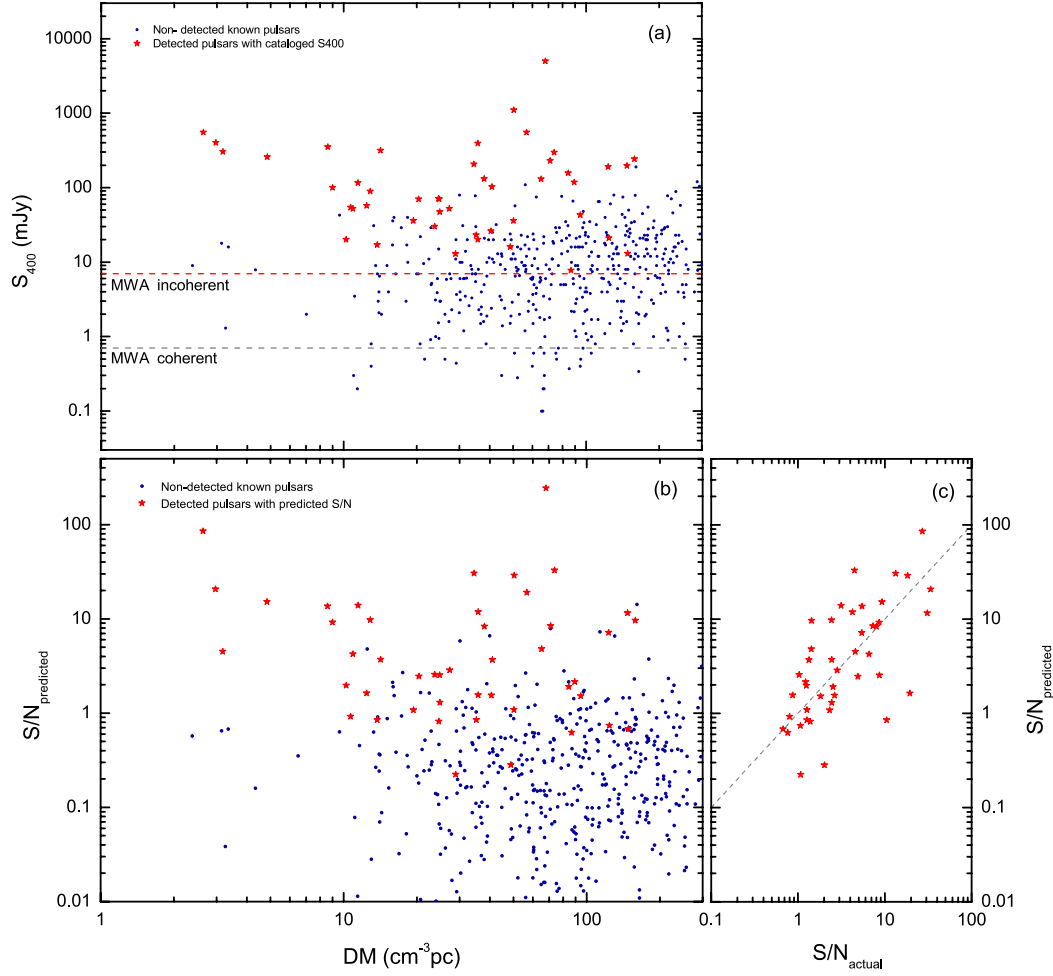


Figure 3.7: (a). Catalogued pulsars that were folded and were or were not detected (red stars and blue points, respectively) shown in DM and S_{400} parameter space. Here we use the S_{400} value from the pulsar catalogue and exclude four detected pulsars that do not have a published S_{400} . The red dashed line shows the sensitivity limit of incoherently-summed MWA data; the grey dashed line shows the current MWA sensitivity for coherently-beamformed data. (b). The predicted S/N against DM for pulsars that we did and did not detect (using the same symbols as in (a)). The mean $S/N_{\text{predicted}}$ was calculated using Eq. (3.4). (c). The predicted S/N vs. the actual S/N for pulsars we detected. Consistent with the $S/N_{\text{predicted}}$, the S/N_{actual} is also the mean S/N calculated using Eq. (3.5). The grey dashed line represent $\frac{(S/N)_{\text{predicted}}}{(S/N)_{\text{actual}}} = 1$

flux.

3.5.3 Future detection prospects

We use the results from our initial census to examine the prospects of detecting pulsars using the full sensitivity of MWA (coherently beamformed data) as well as using the SKA1-Low, i.e. Phase I of SKA-Low. As discussed in section 3.5.2, the estimated sensitivity limit for the incoherent beam is ≈ 7 mJy at 400 MHz. The sensitivity is expected to improve by a factor of $\sqrt{N_{\text{tile}}} \approx 11$ for coherently beamformed MWA-VCS data. However, in reality, this will depend on a number of factors such as calibration accuracy, the number of tiles included, the source and background temperature, and potentially even correlated noise between adjacent tiles. For example, [Bhat et al. \(2016\)](#) report a factor of 10 improvement for their observations of MSP J0437–4715. This is nearly 90% of the theoretical expectation. We therefore assume the theoretical sensitivity limit for the incoherently summed data to be 7 mJy, and that for the coherently beamformed data to be 10 times more sensitive, 0.7 mJy, as shown in Figures 3.7 and 3.8.

SKA1-Low is planned to consist of around 130,000 log-periodic dual-polarised antenna elements, designed for sensitivity from 50 to 350 MHz. From Fig. 19 of the SKA Baseline Design document v2, $A_{\text{eff}}/T_{\text{sys}}$ for SKA1-Low is around $600 \text{ m}^2/\text{K}$ at 200 MHz (towards zenith) and the corresponding T_{sys} is 170 K. Thus, the gain at 200 MHz can be calculated as $G = A_{\text{eff}}/2k_{\text{B}} \approx 37 \text{ m}^2/\text{K}$. We compare the sensitivity limit for SKA1-Low with that for the incoherently summed MWA (see Figure 3.8). $A_{\text{eff}}/T_{\text{sys}}$ for SKA1-Low is approximately 600 times better than the MWA incoherent array (which has $A_{\text{eff}}/T_{\text{sys}} \sim 1 \text{ m}^2/\text{K}$; [Tingay et al. 2013](#)). The sensitivity will further improve by a factor of $\sqrt{3}$ assuming a bandwidth of 100 MHz for SKA1-Low⁸. By factoring in shorter integration times (600 s, i.e. 1/6 of that used for the MWA sensitivity calculation), we estimate the sensitivity limit

⁸Pulsar flux densities, dispersion smearing, scattering broadening and T_{sky} all vary across the large observing frequency range and we do not explicitly account for these effects.

of SKA1-Low to be around 400 times lower than that of the MWA incoherently summed data.

To gain further insight into the pulsar detection prospects of SKA1-Low, we simulated pulsar populations using the PsrPopPy (Bates et al., 2014) code. New functionality has been implemented in PsrPopPy, which calculates the telescope gain as a cosine-square function of the zenith distance, providing more realistic pulsar yields for an aperture array. Using our MWA incoherent census as an input survey with zenith gain $G=0.025$ (maximum gain value in Table 3.1) and considering only pulsars with $(S/N)_{\text{peak}} > 5$, the corresponding detection count is 57. This includes 9 more detections from recent observations (whose profiles are not reported here as the data are still within the proprietary period and will be published separately)⁹. We simulated 120 realisations of pulsar populations to span a wide range of population characteristics (e.g. luminosity distribution, spatial distribution, etc.). For each realisation, we performed 120 survey simulations at a frequency of 200 MHz assuming a bandwidth of 100 MHz and an integration time of 600 s. Thus, we ran 14,400 simulated SKA1-Low surveys in total. The mean value of pulsars detected in this simulated SKA1-Low survey is 9431 ± 1279 , which is over 3.5-times the number of known pulsars to date. We note that the spectral turnover at low-frequencies will also affect the pulsar detection prospects for SKA1-Low, though it is not well characterised for most pulsars.

The predicted SKA1-Low yields from one randomly chosen PsrPopPy simulation (10,409 pulsars detected in this simulation) are plotted in Figure 3.8. To cross-check these results, we ran a simulation of an MWA survey on this specific population model, which predicted 56 detections (also shown in Figure 3.8). We note that the PsrPopPy detections have a very similar S_{400} distribution while the DM distribution extends to lower DM values when compared with the pulsar catalogue. Our results are comparable to those from Keane et al. (2015), who also found the optimum frequency for pulsar searching is 250 MHz for SKA1-Low.

⁹Of the 50 detections we report in this paper, two have $(S/N)_{\text{peak}} \sim 4$ and therefore excluded from this analysis.

For comparison, they predict SKA1-Low will be able to detect ~ 7000 normal pulsars and ~ 900 MSPs.

3.6 Conclusion

We have carried out a census of known southern pulsars using 37 hours of MWA-VCS archival data from observations at 185 MHz. This is a relatively shallow census as the data from all 128 MWA tiles were combined incoherently, yielding $\sim 10\%$ of the sensitivity achievable with the MWA. However, this preserves the large field-of-view ($\sim 450 \text{ deg}^2$ at 185 MHz) and thus facilitates an expedited initial census. We successfully detected 50 pulsars, 6 of which are millisecond pulsars. For ten pulsars, we present the lowest frequency detections available in the literature. For a subset of the pulsars we also present their multi-frequency pulse profiles by combining our data with those from other telescopes, demonstrating a number of profile evolution behaviours with frequency. We use our results to forecast a pulsar survey yield of ~ 9400 using SKA1-Low.

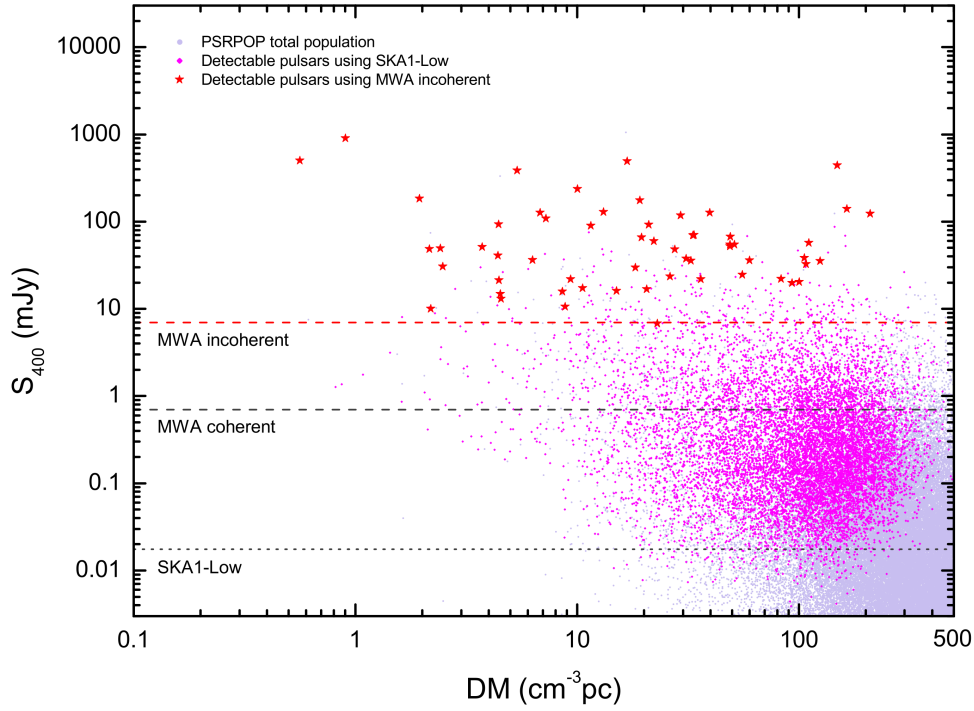


Figure 3.8: An example of a simulated pulsar population and predicted pulsar detections using the MWA (incoherent sum) and SKA1-Low. The light grey points indicate the total pulsar population generated by PsrPopPy using MWA incoherent-sum parameters and a detection number of 57. The red stars indicate the predicted detections from an MWA incoherent survey. The magenta dots indicate the predicted detections from an SKA1-Low survey. The red and grey dashed lines indicate the sensitivity limits for the incoherently and coherently summed MWA data, respectively (identical to Figure 3.7a). The grey dotted line shows the estimated sensitivity limit of SKA1-Low.

Table 3.1: Flux density and other parameters for the 50 catalogued pulsars successfully detected in MWA-VCS archival data.

PSR	Period ¹ (ms)	DM ² (cm ⁻³ pc)	DM _{psrcat} ³ (cm ⁻³ pc)	Gain ⁴ (K/Jy)	T _{sys} ⁵ (K)	S/N _{peak}	S ₁₈₅ ⁶ (mJy)	S ₂₀₀ ⁷ (mJy)	S ₄₀₀ ⁸ (mJy)	Fold time (s)	Obs ID
J0034–0534	1.877	13.77	13.77	0.0135	201	15.26	401±14	65±11	17	2496	1137236608
J0034–0721	943.045	11.12	10.92	0.0143	201	24.71	237±5	292±14	52	2496	1137236608
J0418–4154	757.094	24.54	24.54	0.0133	149	11.36	40±3			3712	1127329112
J0437–4715	5.757	2.65	2.64	0.0225	165	45.14	507±6	834±9	550	2496	1123367368
J0534+2200	33.7	56.78	56.79	0.0081	243	†	†		550	1024	1099414416
J0630–2834	1244.385	34.24	34.42	0.0201	213	52.95	271±3	463±5	206	4416	1101491208
J0742–2822	166.764	73.75	73.78	0.0129	213	15.05	168±8		296	3136	1101491208
J0820–1350	1238.043	40.94	40.94	0.0074	232	9.34	167±13	160±7	102	1024	1101925816
J0823+0159	864.865	23.73	23.73	0.0127	176	5.03	35±5		30	2688	1139324488
J0835–4510	89.39	67.97	67.99	0.0193	313	†	†	7075±207	5000	1216	1139239952
J0837+0610	1273.788	12.86	12.86	0.0163	176	159.12	654±9	286±13	89	2688	1139324488
J0837–4135	751.619	147.45	147.29	0.0233	313	16.29	151±4	95±16	197	1216	1139239952
J0855–3331	1267.621	86.64	86.64	0.0192	313	3.72	46±7	47±8	7.7	1216	1139239952
J0922+0638	430.631	27.3	27.3	0.0064	176	13.88	270±62	100±13	52	1344	1139324488

Continued on next page

PSR	Period ¹ (ms)	DM ² (cm ⁻³ pc)	DM _{psrcat} ³ (cm ⁻³ pc)	Gain ⁴ (K/Jy)	T _{sys} ⁵ (K)	S/N _{peak}	S ₁₈₅ ⁶ (mJy)	S ₂₀₀ ⁷ (mJy)	S ₄₀₀ ⁸ (mJy)	Fold time (s)	Obs ID
J0953+0755	253.09	2.96	2.97	0.0101	173	137.52	2123±16	1072±17	400	1216	1115381072
J1022+1001	16.456	10.25	10.25	0.0094	173	5.91	42±6		20	4864	1115381072
J1112-6926	820.447	148.4	148.4	0.0112	244	4.11	37±10		13	2496	1140972392
J1116-4122	943.199	40.53	40.53	0.0115	211	18.24	139±6	52±7	26	1984	1145367872
J1136+1551	1188.001	5.02	4.85	0.0029	173	50.47	1689±29	684±61	257	1792	1115381072
J1141-6545	394.036	116.08	116.08	0.0102	244	5.6	78±12			2496	1140972392
J1430-6623	785.453	65.08	65.3	0.0132	374	8.89	214±24	190±28	130	576	1131415232
J1440-6344	459.612	124.2	124.2	0.0121	374	5.13	176±34		21	576	1131415232
J1453-6413	179.49	71.03	71.07	0.0117	374	43.13	1244±20	684±23	230	576	1131415232
J1456-6843	263.382	8.62	8.6	0.0124	374	26.27	878±28	738±21	350	576	1131415232
J1507-4352	286.78	49.13	48.7	0.0111	778	13.27	384±27		16	2240	1121173352
J1534-5334	1368.968	24.82	24.82	0.0175	778	55.77	705±22		70	4864	1121173352
J1544-5308	178.565	35.16	35.16	0.0178	778	7.99	102±15		23	4864	1121173352
J1607-0032	421.829	10.6	10.68	0.0081	422	5.29	270±59	137±15	54	384	1117899328
J1645-0317	387.683	35.76	35.76	0.0085	832	27.36	2224±107	774±18	393	576	1116090392
J1709-1640	653.037	24.9	24.89	0.0171	832	15.97	271±18		47	3136	1116090392

Continued on next page

PSR	Period ¹ (ms)	DM ² (cm ⁻³ pc)	DM _{psrcat} ³ (cm ⁻³ pc)	Gain ⁴ (K/Jy)	T _{sys} ⁵ (K)	S/N _{peak}	S ₁₈₅ ⁶ (mJy)	S ₂₀₀ ⁷ (mJy)	S ₄₀₀ ⁸ (mJy)	Fold time (s)	Obs ID
J1731-4744	829.969	123.33	123.33	0.022	832	29.15	424±8	325±28	190	3840	1091793216
J1751-4657	742.405	20.38	20.4	0.0205	832	29.96	411±10		70	3840	1091793216
J1752-2806	562.521	50.25	50.37	0.0199	1021	116.02	2441±28	1504±269	1100	2432	1107478712
J1820-0427	598.044	84.69	84.44	0.0061	832	7.47	1035±120	499±51	157	1792	1116090392
J1823-3106	284.069	50.37	50.24	0.016	567	5.1	105±15		36	2944	1133329792
J1825-0935	768.973	19.38	19.38	0.0088	832	15.31	612±40		36	2112	1116090392
J1900-2600	612.241	37.99	37.99	0.0243	567	39.67	393±11	299±13	131	3712	1133329792
J1902-5105	1.742	36.24	36.25	0.0086	429	5.85	362±55			1664	1116787952
J1913-0440	826.027	89.61	89.39	0.0101	302	8.14	169±22	176±26	118	768	1097404000
J1917+1353	194.627	94.54	94.54	0.0106	385	8.28	237±30		43	1280	1148063920
J1921+2153	1337.39	12.46	12.44	0.0096	408	117.33	2112±49		57	2496	1095506112
J1932+1059	226.536	3.14	3.18	0.0111	408	20.74	362±15	501±47	303	3520	1095506112
J1935+1616	358.768	158.52	158.52	0.0115	408	6.82	106±9		242	3712	1095506112
J1943-1237	972.453	28.92	28.92	0.0136	265	7.16	68±8		12.9	1536	1152636328
J2018+2839	557.991	14.14	14.2	0.0077	331	11.71	561±41		314	576	1131957328
J2022+2854	343.427	24.63	24.63	0.0076	331	7.22	323±48		71	576	1131957328

Continued on next page

PSR	Period ¹ (ms)	DM ² (cm ⁻³ pc)	DM _{psrcat} ³ (cm ⁻³ pc)	Gain ⁴ (K/Jy)	T _{sys} ⁵ (K)	S/N _{peak}	S ₁₈₅ ⁶ (mJy)	S ₂₀₀ ⁷ (mJy)	S ₄₀₀ ⁸ (mJy)	Fold time (s)	Obs ID
J2046–0421	1547.1	36.23	35.8	0.0168	302	6.55	34±7		20	3456	1097404000
J2048–1616	1961.512	11.42	11.46	0.0199	265	17.4	77±5	169±8	116	4736	1152636328
J2145–0750	16.05	9	9	0.0149	259	27.57	282±20		100	4544	1118168248
J2241–5236	2.187	11.41	11.41	0.019	205	16.17	108±6	60±11		5056	1129464688

¹ Best period from our processing.

² Best DM calculated from the data by maximising S/N in frequency vs. pulse phase. The effects of scattering and intrinsic profile evolution with frequency were not accounted for.

³ DM catalogued in PSRCAT.

⁴ As an aperture array, MWA’s gain varies with pointing direction.

⁵ At our observing frequency, T_{sys} is dominated by T_{sky} which is, in turn, dominated by the synchrotron radiation from free electrons in the Galactic magnetic field.

⁶ Flux densities calculated from MWA-VCS detections. The quoted errors are the uncertainties from our estimation of S/N. They are from single epoch measurements and thus do not account for large flux density variations arising from effects such as scintillation. By comparing the pulsars common to both this survey and [Murphy et al. \(2017\)](#), the difference in flux density ranges from 1.5% to 84.5%.

⁷ [Murphy et al. \(2017\)](#) calculated 60 catalogued pulsars’ flux densities from MWA continuum images.

⁸ Flux densities catalogued in PSRCAT.

[†] We can not calculate the flux density for the Crab and Vela because of the significant scattering tails.

Chapter 4

Polarimetric Verification and Analysis of two Bright Southern Pulsars

This work was published by:

Xue, M., S. E., Ord, Tremblay, S. M., Bhat, N. D. R., Sobey, C., Meyers, B. W., McSweeney, S. J., Swainston, N. A., “MWA Tied-Array Processing II: Polarimetric Verification and Analysis of two Bright Southern Pulsars”, 2019, Publications of the Astronomical Society of Australia, Volume 36, id.e025

4.1 Summary

Polarimetric studies of pulsars at low radio frequencies provide important observational insights into the pulsar emission mechanism and beam models. They are also useful for probing the properties of the magneto-ionic interstellar medium (ISM). Aperture arrays are the future of next-generation low-frequency telescopes, for which the MWA is one of the prime examples. These new-generation telescopes, however, require a non-traditional approach to data processing (e.g. calibration and beamforming) compared to conventional single-dish or multi-dish

telescopes. In this published work, we present a detailed verification exercise of the MWA’s pulsar polarimetric capability, using two bright southern pulsars, PSRs J0742–2822 and J1752–2806. For each pulsar (and corresponding calibrators), observations were made in a specially designed observing setup that allows simultaneous coverage of multiple frequency bands across 76–313 MHz, and were taken at multiple zenith angles (from 0° to 50°), all within a single night. We show that the MWA can be reliably calibrated for pulsar polarimetric applications at zenith angles $\lesssim 45^\circ$ and frequencies $\lesssim 270$ MHz. We present the polarimetric profiles for PSRs J0742–2822 and J1752–2806 at frequencies lower than 300 MHz for the first time. We also present an analysis of the degree of linear polarisation and pulse profile evolution with frequency. For PSR J0742–2822, the measured degree of linear polarisation shows a rapid decrease at low frequencies ($\lesssim 300$ MHz), much in contrast with the generally expected trend. This is attributed to depolarisation effects caused by small-scale, turbulent, magneto-ionic ISM in the pulsar’s line-of-sight. Such an effect has not been seen in any other pulsars before, and will be the subject of investigation in the next chapter.

4.2 Introduction

Shortly after the original discovery of pulsars (Hewish et al., 1968), the radio emission from pulsars was found to be polarised (Lyne & Smith, 1968). The polarimetric profiles of pulsars provide useful tools to classify and study pulsar geometry (e.g. Rankin, 1983; Brinkman et al., 2019). Most pulsars tend to show a significant amount of linear polarisation – about 20 per cent, on average, and reaching up to 100 per cent in some cases (e.g. Weltevrede & Johnston, 2008; Han et al., 2009). The degree of linear polarisation generally tends to decrease with increasing observing frequency (e.g. Morris et al., 1981; von Hoensbroech et al., 1998a). The physical explanation for this is not straightforward, though may be due to higher frequencies traversing more of the magnetosphere (Johnston et al., 2008), or the birefringence of plasma in the open field-line region of pulsar

magnetospheres (e.g. McKinnon, 1997). Many pulsars also show some circular polarisation – about 10 per cent, on average (e.g. Gould & Lyne, 1998; Weisberg et al., 1999; Johnston & Kerr, 2018).

The radio emission from pulsars is broadly thought to originate within the open field lines of the magnetosphere, with the emission beam centred on the magnetic axis (e.g. Komesaroff, 1970). Consequently, the linear polarisation position angle (PA) will be determined by the direction of the magnetic field line as it sweeps across our line-of-sight. The PA measured as a function of rotational phase, referred to as the PA curve, is generally expected to delineate an S-shape, i.e., the PA will vary more slowly at the outer wings of the pulse profile compared to the centre. This is referred to as the rotating vector model (RVM; Radhakrishnan & Cooke, 1969). Fitting the RVM model to the observed PAs provides an estimation of the emission beam size and the inclination angle of the magnetic axis with respect to the rotation axis (e.g. Narayan & Vivekanand, 1982; Everett & Weisberg, 2001).

For some pulsars, especially those with medium or low levels of linear polarisation, their PA curves show interruptions of approximately 90° , referred to as orthogonal jumps (e.g. McKinnon & Stinebring, 1998). For example, Karastergiou et al. (2011) present the polarimetric profiles for PSR J0738–4042 at different epochs, and find that the presence of orthogonal jumps in the PA curves are associated with reduced degrees of linear polarisation. Such observational evidence affirms the concept that pulsar emission could comprise two superposed orthogonal polarisation modes (OPMs; e.g. McKinnon & Stinebring, 2000). There have been a number of associated studies from both observational (e.g. Edwards & Stappers, 2004; Noutsos et al., 2015) and theoretical (e.g. Gangadhara, 1997; Melrose et al., 2006; van Straten & Tiburzi, 2017) points of view. However, the nature of the OPMs is still one of the least understood aspects of pulsar emission.

Of the >2600 known pulsars¹ (Manchester et al., 2005a), only around one-

¹<http://www.atnf.csiro.au/people/pulsar/psrcat/>

third have polarimetric properties currently available, and this is mostly limited to ~ 1.4 GHz frequencies. Extensive polarimetric studies have been published by [Gould & Lyne \(1998\)](#) using the Lovell telescope, [Weisberg et al. \(1999\)](#) using the Arecibo telescope, [Manchester et al. \(1998\)](#) and [Johnston & Kerr \(2018\)](#) using the Parkes telescope. There have been a limited number of such investigations at frequencies below ~ 1 GHz. Some studies have been conducted using the Giant Metrewave Radio Telescope (GMRT; [Swarup et al., 1991](#); [Roy et al., 2010](#)), including the Meterwavelength Single-pulse Polarimetric Emission Survey at 333 and 618 MHz [Mitra et al. \(2016\)](#). At lower radio frequencies, [Noutsos et al. \(2015\)](#) undertook polarimetric studies below 200 MHz using the Low-Frequency Array (LOFAR; [van Haarlem et al., 2013](#); [Stappers et al., 2011](#)), for pulsars observable from the northern hemisphere. For southern pulsars, the Murchison Widefield Array (MWA; [Tingay et al., 2013](#); [Wayth et al., 2018](#)) provides an excellent opportunity for polarimetric studies of pulsars at frequencies below ~ 300 MHz. Low-frequency polarisation observations of pulsars provide precise probes of the magneto-ionic ISM; for example, towards reconstructing the structure of the Galactic magnetic field ([Han et al., 2009](#); [Sobey et al., 2019](#)). Furthermore, detailed studies of low-frequency polarimetric profiles, in combination with higher frequency data, can provide further insights into the pulse profile evolution, and potentially help elucidate the magnetospheric radio emission mechanism. They also serve as a useful reference for future pulsar studies planned with the Square Kilometre Array (SKA).

Traditionally, polarimetric studies were mostly performed using large single dish antennas or interferometer telescopes comprised of parabolic dishes. For single dish telescopes like Parkes, polarimetric calibration is achieved by comparing an observed full-Stokes pulse profile to a standard profile template (e.g. using long-term monitoring of PSR J0437–4715). This allows the complex Jones matrix, which describes the transfer function of the signal through the system, to be determined (e.g. [Hamaker et al., 1996](#); [Heiles et al., 2001](#); [Johnston, 2002](#); [van](#)

[Straten, 2013](#)). For interferometers like the Westerbork Synthesis Radio Telescope (WSRT) or GMRT, the procedure for forming a tied-array beam is to add the voltages of all telescopes after correcting their relative phases. This means that the tied-array signal can be calibrated by determining an overall system Jones matrix, and thus the polarisation calibration process is similar to that of single dishes (e.g. [Edwards & Stappers, 2004](#); [Mitra et al., 2016](#)).

For low-frequency aperture-array instruments such as LOFAR, the MWA, and the upcoming SKA-Low (i.e. the low frequency component of the SKA), the approach is quite different. Since the arrays have no moving parts, tile/station beam pointings are formed by electronic manipulation of the dipole signals using analogue/digital beamformers ([Tingay et al., 2013](#); [van Haarlem et al., 2013](#)). This beam response is strongly dependent on the pointing direction and frequency (e.g. [Noutsos et al., 2015](#)) and is more difficult to model compared to that for a single dish. Accurate calibration of the full polarimetric response is necessary for aperture arrays to facilitate reliable polarisation studies. This procedure is fairly complex, due to a number of factors: the wide field of view; multiple receiving elements; frequency-dependent beam shape; the absence of an injected artificial calibration signal; and the modulation of calibration errors by the time-variable ionosphere. Thus, developing a suitable calibration/beamformation strategy for the MWA and verifying that it is satisfactorily robust and reliable is an essential prerequisite for performing any polarimetric pulsar work with these new generation radio arrays.

In Paper 1 of this series, we described the algorithms and pipeline that we have developed to form the tied-array beam products from the summation of calibrated signals of the antenna elements ([Ord et al., 2019](#)). Further to that in this chapter we present the first polarimetric study with the MWA of two bright southern pulsars, PSRs J0742–2822 and J1752–2806, at frequencies below 300 MHz. Our primary goal is to investigate their polarimetric properties as a function of frequency and to ascertain the reliability of the MWA’s polarimet-

ric performance. We describe our observations and data processing methods in Section 4.3. In Section 4.4 we summarise the optimal calibration strategy and reproducibility of the polarimetric profiles. In Section 4.5 we describe how we measure the Faraday rotation and use it to estimate the instrumental leakage. We describe the polarimetric properties of the two pulsars, and compare our profiles with published polarimetric profiles at higher frequencies, in Section 4.6. A discussion of our results is in Section 4.7.

4.3 Observation and data processing

Our observations were taken with the Phase I MWA, where the array was comprised of 128 tiles – each tile consists of 16 dual-polarisation dipole antennas arranged in a regular 4×4 grid, operating at 80–300 MHz. The development of the Voltage Capture System (VCS; Tremblay et al., 2015) extended the capabilities of the MWA from an imaging interferometer, allowing it to record high-time and -frequency resolution voltage data and enabling time-domain astrophysics. This allows the MWA to provide phase-resolved observations of pulsars (e.g. Bhat et al., 2018).

We use multiple observations of two bright polarised pulsars that pass through the zenith at the MWA site, PSRs J0742–2822 and J1752–2806, to empirically examine the MWA’s polarimetric response in the beamforming (tied-array) mode, and its stability across the dipole/antenna beam. Here, we describe the properties of target pulsars, our observing strategy, calibration, beamformation, data reduction procedures, as well as archival MWA observations used for our comparison studies.

4.3.1 Target pulsars

PSR J0742–2822 has a period (P) of 167 ms, and a dispersion measure (DM; the integrated electron column density along the line-of-sight) of $73.73 \text{ cm}^{-3} \text{ pc}$. It is

highly polarised with a linear polarisation degree of around 70% and a flux density of ~ 300 mJy at 400 MHz (Lorimer et al., 1995; Gould & Lyne, 1998; Mitra et al., 2016), and hence a linear polarisation flux density of ~ 200 mJy at 400 MHz.

We note that PSR J0742–2822 is known to exhibit emission mode-changing, however, the timescale is relatively long, typically ~ 95 days (Keith et al., 2013). All of our observations of PSR J0742–2822 were taken during the same night within five hours (see below) and, therefore, it is likely that all of our data were taken when the pulsar was in the same emission mode. This is consistent with our results (see Section 3.2).

PSR J1752–2806 ($P = 563$ ms, $DM=50.37$ cm $^{-3}$ pc) is a moderately polarised pulsar with a linear polarisation degree of around 10% and a flux density of ~ 1100 mJy at 400 MHz (Lorimer et al., 1995; Gould & Lyne, 1998; Mitra et al., 2016); thus, its linear polarisation flux density is ~ 110 mJy at 400 MHz. Typically, flux densities of pulsars follow a power-law with a spectral index of about -1.4 , and so we expect pulsars to be around three times brighter at 200 MHz.

4.3.2 Observing strategy

For each pulsar, we obtained and compared the polarimetric pulse profiles over a range of zenith angles across a wide range of observing frequencies. These data allowed us to assess the quality, reliability, and repeatability of our calibration and beamformation process.

Three specific elements of the data were used to investigate the effect on the polarimetric profiles produced, namely:

- sky position of the target pulsar;
- sky position of the calibrator source;
- calibration strategy, i.e., observing a calibrator source prior to the target versus in-field calibration.

Consequently, the observing strategy that we adopted is as follows. For each of the two target pulsars, we recorded five short observations of 5 minutes each, separated by roughly 1 hour, with the middle observation pointing towards the zenith and the others towards zenith angles (ZA) up to 30° , as shown in Figure 4.1. The five observations for each pulsar are labelled P1 to P5, in the order of the observing start times. We also recorded a 5-minute dedicated calibrator observation before each pulsar observation. Thus, there are also five dedicated calibrator observations in total for each pulsar. Similarly, they are named C1 to C5, in the order of their observing start times (see Figure 4.1). The pointing information for the observations is summarised in Table 4.1.

The VCS records data after the second stage of channelisation in the MWA signal path, with a 10 kHz frequency resolution and a $100 \mu\text{s}$ time resolution. Data from our observations were recorded at frequencies spread across the entire MWA band, from 76.80 MHz to 312.32 MHz, in 24 coarse (1.28 MHz-wide) channels (see Table 4.2). These non-contiguous coarse channels were recorded simultaneously, each split into 128 fine (10 kHz-wide) channels.

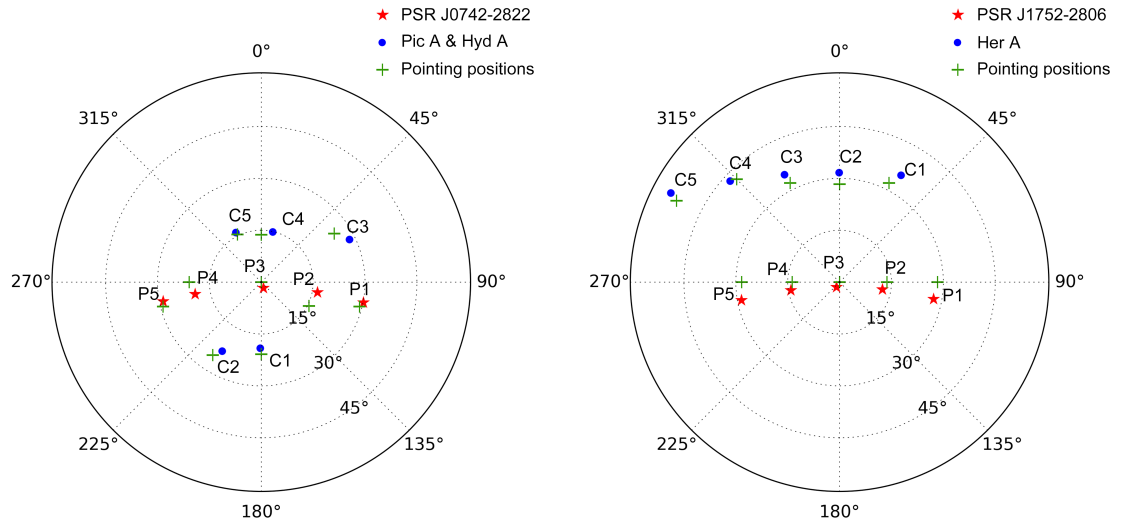


Figure 4.1: (Left) Locations and MWA pointing directions for PSR J0742–2822 and its calibrators Pictor A (C1, C2) and Hydra A (C3–C5). (Right) Locations and MWA pointing directions for PSR J1752–2806 and its calibrator Hercules A. For both panels, the azimuth and zenith angles are shown in horizontal coordinates, azimuth= 0° represents North and azimuth= 90° represents East. Red stars indicate the position of pulsars (labelled P1–P5 in order of observation start time); blue circles indicate the position of calibrators (labelled C1–C5 in order of observation start time); green crosses indicate the pointing centre for each observation. Since the MWA points towards ‘sweet’ spots in the sky (dictated by the analogue beamformer settings), there is usually some offset between the pointing centre direction and the position of the target.

Table 4.1: Observing parameters for PSR J0742–2822, PSR J1752–2806, and calibrator sources.

Target pulsar	J0742–2822 (observed on 2016-02-04)				
Observation ID (GPS time)	1138625088	1138628792	1138633056	1138638456	1138641032
Start time (UTC)	12:44:32	13:46:16	14:57:20	16:27:20	17:10:16
(Az, ZA) (deg)	(104.04, 29.26)	(116.56, 15.37)	(0, 0)	(270, 20.83)	(255.96, 29.26)
Offset to pointing centre (deg)	1.6	4.6	1.8	3.7	1.5
Calibrator	PicA	PicA	HydA	HydA	HydA
Observation ID (GPS time)	1138624768	1138628472	1138632736	1138638136	1138640712
Start time (UTC)	12:39:12	13:40:56	14:52:00	16:22:00	17:04:56
(Az, ZA) (deg)	(180, 20.83)	(213.69, 25.31)	(56.31, 25.31)	(0, 13.72)	(333.44, 15.37)
Offset to pointing centre (deg)	1.8	2.9	4.6	3.3	0.8

Target pulsar	J1752–2806 (observed on 2016-06-10)				
Observation ID (GPS time)	1149605152	1149609232	1149612832	1149616432	1149620392
Start time (UTC)	14:45:36	15:53:36	16:53:36	17:53:36	18:59:36
(Az, ZA) (deg)	(90, 28.31)	(90, 13.72)	(0, 0)	(270, 13.72)	(270, 28.31)
Offset to pointing centre (deg)	4.8	2.5	1.7	2.3	5.0
Calibrator	HerA	HerA	HerA	HerA	HerA
Observation ID (GPS time)	1149604832	1149608912	1149612512	1149616112	1149620072
Start time (UTC)	14:40:16	15:48:16	16:48:16	17:48:16	18:54:16
(Az, ZA) (deg)	(26.57, 32.02)	(0, 28.31)	(333.44, 32.02)	(315, 42.12)	(296.56, 52.68)
Offset to pointing centre (deg)	4.0	3.4	2.9	1.8	2.8

4.3.3 Calibration

In order to coherently sum the signals from the MWA tiles, we need to calibrate the array to determine the direction-independent complex gains (amplitudes and phases) for each tile first. The Real Time System (RTS; [Mitchell et al., 2008](#)) was used for this calibration process. The RTS generated solutions for each tile at each frequency band from calibrator observation. This process utilised the MWA’s analytical beam model. A more detailed description of the calibration process can be found in Section 2.4 of Paper 1.

Each dipole antenna in the MWA array has a beam response, which effectively ‘point’ towards the zenith, and each tile (comprising 4×4 dipoles) has analogue beamformers that add delays to the signals to steer the ‘tile beam’ towards the target source. We can coherently sum the signals from all 128 tiles to form a tied-array beam. In this sense, all of our calibrations can be considered as ‘off-axis’.

For the verification described in this chapter, we used both the dedicated calibrator observations (as described in Section 4.3.2), as well as in-field calibration. For in-field (self) calibration, we processed the complex voltage data from the pulsar observations using an offline version of the MWA correlator ([Ord et al., 2015](#)) to generate visibilities in the same format as the dedicated calibrator observations.

4.3.4 Beamforming

A detailed description of the beamforming process is presented in Paper 1. Here, we briefly summarise the process. We used the calibration solutions to coherently combine the signals from all 128 tiles to form a tied-array (phased array) beam towards the target pulsar by applying phase rotations to correct for geometric delays between the tiles so that the entire array ‘points’ towards the target position. This procedure involves applying direction-independent phase and amplitude corrections from the calibration solutions to the signals received by each tile. Meanwhile, since the calibration solution is direction independent,

Table 4.2: Summary of the centre observing frequencies, f . The dispersion delay at each frequency for PSRs J0742–2822 and J1752–2806 are presented in milliseconds (Δt) and per cent of the pulse period (ΔP).

channel ID	f (MHz)	J0742–2822		J1752–2806	
		Δt (ms)	ΔP (%)	Δt (ms)	ΔP (%)
60	76.80	13.51	8.10	9.23	1.64
61	78.08	12.85	7.71	8.78	1.56
68	87.04	9.28	5.56	6.34	1.13
76	97.28	6.65	3.99	4.54	0.81
84	107.52	4.92	2.95	3.36	0.60
92	117.76	3.75	2.25	2.56	0.46
100	128.00	2.92	1.75	1.99	0.35
116	148.48	1.87	1.12	1.28	0.23
117	149.76	1.82	1.09	1.24	0.22
124	158.72	1.53	0.92	1.05	0.19
132	168.96	1.27	0.76	0.87	0.15
140	179.20	1.06	0.64	0.73	0.13
148	189.44	0.90	0.54	0.61	0.11
156	199.68	0.77	0.46	0.53	0.09
164	209.92	0.66	0.40	0.45	0.08
165	211.20	0.65	0.39	0.44	0.08
172	220.16	0.57	0.34	0.39	0.07
180	230.40	0.50	0.30	0.34	0.06
212	271.36	0.31	0.18	0.21	0.04
220	281.60	0.27	0.16	0.19	0.03
228	291.84	0.25	0.15	0.17	0.03
236	302.08	0.22	0.13	0.15	0.03
243	311.04	0.20	0.12	0.14	0.02
244	312.32	0.20	0.12	0.14	0.02

we rotate the calibration solution towards the target position according to the analytic tile beam model (the same as that used in the RTS calibration process), to retrieve the direction-dependent complex gain components before we apply it in the beamforming operation.

4.3.5 Data reduction and analysis

The beamforming pipeline writes out the data in the PSRFITS format (Hotan et al., 2004). These data were then incoherently de-dispersed and folded using DSPSR² (van Straten & Bailes, 2011) and the timing ephemeris from the pulsar catalogue¹ (Manchester et al., 2005a). For further analysis we mostly used the PSRCHIVE³ software (Hotan et al., 2004; van Straten et al., 2012). The optimal DM (maximising the signal-to-noise ratio in the total intensity pulse profile) was found using the PSRCHIVE `pdmp` routine. The total degree of linear polarisation is estimated as equivalent integrated on-pulse flux of the linearly polarised profile⁴. This is essentially the continuum equivalent quantities as it is estimated from the integrated on-pulse profile.

To obtain the polarimetric profiles for the pulsars and estimate the degree of linear polarisation, we need to correct for the effect of Faraday rotation. We determined the Faraday rotation measure (RM, in units of rad m^{-2}) towards the pulsars using the technique of RM Synthesis (Burn, 1966; Brentjens & de Bruyn, 2005). We used the pre-processing parts of the `rmfit` quadratic fitting function within the PSRCHIVE package (Noutsos et al., 2008) to extract the Stokes I, Q, U, V parameters (as a function of frequency) from the peak of the average total intensity pulse profile. The Stokes parameters were used as an input to the RM Synthesis code written in `python`⁵. We also used the associated RM-CLEAN⁴ method (Heald et al., 2009; Michilli et al., 2018b) to determine the fraction of

²<http://dspsr.sourceforge.net/>

³<http://psrchive.sourceforge.net/>

⁴The residual off-pulse baseline is estimated and subtracted in our analysis.

⁵<https://github.com/gheald/RMtoolkit>

instrumental polarisation leakage near 0 rad m^{-2} . We obtained the dirty and RM CLEAN-ed Faraday spectra (or Faraday dispersion functions) output for each pulsar observation. The RM was recorded as the location of the peak in the clean Faraday spectrum.

The ionosphere imparts additional Faraday rotation, RM_{ion} , to the total observed RM, RM_{obs} . The ionospheric contribution must be subtracted in order to obtain the RM due to the interstellar medium (ISM) alone, i.e., $\text{RM}_{\text{ISM}} = \text{RM}_{\text{obs}} - \text{RM}_{\text{ion}}$. The RM_{ion} is both time and direction dependent and, was estimated towards each target source line-of-sight (at the corresponding ionospheric pierce point) for the average time of each observation. To estimate RM_{ion} , we employed an updated version of `ionFR`⁶ (Sotomayor-Beltran et al., 2013) using input data from: the latest version of the International Geomagnetic Reference Field⁷ (IGRF-12; Thébault et al., 2015); and the International Global Navigation Satellite Systems Service (IGS) vertical total electron content (TEC) maps⁸ (e.g. Hernández-Pajares et al., 2009) for each observation date. Using the Long Wavelength Array, Malins et al. (2018) find that local high-cadence TEC measurements are superior to the global TEC models for ionospheric RM correction. However, the difference between the local measurements and the global models is not significant for our range of observing frequencies.

4.3.6 Archival VCS data

In addition to multiple short observations using non-contiguous frequency channels, we also make use of archival VCS data for PSR J1752–2805 for own comparison studies. Specifically, a 40-minute zenith-pointing observation from June 2015 (observation ID: 1117643248), over a contiguous 30.72 MHz bandwidth at a central frequency of 118.40 MHz. We used an observation of a calibrator source, 3C444, taken six hours later that night (observation ID: 1117643248, with az-

⁶<https://sourceforge.net/projects/ionfarrot/>

⁷<https://www.ngdc.noaa.gov/AGA/vmod/igrf.html>

⁸<ftp://cddis.gsfc.nasa.gov/pub/gps/products/ionex/>

imuth=288.43 deg, ZA=22.02 deg) to calibrate and beamform the data using the same procedure as described above.

4.4 Verification of the polarimetric response

Theoretically, the polarimetric response including leakage for the array can be estimated using the MWA beam models and the intrinsic cross-polarization ratio (IXR) (Carozzi & Woan, 2011). In practice, it is difficult to estimate this accurately due to the discrepancy between the actual beam response and our beam models. Although significant efforts have been made to improve our understanding of the MWA’s actual beam response (e.g. Sutinjo et al., 2015a; Sokolowski et al., 2017; Line et al., 2018), it is still an ongoing area of research. Any discrepancy between the actual beam performance and the assumed beam model will manifest as errors in the polarimetric response that are a function of pointing direction. As described in Paper 1, the current MWA tied-array data processing (calibration and beamforming) still uses a simple analytical beam model. Here, we estimate the polarisation leakage empirically by comparing the results from each target pulsar at different sky coordinates (Az , ZA) calibrated with solutions from multiple (Az , ZA). Through this comparison, we first determine the optimal calibration strategy (Section 3.1), and then estimate the reproducibility of the polarimetric profiles for the two target pulsars (Section 3.2). Given the large range of instrumental polarisation exhibited by a phased array as a function of pointing, any small errors in the calibration process will manifest as large errors in measured polarisation. We therefore use the reproducibility of the pulsar polarimetric profile over a wide range of instrumental polarisation as a proxy for calibratability.

4.4.1 Determining the optimal calibration strategy

In order to determine the optimal calibration strategy, different calibration solutions were used to beamform multiple pointings for both pulsars. For PSR J0742–2822, the in-field calibration and five dedicated calibrations are compared for each of the five short pulsar observations. However, for PSR J1752–2806, we were unable to benefit from in-field calibration because its line-of-sight is closer to that of the Galactic centre ($l = 1.54^\circ$, $b = -0.96^\circ$), where the bright, diffuse sky background makes it difficult for the calibration procedure to converge on satisfactory solutions. At frequencies above 270 MHz, where the MWA beam model is not well determined, in-field calibration may not necessarily converge to satisfactory solution for PSR J0742–2822, which is located away from the Galactic centre ($l = 243.77^\circ$, $b = -2.44^\circ$).

The visualisations shown in Figures 4.2 and 4.3 provide comparisons of the signal-to-noise ratio in total intensity (Figure 4.2) and the instrumental polarisation leakage (Figure 4.3) for each pulsar. We present all combinations of the pulsar pointings (P1 to P5) and calibration observations (C1 to C5, and in-field calibration for PSR J0742–2822) for one example observing frequency. More details regarding the Faraday spectra can be found in sections 4.3.5 and 4.5. For PSR J0742–2822, we found that the in-field calibration is most effective, yielding higher signal-to-noise ratios in total intensity (Figure 4.2a) and slightly lower instrumental polarisation fractions (Figure 4.3a). This is consistent with the conclusion from the MWA image processing (Trott et al., 2016; Hurley-Walker et al., 2017). For PSR J1752–2806, the calibrator observations (C1 to C4) all have satisfactory total intensity signal-to-noise ratios, except for the fifth calibrator observation (C5) that is located at a zenith angle of $>50^\circ$. The fourth calibrator observation shows somewhat less instrumental leakage (Figure 4.3b), and this may be due to the symmetrical projection for both X and Y dipoles at the pointing location.

In summary, the in-field calibration performs well when both the sky model

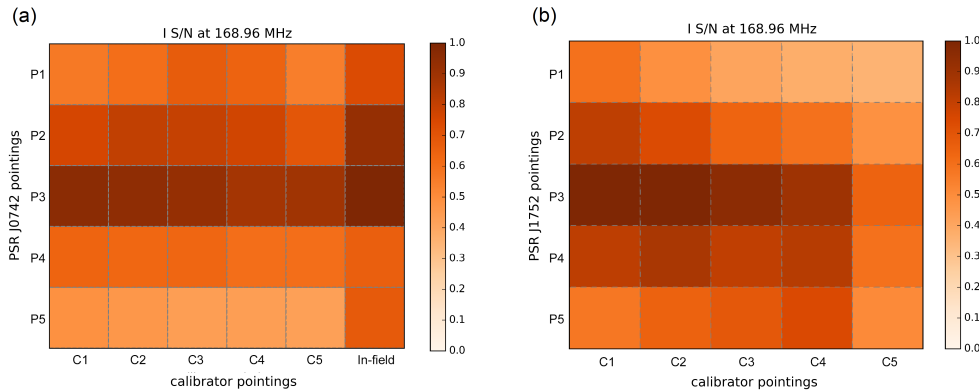


Figure 4.2: Signal-to-noise ratios of the total intensity pulse profiles at 168.96 MHz with a bandwidth of 1.28 MHz, for each of the five pulsar pointings calibrated using each of the five dedicated calibrator observations. All values are normalised to the maximum signal-to-noise ratio among the 25 combinations. (a) PSR J0742–2822 observations, (b) PSR J1752–2806 observations. Note that in-field calibration was not performed for PSR J1752–2806 (see Section 3.1 for details).

and the MWA beam model are sufficiently well determined. Towards lines-of-sight where this is not necessarily true, the dedicated calibrator observation is sufficient. We note that these are preliminary results based on two case studies, and a more detailed analysis involving a larger sample of pulsars would be useful to develop a higher degree of confidence. However, such an exercise is beyond the scope of this chapter.

4.4.2 Reproducibility of pulse profiles

Here, we describe our analysis of the MWA tied-array data at different directions (Az , ZA), which shows that the polarimetric response is satisfactorily reliable for science, such as that demonstrated in the subsequent sections. The total intensities of the pulse profiles are found to be relatively stable, with a $\sim 10\%$ variation in signal-to-noise, especially for calibrator observations where the source was less

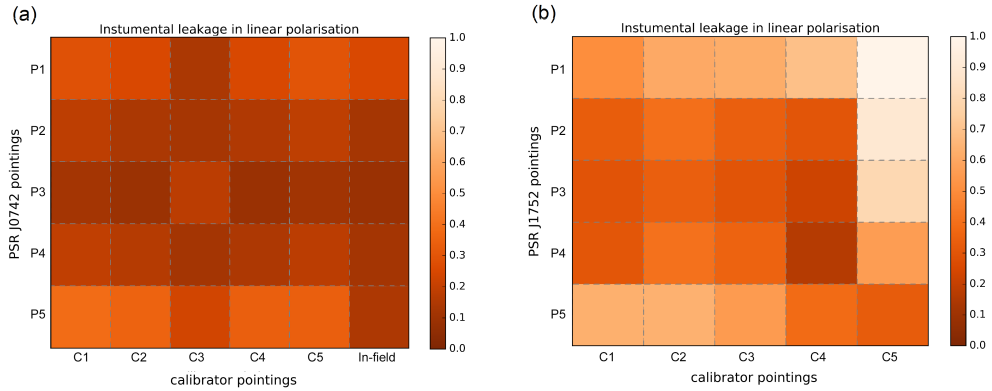


Figure 4.3: Fraction of instrumental polarisation leakage calculated using the RM CLEAN-ed Faraday spectra, for each of the five pulsar pointings calibrated using each of the five dedicated calibrator observations. (a) PSR J0742–2822 observations, (b) PSR J1752–2806 observations.

than 45° from the zenith, e.g., Figures 4.2 and 4.3. The zenith pointing provides the pulse profile with the highest signal-to-noise ratio. This is consistent with our expectation because the MWA has maximum gain and the beam model is more accurately determined for pointings toward the zenith (except at frequencies higher than 270 MHz, see Section 4.7.2). The degree of linear polarisation (over the five different pointing positions and for each observing frequency between 150–270 MHz) varies by $8\pm 5\%$ for PSR J0742–2822 and $4\pm 2\%$ for PSR J1752–2806. Some of this discrepancy can be attributed to intrinsic pulse-to-pulse variations that contribute to the average pulse profile. The number of pulses within the short 5-minute observations is ~ 1800 for PSR J0742–2822 and ~ 500 for PSR J1752–2806. More than approximately 1000 pulses are typically required to construct average pulse profiles that are stable, depending on the pulse phase-jitter properties of the pulsar (e.g. Liu et al., 2012). Nevertheless, the profiles are also qualitatively similar, with the difference between the profiles attributable to the signal-to-noise ratios.

4.5 Faraday rotation measures

We calculated the RM towards PSR J0742–2822 for all five observations separately (using the RM-CLEAN routine) to investigate the change in the apparent RM at different observing epochs and pointing directions. We also calculated the ionospheric Faraday rotation contribution for each observation. The results are summarised in Table 4.3. Before subtracting the ionospheric RM, the observed RM for PSR J0742–2822 ranged from 149.065 to 149.512 rad m^{-2} with a formal error of $\sim 0.05 \text{ rad m}^{-2}$. After subtracting the ionospheric RM, the average RM_{ISM} for PSR J0742–2822 was estimated to be $150.915 \pm 0.097 \text{ rad m}^{-2}$. Thus, at these low frequencies, it is essential to correct for the ionospheric Faraday rotation, but the measurement uncertainty is dominated by the method currently used. Similarly, we determined the RM towards PSR J1752–2806 for all five five-minute observations and also for the 40-minute observation centred at 118.40 MHz. Before subtracting the ionospheric RM, the observed RM ranged from 95.001 to 95.068 rad m^{-2} . The measurement uncertainties for the five short observations are around 0.015 rad m^{-2} , while for the observation centred at 118.40 MHz, the measurement uncertainty is only 0.01 rad m^{-2} . The results are also summarised in Table 4.3.

Figure 4.4 shows the RM CLEAN-ed Faraday spectra for PSR J1752–2806 from all five short observations and the 118.40 MHz observation. The height of the peak at 0 rad m^{-2} , relative to the higher peak at the RM associated with the pulsar signal, indicates the fraction of instrumental polarisation leakage. We also show an example of an RM CLEAN-ed Faraday spectrum for the third short observation of PSR J0742–2822 in Figure 4.5.

We note that the RM measurement uncertainty is proportional to the full width at half maximum (FWHM) of the rotation measure spread function (RMSF; analogous to a PSF in optical telescopes) and inversely proportional to the signal-to-noise ratio in the Faraday spectrum. The use of low-frequencies and wide bandwidths reduces the FWHM of the RMSF, thus reducing the uncertainty on

the RM measurement. At our lowest observing frequencies the pulsar profiles have lower signal-to-noise ratios, while at higher frequencies (particularly above 200 MHz), the instrumental polarisation leakage becomes greater (see Section 4.7.2). Including more of these higher-frequency channels increases the systematic error because the peaks associated with the pulsar signal and the instrumental polarisation in the Faraday spectrum calculated using each coarse frequency channel overlap due to the wider FWHM of the RMSF and increasing instrumental polarisation leakage. To achieve a balance between attaining smaller RM uncertainties by maximising the frequency range used, while reducing systematic errors from including high-frequency channels and noisier low-frequency channels, we adopted the frequency range 148.48–211.20 MHz to calculate the RM for PSR J0742–2822 and 117.76–189.44 MHz for PSR J1752–2806 (see Figures 4.6 and 4.8). For each pulsar, we calculated the Faraday spectrum for each coarse frequency channel individually to assist in deciding these optimum frequency ranges. We note that the RM measurements obtained for each channel (listed in Table 4.2) were all consistent within the formal errors.

Using RM synthesis and the MWA’s large frequency lever arm, we are able to achieve higher precision on the RMs compared to previous studies at higher frequencies published in the literature. For example, the RM measured towards PSR J1752–2806 using the MWA data is more than twice as precise and in excellent agreement ($0.5\text{-}\sigma$) with the value reported in the pulsar catalogue from [Hamilton & Lyne \(1987\)](#). As is evident from Table 3, the largest contribution to the RM uncertainty is the accuracy with which the ionospheric RM can be determined and corrected. Therefore, ongoing efforts to increase the accuracy of the ionospheric RM estimation are essential to fully realise the potential of high precision of RM measurements from low-frequency instruments (e.g. [Malins et al., 2018](#)).

Table 4.3: RM results for PSRs J0742–2822 and J1752–2806.

Target pulsar	J0742–2822 (Literature RM=149.95±0.05 [†] from Johnston et al. 2005)					
Observation ID (GPS time)	1138625088	1138628792	1138633056	1138638456	1138641032	
Observed RM (rad m ⁻²)	149.065±0.055	149.215±0.042	149.233±0.034	149.512±0.045	149.443±0.058	
Ionosphere RM (rad m ⁻²)	-1.975±0.144	-1.672±0.132	-1.466±0.055	-1.509±0.042	-1.485±0.034	
RM _{ISM} = RM _{obs} - RM _{ion}	151.040±0.154	150.887±0.139	150.699±0.065	151.021±0.062	150.928±0.067	
Average RM _{ISM} (rad m ⁻²)	150.915±0.097					

Target pulsar	J1752–2806 (Literature RM=96.0±0.2 from Hamilton & Lyne 1987)					
Observation ID (GPS time)	1149605152	1149609232	1149612832	1149616432	1149620392	1117643248
Observed RM (rad m ⁻²)	95.068±0.017	95.063±0.013	95.031±0.012	95.037±0.012	95.026±0.012	95.001±0.001
Ionosphere RM (rad m ⁻²)	-0.886±0.082	-0.828±0.072	-0.789±0.038	-0.877±0.080	-0.815±0.083	-0.807±0.104
RM _{ISM} = RM _{obs} - RM _{ion}	95.954±0.084	95.891±0.073	95.820±0.040	95.914±0.081	95.841±0.084	95.808±0.104
Average RM _{ISM} (rad m ⁻²)	95.871±0.078					

[†] This value is the observed RM, with no correction for the ionospheric RM value.

4.6 Polarimetric profiles

4.6.1 PSR J0742–2822

We obtained polarimetric profiles for our target pulsars for a number of frequencies within the MWA’s operational frequency range. For PSR J0742–2822, the pulse profiles at the majority of the observing frequencies show significant exponential scattering tails, see Figure 4.6. The reduced telescope sensitivity and the increasing effects of scattering makes it difficult to detect the pulsar at frequencies below 128 MHz. A detailed analysis of scattering properties of this pulsar can be found in [Kirsten et al. \(2019\)](#). Despite the notable scattering, the pulse profile is highly linearly polarised at all frequencies, although the linear polarisation degree decreases towards lower frequencies. This may suggest that the scattering in the ISM gives rise to depolarisation of the pulsar emission; see Section 4.7.1 for further discussion.

Figure 4.7 shows the polarimetric profile of PSR J0742–2822 generated using the combined data from all five short observations over the frequency range 148 MHz to 212 MHz (i.e. 9×1.28 MHz coarse channels). The PA curve shows a $\sim 50^\circ$ swing and flattens towards later pulse phases in the scattering tail.

PSR J0742–2822 was also blindly detected in an all-sky survey of circular polarisation at 200 MHz with the MWA by [Lenc et al. \(2018\)](#). Their measured degree of circular polarisation, $\approx -10\%$, is comparable with our estimation, $-7 \pm 18\%$. This result is also consistent with the $\approx -7\%$ circular polarisation from the Lovell telescope observation at 230 MHz ([Gould & Lyne, 1998](#)).

4.6.2 PSR J1752–2806

Figure 4.8 shows the pulse profiles for PSR J1752–2806 from 97 MHz to 312 MHz. The polarimetric profiles of PSR J1752–2806 show little evolution between 148 MHz and 220 MHz, even though measurably longer scattering tails are seen towards the lower frequencies. The signal-to-noise ratio is comparatively lower at fre-

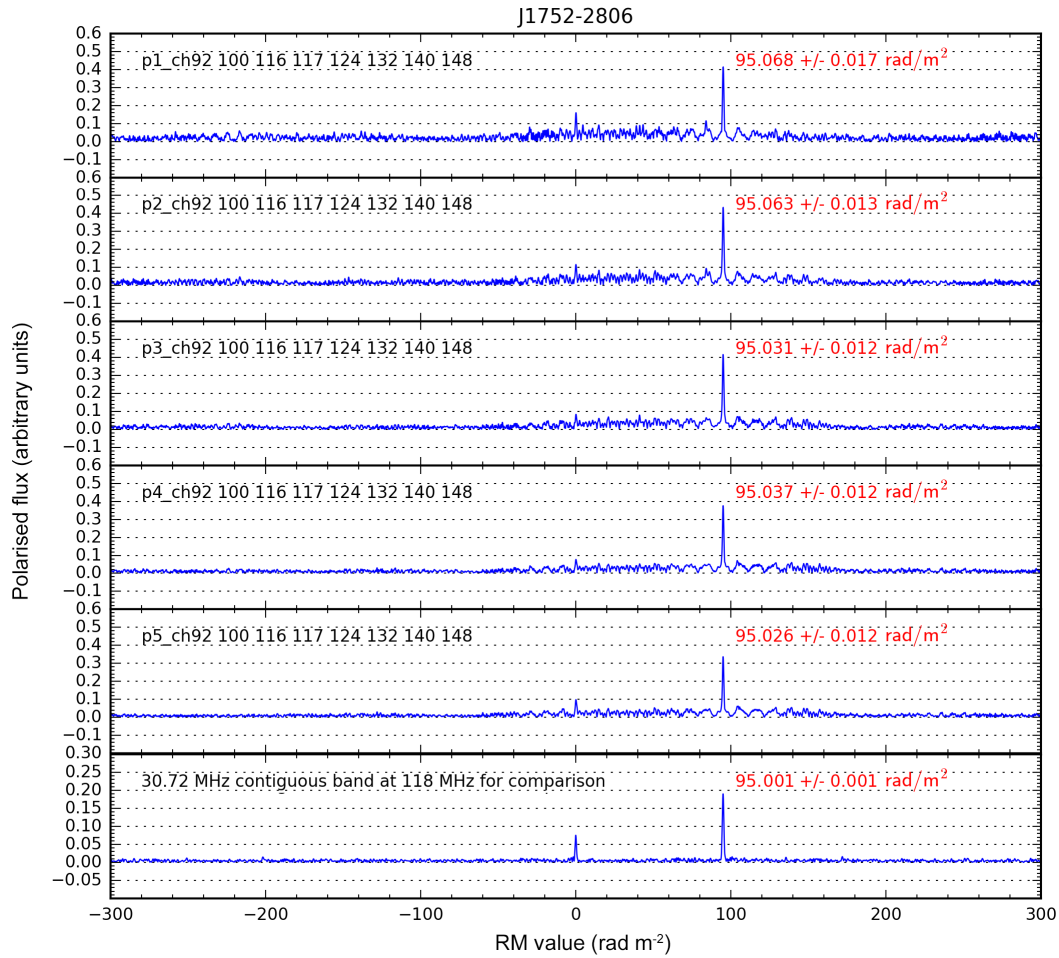


Figure 4.4: RM CLEAN-ed Faraday spectra for PSR J1752–2806. The labels in red show the observed RM prior to the subtraction of the ionospheric RM, and the uncertainty quoted is the formal error. The upper five panels show the Faraday spectra obtained from multiple short observations with observing frequencies 117.76–189.44 MHz. The bottom panel is the result from the observation centred at 118.40 MHz.

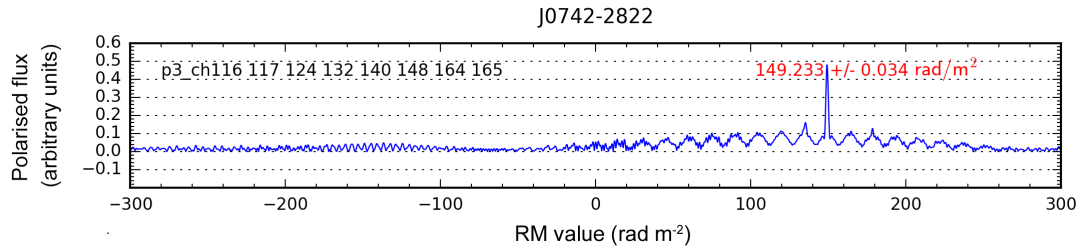


Figure 4.5: RM CLEAN-ed Faraday spectrum for PSR J0742–2822 using the third short observation (P3) with observing frequencies 148.48–211.20 MHz. The label in red is the observed RM prior to the subtraction of the ionospheric RM, and the uncertainty quoted is the formal error.

frequencies below 118 MHz. The profiles at 230 MHz and 312 MHz show reduced linear polarisation while those at 271 MHz and 302 MHz become dominated by instrumental leakage. This may be due to the increased instrumental leakage at frequencies above ≈ 270 MHz (cf. [Sutinjo et al., 2015a](#)), see Section 4.7.2 for further discussion.

Figure 4.9 shows the polarimetric profiles for PSR J1752–2806 using the MWA data centred at 180 MHz and 118 MHz. There appears to be a jump in the PA curve near the leading edge of the pulse profile, at both centre frequencies. This jump is $\sim 68 \pm 8$ deg at 180 MHz and $\sim 59 \pm 5$ deg at 118 MHz. This jump also tentatively appears to coincide with a faint linear polarisation component at the leading edge of the pulse profile which is rather difficult to discern, given the time resolution of our data (see Table 2). Additional observations high quality low-frequency observations will be useful to further investigate this.

A closer examination of the polarimetric profiles at multiple MWA frequencies (Figure 4.8) reveals that the scattering effect is negligible for this pulsar above ~ 150 MHz. However, as can be seen from Figure 4.9 (right panel), the pulse broadening arising from scattering is visibly strong at 118 MHz. Using the deconvolution method (as described in [Bhat et al., 2003](#)), we estimate the scatter broadening time to be 7.7 ± 0.7 ms at 118 MHz (assuming a one-side exponential

PSR J0742-2822

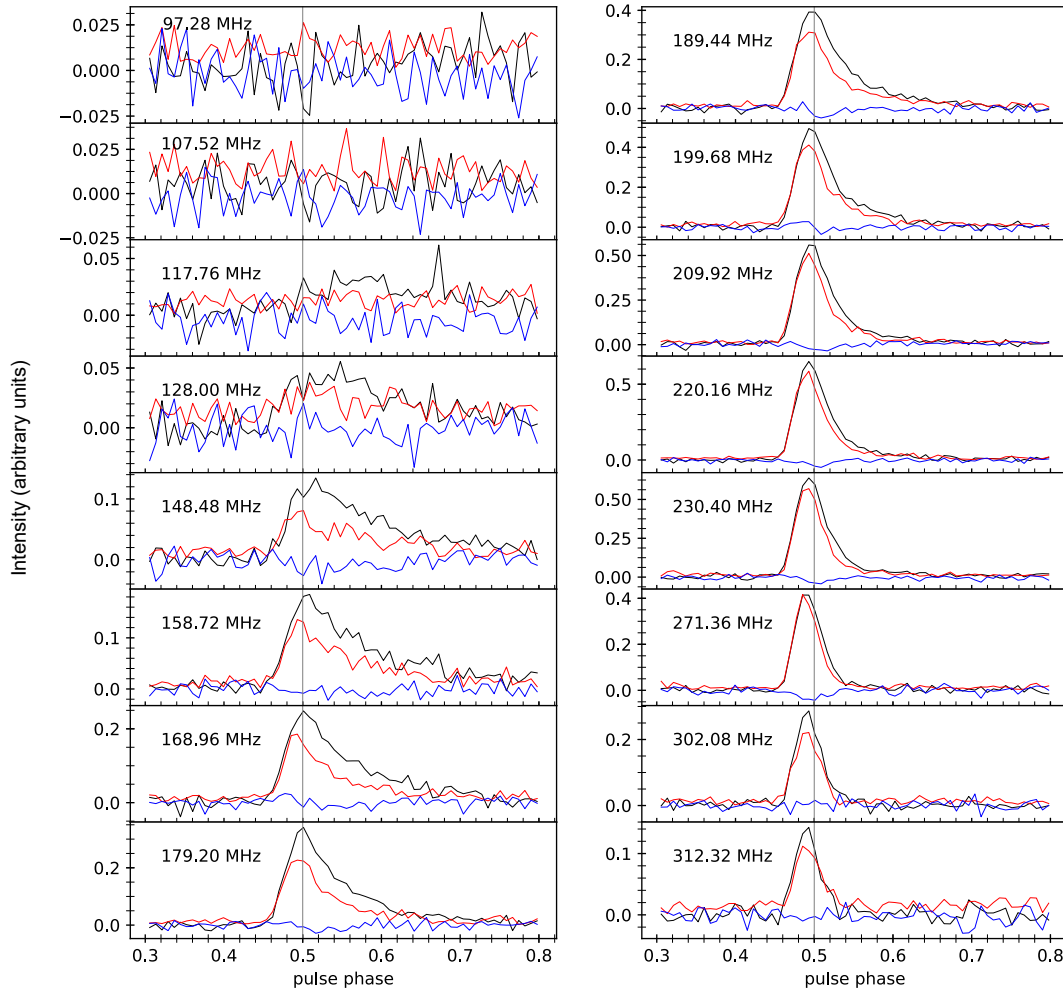


Figure 4.6: Polarimetric profiles for PSR J0742–2822 at frequencies from 97 MHz to 313 MHz, each with a bandwidth of 1.28 MHz. Black lines indicate total intensity (Stokes I), red lines indicate linear polarisation (Stokes $\sqrt{Q^2 + U^2}$), and blue lines indicate circular polarisation (Stokes V). The data used here are the combination of all five short observations of PSR J0742–2822 and calibrated using the fifth calibration observation (C5). Note that the polarisation profiles above 270 MHz are increasingly affected by the instrumental polarisation leakage.

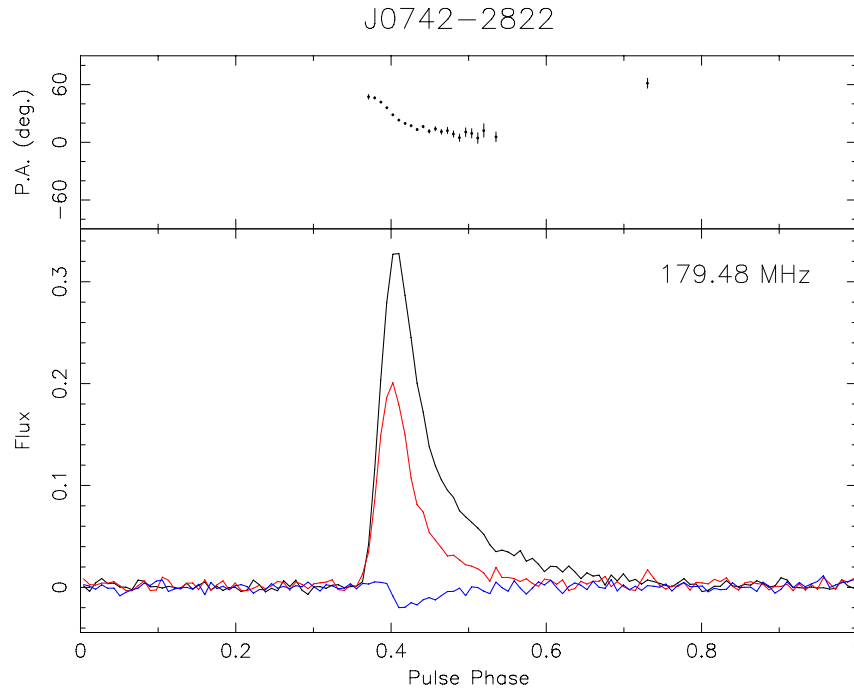


Figure 4.7: Polarimetric profile (lower panel) and PA curve (upper panel) for PSR J0742–2822. The black, red, and blue lines indicate the total intensity, linear polarisation, and circular polarisation, respectively. Here, we use the addition of nine 1.28 MHz channels between 148 MHz and 211 MHz. The profile is generated using the data from all five observations, and calibrated using the fifth calibrator observation. The flux density is shown in arbitrary units.

PSR J1752-2806

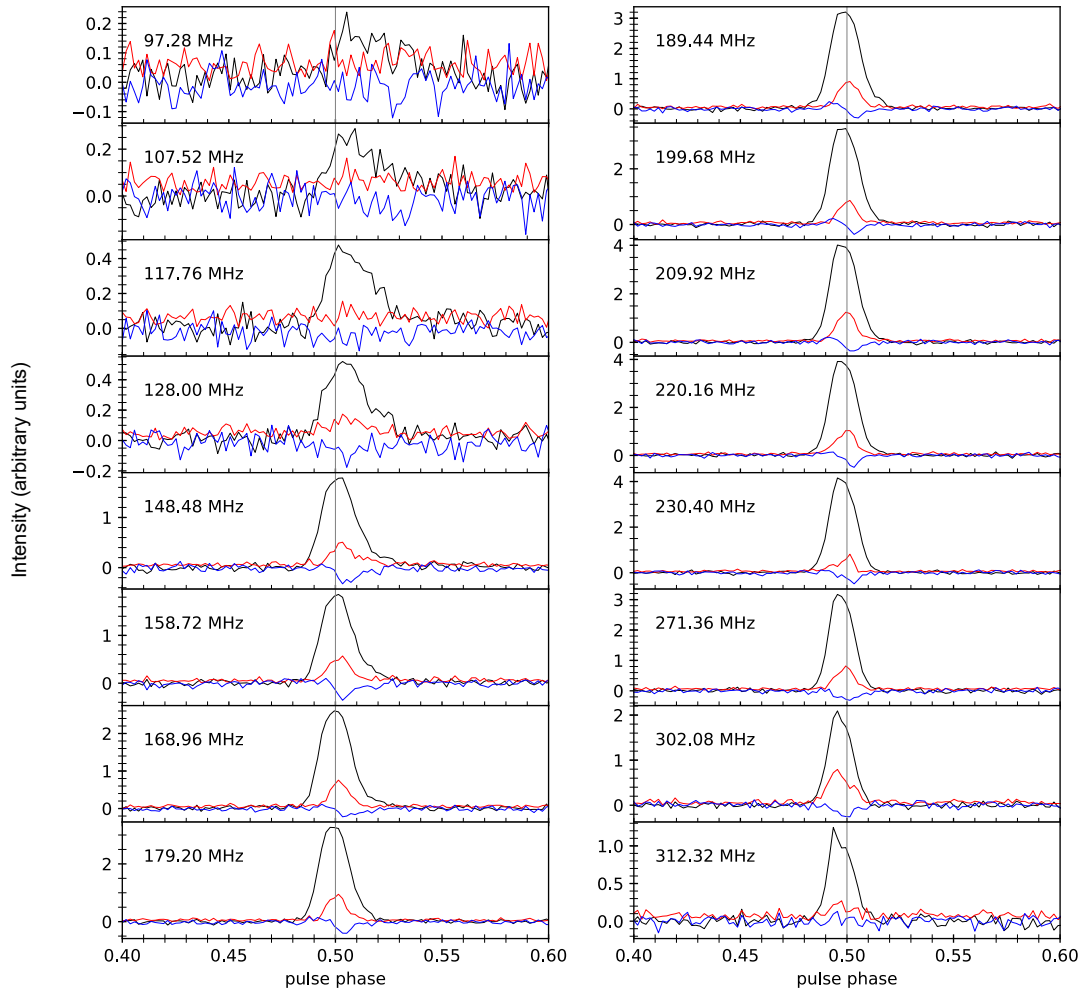


Figure 4.8: Polarimetric profiles for PSR J1752–2806 at frequencies from 97 MHz to 313 MHz, each with a bandwidth of 1.28 MHz. Black lines indicate total intensity (Stokes I), red lines indicate linear polarisation (Stokes $\sqrt{Q^2 + U^2}$), and blue lines indicate circular polarisation (Stokes V). The data used here is the combination of all five short observations of PSR J1752–2806 and calibrated using the fourth calibration observation (C4). Note that the polarisation profiles above 270 MHz are increasingly affected by the instrumental polarisation leakage.

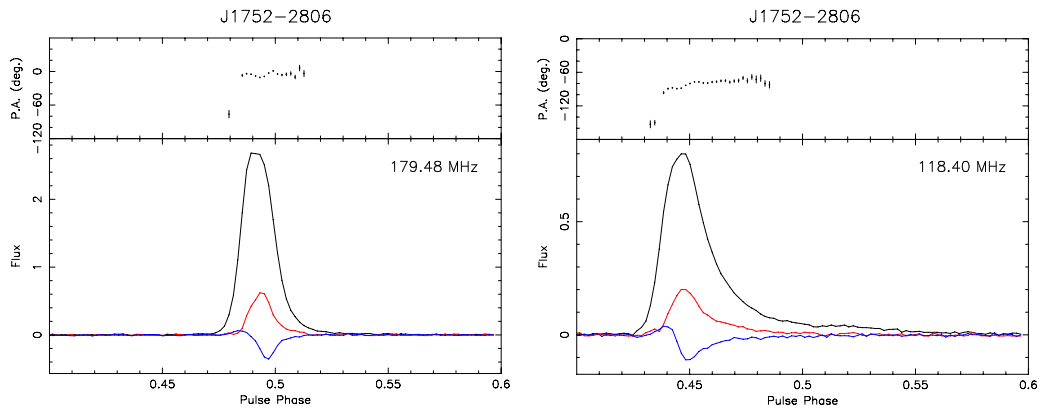


Figure 4.9: Polarimetric pulse profiles (lower panel) and PA curves (upper panel) for PSR J1752–2806. The black, red, and blue lines indicate the total intensity, linear polarisation, and circular polarisation, respectively. The flux densities are in arbitrary units. Left: the average profile for all five short observations for PSR J1752–2806, calibrated using the fourth calibrator observation (C4). Here, we use the addition of nine 1.28 MHz channels between 148 MHz and 211 MHz. Right: the average profile from the MWA data centred at 118 MHz with 30.72 MHz contiguous bandwidth.

for the pulse broadening function).

4.6.3 Comparison with the literature

Figure 4.10 shows the comparison between the polarimetric pulse profiles we obtained using the MWA and those available in the published literature. The MWA provides the lowest frequency pulse profiles. The profiles published in the literature provide additional data at frequencies up to 8400 MHz for PSR J0742–2822 and up to 3100 MHz for PSR J1752–2806.

For PSR J0742–2822, we obtained polarimetric profiles taken with the GMRT at 243 MHz and 325 MHz (Johnston et al., 2008) and Parkes profiles at 732 MHz, 1.4 GHz, 3.1 GHz, 6.2 GHz, and 8.4 GHz (Karastergiou & Johnston, 2006; Johnston et al., 2006). All of these are published in the literature, except for the 243, 325, 732, and 6200 MHz data⁹. Pulse broadening (scattering) arising from multi-path propagation in the ISM can be clearly seen in the MWA and GMRT profiles. The emission is also highly linearly polarised, with a notable decrease towards lower frequencies; see Section 4.7.1 for further discussion.

For PSR J1752–2806, the literature archival data include those from the Lovell telescope (408 MHz and 925 MHz; Gould & Lyne, 1998) and Parkes (691 MHz, 1.4 GHz, 3.1 GHz; Karastergiou & Johnston, 2006; Johnston et al., 2007). The linear polarisation fraction is smaller (<20%), compared to PSR J0742–2822, showing some profile evolution with increasing degrees of polarisation towards lower frequencies. In addition, the circular polarisation fraction is often comparable to that for the linear polarisation, and also shows some evolution with frequency.

⁹www.atnf.csiro.au/people/Simon.Johnston/ppdata/

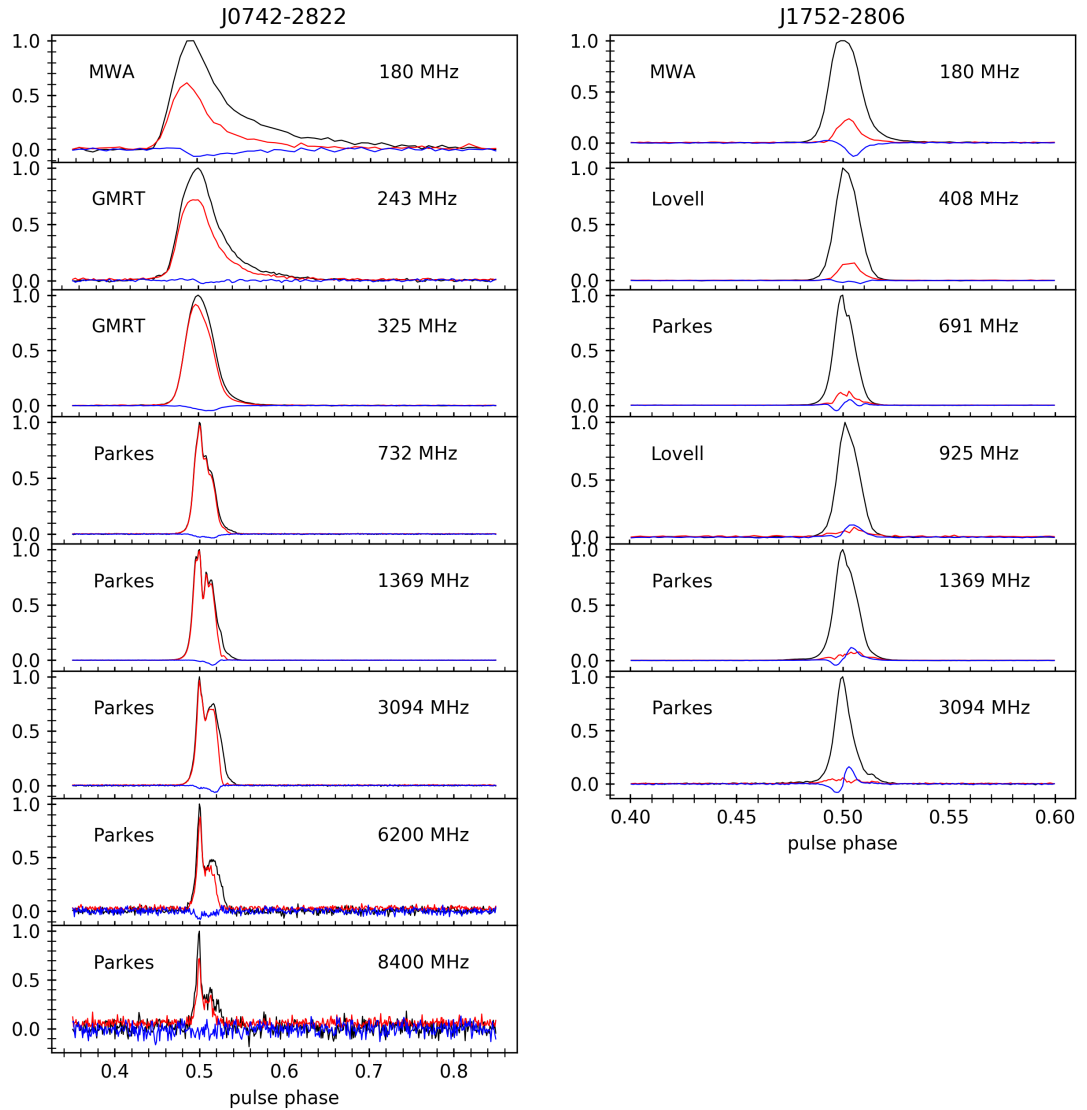


Figure 4.10: Polarimetric profiles for PSR J0742–2822 (left) and J1752–2806 (right) from the MWA and the literature (Gould & Lyne, 1998; Karastergiou & Johnston, 2006; Johnston et al., 2006, 2007, 2008). Black lines indicate the total intensity (Stokes I), red lines indicate linear polarisation (Stokes $\sqrt{Q^2 + U^2}$), and blue lines indicate circular polarisation (Stokes V). The flux density of each of the profiles is normalised (arbitrary units). The labels indicate the telescopes used to observe the pulsars and the centre observing frequencies.

4.7 Discussion

4.7.1 Frequency-dependent degree of linear polarisation

Figure 4.11 shows the measured degree of linear polarisation as a function of the observing frequency for PSR J0742–2822 (left) and PSR J1752–2806 (right). The degree of linear polarisation uncertainty was calculated using the uncertainties in the Stokes I, Q and U parameters and propagating these. For PSR J1752–2806, the observed degree of linear polarisation increases towards lower frequencies, which is in line with the generally expected trend for pulsar emission. However, for PSR J0742–2822, the measured degree of linear polarisation peaks near 732 MHz, whereas it decreases gradually at frequencies $\gtrsim 2$ GHz, and quite rapidly at frequencies < 300 MHz. This is in contradiction to the generally observed trend for many pulsars, where the degree of polarisation increases towards lower frequencies (e.g. Manchester, 1971; Xilouris et al., 1996). We note, therefore, that the frequency-averaged polarisation profile in Figure 4.7 is purely for illustrative purpose, and that for any scientific interpretation, the profile evolution should be taken into account. For the frequency resolution that we have employed (10 kHz), bandwidth depolarisation is expected only for $|RM| \gtrsim 400$ rad m⁻². Moreover, as can be seen in Figure 4.6, PSR J0742–2822 is also significantly scattered by the ISM. Therefore, it is possible that the depolarisation at low frequencies may be caused by interstellar scattering.

There have been several studies in the literature discussing the impact of multi-path propagation in the ISM on the measured polarisation of pulsars (Komesaroff et al., 1972; Li & Han, 2003; Karastergiou, 2009; Noutsos et al., 2009, 2015), which we will briefly review here. In early polarimetric studies of the Vela pulsar (PSR J0835–4510) from 300 MHz to 1.4 GHz, Komesaroff et al. (1972) measured a decrease in the degree of linear polarisation (at the pulse peak) and a smoother PA curve at their lower frequencies. While the smoother PA curve was interpreted as being due to scattering, the reduced degree in linear polari-

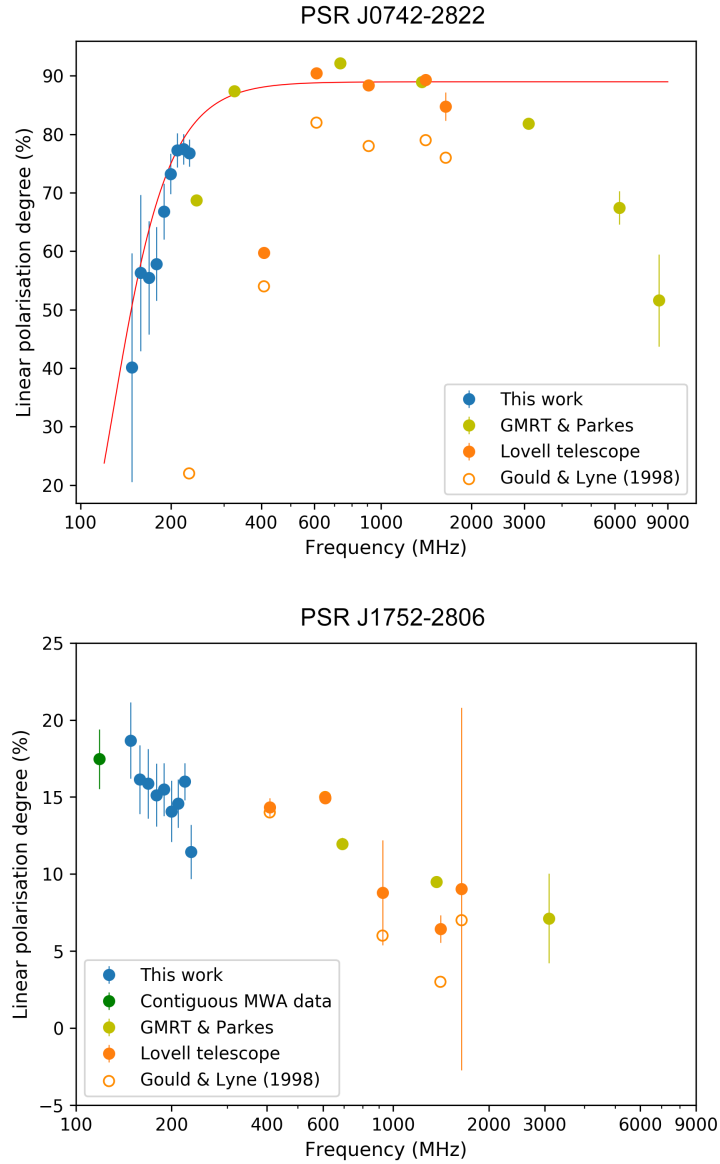


Figure 4.11: Degree of linear polarisation as function of frequency for PSR J0742–2822 (top) and PSR J1752–2806 (bottom). Blue points indicate the degree of linear polarisation using the MWA data between 148 and 230 MHz. Lime-green dots are from GMRT and Parkes data. Unfilled orange dots show the values published in Gould & Lyne (1998) and filled orange dots are calculated using the profiles in Gould & Lyne (1998). For PSR J1752–2806, the dark-green dot shows the linear polarisation observed with the MWA 118 MHz. For PSR J0742–2822, the red line shows the depolarisation factor $\exp(-2\lambda^4\delta\text{RM}^2)$ fit where $\delta\text{RM}=0.13 \text{ rad m}^2$ (see Section 4.7.1). The error bars show the uncertainties that were calculated as described in Section 4.7.1.

sation remained unexplained. Later, the work of [Li & Han \(2003\)](#) investigated the impact of scattering on the PA curves, and suggested that the scattering can potentially flatten the PA curves. [Karastergiou \(2009\)](#) further investigated this effect by comparing the observed profiles for pulsars whose PA curves adhere to the RVM with simulated scattered profiles. Their work suggested that very modest amounts of scattering, together with orthogonal jumps, can lead to significant distortion in the PA curve. [Noutsos et al. \(2009\)](#) investigated phase-resolved RM variations for a sample of pulsars using 1.4 GHz Parkes data and suggested such variations can arise from interstellar scattering. This was further reinforced by [Noutsos et al. \(2015\)](#) using LOFAR data, who also found that three of their pulsars (two of which exhibit significant scattering) show a decrease in the degree of linear polarisation at low frequencies (<200 MHz).

For our MWA observations, the effective time resolution is mainly determined by the scattering time scale τ_s . For example, at a frequency of 180 MHz, τ_s is $\sim 6 \pm 3$ ms ([Kirsten et al., 2019](#)), which corresponds to 5 pulse phase bins given our sampling time resolution (see Table 2). This can potentially cause substantial smearing in polarisation profiles, leading to depolarisation. In such a scenario, a significant flattening of the PA curve is expected at lower frequencies, which is only seen in the trailing edge (i.e. in the scattering tail) of the pulse profile of PSR J0742–2822 (which appears to be the case in the polarisation profile shown in Figure 4.7). At earlier pulse phases, the PA curve shows structure in both the MWA and GMRT low-frequency data (<350 MHz).

We considered the possibility that this depolarisation could be caused by short-term variability in the ionospheric RM. However, if that is the case, the depolarisation factor should relate to the total observation time that we used to generate the polarimetric profiles. To this end, we examined the depolarisation for both short (a few minutes) and long time scales (a few hours), given the constraints of our observations. Specifically, we compared the depolarisation between a) the addition of all five 5-minute short observations and each individual

5-minute observation; b) the first and second halves of each 5-minute observation. We found the depolarisation trends are consistent within the uncertainties. This indicates that the observed depolarisation is unlikely to be caused by the ionosphere. This is further reinforced by the fact that we see no significant depolarisation for PSR J1752–2806, and the ionosphere seems to show consistent behaviour between each pulsar’s observing epochs.

Depolarisation can also arise due to propagation through turbulent plasma components that are irregularly magnetised (e.g. [Burn, 1966](#); [Sokoloff et al., 1998](#)). In this case, stochastic Faraday rotation will depolarise the pulsar emission by a factor of $\exp(-2\lambda^4\delta\text{RM}^2)$ (e.g. [Macquart & Melrose, 2000](#)), where λ is the observing wavelength and δRM is the fluctuation in the RM. By fitting the observed degree of linear polarisation as a function of frequency, we estimate the required RM fluctuation $\delta\text{RM} = 0.13 \pm 0.02 \text{ rad m}^{-2}$ (Figure 4.11). As previously mentioned, for PSR J0742–2822, $\tau_s \sim 6 \pm 3 \text{ ms}$ at 180 MHz ([Kirsten et al., 2019](#)). [Johnston et al. \(1998\)](#) suggest that the scattering screen lies at a distance of $\sim 450 \text{ pc}$, associated with the Gum Nebula. In this case, the estimated size of the scattering disk is $\sim 33 \text{ AU}$. Given that there is typically a greater amount of turbulent structures seen in the general direction of the Gum Nebula, it is possible that the observed RM fluctuation is caused by small-scale, random magneto-ionic components (associated with turbulence) within the scattering screen. Further investigations are required to examine this in more detail, and will be explored in a future publication.

4.7.2 Limitations of data reduction and future work

For the work presented here, we have used the MWA’s analytical beam model to calibrate and beamform the data. The analytical beam model is indeed a reasonably good approximation to the MWA’s tile beam, if we consider total intensity alone. For polarisation, the analytical beam model is acceptable (in terms of performance and stability) for observations at zenith angles $\lesssim 45^\circ$ and

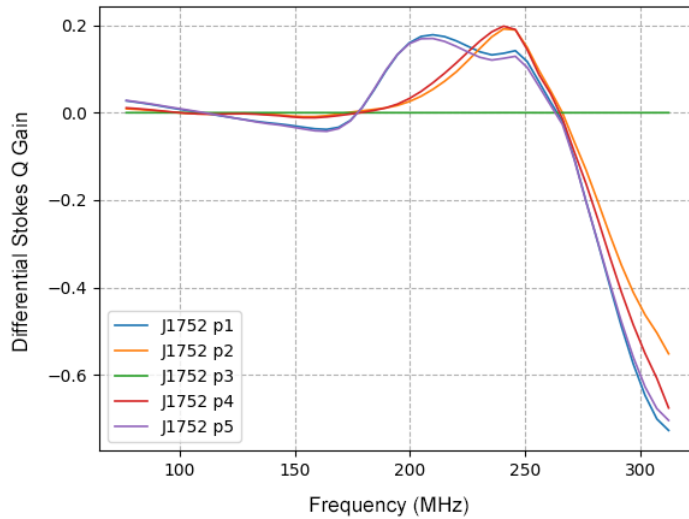


Figure 4.12: An example of the deviation in normalised Stokes Q gain value between the analytical and FEE beam models, as a function of observing frequency, for the directions of the five pointings towards PSR J1752–2806. The legend refers to the pointing positions as presented in Figure 4.1, where ‘p3’ represents the pointing towards zenith.

at frequencies $\lesssim 270$ MHz. Further developments have been made to the MWA tile beam model, including the recent fully-embedded element (FEE) primary beam model (Sokolowski et al., 2017). This is a significant improvement to the analytical model, and provides a more accurate prediction of the polarimetric response at large zenith angles. Therefore, using the FEE model in the calibration and beamforming will likely impart less instrumental polarimetric leakage to the data. This is illustrated in Figure 4.12, which shows the difference between the analytical and FEE beam models for the Stokes Q parameter, for example. The increasing deviation above 270 MHz indicates that the analytical beam model should be used with caution in this range.

In future, we plan to extend this work through improved polarimetric calibration by integrating the FEE beam model into our calibration and beamforming pipeline. This is an important exercise, however, beyond the scope of the present

work, given the much larger computational requirements of the FEE beam model. We also plan to compare the MWA beamformed data with the imaging products (e.g. [Lenc et al., 2017](#)), to provide further insights into the calibration and consistency between the observing modes, and to investigate any further corrections that could be applied to improve the polarimetric response.

Building on the work in this chapter, we further explore the behaviour of the degree of linear polarisation with frequency and pulse phase for more pulsars towards the Gum Nebula region in Chapter 5.

Chapter 5

Probing the ISM towards the Gum Nebula using Pulsar Measurements

5.1 The Gum Nebula and its neighbourhood

The Gum Nebula, discovered by [Gum \(1952\)](#), is a very large region of ionised gas. It is an extensive, conspicuous structure in the $H\alpha$ map in the southern sky, roughly centred at Galactic coordinates $(l, b) = (258^\circ, -6.6^\circ)$ with an angular radius of around 22.7° ([Purcell et al., 2015](#)). Figure 5.1 shows the $H\alpha$ image of the Gum Nebula from [Finkbeiner \(2003\)](#), constructed using the data from Virginia Tech Spectral line Survey (VTSS; [Dennison et al., 1998](#)), Wisconsin H-Alpha Mapper (WHAM; [Reynolds et al., 1998](#)), and the Southern H-Alpha Sky Survey Atlas (SHASSA; [Gaustad et al., 2001](#)). The Gum Nebula lies relatively close to the Sun, ~ 450 pc ([Purcell et al., 2015](#); [Yao et al., 2017](#)), and is an important structure in the local ISM environment. The ISM along the line-of-sight to the Gum Nebula is known to be complex, consisting of multiple overlapping structures, including several H II regions, supernova remnants (SNRs), molecular clouds, and an OB star association.

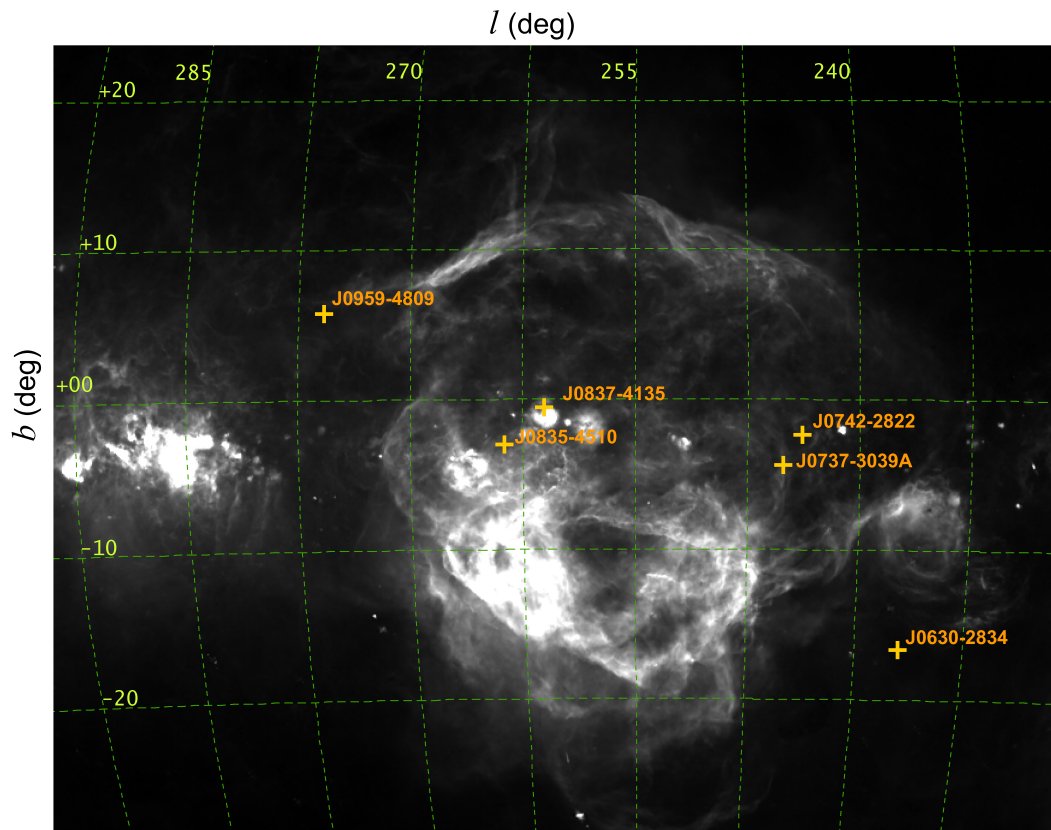


Figure 5.1: An H α image of the Gum Nebula (Finkbeiner, 2003) in Galactic coordinates. In this image, which spans $\sim 65^\circ \times 50^\circ$, the Gum Nebula is seen as a prominent feature with an angular diameter of $\sim 18^\circ$ (i.e. ~ 140 pc, assuming a distance of 450 pc; Yao et al., 2017). Positions of the six pulsars used in this study are shown by yellow crosses with the pulsars' J-names.

Because of its large angular size and significant DM contribution to pulsars within/behind it, the Gum Nebula has been modeled as an independent component in Galactic electron density distribution models such as TC93 (Taylor & Cordes, 1993), NE2001 (Cordes & Lazio, 2002), and the YMW16 (Yao et al., 2017). Estimating the 3-D position of the expansion centre of the Gum Nebula, and its size, is essential for building the Galactic electron density distribution models, as well as understanding the origin and evolution of the Gum Nebula. However, this is not a easy task and the various current methods/estimates suffer from large uncertainties. According to the $H\alpha$ emission, the main body of the Gum Nebula appears to be a nearly circular region with a radius of $\sim 18^\circ$ approximately centered on Galactic coordinates $(l, b) = (258^\circ, -2^\circ)$ (Reynolds, 1976; Chanot & Sivan, 1983). Woermann et al. (2001) conducted a kinematics study of the Gum Nebula using OH masers at 1667 MHz and molecular line data from the literature. They modeled the Gum Nebula with the kinematic centre $(l, b) = (261^\circ, -2.5^\circ)$, and a mean angular radius of 14° . Adopting a non-uniformly expanding shell model, the best-fitting distance of the expansion centre is 400 pc from the Sun with a plausible uncertainty ranging from 200 to 500 pc. Purcell et al. (2015) modeled the Gum Nebula with a spherical shell centred at $(l, b) = (258^\circ, -6.6^\circ)$ with a radius of 22.7° . The Gum Nebula is also modeled in both NE2001 (Cordes & Lazio, 2002) and the YMW16 electron density model (Yao et al., 2017). NE2001 modeled the Gum Nebula with a centre at $(l, b) = (260^\circ, -1^\circ)$, a distance of 500 pc, and a radius of 140 pc (corresponding to an angular radius of 16.3°). In the YMW16 model, the centre is at $(l, b) = (264^\circ, -4^\circ)$, with a distance of 450 pc, and a radius of 125.8 pc (corresponding to an angular radius of 16.2°).

Weaver et al. (1977) suggested that the ionisation state of the Gum Nebula is maintained by the UV photons emitted from two bright, early-type stars: ζ Puppis (an O4 star); and γ^2 Velorum (a Wolf-Rayet star with an O7.5 companion). According to optical interferometer data and parallax measurements from *Hip-*

parcos and *Gaia*, the distance of ζ Pup is 332_{-11}^{+11} pc (van Leeuwen, 2007; Howarth & van Leeuwen, 2019), and 336_{-7}^{+8} pc for γ^2 Vel (van Leeuwen, 2007; North et al., 2007). γ^2 Vel is believed to be a member of the Vela OB2 association, together with another 81 B-type stars whose average distance is 415 ± 10 pc, as measured by *Hipparcos* (de Zeeuw et al., 1999). Cantat-Gaudin et al. (2019) confirmed this average distance using recent *Gaia* DR2 data, and suggest the closest member of the Vela OB2 association lies at a distance of ~ 330 pc, while the farthest is ~ 500 pc. One apparent consequence of this stellar association is the creation of a wind-blown bubble within the Gum Nebula, the IRAS Vela shell, which is a ring-like structure in the IRAS (Infrared Astronomical Satellite; Neugebauer et al., 1984) $100 \mu\text{m}$ far-infrared image with an angular radius of $\sim 7.5^\circ$ (Sahu & Sahu, 1993).

Another interesting structure related to the Gum Nebula is the Vela supernova remnant (Vela SNR). The Vela pulsar (PSR J0835–4510), which is the result of a Type II supernova explosion that occurred $\sim 10^4$ years ago (Taylor et al., 1993) resides in this remnant. The distance of the Vela pulsar was initially thought to be ~ 500 pc, however, substantially revised by parallax measurements made at the beginning of the 21st century. Using parallax measurements from the Hubble Space Telescope, (Caraveo et al., 2001) estimated the distance of the Vela pulsar to be 294_{-50}^{+76} pc, whereas (Dodson et al., 2003) estimated it to be 287_{-17}^{+19} pc using VLBI measurements. The X-ray image of the Vela SNR from *ROSAT* suggests it is roughly a shell with an angular radius of $\sim 4^\circ$, or ~ 20 pc in size at the Vela pulsar’s distance (Bocchino et al., 1994). Sushch et al. (2011) proposed a model describing the interaction between the Vela SNR and the IRAS Vela shell. They suggest that the observed asymmetry of the Vela SNR is due to the envelope of the Vela SNR physically meeting with the IRAS Vela shell (see Figure 5.2). The resulting complex ISM environment makes the observed propagation effects for the Vela pulsar’s signal exhibit some interesting and unique behaviours. For example, Hamilton et al. (1985) found that there is a significant variation in the

measured DM (from 69.1 to 68.2 pc cm⁻³) and RM (from 33.6 to 46.2 rad m⁻²) over fifteen years of observations using a 14-m dish at the University of Tasmania observatory. In this Chapter, using the MWA data and other information from the literature, the DM and RM measured as a function of observing epoch has been extended to cover nearly fifty years. These, along with additional results, are discussed in Section 5.6.

In Chapter 4, we showed that there is a rapid depolarisation exhibited by PSR J0742–2822 at frequencies below ~ 300 MHz, much in contrast with the generally expected trend for pulsar emission. We propose that, as the observed scattering is a result of varying paths that the light from the pulsar takes to reach the observer, the depolarisation is therefore due to the variation of RM between these different paths. We can then characterise the spatial structure of the RM across the pulsar scattering disk by examining the extent of this depolarisation. This turbulent ISM plasma also causes scattering, as exhibited by PSR J0742–2822, which displays significant pulse broadening. The intervening scattering material is generally attributed to the Gum Nebula (e.g. Johnston et al., 1998). Motivated by this intriguing result, we further investigated the depolarisation at low-frequencies, and the intervening scattering material, using MWA observations of multiple pulsars in the general direction of the Gum Nebula. The observations, pulsar selection, and data processing are described in Section 5.2. The Faraday spectra and RMs for the target pulsars are presented in Section 5.3. The polarimetric profiles for these pulsars are presented in Section 5.4. The depolarisation at low frequencies is presented and analysed in Section 5.5. In Section 5.6, we present the long-term variation in the ISM propagation properties towards these pulsars, and specifically for the Vela pulsar in more detail. The implications for the size of the Gum Nebula is discussed in Section 5.7.

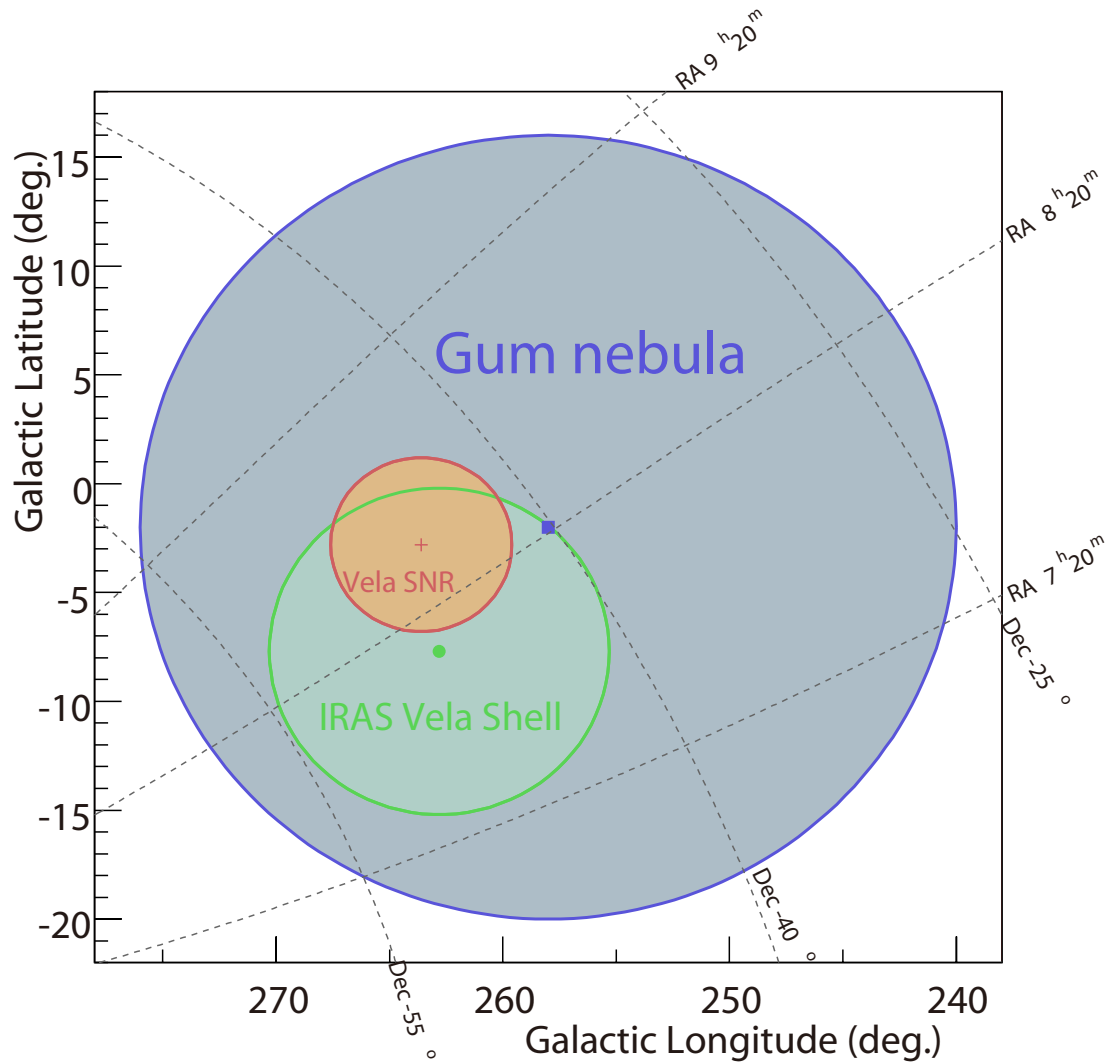


Figure 5.2: The modelled shape and sky position of the Gum nebula (the approximate center is shown as the blue square), the Vela SNR (the Vela pulsar is shown by the orange cross), γ^2 Vel (the green circle), and the IRAS Vela shell proposed by [Sushch et al. \(2011\)](#).

5.2 Observations and data processing

Six pulsars in the vicinity of the Gum Nebula on the sky, PSRs J0630–2834, J0737–3039A, J0742–2822, J0835–4510 (the Vela pulsar), J0837–4135, and J0959–4809, were selected to investigate the ISM via several propagation effects, including the observed depolarisation at low frequencies. This study requires the target pulsars to have measurably high linearly-polarised emission. These six pulsars were selected because they exhibit linear polarisation profiles with signal-to-noise ratios > 7 in one or more MWA observations.

As described in Chapter 2, the MWA-VCS system records channelised voltage signals from each tile. These voltage data are then transferred and archived on tape storage systems at the Pawsey Supercomputing Centre. By forming tied-array beams toward the target pulsars, we obtained full polarisation data products with the maximum array sensitivity. Each MWA observation has a large field-of-view (e.g. $\sim 700 \text{ deg}^2$ at 154 MHz), whose directional gain pattern relates directly to the tile beam shape. The coherent beamforming process results in a much narrower beam (e.g. $\sim 0.1 \text{ deg}^2$ at 154 MHz with the MWA Phase II compact configuration), which is also referred to as a ‘pencil’ beam. Multiple pencil beams can be formed from one MWA-VCS observation towards different target pulsars in the same field-of-view.

Of the six target pulsars used in this work, PSRs J0630–2834, J0737–3039A, and J0742–2822 have sufficiently small angular separations on the sky such that they can all be covered by one MWA pointing, while PSRs J0835–4510, J0837–4135, and J0959–4809 can be covered by another, separate MWA pointing. Data for PSRs J0630–2834, J0737–3039A, and J0742–2822 were recorded during two MWA observations. The first was taken on 2016 February 22, using the Phase I MWA at a centre frequency of 184.96 MHz; the second was taken on 2016 December 06, using the compact configuration of Phase II at a centre frequency of 154.24 MHz. Both of these observations were zenith pointings. PSRs J0835–4510, J0837–4135, and J0959–4809 were covered in four MWA observations. Three of

these were recorded at a centre frequency of 184.96 MHz; the fourth was recorded at 215.68 MHz. All of these used a contiguous bandwidth of 30.72 MHz. The total observing time for two of these observations is relatively short (< 7 minutes), and the sensitivity of one of the other observations was sub-optimal (possibly due to the pointing's large zenith angle). Therefore, PSR J0959–4809, which is less bright than PSRs J0835–4510 and J0837–4135, was only detected in one observation. The parameters of the MWA observations used in this work are summarised Table 5.1.

All of the MWA observations were calibrated using dedicated calibrator observations. Calibration solutions were obtained by means of the RTS pipeline, which were then applied to the respective observations in order to facilitate the formation of pencil beams towards the target pulsars (as described in Chapters 2 and 4). The resulting data products were written out as full-Stokes PSRFITS files. These data were then processed in the same way as described in Section 4.3.5. Incoherent dedispersion and folding were performed on the PSRFITS files using DSPSR (van Straten & Bailes, 2011) and timing ephemerides obtained from the ATNF pulsar catalogue (Version 1.60; Manchester et al., 2005b). The `pdmp` routine in the PSRCHIVE package (Hotan et al., 2004) was used to search for the optimal DMs, which are listed in Table 5.2.

Table 5.1: Parameters of the observations used in this work

Observation ID (GPS time)	Start time (UTC)	(Az, ZA) (deg, deg)	Frequency range (MHz)	Duration (s)	Pulsar detections
1140177088	2016 Feb 22, 11:51:11	(0.0, 0.0)	169.60–200.32	5040	J0630–2834, J0737–3039A, J0742–2822
1165080856	2016 Dec 06, 17:33:59	(0.0, 0.0)	138.88–169.60	3600	J0630–2834, J0737–3039A, J0742–2822
1139239952	2016 Feb 16, 15:32:15	(180.0, 13.7)	169.60–200.32	1160	J0835–4510, J0837–4135, J0959–4809
1177938016	2017 May 04, 12:59:58	(231.3, 49.4)	169.60–200.32	4800	J0835–4510, J0837–4135
1240826896	2019 May 02, 10:07:58	(180.0, 20.8)	169.60–200.32	296	J0835–4510, J0837–4135
1241518520	2019 May 10, 10:15:02	(198.4, 22.0)	200.32–231.04	424	J0835–4510, J0837–4135

5.3 RM determination for target pulsars

The RM towards each of the six target pulsars was calculated using the `RM-CLEAN` routine¹ (Heald et al., 2009; Michilli et al., 2018b), which incorporates RM synthesis and deconvolution techniques. Using the Stokes Q and U parameters from the peak phase bin of the average pulse profile for each 10 kHz frequency channel, ‘dirty’ Faraday spectra were obtained by applying RM synthesis over the 30.72 MHz observing bandwidth. A set of clean model components and an `RM-CLEAN`-ed Faraday spectrum were then recovered from each dirty Faraday spectrum through the deconvolution process; see Figures 5.3 – 5.8.

The height of the peak at 0 rad m^{-2} , relative to the higher peak near the RM associated with the pulsar signal, indicates the fraction of instrumental polarisation leakage. For PSRs J0630–2834, J0742–2822, and J0737–3039A (in both observations), the Faraday spectra present no significant instrumental peak centred around 0 rad m^{-2} , indicating minimal polarisation leakage. This is likely because both observations are zenith pointings, and thus the analytical beam model is a good approximation to the actual polarimetric response of the MWA tiles. However, for PSRs J0835–4510, and J0837–4135, instrumental polarisation leakage can be seen in all four observations. The relative strength of these instrumental peaks compared to the source peaks varies from observation to observation. For a given pulsar, there can be substantial differences in the degree of leakage between different Zenith angle pointings, often more than the difference for multiple pulsars within the same tile beam.

As described in Section 4.3.5, the observed RM (RM_{obs}) determined using this procedure contains both the contribution from the ISM (RM_{ISM}) and the Earth’s ionosphere (RM_{ion}). Therefore, RM_{ISM} , which characterises the electron column density and magnetic field strength of the ISM, can only be obtained after subtracting RM_{ion} from RM_{obs} . The ionospheric Faraday rotation contribution for each observation toward each pulsar was calculated using an updated version

¹<https://github.com/gheald/RMtoolkit>

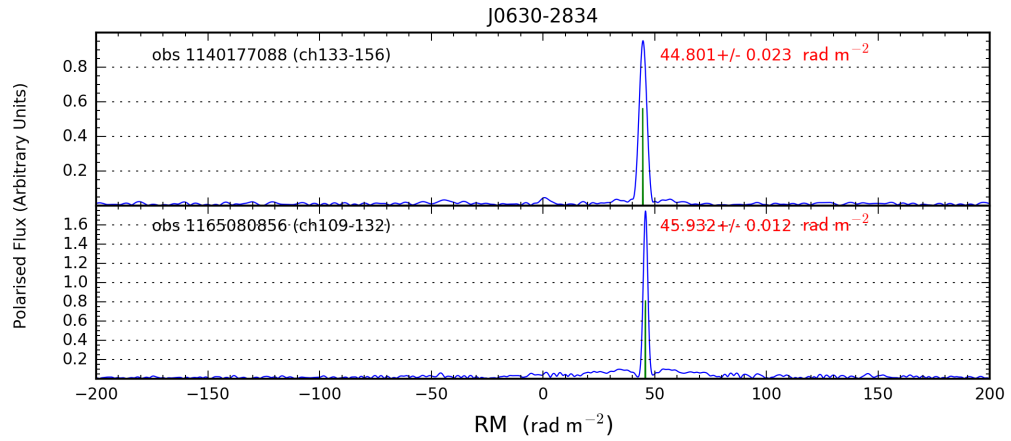


Figure 5.3: The RM-CLEAN-ed Faraday spectra (blue lines) and clean model components (green lines) for PSR J0630–2834. The observation ID on the left of each panel refers to the GPS time of the MWA observation; the observed RM (red text) is the location of the peak and clean model component in Faraday space.

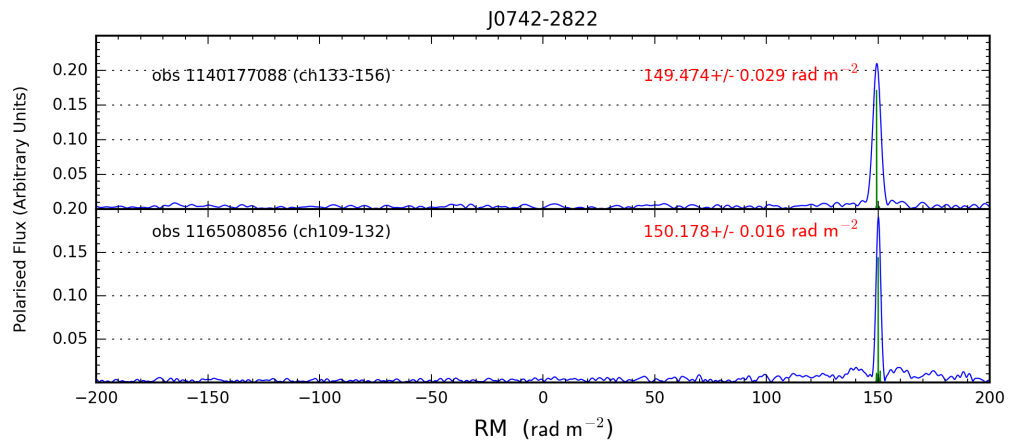


Figure 5.4: The RM-CLEAN-ed Faraday spectra and clean model components for PSR J0742–2822.

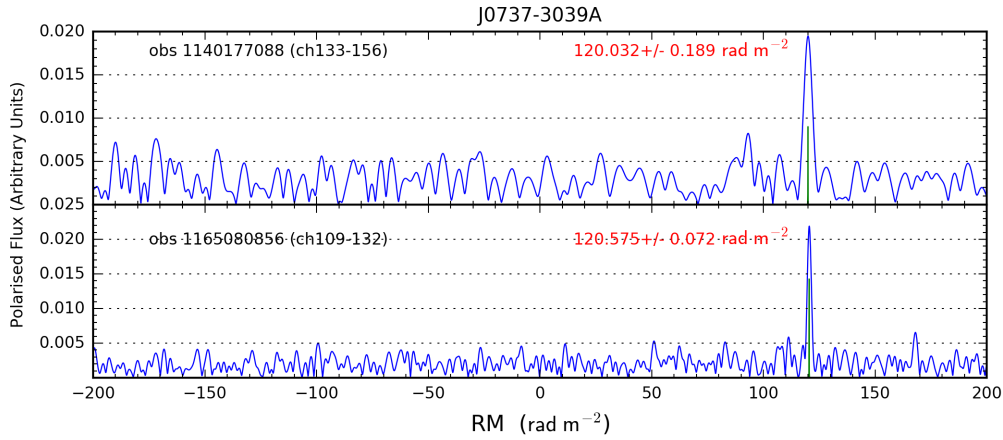


Figure 5.5: The RM-CLEAN-ed Faraday spectra and clean model components for PSR J0737–3039A.

of the `ionFR` software² (Sotomayor-Beltran et al., 2013), with the vertical total electron content (TEC) maps provided by the International Global Navigation Satellite Systems Service (IGS) (e.g. Hernández-Pajares et al., 2009), and the International Geomagnetic Reference Field (IGRF-12; Thébaud et al., 2015).

With the obtained DM and RM_{ISM} , the electron-density-weighted parallel component of the magnetic field averaged along the entire path, $\langle B_{\parallel} \rangle$, towards each pulsar was calculated, using the standard relation below:

$$\langle B_{\parallel} \rangle = 1.23 \mu\text{G} \left(\frac{\text{RM}}{\text{rad m}^{-2}} \right) \left(\frac{\text{DM}}{\text{pc cm}^{-3}} \right)^{-1}. \quad (5.1)$$

The results are summarised in Table 5.2.

²<https://sourceforge.net/projects/ionfarrot/>

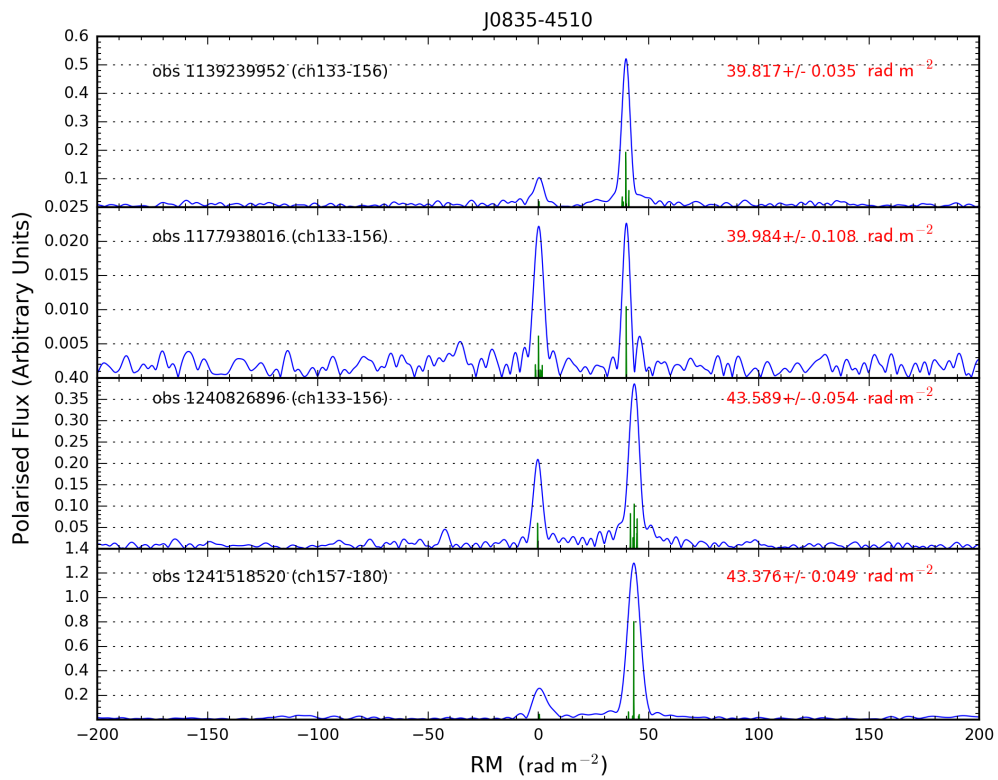


Figure 5.6: The RM-CLEAN-ed Faraday spectra and clean model components for PSR J0835–4510 with the same colours and labels setting as described in Figure 5.3.

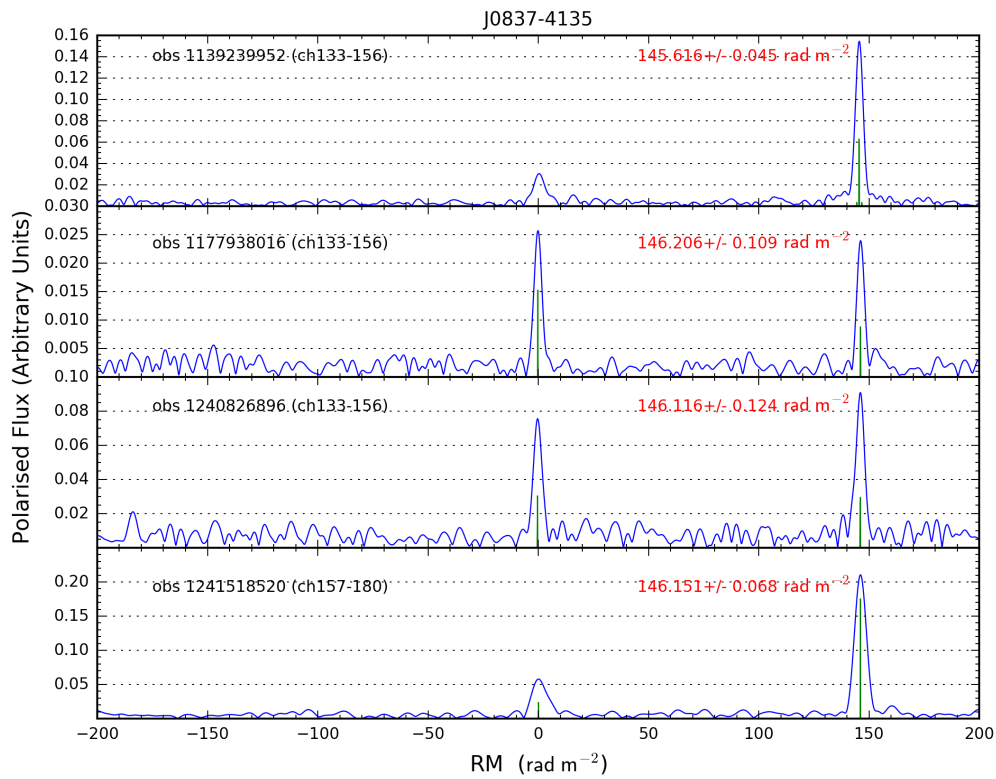


Figure 5.7: The RM-CLEAN-ed Faraday spectra and clean model components for PSR J0837–4135.

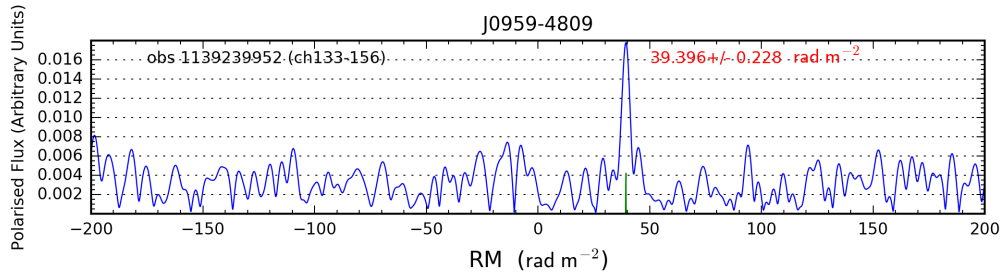


Figure 5.8: The RM-CLEAN-ed Faraday spectrum and clean model component for PSR J0959–4809.

Table 5.2: Measured DMs, RMs and inferred $\langle B_{\parallel} \rangle$ for the target pulsars.

Observation ID (GPS time)	DM (pc cm ⁻³)	RM _{obs} (rad m ⁻²)	RM _{ion} (rad m ⁻²)	RM _{ISM} (rad m ⁻²)	$\langle B_{\parallel} \rangle$ (μ G)
PSR J0630–2834					
1140177088	34.37±0.18	44.801±0.023	1.86±0.15	46.66±0.15	1.67±0.24
1165080856	34.36±0.21	45.932±0.012	0.60±0.14	46.53±0.14	1.67±0.25
PSR J0737–3039A					
1140177088	48.916±0.007	120.03±0.19	1.90±0.16	121.93±0.35	3.07±0.35
1165080856	48.918±0.004	120.575±0.072	0.62±0.15	121.19±0.22	3.05±0.22
PSR J0742–2822					
1140177088	73.814±0.049	149.474±0.029	1.87±0.15	151.35±0.16	2.53±0.16
1165080856	73.810±0.028	150.178±0.016	0.61±0.15	150.78±0.15	2.52±0.15
PSR J0835–4510					
1139239952	67.960±0.013	39.817±0.035	1.55±0.14	41.37±0.14	0.75±0.14
1177938016	67.938±0.026	39.98±0.11	0.69±0.14	40.68±0.17	0.74±0.18
1240826896	67.825±0.026	43.589±0.054	0.777±0.058	44.366±0.079	0.806±0.083
1241518520	67.811±0.041	43.376±0.049	0.781±0.057	44.157±0.075	0.802±0.086
PSR J0837–4135					
1139239952	147.22±0.22	145.616±0.045	1.51±0.13	147.12±0.14	1.23±0.26
1177938016	147.22±0.22	146.21±0.11	0.67±0.13	146.88±0.17	1.23±0.28
1240826896	147.22±0.22	146.12±0.12	0.754±0.058	146.87±0.14	1.23±0.26
1241518520	147.23±0.17	146.151±0.068	0.760±0.056	146.911±0.088	1.23±0.19
PSR J0959–4809					
1139239952	92.4±0.2	39.39±0.23	1.64±0.13	41.03±0.36	0.55±0.41

5.4 Multi-frequency polarimetric profiles and scattering timescales

After de-Faraday rotating the pulse profiles using the RMs derived in the previous section, the Stokes parameters (I , Q , U , V) and the linear polarisation ($L = \sqrt{Q^2 + U^2}$) can be calculated as functions of pulse phase. These were obtained using the PSRCHIVE package (van Straten et al., 2012). After measuring and removing the residual off-pulse baseline, the polarimetric pulse profiles for each target pulsar was generated. In order to better illustrate how the polarimetric pulse profiles of each target pulsar evolve as a function of observing frequency, a set of multi-frequency polarimetric profiles were generated using the MWA data, together with those obtained by other instruments at higher observing frequencies available in the literature.

For three pulsars whose pulse profiles have high signal-to-noise ratios and show obvious profile broadening – PSRs J0742–2822, J0835–4510 (the Vela pulsar), and J0837–4135 – the scattering time measurements are analysed and summarised in a paragraph corresponding to each pulsar.

For PSR J0630–2834, two MWA observations, 1165080856 (138.88–169.60 MHz) and 1140177088 (169.60–200.32 MHz), were used to generate the polarimetric profiles. Given the high detection signal-to-noise ratio, each observation was separated into three 10.24 MHz sub-bands, yielding polarimetric profiles for PSR J0630–2834 at six different frequency bands. For comparison, polarimetric profiles taken with the GMRT at 243 MHz and 325 MHz (Johnston et al., 2008) together with Parkes profiles at 732 MHz, 1.4 GHz, 3.1 GHz, and 8.4 GHz (Johnston et al., 2005, 2006; Karastergiou & Johnston, 2006) are also presented on the multi-frequency plot (Figure 5.9). Note that PSR J0630–2834 shows a very smooth and classical ‘S-shape’ P.A. curve for a wide range of observing frequencies, and therefore, can potentially be used as a calibrator for absolute polarisation phase calibration in future MWA observations.

Similarly, the multi-frequency polarimetric profiles for PSR J0742–2822 are shown in Figure 5.10. Note that the GMRT profiles at 243 and 325 MHz and the Parkes profile at 732 MHz were obtained from a private communication (Dr. Simon Johnston), and are not published in the literature. Parkes profiles at 1.4 GHz, 3.1 GHz, and 8.4 GHz (Johnston et al., 2006; Karastergiou & Johnston, 2006) are also included. Based on the total intensity profile, we estimate the scatter broadening time, τ_{sc} , to be 6.38 ± 0.11 ms at 185 MHz. This value is estimated using the deconvolution technique described in Bhat et al. (2003) and is consistent with work using MWA observations ($\tau_{sc} = 6 \pm 3$ ms at 185 MHz; Kirsten et al., 2019). For comparison, Geyer et al. (2017) estimated $\tau_{sc} = 16.1 \pm 1.6$ ms at 159.6 MHz using LOFAR commissioning data, although these data have lower signal-to-noise than the MWA data presented here, due to the comparatively low elevation and the telescope beam response for LOFAR.

PSR J0737–3039A is not as bright as PSRs J0630–2834 and J0742–2822. Therefore, in order to achieve a higher signal-to-noise ratio, the polarimetric profiles were generated directly using the two MWA observations without separating them into sub-bands (Figure 5.13). Polarimetric profiles and P.A. curves obtained using the entire 30.72 MHz MWA bandwidth for PSRs J0630–2834 and J0742–2822 are also presented in Figure 5.13.

Among the four observations of PSR J0835–4510 (the Vela pulsar), polarimetric profiles from 1240826896 (169.60–200.32 MHz) and 1241518520 (200.32–231.04 MHz) are selected to present in Figure 5.11 because these two observations were taken around the same time (only separated by eight days). The propagation effects for this pulsar show significant variations between different observing epochs, which will be further discussed in Section 5.6. Each observation was separated into three 10.24 MHz sub-bands, yielding polarimetric profiles at six different frequency bands. For comparison, polarimetric profiles taken with the Parkes telescope at 732 MHz, 1.4 GHz, 3.1 GHz, and 8.4 GHz (Johnston et al., 1998; Karastergiou & Johnston, 2006; Johnston et al., 2006; Johnston & Kerr,

2018) are also presented in Figure 5.11. Its P.A. curves and polarimetric profiles at two MWA 10.24 MHz sub-bands (179.84–190.08 MHz and 220.80–231.04 MHz) are presented in Figure 5.14. We estimate $\tau_{sc} = 14 \pm 5$ ms at 215 MHz using the deconvolution technique. Further analysis and discussion of the interstellar scattering measurements for the Vela pulsar are presented in Section 5.6.2.

The multi-frequency polarimetric profiles for PSR J0837–4135 were similarly generated (Figure 5.12). Parkes profiles at 691 MHz (Johnston et al., 2007), 1.4 GHz (Johnston & Kerr, 2018), 3.1 GHz (Johnston et al., 2007), and 8.4 GHz (Johnston et al., 2006) are presented for comparison. Its P.A. curves and polarimetric profiles obtained using the entire 30.72 MHz bandwidth of the MWA observations 1240826896 and 1241518520 are presented in Figure 5.14. Again, using the deconvolution technique, the scatter broadening time τ_{sc} is estimate to be 5.9 ± 0.2 ms at 215 MHz and 9.5 ± 1.5 ms at 185 MHz. This can provide a rough estimation of the scattering index α , which is around 3.2.

PSR J0959–4809 was only detected in observation 1139239952, and it was not separated into sub-bands in order to maintain a good signal-to-noise ratio. Its polarimetric profiles and P.A. curves from the MWA at 184.96 MHz and Parkes telescope at 1.4 GHz (Johnston & Kerr, 2018) are presented in Figure 5.14.

The extent to which pulsar profiles are scatter-broadened is determined by the inhomogeneity in the electron density in the foreground ISM towards each line-of-sight. This, in combination with studying the trend in the degree of linear polarisation with frequency in the scattered pulse profiles, can provide a method to measure the inhomogeneities in the electron density and magnetic field in the turbulent ISM at small scales and is discussed below.

5.5 Depolarisation at low frequencies

From the multi-frequency polarimetric profiles presented in the previous section, a significant decrease in the degree of linear polarisation at observing frequency below ~ 300 MHz is evident for in PSRs J0630–2834, J0742–2822, J0835–4510,

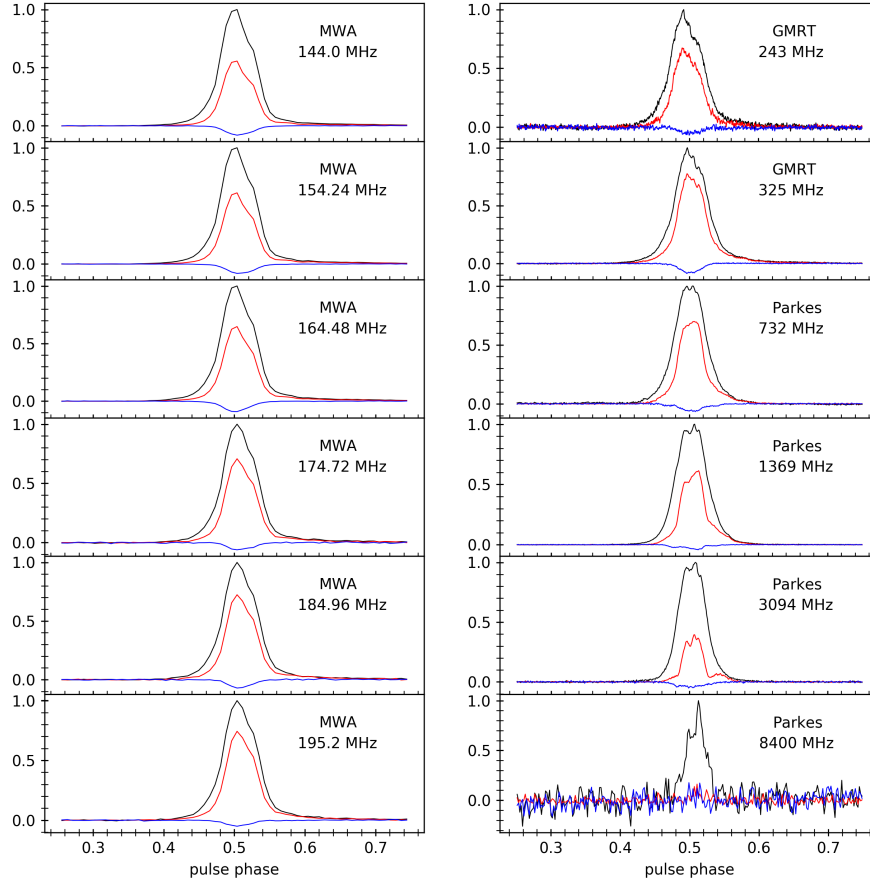


Figure 5.9: The multi-frequency polarimetric profiles for PSR J0630–2834. The left column includes polarimetric profiles obtained from two MWA observations (1165080856, and 1140177088), each observation is separated into three 10.24 MHz sub-bands. The right column includes polarimetric profiles at higher observing frequencies from the literature ([Karastergiou & Johnston, 2006](#); [Johnston et al., 2006, 2008](#)). Black lines indicate the total intensity (Stokes I), red lines indicate linear polarisation (Stokes $\sqrt{Q^2 + U^2}$), and blue lines indicate circular polarisation (Stokes V). The flux density of each of the profiles is normalised (arbitrary units). The labels indicate the telescopes used to observe the pulsars and the centre observing frequencies.

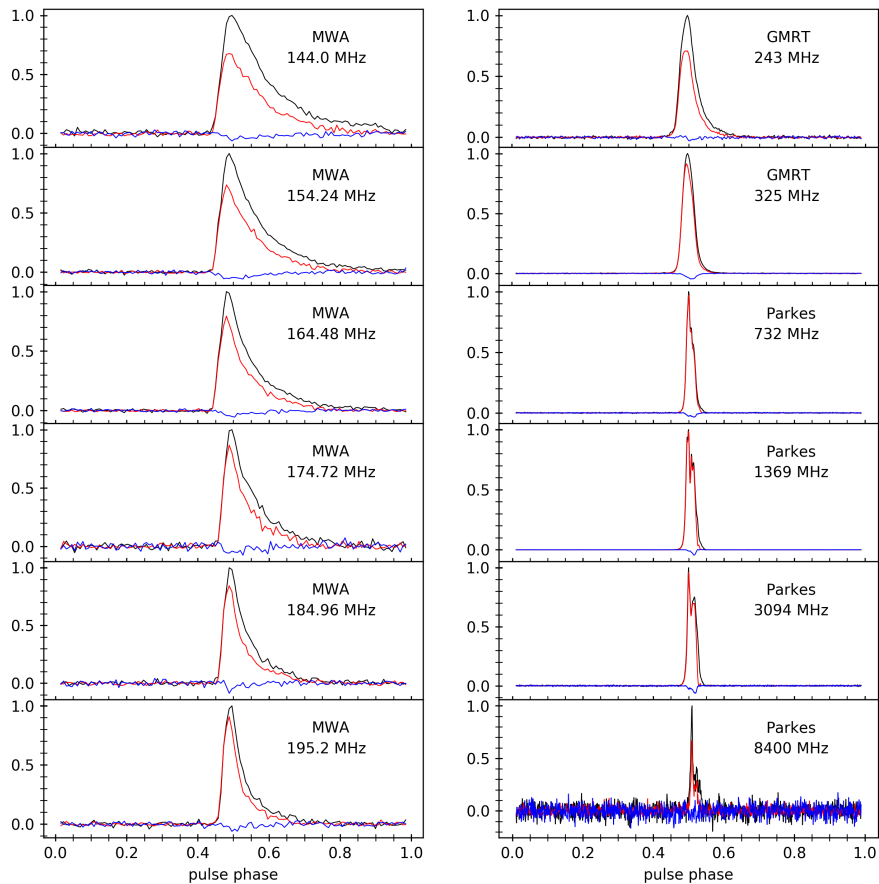


Figure 5.10: The multi-frequency polarimetric profiles for PSR J0742–2822, similar to those for PSR J0630–2834 (Figure 5.9). Comparison profiles at higher observing frequencies are from [Karastergiou & Johnston \(2006\)](#); [Johnston et al. \(2006, 2008\)](#).

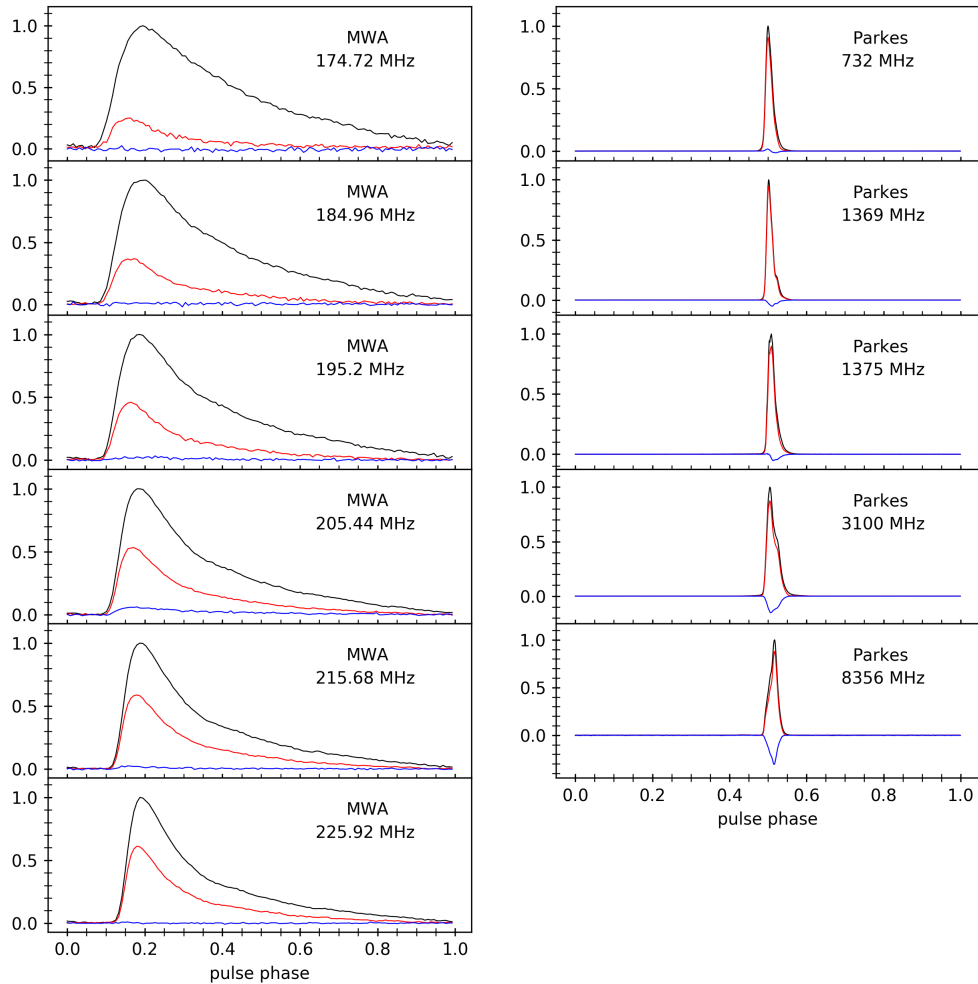


Figure 5.11: The multi-frequency polarimetric profiles for PSR J0835–4510 (the Vela pulsar). The left column shows the profiles obtained from two MWA observations (1240826896 and 1241518520). Each observation is separated into three 10.24 MHz sub-bands. Comparison profiles at higher observing frequencies are from [Johnston et al. \(1998\)](#); [Karastergiou & Johnston \(2006\)](#); [Johnston et al. \(2006\)](#); [Johnston & Kerr \(2018\)](#).

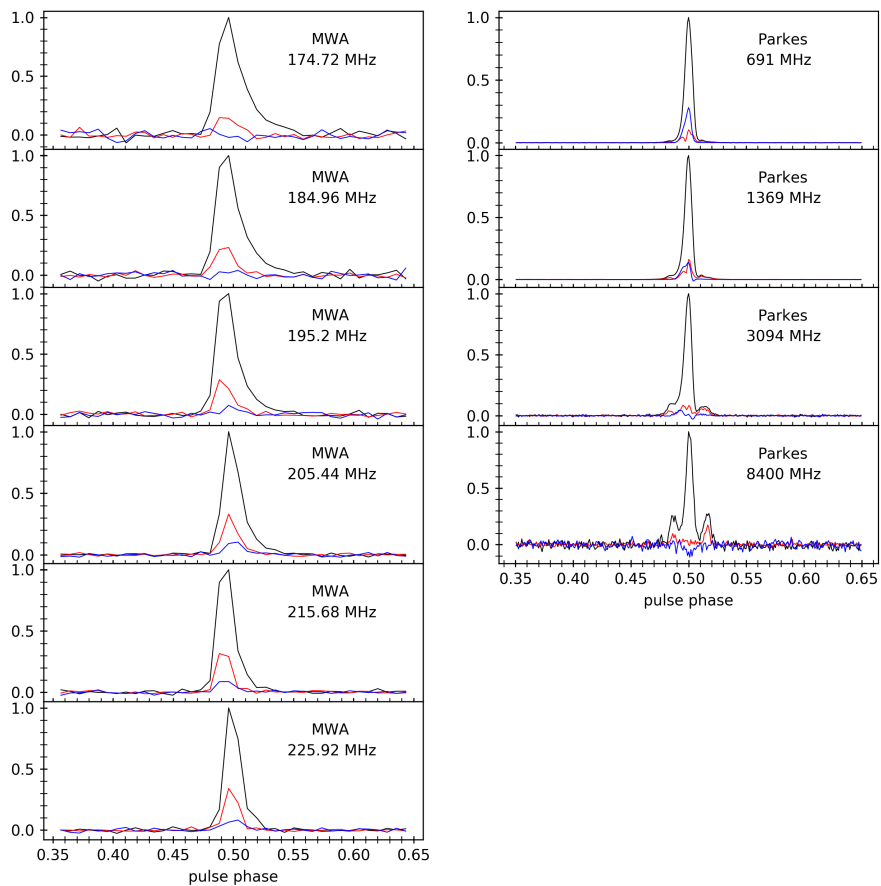


Figure 5.12: The multi-frequency polarimetric profiles for PSR J0837–4135, with the same sub-bands as for PSR J0835–4510 (Figure 5.11). Comparison profiles at higher observing frequencies are from [Karastergiou & Johnston \(2006\)](#); [Johnston et al. \(2006, 2007\)](#); [Johnston & Kerr \(2018\)](#).

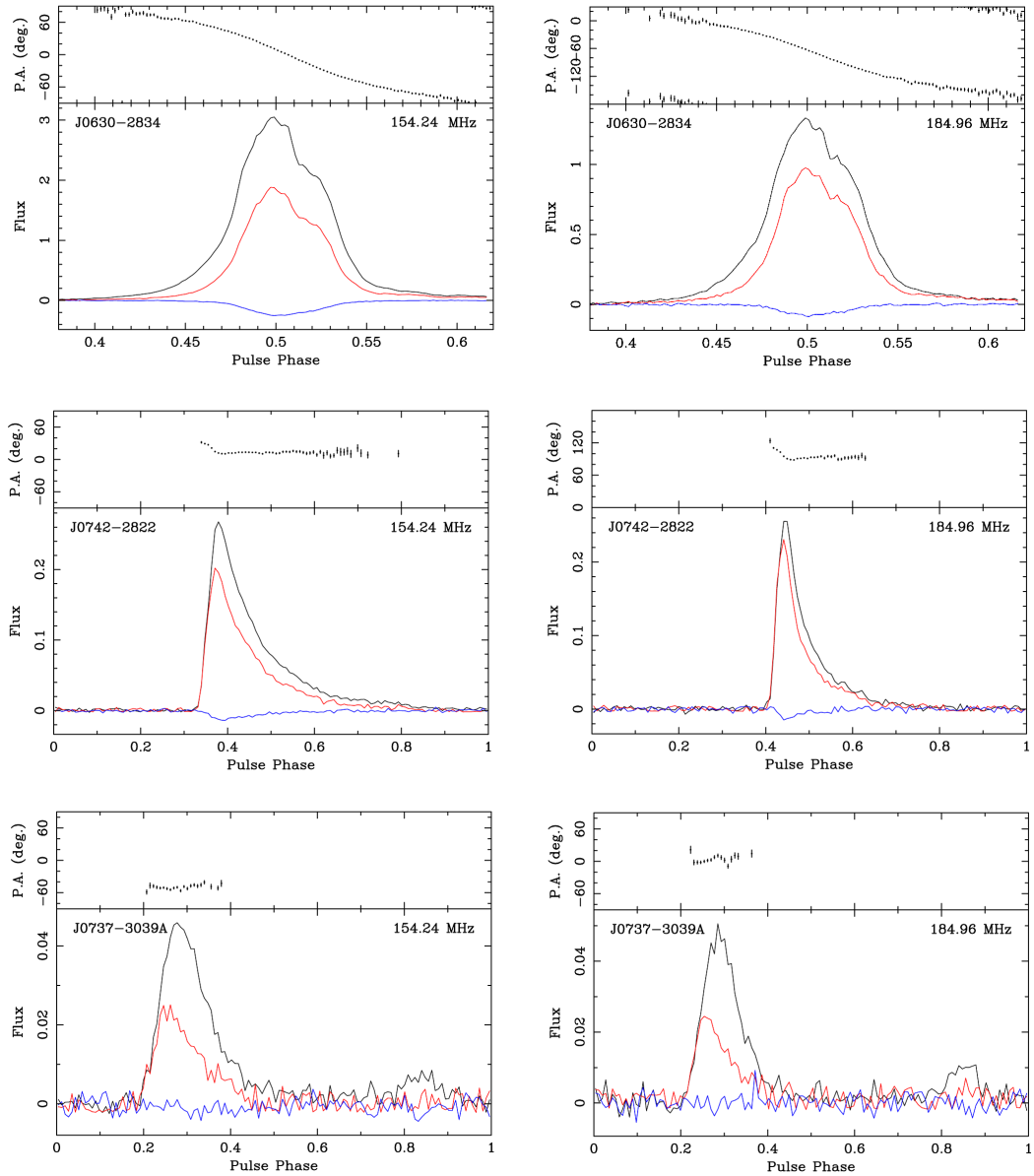


Figure 5.13: The polarimetric profiles and P.A. curves for PSRs J0630-2834, J0742-2822, and J0737-3039A. The left and right columns present profiles obtained from two MWA observations 1165080856 and 1140177088, respectively.

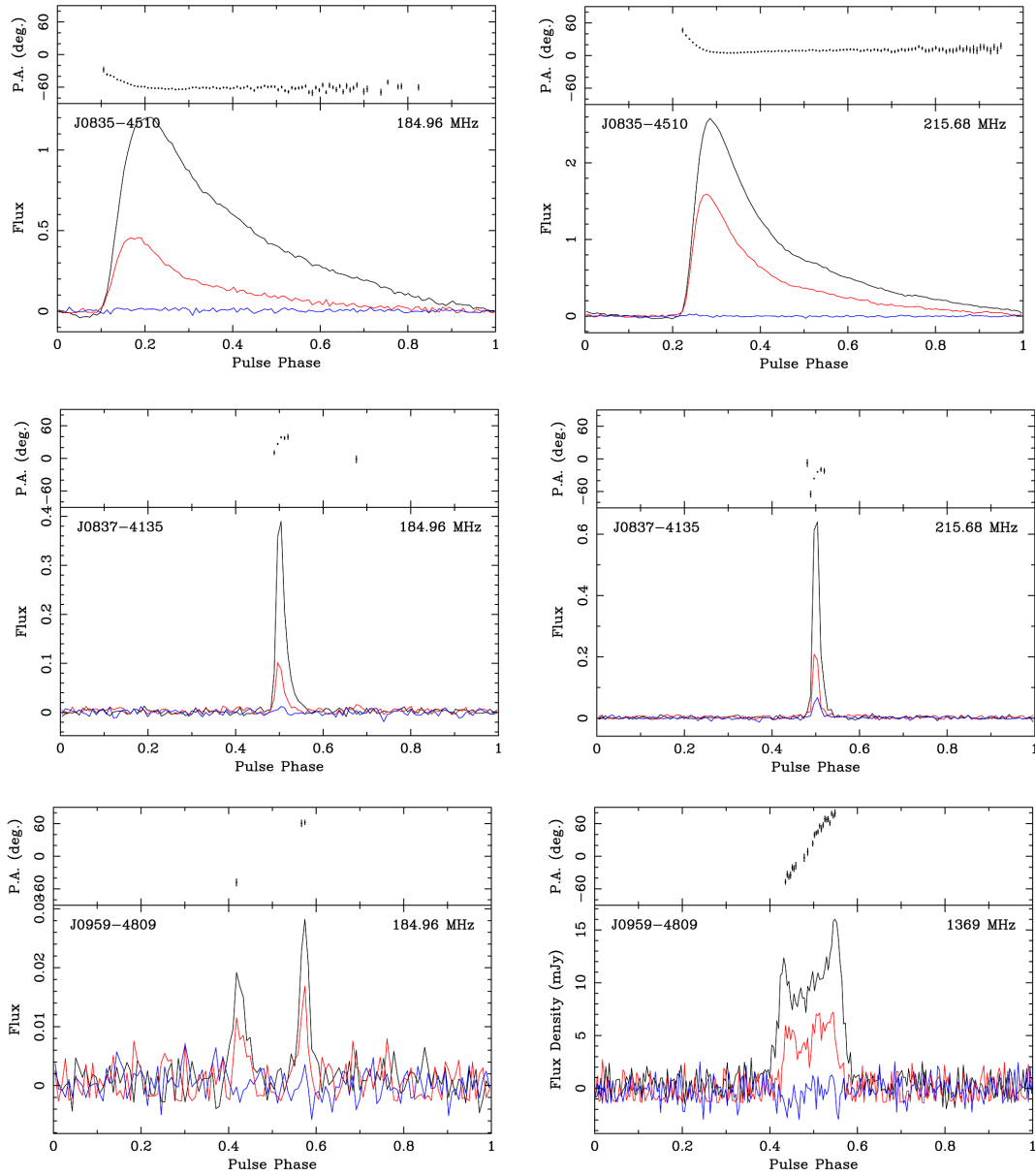


Figure 5.14: The polarimetric profiles and P.A. curves for PSRs J0835–4510, J0837–4135, and J0959–4809. Profiles for J0835–4510 make use of two 10.24 kHz sub-bands from MWA observations 1240826896 and 1241518520; profiles for J0837–4135 make use of the entire 30.72 MHz bandwidth of the two MWA observations. For J0959–4809, the polarimetric profile in the left panel is obtained from MWA observation 1139230052 with 30.72 MHz bandwidth, while the right panel shows the Parkes profile from [Johnston & Kerr \(2018\)](#).

and J0837–4135. PSR J0737–3039A and J0959–4809 were not further investigated here due to the lack of polarisation information at multiple frequencies. In order to analyse the depolarisation trend quantitatively, the degree of linear polarisation (equivalent integrated on-pulse flux of the linearly polarised profile) were calculated for these four pulsars within each 10.24 MHz sub-band. Combining these with the literature values, the measured degree of linear polarisation as a function of the observing frequency are shown in Figures 5.15–5.18.

Note that although all these four pulsars show depolarisation at low radio frequencies, PSR J0630–2834 is relatively special compare to the other three. It does not show obvious scattering broadening as what others have. While the behaviour for PSRs J0742–2822 and J0835–4510 present in this Chapter is in line with the behaviour of PSR J0742–2822 originally seen in MWA observations using non-contiguous frequency channels (see Chapter 4). In Section 4.7.1, several possible explanations for the depolarisation towards low frequencies were discussed. We concluded that the depolarisation is most likely caused by random small-scale spatial fluctuations of the RM in the turbulent plasma within the nebula. This turbulent plasma will also lead to multi-path scattering. According to [Burn \(1966\)](#), if the scale of the RM fluctuations $l_{\text{RM}} \ll \theta_s d_s$, where θ_s is the scattering disk size and d_s is the distance to the scattering screen, the corresponding Faraday spectrum component can be well represented by a Gaussian component with variance $\sigma^2 = \delta\text{RM}^2$. The observed degree of linear polarisation at wavelength λ is, therefore,

$$p(\lambda) = p_i \exp(-2\lambda^4 \delta\text{RM}^2), \quad (5.2)$$

where p_i is the intrinsic degree of linear polarisation.

For PSR J0837–4135, the $p(\lambda)$ obtained from MWA observations 1139239952, 1240826896 and 1241518520 are presented, along with those at higher frequencies obtained using Parkes profiles ([Johnston et al., 2005, 2006](#); [Karastergiou & Johnston, 2006](#); [Johnston & Kerr, 2018](#)) and from the literature ([Hamilton et al., 1977](#); [McCulloch et al., 1978](#)). Fitting for δRM is not performed for PSR J0837–

4135 because of the large uncertainty in $p(\lambda)$ at several frequency bands and the complex behaviour of $p(\lambda)$, which is probably due to the intrinsic profile evolution with frequency, see Figure 5.18.

By fitting the observed degree of linear polarisation $p(\lambda)$ as a function of wavelength λ in the form of Eq. (5.2), the required RM fluctuation, δRM , was estimated for PSRs J0630–2834, J0742–2822, and J0835–4510. While for PSR 0837–4135, fitting for δRM is not performed because of the relatively large uncertainty of the obtained degree of linear polarisation. The fitting procedure has an implicit assumption that the intrinsic degree of linear polarisation, p_i , is unchanged at those bands used for the fitting. As a first-order assumption, this is not unreasonable. In the case that the intrinsic degree of linear polarisation p_i is not a constant at low frequencies (i.e. increasing at lower frequencies), the measured δRM becomes a lower limit.

For PSRs J0630–2834, the lack of obvious scattering effect makes the explanation for its depolarisation at low frequencies not as straight forward as PSRs J0742–2822 and J0835–4510. Considering its long pulse period (1.244 s), it is reasonable not to expect scattering to be visible in the pulse shape. This does not mean there is completely no multipath scattering happens toward its pulse signal, and we can kind of infer the existence of scattering based on the depolarisation. Further discussion on this can be found in Section 5.5.5.

5.5.1 PSR J0742–2822

As shown in Figure 5.15, the degree of linear polarisation for PSR J0742–2822 obtained from more recent MWA observations is slightly higher than that from [Xue et al. \(2019\)](#) (Chapter 4), though generally consistent within uncertainties. The $p(\lambda)$ obtained using Parkes and GMRT profiles from [Johnston et al. \(2005, 2006\)](#); [Karastergiou & Johnston \(2006\)](#); [Johnston et al. \(2008\)](#) are presented, as well as those published in [McCulloch et al. \(1978\)](#) and [Gould & Lyne \(1998\)](#). Fitting for Eq. (5.2) is performed with MWA observations 1165080856, 1140177088,

and those in the literature below 1.4 GHz. The best fit $\delta\text{RM} = 0.111 \text{ rad m}^2$ and $p_i = 89.43\%$. For comparison, using data from [Xue et al. \(2019\)](#), the best fit $\delta\text{RM} = 0.128 \text{ rad m}^2$ and $p_i = 89.47\%$.

5.5.2 PSR J0835–4510

For PSR J0835–4510, $p(\lambda)$ are calculated using MWA observations 1139239952, 1240826896 and 1241518520. Note that the pointing for the MWA observation 1177938016 has a large zenith angle (49.4°) and its sensitivity performance is significantly worse than the other three observations. Therefore, this observation is only used for calculating the RM, but not used to calculate $p(\lambda)$ for either PSR J0835–4510 or J0837–4135 due to the higher instrumental polarisation leakage. The $p(\lambda)$ obtained using Parkes profiles ([Johnston et al., 2005, 2006](#); [Karastergiou & Johnston, 2006](#); [Johnston & Kerr, 2018](#)), and from literature ([Hamilton et al., 1977](#); [McCulloch et al., 1978](#)) are also presented in Figure 5.16. Fitting for Eq. 5.2 is performed twice because the propagation effects for this pulsar show significant variations between different observing epochs (see Section 5.6 for further discussion), one using data points from MWA observations 1240826896, 1241518520, and literature data points below 1.4 GHz ($\delta\text{RM} = 0.287 \text{ rad m}^2$, $p_i = 91.32\%$); another using data points from MWA observation 1139239952, and literature data points below 1.4 GHz ($\delta\text{RM} = 0.334 \text{ rad m}^2$, $p_i = 90.80\%$). Since the fitting is done in λ^2 space, the results are more heavily weighted by the low-frequency data.

5.5.3 PSR J0630–2834

For PSR J0630–2834, the degree of linear polarisation decreases significantly with increasing observing frequency above 300 MHz ([Hamilton et al., 1977](#); [McCulloch et al., 1978](#); [Gould & Lyne, 1998](#); [Johnston et al., 2005, 2006](#); [Karastergiou & Johnston, 2006](#); [Johnston et al., 2008](#)), see Figure 5.17. It also shows depolarisation Unlike PSR J9742–2822 and PSR J0835–4510 just discussed in the two

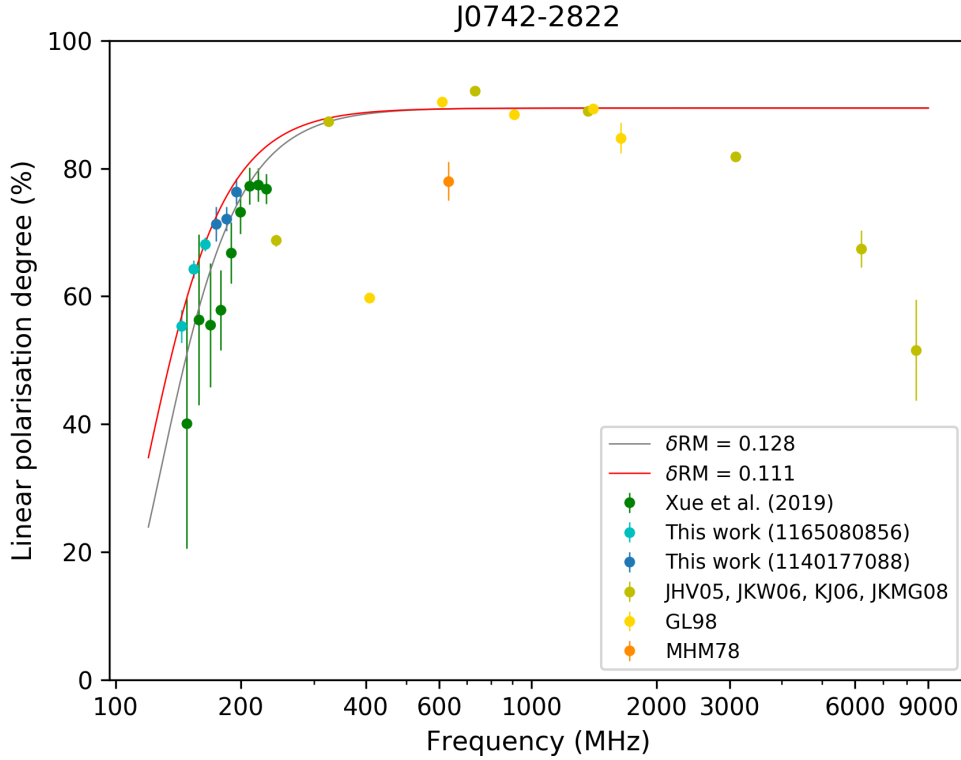


Figure 5.15: Degree of linear polarisation as function of frequency for PSR J0742–2822. Values obtained from MWA observations 1165080856, 1140177088 and from [Xue et al. \(2019\)](#) are plotted in cyan, blue and dark green, respectively. Values calculated using Parkes and GMRT profiles from [Johnston et al. \(2005, 2006\)](#); [Karastergiou & Johnston \(2006\)](#); [Johnston et al. \(2008\)](#) are plotted in light green. Values published in [McCulloch et al. \(1978\)](#) and [Gould & Lyne \(1998\)](#) are plotted in orange and yellow, respectively. The grey line shows the depolarisation factor $\exp(-2\lambda^4\delta\text{RM}^2)$ where $\delta\text{RM} = 0.128 \text{ rad m}^2$, fitted with data points from [Xue et al. \(2019\)](#); the red line shows where $\delta\text{RM} = 0.111 \text{ rad m}^2$, fitted with data points from MWA observations 1165080856, 1140177088, and those in the literature below 1.4 GHz.

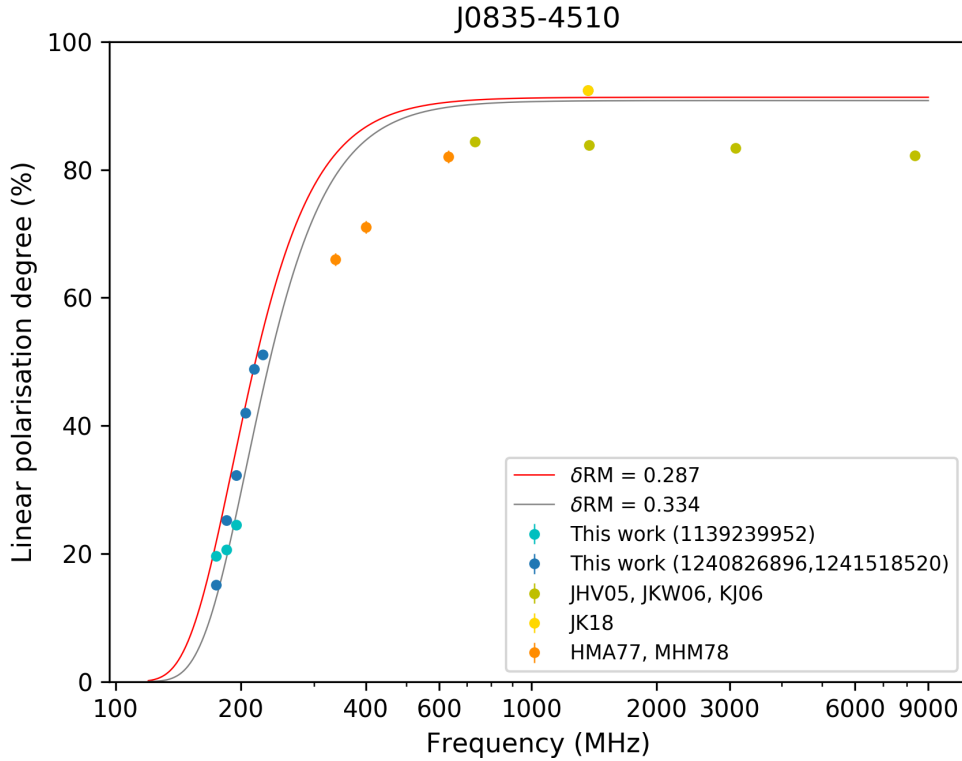


Figure 5.16: Degree of linear polarisation as function of frequency for PSR J0835–4510. Values obtained from MWA observation 1139239952 is plotted in cyan; values obtained from MWA observations 1240826896 and 1241518520 are plotted in blue. Values given by [Hamilton et al. \(1977\)](#) and [McCulloch et al. \(1978\)](#) are plotted in orange. Values calculated using Parkes profiles from [Johnston et al. \(2005, 2006\)](#); [Karastergiou & Johnston \(2006\)](#) are plotted in light green; the 1.4 GHz value calculated using Parkes profiles from [Johnston & Kerr \(2018\)](#) is plotted in yellow. The red line shows the depolarisation factor $\exp(-2\lambda^4\delta\text{RM}^2)$ where $\delta\text{RM} = 0.287 \text{ rad m}^{-2}$, fitted with data points from MWA observations 1240826896 and 1241518520, and those from the literature below 1.4 GHz; the grey line shows where $\delta\text{RM} = 0.334 \text{ rad m}^{-2}$, fitted with data points from MWA observation 1139239952, and those in the literature below 1.4 GHz. The reason for separate fits is explained in the text.

previous subsections, PSR J0630–2834 does not show obvious scattering broadening. Considering its long pulse period (1.244 s), it is not unexpected. However, the depolarisation still occurs for PSR J0630–2834 at low observing frequencies, despite the lack of obvious scattering effect.

Fitting for Eq. (5.2) is performed with only $p(\lambda)$ obtained using MWA observations 1165080856, 1140177088. The best fit $\delta\text{RM} = 0.102 \text{ rad m}^2$ and $p_i = 74.50\%$. Since PSR J0630–2834 is $\sim 28^\circ$ away from the centre of the Gum Nebula, signals from PSR J0630–2834 were assumed to be unaffected by the Gum Nebula. Deller et al. (2009) measured the distance for PSR J0630–2834, 320_{-40}^{+52} pc, using VLBI annual parallax. Alternatively, using the YMW16 electron density model (Yao et al., 2017), which models the Gum Nebula with a radius $\sim 23^\circ$, the resulting DM distance for PSR J0630–2834 is 2.07 kpc. Using the NE2001 model (Cordes & Lazio, 2002), the distance for PSR J0630–2834 is 1.45 kpc.

Considering the large discrepancy between the parallax distance and the DM distance, along with the depolarisation at low frequencies presented in this work, the size of the ionised region associated with the Gum Nebula might be larger than previously thought. Alternatively, there might be an over-density of electrons associated with another unknown structure along the line-of-sight.

5.5.4 PSR J0837–4135

For PSR J0837–4135, the $p(\lambda)$ obtained from MWA observations 1139239952, 1240826896 and 1241518520 are presented, along with those at higher frequencies obtained using Parkes profiles (Johnston et al., 2005, 2006; Karastergiou & Johnston, 2006; Johnston & Kerr, 2018) and from the literature (Hamilton et al., 1977; McCulloch et al., 1978). Fitting for δRM is not performed for PSR J0837–4135 because of the large uncertainty in $p(\lambda)$ at several frequency bands and the complex behaviour of $p(\lambda)$, which is probably due to the intrinsic profile evolution with frequency, see Figure 5.18.

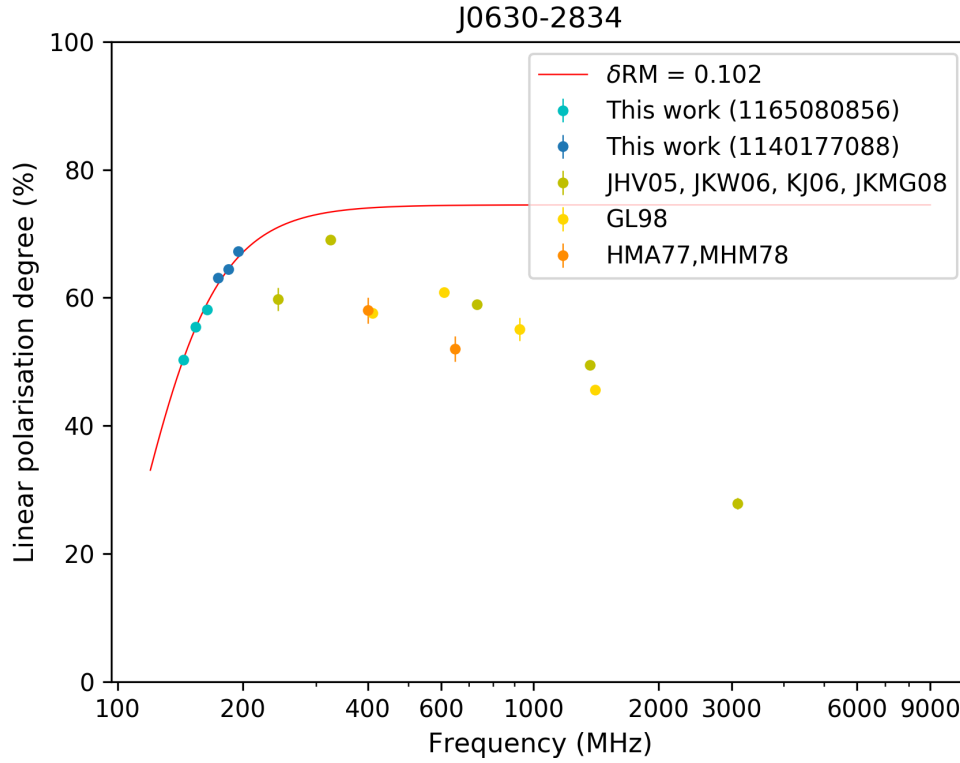


Figure 5.17: Degree of linear polarisation as function of frequency for PSR J0630–2834. Values obtained from MWA observations 1165080856 and 1140177088 are plotted in cyan and blue, respectively. Values calculated using Parkes and GMRT profiles from Johnston et al. (2005, 2006); Karastergiou & Johnston (2006); Johnston et al. (2008) are plotted in light green. Values given by Hamilton et al. (1977) and McCulloch et al. (1978) are plotted in orange; those from Gould & Lyne (1998) are plotted in yellow. The red line shows the depolarisation factor $\exp(-2\lambda^4\delta RM^2)$ where $\delta RM=0.102$ rad m², fitted with data points from MWA observations 1165080856 and 1140177088 alone.

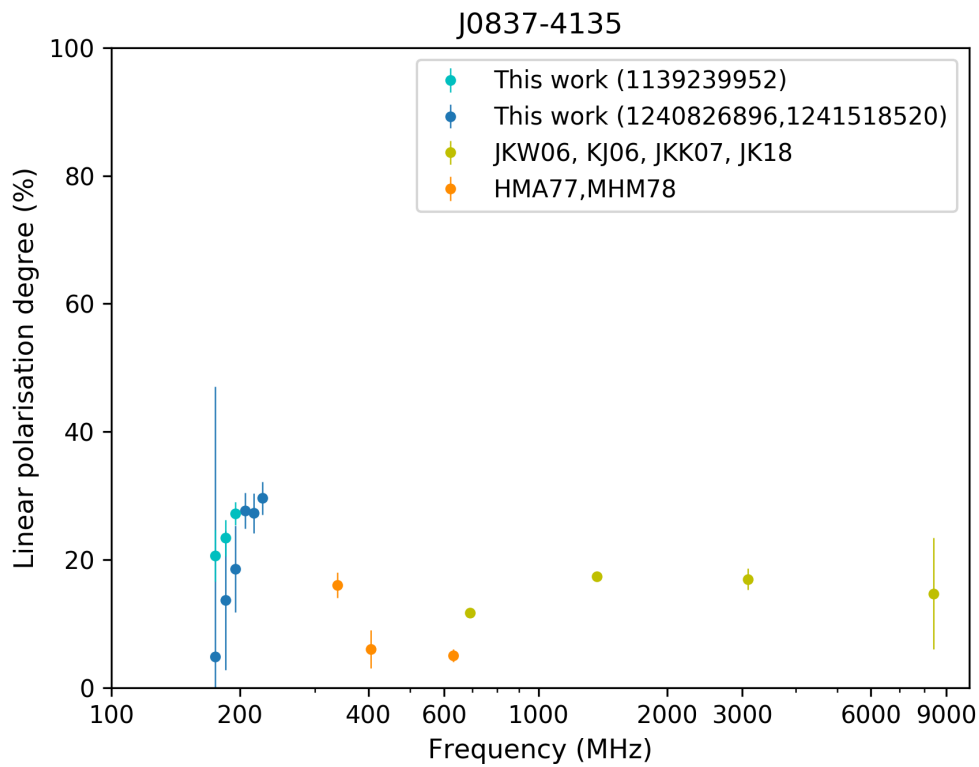


Figure 5.18: Degree of linear polarisation as function of frequency for PSR J0837–4135. Values obtained from MWA observation 1139239952 is plotted in cyan; values obtained from MWA observations 1240826896 and 1241518520 are plotted in blue. Values given by [Hamilton et al. \(1977\)](#) and [McCulloch et al. \(1978\)](#) are plotted in orange. Values calculated using Parkes profiles from [Johnston et al. \(2005, 2006\)](#); [Karastergiou & Johnston \(2006\)](#); [Johnston & Kerr \(2018\)](#) are plotted in light green.

5.5.5 Phase-related depolarisation analysis

The depolarisation analysis presented in the previous section was conducted using the value of the polarisation degree integrated over the whole pulse profile. This was a first-order estimation used to maximise signal-to-noise. As has been addressed in the literature, e.g. [Komesaroff et al. \(1972\)](#) and [Li & Han \(2003\)](#), a scattering screen (with anisotropic electron density but uniform Faraday rotation) will smoothen the P.A. curve but not strongly depolarise the linear polarisation (for a simple, canonical pulse profile). Here, we further test our hypothesis that the low-frequency depolarisation measured is caused by a Faraday-rotating scattering screen with a random component, δRM . If this is the case, we expect that emission from later on-pulse phase bins will show greater depolarisation due to propagation through a larger area of the scattering screen. Therefore, I calculate the degree of polarisation for different pulse phase ranges for these pulsars, e.g. with the highest signal-to-noise versus the one where the scattering tail is more prominent. This is attempted for PSRs J0742–2822 and J0835–4510 (Vela pulsar).

In this analysis, the on-pulse phase bins are separated into three parts: 1) area before the peak intensity (leading edge); 2) the phase bin corresponding to the peak intensity; and 3) area after the peak (trailing edge). The degree of linear polarisation was calculated for these three pulse-phase areas and using six frequency bands for both PSRs J0742–2822 and J0835–4510. The results are shown in [Figure 5.19](#) and [5.20](#).

For both PSRs J0742–2822 and J0835–4510, the leading pulse profile phase bins show greater linear polarisation degrees compared to those from later phase bins. The rapid depolarisation towards lower radio frequencies can be seen in all three phase bin areas. However, the difference in linear polarisation degrees from the leading to the trailing edge is greater for PSR J0742–2822 ($\sim 70\%$) than for PSR J0835–4510 ($\sim 60\%$). These effects may be a result of the scattering time relative to the pulse period, which is greater for PSR J0835–4510 than PSR

J0742–2822, see Figures 5.13 and 5.14. The emission from the scattering tail will interfere with the following pulse, resulting in depolarisation of the leading edges of the pulse profile as well. This may be the case for both pulsars but is more prominent for PSR J0835–4510. For both pulsars, the results are consistent with the behaviour expected from the foreground scattering screen with spatially varying Faraday rotation, quantified as differential Faraday rotation, δRM , measured in the previous section. This results suggest that in the future, a phase-resolved analysis of the degree of linear polarisation using a wide range of quasi-simultaneous radio frequencies can provide even more information about the small-scale ISM characteristics.

I also carried out a similar analysis for PSR J0630–2834, which does not show a significantly scatter-broadened profile but does show depolarisation towards lower frequencies (see Figure 5.17). The long pulse period of PSR J0630–2834 (1.244 s) means that one single phase bin is equivalent to ~ 10 ms, since the pulse profile is constructed using 128 rotational phase-bins. Therefore, the scatter broadening likely affects each on-pulse phase bin. In this case, the PA swing, together with the multi-path scattering effect, will also cause depolarisation, and may therefore show no trend in the phase-resolved analysis (unlike for PSRs J0742–2822 and J0835–4510). This analysis underlines the fact that the pulse profile of PSR J0630–2834 shows greater intrinsic pulse profile evolution at low frequencies (compared to PSRs J0742–2822 and J0835–4510), with the trailing pulse profile component decreasing in flux density compared to the main peak towards lower frequencies (see Figure 5.9). This complicates the analysis, since the depolarisation observed at low frequencies may not only be caused by a foreground scattering screen. Again, a more detailed phase-resolved analysis using a wide range of radio frequencies quasi-simultaneously would provide greater information with which to study the intrinsic emission and the propagation effects but is beyond the scope of this work.

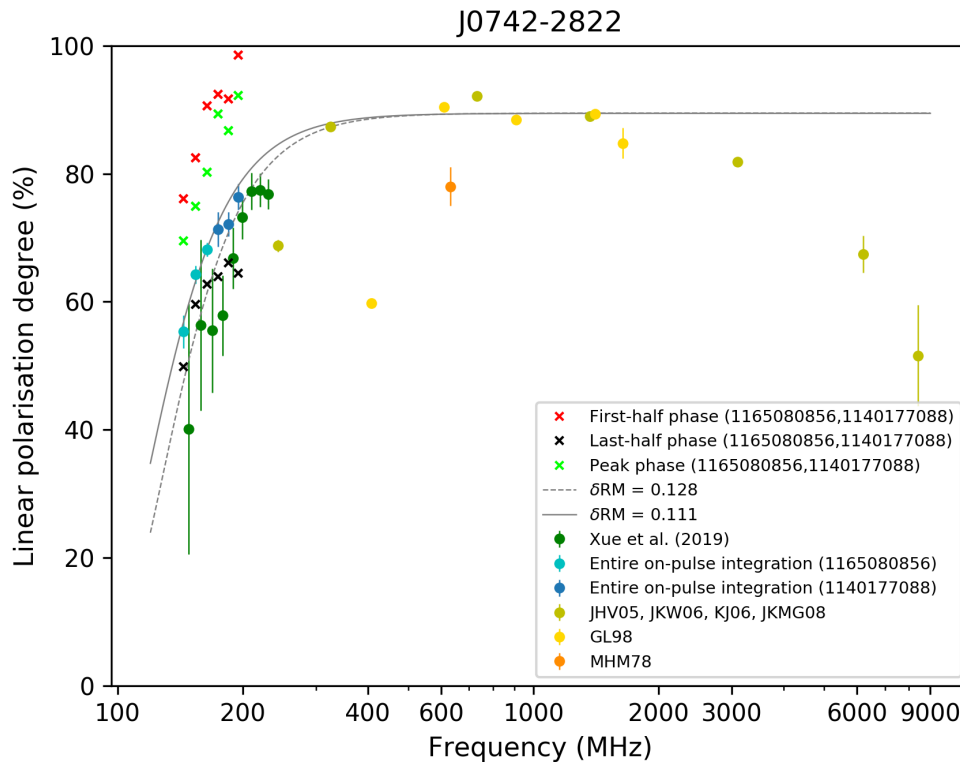


Figure 5.19: Degree of linear polarisation as function of frequency for PSR J0742–2822. Mostly the same with Figure 5.15, but with additional phase-related depolarisation analysis results. Red crosses indicate the polarisation degree for six MWA bands (from observations 1165080856 and 1140177088) calculated with phase bins before the peak; green crosses indicate those calculated with the peak phase bin only; and black crosses indicate those calculated with phase bins after the peak.

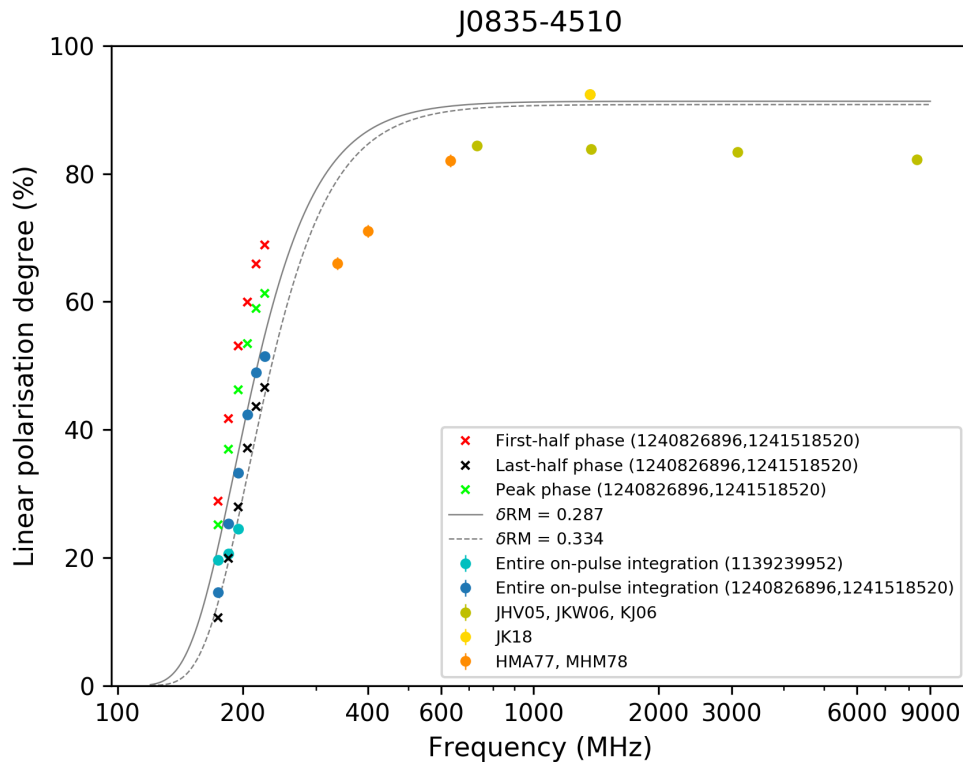


Figure 5.20: Degree of linear polarisation as function of frequency for PSR J0835–4510. Mostly the same with Figure 5.16, but with additional phase-related depolarisation analysis results. Red crosses indicate the polarisation degree for six MWA bands (from observations 12408268986 and 1241518520) calculated with phase bins before the peak; green crosses indicate those calculated with the peak phase bin only; and black crosses indicate those calculated with phase bins after the peak.

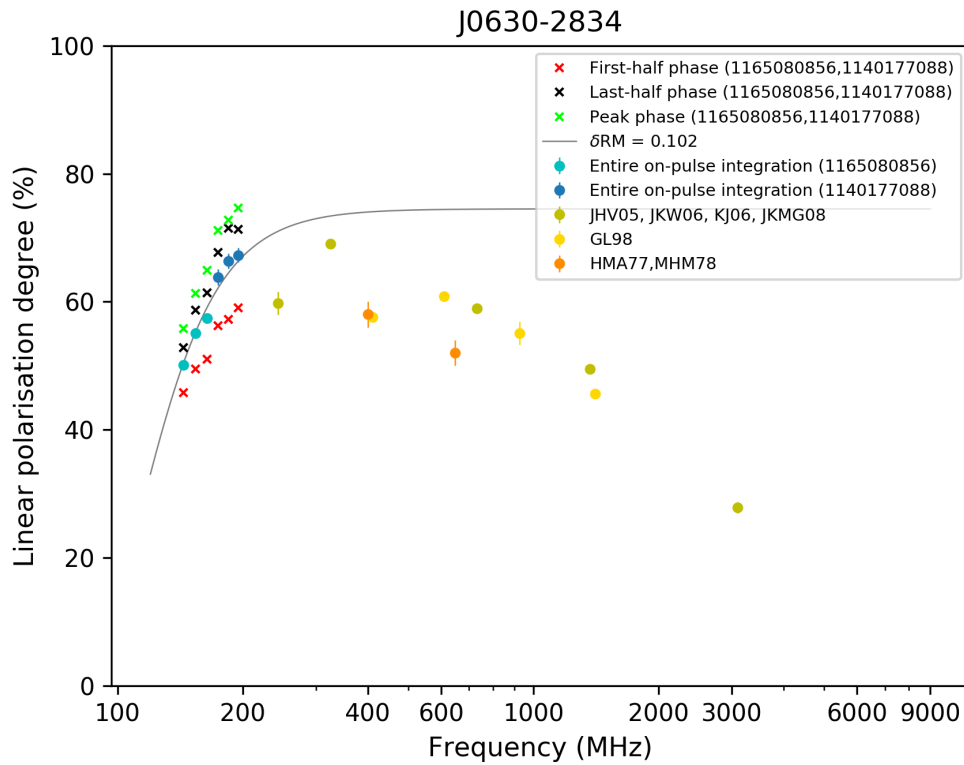


Figure 5.21: Degree of linear polarisation as function of frequency for PSR J0630–2834. Mostly the same with Figure 5.17, but with additional phase-related depolarisation analysis results. Red crosses indicate the polarisation degree for six MWA bands (from observations 1165080856 and 1140177088) calculated with phase bins before the peak; green crosses indicate those calculated with the peak phase bin only; and black crosses indicate those calculated with phase bins after the peak.

5.6 Long-term variations in the propagation properties of the ISM

Up to this point, the spatial variations of RM and its effect on pulsar polarisation have been considered. As pulsars and the ISM are not static, these spatial variations should also manifest as temporal variations, albeit on much longer time scales.

For each pulsar, comparing the DM and RM obtained at different observing epochs provides a direct method for investigating the small-scale properties of the intervening ISM (e.g. [Backer et al., 1993](#); [You et al., 2007](#); [Yan et al., 2011](#); [Lam et al., 2016](#)). However, these studies require long-term, precise measurements of the pulsar's DM and RM. This is most often done for bright millisecond pulsars motivated by pulsar timing arrays, or bright young pulsars like the Crab or the Vela pulsars. Except for the Vela pulsar, the other five target pulsars studied in this work have limited historical observational data in the literature. Moreover, early results often do not take into account the ionospheric RM, which introduces an additional systematic uncertainty in the RM measurement. For these five pulsars, their long-term variation in DM and RM is not significant compared to the measurement uncertainties, as summarised in [Table 5.3](#). The Vela pulsar, on the other hand, exhibits a significant long-term variation in its DM and RM, which was first reported over thirty years ago (e.g. [Hamilton et al., 1985](#)). The Vela pulsar is extremely bright, and strongly linearly polarised; thus, there are a lot of published polarimetric data available for comparison. Using the MWA data, the DM and RM were measured towards the Vela pulsar as a function of observing epoch, extending the baseline of measurements to nearly fifty years. Our results and analysis are presented in the following subsections.

Table 5.3: DM and RM measurements for target pulsars

Observing Epoch	DM (pc cm^{-3})	RM_{obs} (rad m^{-2})	Reference
PSR J0630–2834			
Sep 1979	34.36 ± 0.08	46.19 ± 0.09	Taylor & Cordes (1993)
Oct 1991		45.7 ± 0.5	van Ommen et al. (1997)
Dec 2000	34.47	46.6 ± 1.3	Han et al. (2006)
Nov 2005		46.53 ± 0.12	Johnston et al. (2005)
16 Feb 2008		45.4 ± 0.7	Han et al. (2018)
22 Feb 2016	34.37 ± 0.18	44.801 ± 0.023	This work
06 Dec 2016	34.36 ± 0.21	45.932 ± 0.012	This work
PSR J0737–3039A			
2003 to 2006	48.920 ± 0.005		Kramer et al. (2006)
Dec 2003		112.3 ± 1.5	Demorest et al. (2004)
Apr 2004		118.4 ± 0.3	Hotan et al. (2005)
22 Feb 2016	48.916 ± 0.007	120.03 ± 0.19	This work
06 Dec 2016	48.918 ± 0.004	120.575 ± 0.072	This work
PSR J0742–2822			
May 1986	73.77 ± 0.02	150.4 ± 0.05	Taylor & Cordes (1993)
Oct 1991		149.9 ± 0.5	van Ommen et al. (1997)
Aug 2006	73.8	156 ± 5	Han et al. (1999)
Nov 2005		149.95 ± 0.05	Johnston et al. (2005)
Aug 2006	73.78	148.5 ± 0.6	Noutsos et al. (2008)
22 Feb 2016	73.814 ± 0.049	149.474 ± 0.029	This work
06 Dec 2016	73.810 ± 0.028	150.178 ± 0.016	This work
PSR J0837–4135			
Jul 1987	147.6 ± 0.1	135.8 ± 0.3	Taylor & Cordes (1993)
Oct 1991		134 ± 2	van Ommen et al. (1997)

Table 5.3 Continued

Oct 2005	147.21±0.01	145±1	Johnston et al. (2007)
11 Feb 2016	147.217±0.218	145.616±0.045	This work
04 May 2017	147.217±0.219	146.21±0.11	This work
02 May 2019	147.217±0.219	146.12±0.12	This work
10 May 2019	147.232±0.173	146.151±0.068	This work
PSR J0959–4809			
Dec 2000	92.70	50±6	Han et al. (2006)
11 Feb 2016	92.375±0.195	39.39±0.23	This work

5.6.1 DM and RM variations towards the Vela pulsar

Based on observations of the Vela pulsar (PSR J0835–4510) between 1970 and 1984 using a 14-m dish at the University of Tasmania observatory, [Hamilton et al. \(1985\)](#) found that its DM significantly decreased from 69.1 to 68.2 pc cm⁻³, while its RM increased from 33.6 to 46.2 rad m⁻². Since then, multiple measurements of the Vela pulsar have been recorded in different publications, from different telescopes. [van Ommen et al. \(1997\)](#) carried out a polarimetric study of a set of southern pulsars at 950 MHz using the Parkes telescope and at 800 MHz using the Mt Pleasant 26-m telescope. According to their work, the RM for the Vela pulsar was 36.2 ± 1.2 rad m⁻² in January 1990, while in October 1991, it was 36.0 ± 0.5 rad m⁻². Unfortunately, they did not report the DMs of their target pulsars in the paper. [Johnston et al. \(2005\)](#) measured the RM for the Vela pulsar, 31.38 ± 0.01 rad m⁻², in November 2004, with no simultaneous DM measurement reported. [Sallmen et al. \(2006\)](#) monitored the Vela pulsar at 327 and 610 MHz without polarimetric information using the 25-m telescope in Green Bank Observatory. Their results indicate that the DM has decreased from 68.21 pc cm⁻³ in June 1995 to 68.05 pc cm⁻³ in September 1999. [Noutsos et al. \(2008\)](#) and [Han et al.](#)

(2018) both measured RMs for a large set of pulsars and used them to study the Galactic magnetic field. For the Vela pulsar, they both reported the DM to be 67.99 pc cm^{-3} , while the RM was $29.9 \pm 0.6 \text{ rad m}^{-2}$ on 06 August 2006 (Noutsos et al., 2008) and $30.4 \pm 0.6 \text{ rad m}^{-2}$ on 27 August 2006 (Han et al., 2018). Lenc et al. (2017) detected the Vela pulsar in a polarimetric image from the MWA (and therefore unable to measure the DM) and the RM was measured to be $37.3 \pm 0.1 \text{ rad m}^{-2}$ in November 2013.

Combining the measurements from the literature and those obtained in this work (see Table 5.2), I extended the long-term study of the DM and RM towards the Vela pulsar (Figure 5.22). For the data points that have both RM and DM recorded simultaneously, the (average) magnetic field component parallel to the line-of-sight, B_{\parallel} is estimated using Eq. 5.1.

From Figure 5.22, we can see that over fifty years, the DM of the Vela pulsar continuously decreases and is generally consistent with the conclusion of Hamilton et al. (1985), although the decrease is not uniform in time. However, the RM of the Vela pulsar behaves differently. It is no longer a monotonically increasing function with the observing epoch (Hamilton et al., 1985), but can be roughly considered as three segments of connected linear functions. Based on weighted least-squares linear fits, Hamilton et al. (1985) suggested the increasing rate for the first section (from 1970 to 1984) is $0.73 \text{ rad m}^{-2} \text{ yr}^{-1}$. Similarly, the rate of change in RM for the second section (from 1984 to 2006) and third section (from 2006 to 2019) are estimated to be $-0.67 \pm 0.16 \text{ rad m}^{-2} \text{ yr}^{-1}$ and $1.08 \pm 0.05 \text{ rad m}^{-2} \text{ yr}^{-1}$, respectively.

In order to explain the decreasing DM and increasing RM from 1970 to 1984, Hamilton et al. (1985) suggested that the observed DM and RM (DM_{total} , RM_{total}) are the summation of the contribution of the diffuse environmental ISM (DM_{diffuse} , RM_{diffuse}) and a plasma wedge with excess electron density (DM_{wedge} , RM_{wedge}). Since the diffuse ISM contribution is expected to be relatively stable over long timescales, the decrease in DM_{total} indicates a decrease in DM_{wedge} due to the

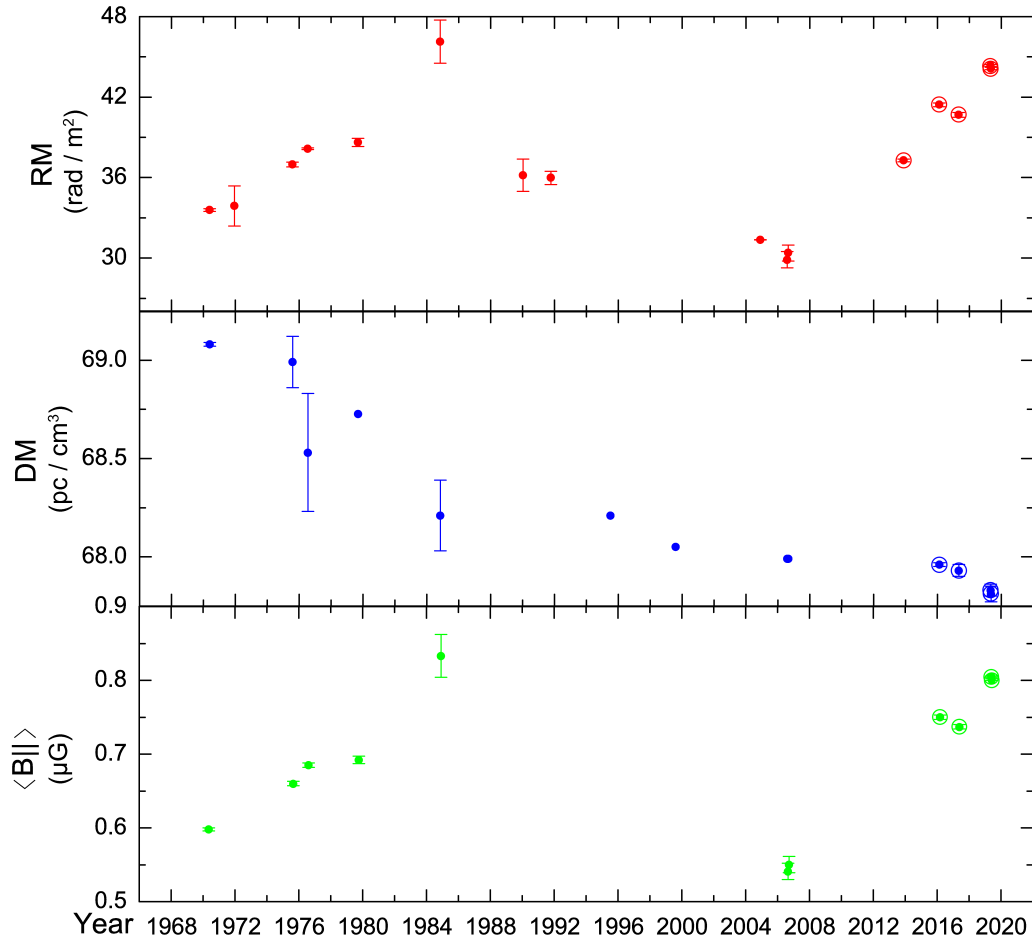


Figure 5.22: The long-term variation of the RM, DM and inferred $\langle B_{\parallel} \rangle$ for the Vela pulsar from 1970 to 2019. The top and middle panels present the RMs and DMs, respectively, for the Vela pulsar observed at different epochs from the literature (Hamilton et al., 1985; van Ommen et al., 1997; Johnston et al., 2005; Sallmen et al., 2006; Noutsos et al., 2008; Han et al., 2018; Lenc et al., 2017) together with values obtained from this work using the MWA (which are highlighted using open circles). For those data points that have both RM and DM recorded, the average magnetic field parallel to the line-of-sight, B_{\parallel} , is estimated using Eq. 5.1, and is shown in the bottom panel.

relative motion between the pulsar and the plasma wedge. The increase in the observed RM (RM_{total}) is caused by the decreasing negative contribution of this plasma wedge (RM_{wedge}), which implies the parallel component of the magnetic field of the plasma wedge ($B_{\parallel}^{\text{wedge}}$) is directed towards the pulsar, opposite to the mean interstellar magnetic field in this direction ($B_{\parallel}^{\text{diffuse}}$). Schematic plots describing this model are shown in Figure 5.23.

According to this theory, the parallel component of the magnetic field in this plasma wedge can be estimated using

$$B_{\parallel}^{\text{wedge}} = 1.23 \left(\frac{d\text{RM}}{dt} \right) \left(\frac{d\text{DM}}{dt} \right)^{-1}, \quad (5.3)$$

where DM is measured in units of pc cm^{-3} , RM is in rad m^{-2} , and B_{\parallel} is in μG . Hamilton et al. (1985) obtained $d\text{RM}/dt = 0.73 \text{ rad m}^{-2} \text{ yr}^{-1}$, $d\text{DM}/dt = 0.040 \text{ pc cm}^{-3} \text{ yr}^{-1}$, and therefore $B_{\parallel} = 22 \mu\text{G}$.

Applying this method using the more recent data, in the third section (from 2006 to 2019), $d\text{RM}/dt = 1.08 \pm 0.05 \text{ rad m}^{-2} \text{ yr}^{-1}$, $d\text{DM}/dt = 0.012 \pm 0.003 \text{ pc cm}^{-3} \text{ yr}^{-1}$, giving $B_{\parallel}^{\text{wedge}} = 90 \mu\text{G}$. If one only considers data points obtained using the MWA (from 2013 to 2019), $d\text{RM}/dt = 0.98 \pm 0.47 \text{ rad m}^{-2} \text{ yr}^{-1}$, $d\text{DM}/dt = 0.049 \pm 0.007 \text{ pc cm}^{-3} \text{ yr}^{-1}$, and therefore $B_{\parallel}^{\text{wedge}} = 20 \mu\text{G}$.

Calculating $B_{\parallel}^{\text{wedge}}$ using Eq.(5.3) assumes that the RM and DM variations have a strong linear correlation, which implies that the magnetic field is uniform along the plasma wedge. However, it seems less likely that this is the case, as the RMs obtained from observations taken between 1984 and 2019 no longer follow the monotonically increasing trend. The RM decreases from 1984 to 2006 and starts to increase again in 2006, while the DM decreased consistently over the past fifty years. An alternative explanation is that the variation in observed RM is caused by the inhomogeneously distributed magnetic field in the plasma wedge. In this case, the increasing/decreasing trend in Vela's RM requires a change in magnetic field strength but does not necessarily require the magnetic field to change direction. This plasma wedge may be part of the Vela SNR, and the inhomogeneous magnetic field is associated with the filamentary structure of

the SNR (Sushch et al., 2011). This model does not tell us whether $B_{\parallel}^{\text{wedge}}$ is in the same direction as $B_{\parallel}^{\text{total}}$ or not. Since the observed $\langle B_{\parallel}^{\text{total}} \rangle$ (averaged along the entire path) is relatively weak (0.55 to 0.85 μG) compared to other pulsars studied in this work and the local Galactic magnetic field strength ($\sim 2 \mu\text{G}$; e.g. Beck, 2001; Han et al., 2006), it is possible that the $B_{\parallel}^{\text{wedge}}$ has an opposite direction to $B_{\parallel}^{\text{total}}$, as proposed by Hamilton et al. (1985). In this case, a large RM contribution ($> 46 \text{ rad m}^{-2}$) from the intervening ISM is required. Since the Vela pulsar is only $287_{-17}^{+19} \text{ pc}$ away (Dodson et al., 2003), it is quite unusual to accumulate such an RM if only considering the nearby diffuse Galactic ISM. Therefore, in this case, the $\text{RM}_{\text{diffuse}}$ is likely caused by contributions from the ISM and the Gum Nebula interior. Schematic plots describing this model can be found in Figure 5.24. Nevertheless, it is also possible that $B_{\parallel}^{\text{wedge}}$ and $B_{\parallel}^{\text{diffuse}}$ are both pointing towards the observer (as shown in Figure 5.25).

5.6.2 Scatter broadening measurements for the Vela pulsar

The pulses from the Vela pulsar undergo prominent pulse broadening caused by multi-path scattering at MWA frequencies. Figure 5.26 presents total intensity profiles for the Vela pulsar using the entire 30.72 MHz MWA bandwidth centred at 184.96 MHz obtained from three different observing sessions. These three profiles exhibit significantly different pulse broadening that can be clearly recognised by eye. In all cases, the scattering tail extends beyond a single pulse period, which renders the off-pulse baseline undetectable. Therefore, it is difficult to precisely measure the scattering time scale τ_{sc} . A rough estimate of τ_{sc} can be achieved by using the minimum value along the profile as the baseline and calculating the time it takes for the signal to drop to $1/e$ of the peak value. This estimation results in $\tau_{sc} = 43.63 \text{ ms}$ (for obs 1139239952 on 11 Feb 2016), $\tau_{sc} = 42.59 \text{ ms}$ (for obs 1177938016 on 04 May 2017), and $\tau_{sc} = 30.59 \text{ ms}$ (for obs 1240826896 on 02 May 2019). Thus, τ_{sc} has apparently changed $\sim 13 \text{ ms}$ at 184.96 MHz over three

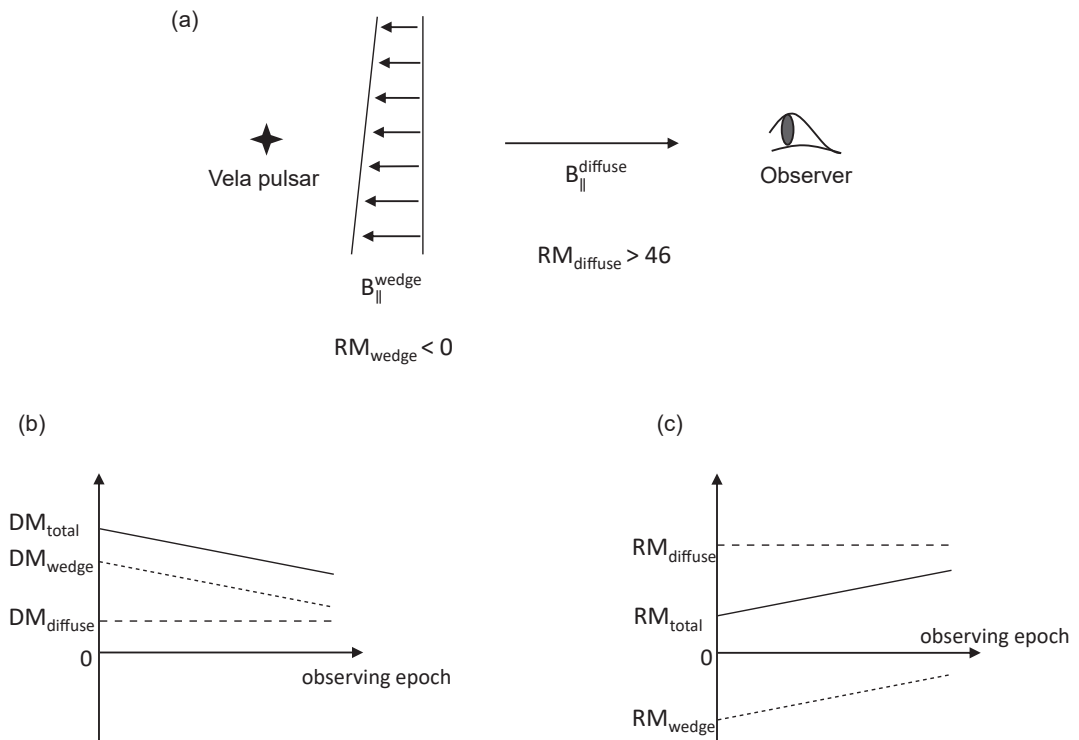


Figure 5.23: (a) A schematic plot to explain the observed DM and RM variation for the Vela pulsar suggested by [Hamilton et al. \(1985\)](#); (b) The trend (not to scale) of the observed total DM (DM_{total}): DM contributed by the plasma wedge (DM_{wedge}), and DM contributed by the diffuse environmental ISM (DM_{diffuse}) according to the model shown in panel (a), where $DM_{\text{total}} = DM_{\text{wedge}} + DM_{\text{diffuse}}$; (c) The same as panel (b), but for the RM.

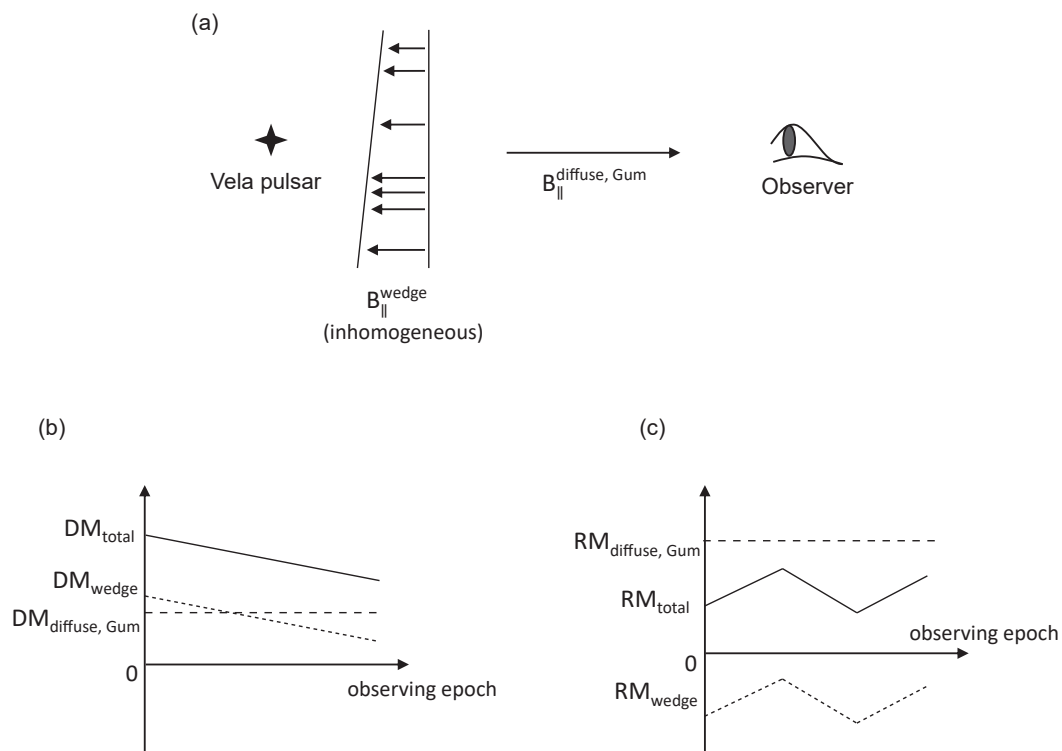


Figure 5.24: (a) A schematic plot to explain the observed DM and RM variation for the Vela pulsar with an inhomogeneously distributed $B_{\parallel}^{\text{wedge}}$ whose direction is opposite to the $B_{\parallel}^{\text{diffuse, Gum}}$; (b) and (c) are the same as in Figure 5.23, but adjusted for this scenario.

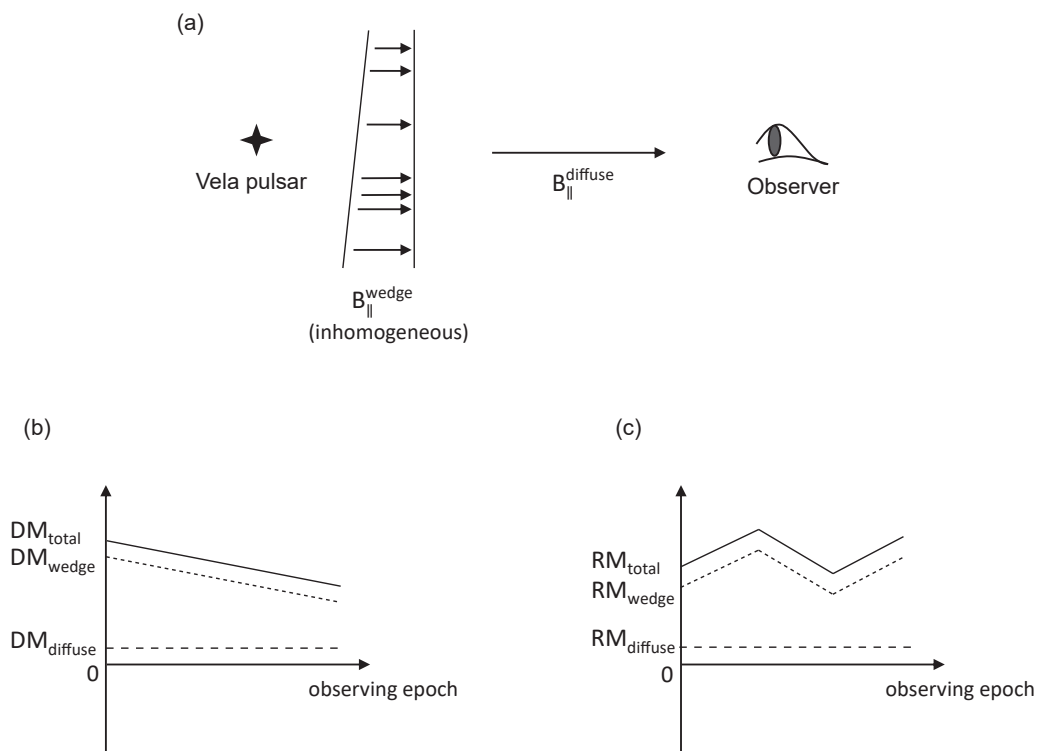


Figure 5.25: (a) A schematic plot to explain the observed DM and RM variation for the Vela pulsar with an inhomogeneously distributed $B_{\parallel}^{\text{wedge}}$ whose direction is the same with the $B_{\parallel}^{\text{diffuse}}$; (b) and (c) are the same as in Figure 5.23, but adjusted for this scenario.

years.

Note that this is only a first-order rough estimation, since we do not know how much the minimum value is offset above the actual off-pulse baseline. Consider the pulse peak at phase t_0 , which drops to $1/e$ of the peak value at phase t_1 (using the minimum value in the profile as the baseline). Denoting the total intensity $I(t_0) = p$, then $I(t_1) = p/e$, and assuming the minimum value in the profile exceeds the actual off-pulse baseline by x , the actual ratio between $I(t_0)$ and $I(t_1)$ is

$$\frac{I(t_1)}{I(t_0)} = \frac{p/e + x}{p + x} = \frac{1}{e} \cdot \frac{p + ex}{p + x} > \frac{1}{e}. \quad (5.4)$$

Consequently, at phase t_1 , the pulse amplitude has actually not yet dropped to $1/e$ of the peak value. Therefore, this process underestimates τ_{sc} to some extent, depending on the level of x . A larger τ_{sc} will result in a greater x , and thus a more strongly underestimated τ_{sc} . Ergo, the actual difference between τ_{sc} obtained from the three observing epochs is even larger than the estimated ~ 13 ms.

Using an MWA observation taken on 31 Oct 2014, and fitting the profile using a thin screen model, [Kirsten et al. \(2019\)](#) obtained a $\tau_{sc} = 14.1$ ms for the Vela pulsar at 256.64 MHz, and $\tau_{sc} = 31.2$ ms at 210.56 MHz. Scaling these numbers to 184.96 MHz with the measured scattering index $\alpha = -4.0 \pm 1.5$ results in $\tau_{sc} = 52.3$ ms. This is consistent with our estimate being a lower-limit due to the scattering tail being wrapped.

The significant τ_{sc} variation between different observing epochs indicates that there is a substantial variation in the distribution of the material in the scattering disk. It is likely that the material causing the scattering of the Vela pulsar's signal is also the dense plasma wedge that causes the long-term variation of the DM and RM. This turbulent material can consist of small-scale stochastic magnetic fields, which can cause a change in the observed RM, as well as depolarise electromagnetic signals, as presented in the previous subsection.

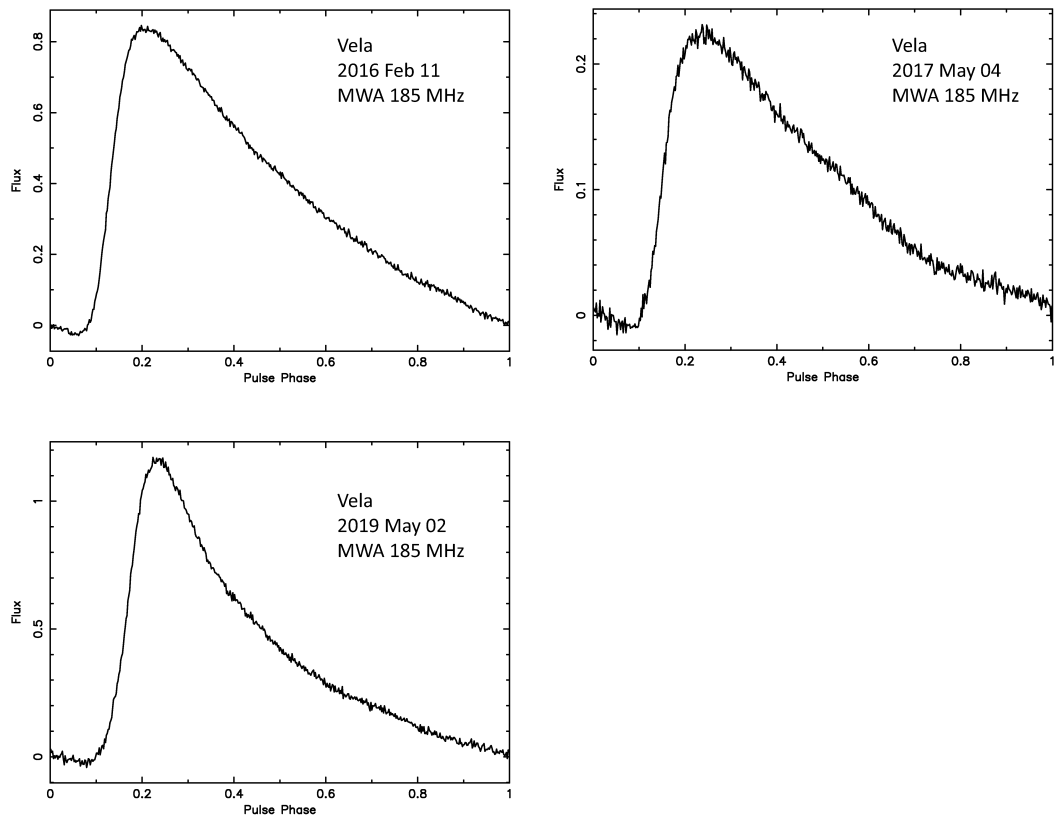


Figure 5.26: Vela pulsar’s total intensity pulse profiles using the entire 30.72 MHz MWA bandwidth centred at 185 MHz obtained from three different epochs. Significant differences in the scattering time scale (shape of exponential scattering tail) can be seen.

5.7 Discussion

Based on different ISM tracers, there have been multiple estimations of the size of the Gum Nebula. Here, we discuss how the pulsar measurements from this work can help restrict the Gum Nebula model. PSR J0630–2834, with Galactic coordinates $(l, b) = (236.95^\circ, -16.76^\circ)$, is 28° away from the centre of the Gum Nebula according to the NE2001 model, and 30° away according to the YMW16 model. The signal from PSR J0630–2834 is thought to be unaffected by the Gum Nebula. From the $H\alpha$ emission map (Finkbeiner, 2003), the pulsar indeed seems to be outside the range of the Gum Nebula. However, although this pulsar do not present significant scattering broadening directly on its pulse profile, as what has been analysed in Section 5.5.5, its linearly polarised emission undergoes depolarisation which indicate the existence of scattering effect.

It is noteworthy that for PSR J0630–2834, there is a significant discrepancy between the VLBI annual parallax distance (320_{-40}^{+52} pc; Deller et al., 2009) and the distance inferred from its DM using either the NE2001 model (1.45 kpc) or the YMW16 model (2.07 kpc). Therefore, between PSR J0630–2834 and us, there should be an excess of electrons that is not taken into account in either electron density model. Either the Gum Nebula is more extensive than modeled, or, there are additional unmodeled ISM structures along the line-of-sight. This structure does not show strong $H\alpha$ emission, but still causes significant propagation effects to the signals traversing through it. Considering the Gum Nebula model suggested by Purcell et al. (2015), which adopts an angular radius of 22.7° , PSR J0630–2834 lies 23.4° away from the nebula centre, and close to the edge of the nebula.

For the Vela pulsar, it is also worth discussing whether the Gum Nebula contributes to the observed propagation effects or not. The ISM structure along the line-of-sight toward the Vela pulsar is quite complex. The Vela pulsar ($l = 263.55^\circ, b = -2.79^\circ$) lies 4° away from the centre of the Gum Nebula (according to the NE2001 model), and 1.1° away (according to the YMW16 model). The

parallax distance, 287_{-17}^{+19} pc (Dodson et al., 2003), places it in the foreground of the Gum Nebula, according to the model of Woermann et al. (2001), the NE2001 model and YMW16 model. In this case, the observed propagation effects are caused by the Vela supernova remnant (which does not have independent distance measurement but usually thought to be associated with the Vela pulsar) and the diffuse Galactic environmental ISM, without any contribution from the Gum Nebula. The Gum Nebula model advanced by Purcell et al. (2015) suggests that the Vela pulsar would be located just inside the front edge of the nebula. Based on the VLBI measurements of the scintillation pattern, Desai et al. (1992) suggest the fractional distance to the scattering screen, $d_s/D = 0.81 \pm 0.03$, where d_s represents the distance between the scattering screen and the observer, D represents the distance from the observer to the pulsar, assuming a single thin screen model. Popov et al. (2019) obtained similar results, suggesting that d_s/D is between 0.79 to 0.87. This suggests that the distance from the scattering screen to the pulsar is between 37–60 pc, which is significantly larger than the radius of the Vela SNR (20 pc; Bocchino et al., 1994). Therefore, since the scatter screen for Vela should be further away from the pulsar than the SNR size according to these scintillation studies, there must be some other ISM components that also contribute to the scattering effect we observed, and the front edge of the Gum Nebula is a very likely contributor. Desai et al. (1992) argues that when considering an extra contribution from the scattering material from the Gum Nebula, the scattering screen would necessarily be closer to the pulsar, thus more consistent with the measurement of the SNR radius. Therefore, it is likely that the Gum Nebula and the Vela SNR both contribute to the scattering of the Vela pulsar’s signal. This can also help explain the long-term DM/RM variation trend for the Vela pulsar and why the depolarisation factor $\exp(-2\lambda^4\delta\text{RM}^2)$ does not provide as nice a fit for the Vela pulsar as for the other pulsars (PSRs J0630–2834 and J0742–2822).

Overall, considering the depolarisation of four target pulsars (PSRs J0630–

2834, J0742-2822, J0835-4510, J0837-4135), the distance discrepancy for PSR J0630-2834, and the propagation effects measured towards the Vela pulsar, a larger Gum Nebula, e.g. as proposed by [Purcell et al. \(2015\)](#), is preferred.

5.8 Conclusion

In this Chapter, polarimetric studies for six pulsars towards the general direction of the Gum Nebula were conducted using the MWA. The DMs, RMs and polarimetric profiles were obtained. For the four pulsars whose degree of linear polarisation were obtained at sufficient multi-frequency bands (including at high radio frequencies from the literature), depolarisation at frequencies below 300 MHz (δRM between $0.111 - 0.334 \text{ rad m}^{-2}$) are observed which further confirmed the results in [Xue et al. \(2019\)](#) (Chapter 4). For PSRs J0742-2822, and J0835-4510, I further investigate this rapid depolarisation towards low frequencies and suggest that the behaviour is consistent with that expected from a foreground scattering screen with spatially varying Faraday rotation. In these cases, this screen is likely to be located in the Gum Nebula and/or the Vela SNR, respectively. In the future, measurements for more pulsar samples in this general direction together with their independent distance (e.g. from annual parallax) can provide valuable constraints to better model the Gum Nebula (in three-dimensions), an important component of the electron density model of the Galaxy.

For the Vela pulsar, using the MWA data and other literature values, the DM and RM are measured as a function of observing epoch over nearly fifty years. The DM shows a monotonic decreasing trend from 69.1 to 67.8 pc cm^{-3} in the past fifty years; while the RM first increased from 33.6 to 46.2 rad m^{-2} (1975 – 1984), then dropped to a low of 29.9 rad m^{-2} in 2006, and started to increase again, reaching 44.4 rad m^{-2} in 2019. The pulse profiles for the Vela pulsar obtained from three different MWA observing sessions also exhibit significantly different scatter broadening properties. These results suggest there is a plasma wedge with a varying degree of turbulence, and an inhomogeneously distributed

magnetic field that lies between the observer and the Vela pulsar. It is likely that the signal from the Vela pulsar (whose parallax distance is much smaller than generally considered in the literature, which makes it places the front edge of the Gum Nebula) propagates through ionised material in both the Vela SNR and the Gum Nebula.

In the future, monitoring more pulsars to obtain (low-frequency) polarimetric profiles and to measure the ISM propagation effects using more sensitive radio telescopes (such as the GMRT) may enable a more systematic study and a more detailed model of the turbulent magneto-ionic gas in the Gum Nebula region. In Chapter 6, the future prospects of this work will be discussed in more detail. Further investigation of the variability in DM and/or RM for nearby pulsars towards the Gum Nebula region will provide useful insights into the small-scale properties of the ISM individually and may present the possibility to disentangle the properties of the Gum Nebula and the Vela SNR environments. Studying this effect for bright millisecond pulsars that are monitored as part of the International Pulsar Timing Array also presents the prospect of improving the pulsar timing precision for higher frequency timing observations.

Chapter 6

Summary and future prospects

The ISM propagation effects (e.g. dispersion, Faraday rotation, and scattering) on pulsar signals are strongly frequency dependent and are more pronounced at low radio frequencies. This makes low-frequency pulsar observations ideal for the determination of ISM properties. In this thesis, I studied the small-scale structure of the local ISM using low-frequency polarimetric observations of pulsars obtained using the MWA. In particular, my analysis has led to new insights pertaining to the plasma distribution, turbulence and the magnetic field strength in the direction of the Gum Nebula and its vicinity.

The MWA, initially designed as an imaging interferometer, was not capable of providing high time resolution data products in its original standard observing mode. High time resolution pulsar science with the MWA was realised in a non-traditional way, by adding the Voltage Capture System (VCS) in the signal path in 2014. This allowed us to record raw voltage data from each of the 128 MWA tiles, but with an aggregate a huge data rate of 28 TB per hour. These data can then be reduced in different ways (e.g. incoherent summation; coherent beamforming or tied-array processing; and off-line correlation), thereby providing users with maximum flexibility. However, the various types of data products required custom-built software tools to process them, which were under development at the time the work for this thesis commenced. Therefore, part of this thesis involved

the development and testing of some aspects of the pulsar processing pipeline of the MWA-VCS, particularly the verification of its polarimetric performance.

I first carried out an initial pulsar census with incoherently summed MWA-VCS data (Chapter 3; [Xue et al., 2017](#)). The incoherent summation preserves the large field-of-view provided by the MWA, allowing multiple pulsars to be observed simultaneously and thus facilitating an expedited initial pulsar census without a huge demand of computational resources. However, this provides only a modest sensitivity, nominally $\sim 10\%$ of that achievable with the MWA using tied-array beams. This census involved the processing of 37 hours of MWA-VCS archival data (~ 1 PB), which covers $\sim 17,000$ deg² of sky, taken from the first two years of the MWA-VCS operation (2014 – 2016). This initial census resulted in the successful detection of 50 pulsars, including six millisecond pulsars and two in binary systems. Combining the MWA detections with published data from other telescopes, multi-frequency pulse profiles were presented for a subset of the detected pulsars. The results of this census were then used to improve pulsar population models for our Galaxy and to provide further insights into pulsar detection prospects for the SKA1-Low. A conservative forecast is that a survey using SKA1-Low can potentially detect ~ 9400 pulsars, which is more than triple the number of pulsars known to date.

Verifying the polarimetric performance of the new software beamformer was an important prerequisite before putting it into science applications. Using observations of two bright southern pulsars, PSRs J0742–2822 and J1752–2806, I conducted a detailed, empirical characterisation of the polarimetric performance of the MWA’s tied-array processing pipeline (Chapter 4; [Xue et al., 2019](#)). The results demonstrate that the MWA can be reliably calibrated for pulsar polarimetric applications at zenith angles $\lesssim 45^\circ$ and frequencies $\lesssim 270$ MHz. This exercise also revealed useful insights into optimal calibration strategies, which will inform the design of the real-time beamformer planned for future MWA upgrades. This GPU-based, real-time beamformer will potentially provide flexible

sub-arraying and the ability to form multiple beams at a time, greatly reducing the data transfer, storage, and processing workload for pulsar studies using the MWA. This verification exercise with the MWA thus helped to define the parameter space within which reliable pulsar polarimetry is feasible, notwithstanding the inherent complexity of calibrating aperture-array telescopes. It also brings in a great deal of experience and confidence on polarimetric studies of pulsars using future facilities such as SKA1-Low, which is expected to have a more complex beam response.

The empirical verification of the polarimetric response of the MWA tied-array mode using PSRs J0742–2822 and J1752–2806 also led to the first low-frequency polarimetric studies of these two southern pulsars, as well as high-precision determinations of their Faraday rotation measurements. Moreover, the degree of linear polarisation of PSR J0742–2822 showed a steady (and rapid) decline at the lower frequencies of the MWA. This stands in contrast with the generally expected trend for pulsar emission, and can be attributed to depolarisation caused by stochastic Faraday rotation from turbulent ISM in the Gum Nebula. This was followed by detailed polarimetric studies of six pulsars towards the general direction of the Gum Nebula to further investigate this intriguing effect (Chapter 5). Depolarisation at low-frequencies were observed for four pulsars whose degree of linear polarisation was measured in a sufficient number of frequency bands, which further confirmed that the Gum Nebula contains turbulent plasma that generates the stochastic Faraday rotation. A particular focus was given to the Vela pulsar, in light of the variation of DM and RM seen with the observing epoch over a time span of nearly fifty years. In addition, the scatter broadening properties of the Vela pulsar also show significant variation between different observing epochs. Our results suggest that there is likely a plasma wedge with a varying degree of turbulence, and an inhomogeneously distributed magnetic field in the line of sight toward the Vela pulsar.

Monitoring the dispersion, Faraday rotation, and scattering of the Vela pul-

sar can potentially be conducted with the verification arrays of the SKA-Low located at the Murchison Radio-astronomy Observatory, e.g. the Engineering Development Array (EDA, a 35-m SKA-Low station equivalent built out of MWA dipole elements; [Wayth et al., 2017](#)), and the Aperture Array Verification System¹ (AAVS, an SKA-Low station built out of the second revision antennas under consideration for the SKA-Low). Such an exercise can help characterise the polarimetric response of the EDA and the AAVS. Once the performance of these arrays are verified, they can potentially be used for high-precision, long-term monitoring of ISM propagation effects toward the Vela pulsar (and/or other southern pulsars whose DMs/RMs vary with time).

In the future, the work in Chapter 5 can be extended into a more systematic study to develop a more detailed model of the turbulent magneto-ionic gas in the Gum Nebula, using low-frequency polarimetric measurements of a larger sample of pulsars in (or near) the direction of the nebula. In order to ensure a large sample of pulsars that can contribute to such a study, high sensitivity radio telescopes such as the upgraded GMRT (uGMRT) can also be employed to observe pulsars with relatively modest flux densities.

Plans are also underway to carry out a low-frequency, full polarimetric census of the Southern pulsars using the MWA. The pulsar processing pipeline of the MWA has undergone several advancements since the initial pulsar census was conducted. The software beamformer has matured, with more computationally efficient algorithms, and is now routinely used. Forming a tied-array beam now takes ~ 1.5 times real observation time, which is roughly five times faster compared to the nominal execution times in 2017. Moreover, a multi-pixel software beamformer for the MWA tied-array processing is currently under development, and will potentially improve the beamforming efficiency by another factor of four to five. These improvements make it possible for us to embark on a full pulsar census with the MWA to obtain high fidelity polarimetric pulse profiles for a large

¹www.mwatelescope.org/telescope/external/aavs

sample of pulsars in the Southern sky. Such a collection of low-frequency profiles, together with those published profiles at higher frequencies, can be used to develop a more complete picture of how pulsar polarimetric profiles evolve with the observing frequency. This will greatly improve our understanding of the pulsar emission mechanism, beam geometry, and magnetospheric properties. It will also provide high-precision measurements of DMs and RMs for a large sample of Southern pulsars. Furthermore, similar high-precision measurements of DMs and RMs using advanced low-frequency instruments equipped with a large instantaneous frequency coverage (and the ability to deal with massive data volumes) such as the new Ultra-Wideband Low (UWL) receiver at Parkes (700 MHz to 4 GHz; [Hobbs et al., 2019b](#)) in the Southern Hemisphere, as well as LOFAR, LWA, and the Canadian Hydrogen Intensity Mapping Experiment (CHIME; [Bandura et al., 2014](#)) in the Northern Hemisphere, will provide useful information that will help refine the models for the Galactic electron density distribution and magnetic field.

Appendices

Appendix A

Statement of Originality

This section is to comply with the requirement that all co-authors of work included in this thesis outline their contributions. In communicating this statement to the co-authors, they were also informed that the lack of a response would be taken as unconditional tacit approval. Otherwise, all co-authors have read and agreed to the following statement, and their responses can be found afterward.

A.1 Statement of contribution for Chapter 3











In Chapter 3, we present the results of an initial time-resolved census of known pulsars using the MWA. This work was published by:

Xue, M., Bhat, N. D. R., Tremblay, S. E., Ord, S. M., Sobey, C., Swainston, N. A., Kaplan, D. L., Johnston, Simon, Meyers, B. W., McSweeney, S. J., “A Census of Southern Pulsars at 185 MHz”, 2017, Publications of the Astronomical Society of Australia, Volume 34, id.e070 14 pp.

The idea of doing an initial census of southern pulsars with the incoherently summed MWA-VCS archival data was proposed by Dr. Ramesh Bhat, Dr. Steven Tremblay, and Dr. Stephen Ord. Nine hours MWA archival data from the MWA FRB searching project were processed by Dr. Steven Tremblay. The other twenty-eight hours MWA data were reduced and analysed by myself

under the supervision of Dr. Ramesh Bhat, Dr. Steven Tremblay, Dr. Stephen Ord and Dr. Charlotte Sobey. Nicholas Swainston developed the software to generate a list of known pulsars covered in the primary beam of a given observation, and this was integrated into the pulsar processing pipeline. Dr. Simon Johnston provided high-frequency pulse profiles for 16 pulsars observed by the Parkes and GMRT telescopes for multi-frequency comparison studies. A/Prof. David Kaplan provided useful guidance on estimating the system sensitivity ($A_{\text{eff}}/T_{\text{sys}}$) for the MWA primary beam when pointing to different directions. I prepared the manuscript and Dr. Ramesh Bhat, Dr. Steven Tremblay, Dr. Stephen Ord and Dr. Charlotte Sobey aided in the writing process by providing guidance in terms of the structure and contextual discussion as well as improving the English and the clarity of presentation, both before and after referee comments were received. Bradley Meyers and Samuel McSweeney also helped with improving the language and stylistic aspects of the presentation.

1. Chapter 3. Paper "A Census of Southern Pulsars at 185 MHz", Publications of the Astronomical Society of Australia, 2017, Volume 34, id.e070 14 pp

	Conception and design	Data acquisition	Data processing & analysis	Model calculation	interpretation & discussion	Manuscript writing, revision and finalisation
Ms. Mengyao Xue	x	x	x	x	x	x
	I acknowledge that these represent my contribution to the above result output. Signed. 					
Dr. Ramesh Bhat	x	x	x	x	x	x
	I acknowledge that these represent my contribution to the above result output. Signed. 					
Dr. Steven Tremblay	x	x	x	x	x	x
	I acknowledge that these represent my contribution to the above result output. Signed. 					
Dr. Stephen Ord	x	x		x	x	x
	I acknowledge that these represent my contribution to the above result output. Signed. 					
Dr. Charlotte Sobey			x	x	x	x
	I acknowledge that these represent my contribution to the above result output. Signed. 					
Mr. Nicholas Swainston			x		x	
	I acknowledge that these represent my contribution to the above result output. Signed. 					
Dr. David Kaplan				x	x	
	I acknowledge that these represent my contribution to the above result output. Signed. 					
Dr. Simon Johnston		x			x	
	I acknowledge that these represent my contribution to the above result output. Signed. 					
Dr. Bradley Meyers					x	x
	I acknowledge that these represent my contribution to the above result output. Signed. 					
Dr. Samuel McSwency					x	x
	I acknowledge that these represent my contribution to the above result output. Signed. 					

Below are the co-authors' response to this statement of contribution:

Ramesh Bhat <rameshbhatnd@gmail.com>

Agreed.

Stephen Ord <Stephen.Ord@csiro.au>

Hi,

Agreed.

S.

Steven Tremblay <Steven.Tremblay@curtin.edu.au>

Hi Mengyao,

I fully agree with this statement of originality.

Dr. Steven Tremblay

Charlotte Sobey <Charlotte.Sobey@csiro.au>

Hi Mengyao,

That looks fine to me!

See you tomorrow at the pulsar meeting!

Many thanks and best wishes,

Charlotte

Nicholas Swainston <nickaswainston@gmail.com>

Agreed

David Kaplan <kaplan@uwm.edu>

I approve.

Simon Johnston <Simon.Johnston@csiro.au>

Fine with me.

Simon

Bradley Meyers <bradley.meyers@postgrad.curtin.edu.au>

Hi Mengyao,

Forgive me, but I thought you had already send this around on 20 August?

Regardless of that, I confirm that my contribution to this work is consistent with your statement of originality.

Regards,

Bradley Meyers

Samuel McSweeney <sammy.mcsweeney@gmail.com>

Agreed!









A.2 Statement of contribution for Chapter 4

In Chapter 4, we present a verification of the MWA’s pulsar polarimetry capability, using two bright southern pulsars, PSRs J0742–2822 and J1752–2806. This work was published by:

Xue, M., S. E., Ord, Tremblay, S. M., Bhat, N. D. R., Sobey, C., Meyers, B. W., McSweeney, S. J., Swainston, N. A., “MWA Tied-Array Processing II: Polarimetric Verification and Analysis of two Bright Southern Pulsars”, 2019, Publications of the Astronomical Society of Australia, Volume 36, id.e025

The idea of doing polarimetric verification of the MWA tied-array mode and the polarimetric studies of two bright southern pulsars was proposed by Dr. Stephen Ord, Dr. Ramesh Bhat, and Dr. Steven Tremblay. Except for the MWA observation of PSR J1752-2806 at 118 MHz with a 30 MHz contiguous frequency coverage, which was processed by Nicholas Swainston, all other data were processed and analysed by myself, under the supervision of Dr. Ramesh Bhat, Dr. Steven Tremblay, Dr. Stephen Ord and Dr. Charlotte Sobey. Dr. Charlotte Sobey helped with the calculation of the ionospheric Faraday rotation measure. I wrote the first draft of the paper, while Dr. Ramesh Bhat, Dr. Steven Tremblay, Dr. Stephen Ord and Dr. Charlotte Sobey aided in the further revisions of the paper by providing guidance in terms of the structure and contextual discussion as well as improving the English and the clarity of presentation, both before and after the referee comments were received. Bradley Meyers and Samuel McSweeney also helped with improving the language and stylistic aspects of the presentation.

2. Chapter 4. Paper "MWA Tied-Array Processing II: Polarimetric Verification and Analysis of two Bright Southern Pulsars" Publications of the Astronomical Society of Australia, 2019, Volume 36, id.e025

	Conception and design	Data acquisition	Data processing & analysis	Model calculation	interpretation & discussion	Manuscript writing, revision and finalisation
Ms. Mengyao Xue	x	x	x	x	x	x
	I acknowledge that these represent my contribution to the above result output. Signed. 					
Dr. Stephen Ord	x	x		x	x	x
	I acknowledge that these represent my contribution to the above result output. Signed. 					
Dr. Steven Tremblay	x	x	x	x	x	
	I acknowledge that these represent my contribution to the above result output. Signed. 					
Dr. Ramesh Bhat	x	x	x	x	x	x
	I acknowledge that these represent my contribution to the above result output. Signed. 					
Dr. Charlotte Sobey		x	x	x	x	x
	I acknowledge that these represent my contribution to the above result output. Signed. 					
Dr. Bradley Meyers					x	x
	I acknowledge that these represent my contribution to the above result output. Signed. 					
Dr. Samuel McSweeney					x	x
	I acknowledge that these represent my contribution to the above result output. Signed. 					
Mr. Nicholas Swainston		x			x	
	I acknowledge that these represent my contribution to the above result output. Signed. 					

Below are the co-authors' response to this statement of contribution:

Stephen Ord <Stephen.Ord@csiro.au>

Hiya

I agree to the statement of originality.

Best,

Steve

Steven Tremblay <Steven.Tremblay@curtin.edu.au>

Hi Mengyao,

I fully agree with this statement of originality.

Dr. Steven Tremblay

Ramesh Bhat <rameshbhatnd@gmail.com>

Yes, I agree.

Cheers

Ramesh

Bradley Meyers <bradley.meyers@postgrad.curtin.edu.au>

Hi Mengyao,

I agree that the written statement of originality accurately represents my contribution to this work.

Cheers,

Bradley Meyers

Samuel McSweeney <sammy.mcsweeney@gmail.com>

Agreed!

Nicholas Swainston <nickaswainston@gmail.com>

I agree.

Cheers,

Nick

Appendix B

Copyright permission

Chapters 3 and 4 were both published in Publications of the Astronomical Society of Australia (PASA) and below are the permissions licence from the publisher, approving me to include these two journal articles in my PhD thesis.



CAMBRIDGE
UNIVERSITY PRESS

Mengyao Xue
PHD Candidate
Curtin University
1 Turner Avenue
Bentley WA 6102

Australia & New Zealand
477 Williamstown Road
Port Melbourne
Victoria 3207
Australia

Correspondence
Private Bag 31
Port Melbourne
Victoria 3207
Australia

Friday, 02 August 2019

www.cambridge.edu.au

Telephone +61 (03) 8671 1400

Fax +61 (03) 9676 9966

Email info@cambridge.edu.au

ABN 28 508 204 178

Dear Mengyao,

Xue, M., Bhat, N. D. R., Tremblay, S. E., Ord, S. M., Sobey, C., Swainston, N. A., Kaplan, D. L., Johnston, S., Meyers, B. W., McSweeney, S. J., '*A Census of Southern Pulsars at 185 MHz*', Publications of the Astronomical Society of Australia, Cambridge University Press, (2017) Vol 34, e070.

Xue, M., Ord, S. M., Bhat, N. D. R., Sobey, C., Meyers, B. W., McSweeney, S. J., Swainston, N. A., '*MWA tied-array processing II: Polarimetric verification and analysis of two bright southern pulsars*', Publications of the Astronomical Society of Australia, Cambridge University Press, (2019), Vol 36, e025.

Thank you for notification dated 30 July 2019, in which you requested permission to include the above two journal articles in your PhD thesis for Curtin University. You are the first author of the journal articles and your intention is to reuse the content in your PhD. Your PhD will subsequently be placed in Curtin University's repository.

Non-Exclusive Permission is granted subject to the following conditions:

1. The integrity of the material must be assured.
2. That you have checked that the passage(s) in question do(es) not acknowledge any other source(s).

Cambridge gives no warranty or indemnity in respect of any third party copyright material in the article/chapter and the licensee must seek their own permission clearance.

3. Full acknowledgement of the source should be given (author, title, Cambridge University Press, year of publication) together with the appropriate copyright notice, to appear with the article.
4. That you include a link to our online catalogue at:
<https://doi.org/10.1017/pasa.2017.66>
<https://doi.org/10.1017/pasa.2019.19>

Yours sincerely,

Alice Warren
Office Manager / Executive Assistant
Cambridge University Press, Australia and New Zealand

Bibliography

- J. Antoniadis, et al. (2013). ‘A Massive Pulsar in a Compact Relativistic Binary’. *Science* **340**(6131):448.
- J. W. Armstrong, et al. (1981). ‘Density power spectrum in the local interstellar medium’. *Nature* **291**(5816):561–564.
- J. W. Armstrong, et al. (1995). ‘Electron Density Power Spectrum in the Local Interstellar Medium’. *ApJ* **443**:209.
- W. Baade & F. Zwicky (1934). ‘Remarks on Super-Novae and Cosmic Rays’. *Physical Review* **46**:76–77.
- D. C. Backer (1973). ‘Pulsar Fluctuation Spectra and the Generalized Drifting-Subpulse Phenomenon’. *ApJ* **182**:245–276.
- D. C. Backer, et al. (1993). ‘Temporal Variations of Pulsar Dispersion Measures’. *ApJ* **404**:636.
- D. C. Backer, et al. (1982). ‘A millisecond pulsar’. *Nature* **300**:615–618.
- D. C. Backer, et al. (1976). ‘Orthogonal mode emission in geometric models of pulsar polarisation’. *Nature* **263**:202–207.
- K. Bandura, et al. (2014). ‘Canadian Hydrogen Intensity Mapping Experiment (CHIME) pathfinder’. In Proc. SPIE, vol. 9145 of *Society of Photo-Optical Instrumentation Engineers (SPIE) Conference Series*, p. 914522.

- K. Bansal, et al. (2019). ‘Scattering Study of Pulsars below 100 MHz Using LWA1’. *ApJ* **875**(2):146.
- J. J. Barnard & J. Arons (1986). ‘Wave Propagation in Pulsar Magnetospheres: Refraction of Rays in the Open Flux Zone’. *ApJ* **302**:138.
- N. Barry, et al. (2019). ‘Improving the EoR Power Spectrum Results from MWA Season 1 Observations’. *arXiv e-prints* p. arXiv:1909.00561.
- R. Basu & D. Mitra (2018). ‘Characterizing the nature of subpulse drifting in pulsars’. *MNRAS* **475**(4):5098–5107.
- S. D. Bates, et al. (2014). ‘PSRPOPPy: an open-source package for pulsar population simulations’. *MNRAS* **439**:2893–2902.
- S. D. Bates, et al. (2013). ‘The pulsar spectral index distribution’. *MNRAS* **431**(2):1352–1358.
- R. Beck (2001). ‘Galactic and Extragalactic Magnetic Fields’. *Space Science Reviews* **99**:243–260.
- E. M. Berkhuisen, et al. (1971). ‘Are the galactic loops supernova remnants?’. *A&A* **14**:252.
- N. D. R. Bhat, et al. (2008). ‘Gravitational-radiation losses from the pulsar white-dwarf binary PSR J1141 6545’. *Phys. Rev. D* **77**(12):124017.
- N. D. R. Bhat, et al. (2004). ‘Multifrequency Observations of Radio Pulse Broadening and Constraints on Interstellar Electron Density Microstructure’. *ApJ* **605**:759–783.
- N. D. R. Bhat, et al. (2003). ‘A CLEAN-based Method for Deconvolving Interstellar Pulse Broadening from Radio Pulses’. *ApJ* **584**:782–790.
- N. D. R. Bhat, et al. (2016). ‘Scintillation Arcs in Low-frequency Observations of the Timing-array Millisecond Pulsar PSR J0437-4715’. *ApJ* **818**:86.

- N. D. R. Bhat, et al. (2014). ‘The Low-frequency Characteristics of PSR J0437-4715 Observed with the Murchison Wide-field Array’. *ApJ* **791**:L32.
- N. D. R. Bhat, et al. (1999). ‘Long-Term Scintillation Studies of Pulsars. I. Observations and Basic Results’. *ApJS* **121**:483–513.
- N. D. R. Bhat, et al. (2018). ‘Observations of Low-frequency Radio Emission from Millisecond Pulsars and Multipath Propagation in the Interstellar Medium’. *ApJS* **238**:1.
- S. Bhatnagar & R. Nityananda (2001). ‘Solving for closure errors due to polarization leakage in radio interferometry of unpolarized sources’. *A&A* **375**:344–350.
- A. Bilous, et al. (2015). ‘A LOFAR census of non-recycled pulsars: average profiles, dispersion measures, flux densities, and spectra’. *ArXiv e-prints*.
- A. V. Bilous, et al. (2016). ‘A LOFAR census of non-recycled pulsars: average profiles, dispersion measures, flux densities, and spectra’. *A&A* **591**:A134.
- F. Bocchino, et al. (1994). ‘ROSAT PSPC Observation of the Northeast Region of the VELA Supernova Remnant. I. Evidence of Thermal Structure on a Scale of 5’. *ApJ* **437**:209.
- J. D. Bowman, et al. (2013). ‘Science with the Murchison Widefield Array’. *PASA* **30**:e031.
- M. A. Brentjens & A. G. de Bruyn (2005). ‘Faraday rotation measure synthesis’. *A&A* **441**:1217–1228.
- C. Brinkman, et al. (2019). ‘Investigation of the mode-switching phenomenon in pulsar B0329+54 through polarimetric analysis’. *MNRAS* **484**:2725–2734.
- M. Burgay, et al. (2003). ‘An increased estimate of the merger rate of double neutron stars from observations of a highly relativistic system’. *Nature* **426**:531–533.

- M. Burgay, et al. (2006). ‘The Parkes High-Latitude pulsar survey’. *MNRAS* **368**:283–292.
- B. J. Burn (1966). ‘On the depolarization of discrete radio sources by Faraday dispersion’. *MNRAS* **133**:67.
- T. Cantat-Gaudin, et al. (2019). ‘A ring in a shell: the large-scale 6D structure of the Vela OB2 complex’. *A&A* **621**:A115.
- P. A. Caraveo, et al. (2001). ‘The Distance to the Vela Pulsar Gauged with Hubble Space Telescope Parallax Observations’. *ApJ* **561**(2):930–937.
- C. Y. Cardall, et al. (2001). ‘Effects of Strong Magnetic Fields on Neutron Star Structure’. *ApJ* **554**:322–339.
- T. D. Carozzi & G. Woan (2011). ‘A Fundamental Figure of Merit for Radio Polarimeters’. *IEEE Transactions on Antennas and Propagation* **59**:2058–2065.
- A. Chanot & J. P. Sivan (1983). ‘The GUM nebula : new photometric and spectrophotometric results.’. *A&A* **121**:19–25.
- S. Chatterjee, et al. (2009). ‘Precision Astrometry with the Very Long Baseline Array: Parallaxes and Proper Motions for 14 Pulsars’. *The Astrophysical Journal* **698**(1):250–265.
- S. Chatterjee, et al. (2017). ‘A direct localization of a fast radio burst and its host’. *Nature* **541**(7635):58–61.
- J. J. Condon (1974). ‘Confusion and Flux-Density Error Distributions’. *ApJ* **188**:279–286.
- J. M. Cordes (1978). ‘Observational limits on the location of pulsar emission regions’. *ApJ* **222**:1006–1011.

- J. M. Cordes & T. J. W. Lazio (2002). ‘NE2001.I. A New Model for the Galactic Distribution of Free Electrons and its Fluctuations’. *ArXiv Astrophysics e-prints* .
- J. M. Cordes & B. J. Rickett (1998). ‘Diffractive Interstellar Scintillation Timescales and Velocities’. *ApJ* **507**(2):846–860.
- J. M. Cordes, et al. (1985). ‘Small-scale electron density turbulence in the interstellar medium.’. *ApJ* **288**:221–247.
- D. P. Cox & R. J. Reynolds (1987). ‘The local interstellar medium.’. *ARA&A* **25**:303–344.
- R. Crochiere & L. Rabiner (1983). *Multirate Digital Signal Processing*. Prentice-Hall Signal Processing Series: Advanced monographs. Prentice-Hall.
- H. T. Cromartie, et al. (2019). ‘Relativistic Shapiro delay measurements of an extremely massive millisecond pulsar’. *arXiv e-prints* p. arXiv:1904.06759.
- K. Davidson & Y. Terzian (1969). ‘Dispersion Measures of Pulsars’. *AJ* **74**:849.
- P. T. de Zeeuw, et al. (1999). ‘A HIPPARCOS Census of the Nearby OB Associations’. *AJ* **117**(1):354–399.
- A. T. Deller, et al. (2019). ‘Microarcsecond VLBI Pulsar Astrometry with PSR π II. Parallax Distances for 57 Pulsars’. *The Astrophysical Journal* **875**(2):100.
- A. T. Deller, et al. (2009). ‘Precision Southern Hemisphere VLBI Pulsar Astrometry. II. Measurement of Seven Parallaxes’. *The Astrophysical Journal* **701**(2):1243–1257.
- A. T. Deller, et al. (2008). ‘Extremely High Precision VLBI Astrometry of PSR J0437-4715 and Implications for Theories of Gravity’. *ApJ* **685**(1):L67.

- P. Demorest, et al. (2004). ‘Orientations of Spin and Magnetic Dipole Axes of Pulsars in the J0737-3039 Binary Based on Polarimetry Observations at the Green Bank Telescope’. *ApJ* **615**(2):L137–L140.
- P. B. Demorest, et al. (2010). ‘A two-solar-mass neutron star measured using Shapiro delay’. *Nature* **467**:1081–1083.
- B. Dennison, et al. (1998). ‘An imaging survey of northern galactic H α emission with arcminute resolution’. *PASA* **15**(1):147–48.
- K. M. Desai, et al. (1992). ‘A Speckle Hologram of the Interstellar Plasma’. *ApJ* **393**:L75.
- R. Dodson, et al. (2003). ‘The Vela Pulsar’s Proper Motion and Parallax Derived from VLBI Observations’. *ApJ* **596**(2):1137–1141.
- T. Dolch, et al. (2014). ‘A 24 Hr Global Campaign to Assess Precision Timing of the Millisecond Pulsar J1713+0747’. *ApJ* **794**:21.
- J. Y. Donner, et al. (2019). ‘First detection of frequency-dependent, time-variable dispersion measures’. *A&A* **624**:A22.
- B. T. Draine (2011). *Physics of the Interstellar and Intergalactic Medium*.
- R. T. Edwards & B. W. Stappers (2004). ‘Ellipticity and deviations from orthogonality in the polarization modes of PSR B0329+54’. *A&A* **421**:681–691.
- J. E. Everett & J. M. Weisberg (2001). ‘Emission Beam Geometry of Selected Pulsars Derived from Average Pulse Polarization Data’. *ApJ* **553**:341–357.
- C.-A. Faucher-Giguère & V. M. Kaspi (2006). ‘Birth and Evolution of Isolated Radio Pulsars’. *ApJ* **643**:332–355.
- D. P. Finkbeiner (2003). ‘A Full-Sky H α Template for Microwave Foreground Prediction’. *ApJS* **146**(2):407–415.

- T. M. O. Franzen, et al. (2016). ‘The 154 MHz radio sky observed by the Murchison Widefield Array: noise, confusion, and first source count analyses’. *MNRAS* **459**:3314–3325.
- R. T. Gangadhara (1997). ‘Orthogonal polarization mode phenomenon in pulsars.’. *A&A* **327**:155–166.
- J. E. Gaustad, et al. (2001). ‘A Robotic Wide-Angle H α Survey of the Southern Sky’. *PASP* **113**(789):1326–1348.
- M. Geyer, et al. (2017). ‘Scattering analysis of LOFAR pulsar observations’. *MNRAS* **470**(3):2659–2679.
- D. M. Gould & A. G. Lyne (1998). ‘Multifrequency polarimetry of 300 radio pulsars’. *MNRAS* **301**:235–260.
- C. S. Gum (1952). ‘A large H II region at galactic longitude 226 deg.’. *The Observatory* **72**:151–154.
- Y. Gupta (1995). ‘On the Correlation between Proper Motion Velocities and Scintillation Velocities of Radio Pulsars’. *ApJ* **451**:717.
- Y. Gupta, et al. (1993). ‘Refractive interstellar scintillation of pulsar intensities at 74 MHz’. *ApJ* **403**:183–201.
- C. R. Gwinn, et al. (1993). ‘Angular Broadening of Pulsars and the Distribution of Interstellar Plasma Fluctuations’. *ApJ* **410**:673.
- J. P. Hamaker, et al. (1996). ‘Understanding radio polarimetry. I. Mathematical foundations.’. *A&AS* **117**:137–147.
- P. A. Hamilton, et al. (1985). ‘Changing parameters along the path to the VELA pulsar.’. *MNRAS* **214**:5P–8.
- P. A. Hamilton & A. G. Lyne (1987). ‘Faraday rotation measurements on 163 pulsars’. *MNRAS* **224**:1073–1081.

- P. A. Hamilton, et al. (1977). ‘Polarization characteristics of southern pulsars - I. 400-MHz observations.’. *MNRAS* **180**:1.
- J. L. Han, et al. (2009). ‘Polarization Observations of 100 Pulsars at 774 MHz by the Green Bank Telescope’. *ApJS* **181**:557–571.
- J. L. Han, et al. (2006). ‘Pulsar Rotation Measures and the Large-Scale Structure of the Galactic Magnetic Field’. *ApJ* **642**:868–881.
- J. L. Han, et al. (1999). ‘Pulsar rotation measures and the magnetic structure of our Galaxy’. *MNRAS* **306**(2):371–380.
- J. L. Han, et al. (2018). ‘Pulsar Rotation Measures and Large-scale Magnetic Field Reversals in the Galactic Disk’. *ApJS* **234**(1):11.
- C. G. T. Haslam, et al. (1981). ‘A 408 MHz all-sky continuum survey. I - Observations at southern declinations and for the North Polar region’. *A&A* **100**:209–219.
- C. G. T. Haslam, et al. (1982). ‘A 408 MHz all-sky continuum survey. II - The atlas of contour maps’. *A&AS* **47**:1.
- T. E. Hassall, et al. (2012). ‘Wide-band simultaneous observations of pulsars: disentangling dispersion measure and profile variations’. *A&A* **543**:A66.
- G. Heald, et al. (2009). ‘The Westerbork SINGS survey. II Polarization, Faraday rotation, and magnetic fields’. *A&A* **503**:409–435.
- C. Heiles, et al. (2001). ‘Mueller Matrix Parameters for Radio Telescopes and Their Observational Determination’. *PASP* **113**:1274–1288.
- D. J. Helfand, et al. (1977). ‘Pulsar flux observations: long-term intensity and spectral variations.’. *AJ* **82**:701–705.
- W. Hermsen, et al. (2013). ‘Synchronous X-ray and Radio Mode Switches: A Rapid Global Transformation of the Pulsar Magnetosphere’. *Science* **339**:436.

- M. Hernández-Pajares, et al. (2009). ‘The IGS VTEC maps: a reliable source of ionospheric information since 1998’. *Journal of Geodesy* **83**(3):263–275.
- J. W. T. Hessels, et al. (2006). ‘A Radio Pulsar Spinning at 716 Hz’. *Science* **311**(5769):1901–1904.
- A. Hewish, et al. (1968). ‘Observation of a Rapidly Pulsating Radio Source’. *Nature* **217**:709–713.
- G. Hobbs (2013). ‘The Parkes Pulsar Timing Array’. *Classical and Quantum Gravity* **30**(22):224007.
- G. Hobbs, et al. (2010). ‘The International Pulsar Timing Array project: using pulsars as a gravitational wave detector’. *Classical and Quantum Gravity* **27**(8):084013.
- G. Hobbs, et al. (2019a). ‘The role of FAST in pulsar timing arrays’. *Research in Astronomy and Astrophysics* **19**(2):020.
- G. Hobbs, et al. (2004). ‘Long-term timing observations of 374 pulsars’. *MNRAS* **353**(4):1311–1344.
- G. Hobbs, et al. (2019b). ‘An ultra-wide bandwidth (704 to 4032 MHz) receiver for the Parkes radio telescope’. *arXiv e-prints* p. arXiv:1911.00656.
- J. A. Högbom (1974). ‘Aperture Synthesis with a Non-Regular Distribution of Interferometer Baselines’. *A&AS* **15**:417.
- A. W. Hotan, et al. (2005). ‘PSR J0737-3039A: baseband timing and polarimetry’. *MNRAS* **362**(4):1267–1272.
- A. W. Hotan, et al. (2006). ‘High-precision baseband timing of 15 millisecond pulsars’. *Monthly Notices of the Royal Astronomical Society* **369**(3):1502–1520.
- A. W. Hotan, et al. (2004). ‘PSRCHIVE and PSRFITS: An Open Approach to Radio Pulsar Data Storage and Analysis’. *PASA* **21**:302–309.

- T. A. Howard, et al. (2016). ‘Measuring the Magnetic Field of Coronal Mass Ejections Near the Sun Using Pulsars’. *ApJ* **831**:208.
- I. D. Howarth & F. van Leeuwen (2019). ‘The distance, rotation, and physical parameters of ζ Pup’. *MNRAS* **484**(4):5350–5361.
- R. A. Hulse & J. H. Taylor (1975). ‘Discovery of a pulsar in a binary system.’. *ApJ* **195**:L51–L53.
- N. Hurley-Walker, et al. (2017). ‘GaLactic and Extragalactic All-sky Murchison Widefield Array (GLEAM) survey - I. A low-frequency extragalactic catalogue’. *MNRAS* **464**:1146–1167.
- F. Jankowski, et al. (2018). ‘Spectral properties of 441 radio pulsars’. *Monthly Notices of the Royal Astronomical Society* **473**(4):4436–4458.
- G. Janssen, et al. (2015). ‘Gravitational Wave Astronomy with the SKA’. *Advancing Astrophysics with the Square Kilometre Array (AASKA14)* p. 37.
- R. J. Jennings, et al. (2018). ‘Binary Pulsar Distances and Velocities from Gaia Data Release 2’. *The Astrophysical Journal* **864**(1):26.
- S. Johnston (2002). ‘Single Dish Polarisation Calibration’. *PASA* **19**:277–281.
- S. Johnston, et al. (2005). ‘Evidence for alignment of the rotation and velocity vectors in pulsars’. *MNRAS* **364**:1397–1412.
- S. Johnston, et al. (2008). ‘Multifrequency integrated profiles of pulsars’. *MNRAS* **388**:261–274.
- S. Johnston, et al. (2006). ‘High-frequency observations of southern pulsars’. *MNRAS* **369**:1916–1928.
- S. Johnston & M. Kerr (2018). ‘Polarimetry of 600 pulsars from observations at 1.4 GHz with the Parkes radio telescope’. *MNRAS* **474**:4629–4636.

- S. Johnston, et al. (2007). ‘Evidence for alignment of the rotation and velocity vectors in pulsars - II. Further data and emission heights’. *MNRAS* **381**:1625–1637.
- S. Johnston, et al. (1998). ‘Scintillation parameters for 49 pulsars’. *MNRAS* **297**:108–116.
- A. Karastergiou (2009). ‘The complex polarization angles of radio pulsars: orthogonal jumps and interstellar scattering’. *MNRAS* **392**:L60–L64.
- A. Karastergiou & S. Johnston (2006). ‘Absolute polarization position angle profiles of southern pulsars at 1.4 and 3.1 GHz’. *MNRAS* **365**:353–366.
- A. Karastergiou, et al. (2015). ‘Understanding pulsar magnetospheres with the SKA’. *Advancing Astrophysics with the Square Kilometre Array (AASKA14)* p. 38.
- A. Karastergiou, et al. (2011). ‘A transient component in the pulse profile of PSR J0738-4042’. *MNRAS* **415**:251–256.
- V. M. Kaspi, et al. (2000). ‘Discovery of a Young Radio Pulsar in a Relativistic Binary Orbit’. *ApJ* **543**:321–327.
- D. Kaur, et al. (2019). ‘A High Time-resolution Study of the Millisecond Pulsar J2241–5236 at Frequencies Below 300 MHz’. *ApJ* **882**(2):133.
- E. Keane, et al. (2015). ‘A Cosmic Census of Radio Pulsars with the SKA’. *Advancing Astrophysics with the Square Kilometre Array (AASKA14)* p. 40.
- M. J. Keith, et al. (2011). ‘Discovery of millisecond pulsars in radio searches of southern Fermi Large Area Telescope sources’. *MNRAS* **414**:1292–1300.
- M. J. Keith, et al. (2013). ‘A connection between radio state changing and glitch activity in PSR J0742-2822’. *MNRAS* **432**(4):3080–3084.

- M. Kerr, et al. (2012). ‘Five New Millisecond Pulsars from a Radio Survey of 14 Unidentified Fermi-LAT Gamma-Ray Sources’. *ApJ* **748**:L2.
- J. Kijak & J. Gil (1998). ‘Radio emission regions in pulsars’. *MNRAS* **299**:855–861.
- J. Kijak & J. Gil (2003). ‘Radio emission altitude in pulsars’. *A&A* **397**:969–972.
- J. Kijak, et al. (1998). ‘Pulse shapes of radio pulsars at 4.85 GHz’. *A&AS* **127**:153–165.
- F. Kirsten, et al. (2019). ‘Probing Pulsar Scattering between 120 and 280 MHz with the MWA’. *ApJ* **874**(2):179.
- M. M. Komesaroff (1970). ‘Possible Mechanism for the Pulsar Radio Emission’. *Nature* **225**:612–614.
- M. M. Komesaroff, et al. (1972). ‘Linear polarization and spectrum of PSR 0833-45 and the effects of scattering’. *Australian Journal of Physics* **25**:759.
- M. M. Komesaroff, et al. (1970). ‘Linear Polarization and Pulse Shape Measurements on Nine Pulsars’. *Astrophys. Lett.* **5**:37.
- V. I. Kondratiev, et al. (2016a). ‘A LOFAR census of millisecond pulsars’. *A&A* **585**:A128.
- V. I. Kondratiev, et al. (2016b). ‘A LOFAR census of millisecond pulsars’. *A&A* **585**:A128.
- B. Koribalski, et al. (1995). ‘H i Line Measurements of Eight Southern Pulsars’. *The Astrophysical Journal* **441**:756.
- M. Kramer, et al. (1999). ‘The Characteristics of Millisecond Pulsar Emission. III. From Low to High Frequencies’. *ApJ* **526**(2):957–975.
- M. Kramer, et al. (2006). ‘Tests of General Relativity from Timing the Double Pulsar’. *Science* **314**(5796):97–102.

- M. Kramer, et al. (1998). ‘The Characteristics of Millisecond Pulsar Emission. I. Spectra, Pulse Shapes, and the Beaming Fraction’. *ApJ* **501**:270–285.
- A. D. Kuzmin, et al. (1998). ‘Catalogue of time aligned profiles of 56 pulsars at frequencies between 102 and 10500 MHz’. *A&AS* **127**:355–366.
- A. D. Kuz'min & B. Y. Losovskii (1999). ‘Observations of the mean profiles of radio pulsars and the structures of their emitting regions at 102 MHz’. *Astronomy Reports* **43**:288–304.
- M. T. Lam, et al. (2016). ‘Systematic and Stochastic Variations in Pulsar Dispersion Measures’. *ApJ* **821**(1):66.
- H. C. Lambert & B. J. Rickett (1999). ‘On the Theory of Pulse Propagation and Two-Frequency Field Statistics in Irregular Interstellar Plasmas’. *ApJ* **517**(1):299–317.
- C. Lange, et al. (1998). ‘Radio pulsar microstructure at 1.41 and 4.85 GHz’. *A&A* **332**:111–120.
- J. M. Lattimer & M. Prakash (2001). ‘Neutron Star Structure and the Equation of State’. *ApJ* **550**:426–442.
- K. D. Lawson, et al. (1987). ‘Variations in the Spectral Index of the Galactic Radio Continuum Emission in the Northern Hemisphere’. *MNRAS* **225**:307.
- T. J. Lazio, et al. (1990). ‘Faraday Rotation Measure Variations in the Cygnus Region and the Spectrum of Interstellar Plasma Turbulence’. *ApJ* **363**:515.
- K. H. Lee & L. C. Lee (2019). ‘Interstellar turbulence spectrum from in situ observations of Voyager 1’. *Nature Astronomy* **3**:154–159.
- L. C. Lee & J. R. Jokipii (1975). ‘Strong scintillations in astrophysics. III. The fluctuations in intensity.’. *ApJ* **202**:439–453.

- L. C. Lee & J. R. Jokipii (1976). ‘The irregularity spectrum in interstellar space.’. *ApJ* **206**:735–743.
- E. Lenc, et al. (2017). ‘The Challenges of Low-Frequency Radio Polarimetry: Lessons from the Murchison Widefield Array’. *PASA* **34**:e040.
- E. Lenc, et al. (2018). ‘An all-sky survey of circular polarization at 200 MHz’. *MNRAS* **478**:2835–2849.
- W. Li, et al. (2018). ‘Comparing Redundant and Sky-model-based Interferometric Calibration: A First Look with Phase II of the MWA’. *The Astrophysical Journal* **863**(2):170.
- X. H. Li & J. L. Han (2003). ‘The effect of scattering on pulsar polarization angle’. *A&A* **410**:253–256.
- J. L. B. Line, et al. (2018). ‘In situ measurement of MWA primary beam variation using ORBCOMM’. *Publications of the Astronomical Society of Australia* **35**:45.
- K. Liu, et al. (2012). ‘Profile-shape stability and phase-jitter analyses of millisecond pulsars’. *MNRAS* **420**:361–368.
- C. J. Lonsdale, et al. (2009). ‘The Murchison Widefield Array: Design Overview’. *IEEE Proceedings* **97**:1497–1506.
- D. Lorimer & M. Kramer (2005). *Handbook of Pulsar Astronomy*. Cambridge Observing Handbooks for Research Astronomers. Cambridge University Press.
- D. R. Lorimer (2008). ‘Binary and Millisecond Pulsars’. *Living Reviews in Relativity* **11**:8.
- D. R. Lorimer, et al. (2007). ‘A Bright Millisecond Radio Burst of Extragalactic Origin’. *Science* **318**:777.

- D. R. Lorimer, et al. (2006). ‘The Parkes Multibeam Pulsar Survey - VI. Discovery and timing of 142 pulsars and a Galactic population analysis’. *MNRAS* **372**:777–800.
- D. R. Lorimer, et al. (1995). ‘Multifrequency flux density measurements of 280 pulsars’. *MNRAS* **273**:411–421.
- A. Lyne, et al. (2010). ‘Switched Magnetospheric Regulation of Pulsar Spin-Down’. *Science* **329**(5990):408.
- A. G. Lyne (1971). ‘Mode changing in pulsar radiation’. *MNRAS* **153**:27P.
- A. G. Lyne, et al. (2004). ‘A Double-Pulsar System: A Rare Laboratory for Relativistic Gravity and Plasma Physics’. *Science* **303**:1153–1157.
- A. G. Lyne & D. R. Lorimer (1994). ‘High birth velocities of radio pulsars’. *Nature* **369**:127–129.
- A. G. Lyne & R. N. Manchester (1988). ‘The shape of pulsar radio beams’. *MNRAS* **234**:477–508.
- A. G. Lyne, et al. (1985). ‘The galactic population of pulsars’. *MNRAS* **213**:613–639.
- A. G. Lyne & B. J. Rickett (1968). ‘Radio Observations of Five Pulsars’. *Nature* **219**(5161):1339–1342.
- A. G. Lyne & F. G. Smith (1968). ‘Linear Polarization in Pulsating Radio Sources’. *Nature* **218**:124–126.
- A. G. Lyne & F. G. Smith (1989). ‘Pulsar rotation measures and the galactic magnetic field’. *MNRAS* **237**:533–541.
- J.-P. Macquart & D. B. Melrose (2000). ‘Circular polarization induced by scintillation in a magnetized medium’. *Phys. Rev. E* **62**:4177–4188.

- J. B. Malins, et al. (2018). ‘Modeling the Ionosphere with GPS and Rotation Measure Observations’. *Radio Science* **53**:724–738.
- V. M. Malofeev (1996). ‘Pulsar Radio Spectra’. In S. Johnston, M. A. Walker, & M. Bailes (eds.), *IAU Colloq. 160: Pulsars: Problems and Progress*, vol. 105 of *Astronomical Society of the Pacific Conference Series*, p. 271.
- V. M. Malofeev, et al. (2000). ‘Flux Densities of 235 Pulsars at 102.5 MHz’. *Astronomy Reports* **44**:436–445.
- R. N. Manchester (1971). ‘Observations of Pulsar Polarization at 410 and 1665 MHz’. *ApJS* **23**:283.
- R. N. Manchester (1972). ‘Pulsar Rotation and Dispersion Measures and the Galactic Magnetic Field.’. *ApJ* **172**:43.
- R. N. Manchester, et al. (1998). ‘Polarization observations of 66 southern pulsars’. *MNRAS* **295**:280–298.
- R. N. Manchester, et al. (2013). ‘The Parkes Pulsar Timing Array Project’. *PASA* **30**:e017.
- R. N. Manchester, et al. (2005a). ‘The Australia Telescope National Facility Pulsar Catalogue’. *AJ* **129**:1993–2006.
- R. N. Manchester, et al. (2005b). ‘The Australia Telescope National Facility Pulsar Catalogue’. *AJ* **129**:1993–2006.
- R. N. Manchester & IPTA (2013). ‘The International Pulsar Timing Array’. *Classical and Quantum Gravity* **30**(22):224010.
- R. N. Manchester, et al. (2001). ‘The Parkes multi-beam pulsar survey - I. Observing and data analysis systems, discovery and timing of 100 pulsars’. *MNRAS* **328**:17–35.

- R. N. Manchester & J. H. Taylor (1981). ‘Observed and derived parameters for 330 pulsars.’. *The Astronomical Journal* **86**:1953–1973.
- O. Maron, et al. (2000). ‘Pulsar spectra of radio emission’. *A&AS* **147**:195–203.
- D. N. Matsakis, et al. (1997). ‘A statistic for describing pulsar and clock stabilities.’. *A&A* **326**:924–928.
- A. M. Matthews, et al. (2016). ‘The NANOGrav Nine-year Data Set: Astrometric Measurements of 37 Millisecond Pulsars’. *The Astrophysical Journal* **818**(1):92.
- P. M. McCulloch, et al. (1978). ‘Polarization characteristics of southern pulsars - II. 640-MHz observations.’. *MNRAS* **183**:645–676.
- M. M. McKinnon (1997). ‘Birefringence as a Mechanism for the Broadening and Depolarization of Pulsar Average Profiles’. *ApJ* **475**:763–769.
- M. M. McKinnon & D. R. Stinebring (1998). ‘A Statistical Model for the Orthogonal Modes of Polarization in Pulsar Radio Emission’. *ApJ* **502**:883–897.
- M. M. McKinnon & D. R. Stinebring (2000). ‘The Mode-separated Pulse Profiles of Pulsar Radio Emission’. *ApJ* **529**:435–446.
- M. A. McLaughlin (2013). ‘The North American Nanohertz Observatory for Gravitational Waves’. *Classical and Quantum Gravity* **30**(22):224008.
- D. Melrose, et al. (2006). ‘An empirical model for the polarization of pulsar radio emission’. *MNRAS* **365**:638–646.
- S. Mereghetti, et al. (2016). ‘A Deep Campaign to Characterize the Synchronous Radio/X-Ray Mode Switching of PSR B0943+10’. *ApJ* **831**:21.
- S. Mereghetti, et al. (2015). ‘Magnetars: Properties, Origin and Evolution’. *Space Sci. Rev.* **191**:315–338.
- B. W. Meyers, et al. (2018). ‘Hunting for Radio Emission from the Intermittent Pulsar J1107-5907 at Low Frequencies’. *ApJ* **869**(2):134.

- B. W. Meyers, et al. (2017). ‘Spectral Flattening at Low Frequencies in Crab Giant Pulses’. *ApJ* **851**:20.
- B. W. Meyers, et al. (2019). ‘The emission and scintillation properties of RRAT J2325-0530 at 154 MHz and 1.4 GHz’. *PASA* **36**:e034.
- D. Michilli, et al. (2018a). ‘Low-frequency pulse profile variation in PSR B2217+47: evidence for echoes from the interstellar medium’. *MNRAS* **476**(2):2704–2716.
- D. Michilli, et al. (2018b). ‘An extreme magneto-ionic environment associated with the fast radio burst source FRB 121102’. *Nature* **553**:182–185.
- D. A. Mitchell, et al. (2008). ‘Real-Time Calibration of the Murchison Widefield Array’. *IEEE Journal of Selected Topics in Signal Processing* **2**:707–717.
- D. Mitra, et al. (2016). ‘Meterwavelength Single-pulse Polarimetric Emission Survey’. *ApJ* **833**:28.
- D. Mitra & J. M. Rankin (2002). ‘Toward an Empirical Theory of Pulsar Emission. VII. On the Spectral Behavior of Conal Beam Radii and Emission Heights’. *ApJ* **577**:322–336.
- D. Morris, et al. (1981). ‘Depolarisation of pulsar integrated pulse profiles.’. *A&A* **100**:107–112.
- T. Murphy, et al. (2017). ‘Low-Frequency Spectral Energy Distributions of Radio Pulsars Detected with the Murchison Widefield Array’. *PASA* **34**:e020.
- R. Narayan & M. Vivekanand (1982). ‘Geometry of pulsar beams - Relative orientations of rotation axis, magnetic axis, and line of sight’. *A&A* **113**:L3–L6.
- G. Neugebauer, et al. (1984). ‘The Infrared Astronomical Satellite (IRAS) mission.’. *ApJ* **278**:L1–L6.

- J. E. Noordam (2004). ‘LOFAR calibration challenges’. In J. Oschmann, Jacobus M. (ed.), *Ground-based Telescopes*, vol. 5489 of *Society of Photo-Optical Instrumentation Engineers (SPIE) Conference Series*, pp. 817–825.
- J. R. North, et al. (2007). ‘ γ^2 Velorum: orbital solution and fundamental parameter determination with SUSI’. *MNRAS* **377**(1):415–424.
- A. Noutsos, et al. (2008). ‘New pulsar rotation measures and the Galactic magnetic field’. *MNRAS* **386**:1881–1896.
- A. Noutsos, et al. (2009). ‘Phase-resolved Faraday rotation in pulsars’. *MNRAS* **396**:1559–1572.
- A. Noutsos, et al. (2015). ‘Pulsar polarisation below 200 MHz: Average profiles and propagation effects’. *A&A* **576**:A62.
- R. Novick, et al. (1977). ‘The effect of vacuum birefringence on the polarization of X-ray binaries and pulsars.’. *ApJ* **215**:L117–L120.
- A. R. Offringa, et al. (2015). ‘The Low-Frequency Environment of the Murchison Widefield Array: Radio-Frequency Interference Analysis and Mitigation’. *PASA* **32**:e008.
- S. M. Ord, et al. (2015). ‘The Murchison Widefield Array Correlator’. *PASA* **32**:e006.
- S. M. Ord, et al. (2019). ‘MWA tied-array processing I: Calibration and beam-formation’. *PASA* **36**:e030.
- S. I. Oronsaye, et al. (2015). ‘Simultaneous Observations of Giant Pulses from the Crab Pulsar, with the Murchison Widefield Array and Parkes Radio Telescope: Implications for the Giant Pulse Emission Mechanism.’. *ApJ* **809**:51.
- J. P. Ostriker & J. E. Gunn (1971). ‘Do Pulsars Make Supernovae?’. *ApJ* **164**:L95.

- A. Parsons, et al. (2012). ‘A Sensitivity and Array-configuration Study for Measuring the Power Spectrum of 21 cm Emission from Reionization’. *The Astrophysical Journal* **753**(1):81.
- E. Petroff, et al. (2013). ‘Dispersion measure variations in a sample of 168 pulsars’. *MNRAS* **435**(2):1610–1617.
- J. A. Phillips & A. Wolszczan (1991). ‘Time Variability of Pulsar Dispersion Measures’. *ApJ* **382**:L27.
- M. Pilia, et al. (2016). ‘Wide-band, low-frequency pulse profiles of 100 radio pulsars with LOFAR’. *A&A* **586**:A92.
- Planck Collaboration, et al. (2011). ‘Planck early results. I. The Planck mission’. *A&A* **536**:A1.
- M. V. Popov, et al. (2019). ‘Anisotropic Scattering of the Radio Emission of the Pulsar B0833-45 in the Vela Supernova Remnant’. *Astronomy Reports* **63**(5):391–403.
- T. Prabu, et al. (2015). ‘A digital-receiver for the MurchisonWidefield Array’. *Experimental Astronomy* **39**:73–93.
- C. R. Purcell, et al. (2015). ‘A Radio-Polarisation and Rotation Measure Study of the Gum Nebula and Its Environment’. *ApJ* **804**(1):22.
- V. Radhakrishnan & D. J. Cooke (1969). ‘Magnetic Poles and the Polarization Structure of Pulsar Radiation’. *Astrophys. Lett.* **3**:225.
- R. J. Rand & S. R. Kulkarni (1989). ‘The Local Galactic Magnetic Field’. *The Astrophysical Journal* **343**:760.
- R. J. Rand & A. G. Lyne (1994). ‘New Rotation Measures of Distant Pulsars in the Inner Galaxy and Magnetic Field Reversals’. *MNRAS* **268**:497.

- J. M. Rankin (1983). ‘Toward an empirical theory of pulsar emission. I Morphological taxonomy.’. *ApJ* **274**:333–368.
- J. M. Rankin (1993a). ‘Toward an Empirical Theory of Pulsar Emission. VI. The Geometry of the Conal Emission Region’. *ApJ* **405**:285.
- J. M. Rankin (1993b). ‘Toward an Empirical Theory of Pulsar Emission. VI. The Geometry of the Conal Emission Region: Appendix and Tables’. *ApJS* **85**:145.
- S. M. Ransom (2001). *New search techniques for binary pulsars*. Ph.D. thesis, Harvard University.
- R. J. Reynolds (1976). ‘Observations of the Gum nebula with a Fabry-Perot spectrometer.’. *ApJ* **203**:151–153.
- R. J. Reynolds, et al. (1998). ‘The Wisconsin H α Mapper (WHAM): A Brief Review of Performance Characteristics and Early Scientific Results’. *PASA* **15**(1):14–18.
- B. J. Rickett (1969). ‘Frequency Structure of Pulsar Intensity Variations’. *Nature* **221**(5176):158–159.
- B. J. Rickett (1977). ‘Interstellar scattering and scintillation of radio waves.’. *ARA&A* **15**:479–504.
- B. J. Rickett, et al. (1984). ‘Slow scintillation in the interstellar medium.’. *A&A* **134**:390–395.
- J. Roy, et al. (2010). ‘A real-time software backend for the GMRT’. *Experimental Astronomy* **28**:25–60.
- M. A. Ruderman & P. G. Sutherland (1975). ‘Theory of pulsars: polar gaps, sparks, and coherent microwave radiation.’. *ApJ* **196**:51–72.
- M. S. Sahu & K. C. Sahu (1993). ‘Kinematics of the ionized gas in Puppis-Vela including the GUM nebula.’. *A&A* **280**:231–240.

- S. Sallmen, et al. (2006). ‘Probing the Interstellar Medium using the Vela Pulsar’. In *American Astronomical Society Meeting Abstracts*, vol. 209, p. 172.28.
- P. A. G. Scheuer (1968). ‘Amplitude Variations in Pulsed Radio Sources’. *Nature* **218**(5145):920–922.
- D. H. F. M. Schnitzeler, et al. (2009). ‘WSRT Faraday tomography of the Galactic ISM at $\lambda \sim 0.86$ m. I. The GEMINI data set at $(l, b) = (181^\circ, 20^\circ)$ ’. *A&A* **494**(2):611–622.
- J. H. Seiradakis, et al. (1995). ‘Pulsar profiles at high frequencies. I. The data.’. *A&AS* **111**:205.
- W. Sieber (1973). ‘Pulsar Spectra’. *A&A* **28**:237.
- W. Sieber (1982). ‘Causal relationship between pulsar long-term intensity variations and the interstellar medium.’. *A&A* **113**:311–313.
- W. Sieber (1997). ‘Geometrical effects on radio pulsar profiles and spectra.’. *A&A* **321**:519–522.
- J. H. Simonetti & J. M. Cordes (1988). ‘Interstellar electron density and magnetic field irregularities on 0.001 to 100 parsec scales’. In J. M. Cordes, B. J. Rickett, & D. C. Backer (eds.), *Radio Wave Scattering in the Interstellar Medium*, vol. 174 of *American Institute of Physics Conference Series*, pp. 134–138.
- J. H. Simonetti, et al. (1984). ‘Small-scale variations in the galactic magnetic field : the rotation measure structure function and birefringence in interstellar scintillations.’. *ApJ* **284**:126–134.
- F. G. Smith (1968). ‘Faraday Rotation of Radio Waves from the Pulsars’. *Nature* **220**:891–892.
- C. Sobey, et al. (2019). ‘Low-frequency Faraday rotation measures towards pulsars using LOFAR: probing the 3D Galactic halo magnetic field’. *MNRAS* **484**(3):3646–3664.

- D. D. Sokoloff, et al. (1998). ‘Depolarization and Faraday effects in galaxies’. *MNRAS* **299**:189–206.
- M. Sokolowski, et al. (2017). ‘Calibration and Stokes Imaging with Full Embedded Element Primary Beam Model for the Murchison Widefield Array’. *PASA* **34**:e062.
- C. Sotomayor-Beltran, et al. (2013). ‘Calibrating high-precision Faraday rotation measurements for LOFAR and the next generation of low-frequency radio telescopes’. *A&A* **552**:A58.
- B. W. Stappers, et al. (2011). ‘Observing pulsars and fast transients with LOFAR’. *A&A* **530**:A80.
- D. R. Stinebring, et al. (1996). ‘Refractive and Diffractive Scintillation of the Pulsar PSR B0329+54’. *ApJ* **460**:460.
- D. R. Stinebring, et al. (2001). ‘Faint Scattering Around Pulsars: Probing the Interstellar Medium on Solar System Size Scales’. *ApJ* **549**(1):L97–L100.
- K. Stovall, et al. (2015). ‘Pulsar Observations Using the First Station of the Long Wavelength Array and the LWA Pulsar Data Archive’. *ApJ* **808**:156.
- I. Sushch, et al. (2011). ‘Modeling of the Vela complex including the Vela supernova remnant, the binary system γ^2 Velorum, and the Gum nebula’. *A&A* **525**:A154.
- A. Sutinjo, et al. (2015a). ‘Understanding instrumental Stokes leakage in Murchison Widefield Array polarimetry’. *Radio Science* **50**:52–65.
- A. Sutinjo, et al. (2015b). ‘Understanding instrumental Stokes leakage in Murchison Widefield Array polarimetry’. *Radio Science* **50**:52–65.
- G. Swarup, et al. (1991). ‘The Giant Metre-Wave Radio Telescope’. *Current Science, Vol. 60, NO.2/JAN25, P. 95, 1991* **60**:95.

- G. B. Taylor, et al. (2012). ‘First Light for the First Station of the Long Wavelength Array’. *Journal of Astronomical Instrumentation* **1**:1250004–284.
- J. H. Taylor & J. M. Cordes (1993). ‘Pulsar distances and the galactic distribution of free electrons’. *ApJ* **411**:674–684.
- J. H. Taylor & R. N. Manchester (1977). ‘Recent observations of pulsars’. *ARA&A* **15**:19–44.
- J. H. Taylor, et al. (1993). ‘Catalog of 558 Pulsars’. *ApJS* **88**:529.
- J. H. Taylor & D. R. Stinebring (1986). ‘Recent progress in the understanding of pulsars’. *ARA&A* **24**:285–327.
- J. H. Taylor & J. M. Weisberg (1982). ‘A new test of general relativity - Gravitational radiation and the binary pulsar PSR 1913+16’. *ApJ* **253**:908–920.
- J. H. Taylor, et al. (1992). ‘Experimental constraints on strong-field relativistic gravity’. *Nature* **355**(6356):132–136.
- E. Thébault, et al. (2015). ‘International Geomagnetic Reference Field: the 12th generation’. *Earth, Planets and Space* **67**(1):79.
- D. Thornton, et al. (2013). ‘A Population of Fast Radio Bursts at Cosmological Distances’. *Science* **341**:53–56.
- S. E. Thorsett (1991). ‘Frequency dependence of pulsar integrated profiles’. *ApJ* **377**:263–267.
- S. J. Tingay, et al. (2013). ‘The Murchison Widefield Array: The Square Kilometre Array Precursor at Low Radio Frequencies’. *PASA* **30**:e007.
- M. Toscano, et al. (1998). ‘Spectra of Southern Pulsars’. *ApJ* **506**:863–867.
- S. E. Tremblay, et al. (2015). ‘The High Time and Frequency Resolution Capabilities of the Murchison Widefield Array’. *PASA* **32**:e005.

- C. M. Trott, et al. (2016). ‘CHIPS: The Cosmological H I Power Spectrum Estimator’. *ApJ* **818**:139.
- C. L. Van Eck, et al. (2011). ‘Modeling the Magnetic Field in the Galactic Disk Using New Rotation Measure Observations from the Very Large Array’. *ApJ* **728**:97.
- M. P. van Haarlem, et al. (2013). ‘LOFAR: The LOw-Frequency ARray’. *A&A* **556**:A2.
- R. van Haasteren, et al. (2011). ‘Placing limits on the stochastic gravitational-wave background using European Pulsar Timing Array data’. *MNRAS* **414**(4):3117–3128.
- F. van Leeuwen (2007). ‘Validation of the new Hipparcos reduction’. *A&A* **474**(2):653–664.
- T. D. van Ommen, et al. (1997). ‘Polarimetric observations of southern pulsars at 800 and 950 MHz’. *MNRAS* **287**(2):307–327.
- W. van Straten (2013). ‘High-fidelity Radio Astronomical Polarimetry Using a Millisecond Pulsar as a Polarized Reference Source’. *The Astrophysical Journal Supplement Series* **204**:13.
- W. van Straten & M. Bailes (2011). ‘DSPSR: Digital Signal Processing Software for Pulsar Astronomy’. *PASA* **28**:1–14.
- W. van Straten, et al. (2012). ‘Pulsar Data Analysis with PSRCHIVE’. *Astronomical Research and Technology* **9**:237–256.
- W. van Straten & C. Tiburzi (2017). ‘The Statistics of Radio Astronomical Polarimetry: Disjoint, Superposed, and Composite Samples’. *ApJ* **835**:293.
- N. R. Vandenberg (1974). *Meter-Wavelength Observations of Pulsars Using Very-Long Interferometry*. Ph.D. thesis, Maryland Univ., College Park.

- A. von Hoensbroech, et al. (1998a). ‘On the high frequency polarization of pulsar radio emission’. *A&A* **334**:571–584.
- A. von Hoensbroech, et al. (1998b). ‘Natural polarization modes in pulsar magnetospheres’. *A&A* **336**:209–219.
- R. Wayth, et al. (2017). ‘The Engineering Development Array: A Low Frequency Radio Telescope Utilising SKA Precursor Technology’. *PASA* **34**:e034.
- R. B. Wayth, et al. (2018). ‘The Phase II Murchison Widefield Array: Design overview’. *PASA* **35**:33.
- R. Weaver, et al. (1977). ‘Interstellar bubbles. II. Structure and evolution.’. *ApJ* **218**:377–395.
- J. M. Weisberg, et al. (1979). ‘Neutral hydrogen absorption in the spectra of four low-latitude pulsars.’. *Astronomy and Astrophysics* **77**:204–209.
- J. M. Weisberg, et al. (1999). ‘Arecibo 1418 MHz Polarimetry of 98 Pulsars: Full Stokes Profiles and Morphological Classifications’. *ApJS* **121**:171–217.
- J. M. Weisberg, et al. (2008). ‘Arecibo H I Absorption Measurements of Pulsars and the Electron Density at Intermediate Longitudes in the First Galactic Quadrant’. *The Astrophysical Journal* **674**(1):286–294.
- P. Weltevrede & S. Johnston (2008). ‘Profile and polarization characteristics of energetic pulsars’. *MNRAS* **391**:1210–1226.
- B. Woermann, et al. (2001). ‘Kinematics of the Gum nebula region’. *MNRAS* **325**(3):1213–1227.
- K. M. Xilouris, et al. (1996). ‘Emission properties of pulsars at mm-wavelengths.’. *A&A* **309**:481–492.
- M. Xue, et al. (2017). ‘A Census of Southern Pulsars at 185 MHz’. *PASA* **34**:e070.

-
- M. Xue, et al. (2019). ‘MWA tied-array processing II: Polarimetric verification and analysis of two bright southern pulsars’. *PASA* **36**:e025.
- W. M. Yan, et al. (2011). ‘Rotation measure variations for 20 millisecond pulsars’. *Ap&SS* **335**(2):485–498.
- J. M. Yao, et al. (2017). ‘A New Electron-density Model for Estimation of Pulsar and FRB Distances’. *ApJ* **835**(1):29.
- X. P. You, et al. (2007). ‘Dispersion measure variations and their effect on precision pulsar timing’. *MNRAS* **378**(2):493–506.

Every reasonable effort has been made to acknowledge the owners of copyright material. I would be pleased to hear from any copyright owner who has been omitted or incorrectly acknowledged.

